

The impact of non-perturbative effects in dark matter production and detection

Dissertation

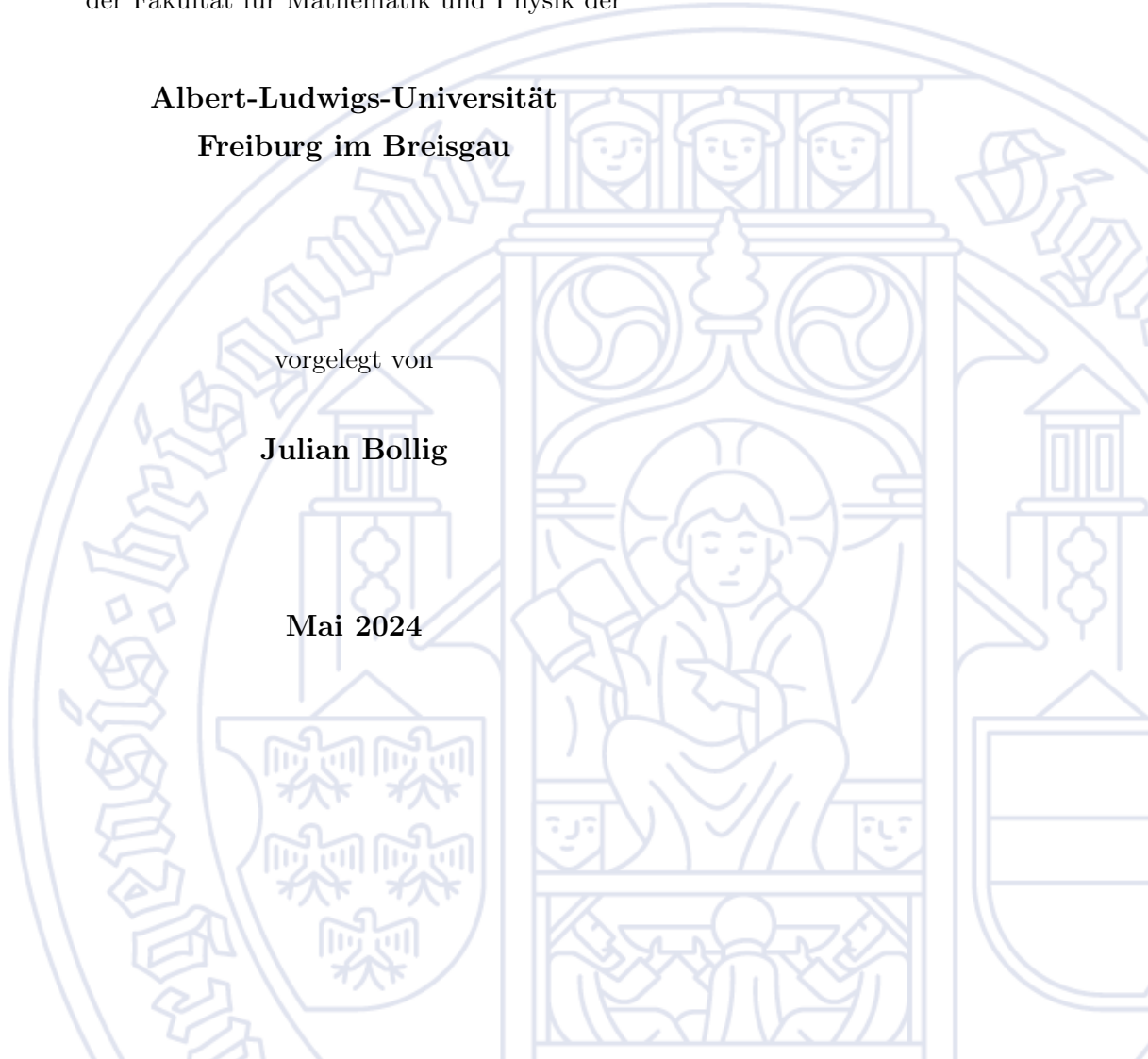
zur Erlangung des Doktorgrades
der Fakultät für Mathematik und Physik der

**Albert-Ludwigs-Universität
Freiburg im Breisgau**

vorgelegt von

Julian Bollig

Mai 2024



Dekan: Prof. Dr. Michael Růžička

Referent: JProf. Dr. Stefan Vogl

Korreferent: Prof. Dr. Heidi Rzehak

Tag der mündlichen Prüfung: 25.07.2024

Dark matter stands out as one of the most important unsolved mysteries in particle physics and cosmology. We investigate the influence of non-perturbative effects on the production of dark matter as well as their impact on direct and indirect detection to attain insight on its fundamental nature. Specifically, we focus on Sommerfeld enhancement and the formation of dark matter bound states both of which can alter the total dark matter annihilation cross section and thus modify dark matter observables in the early and late Universe. To this end, we conducted two studies focusing on different dark matter observables, which are likely to be probed by upcoming experiments.

In the first study, we investigate the production properties of a dark matter candidate with feeble couplings to Standard Model fermions mediated by a dark scalar in the TeV mass range. The scalar possesses Standard Model quantum numbers, allowing for a sizable new physics production cross-section at the LHC. By analyzing dark matter production through freeze-in and the superWIMP mechanisms, we discover a significant suppression of the dark matter yield in the latter due to non-perturbative effects, which favors higher masses for the scalar mediator. Thus, we conclude that testing this scenario, even after the HL-LHC upgrade, poses a greater challenge than anticipated.

For our second study, we focus on indirect detection properties of a dark matter candidate in the TeV mass range. It possesses scalar- and pseudo-scalar couplings to a massive dark mediator, which connects to the Standard model. Scalar interactions induce an attractive Yukawa potential in the dark sector, which facilitates non-perturbative effects. We discuss their impact on the relic density of dark matter and their effect on indirect detection. Regarding the latter, we examine current limits on indirect detection signals by Planck and Fermi-LAT as well as prospects from CTA. We find that large portions of the model's parameter space are testable in the near future.

Dunkle Materie ist eines der wichtigsten ungelösten Rätsel in der Teilchenphysik und Kosmologie unserer Zeit. Wir untersuchen den Einfluss von nicht-perturbativen Effekten auf die Produktion und den direkten wie indirekten Nachweis von Dunkler Materie, um Einblicke in ihre Natur zu erhalten. Insbesondere konzentrieren wir uns auf das Phänomen der Sommerfeld-Verstärkung und die Möglichkeit, Bindungszustände Dunkler Materie zu bilden. Beide Effekte können den Wirkungsquerschnitt der Annihilation von Dunkler Materie verändern und somit Dunkle Materie Observablen im frühen und späten Universum modifizieren. Zu diesem Zweck haben wir zwei Studien durchgeführt, die Fokus auf Observablen Dunkler Materie legen, welche aller Voraussicht nach durch bevorstehende Experimente getestet werden können.

In der ersten Studie untersuchen wir die Produktionseigenschaften eines Dunkle Materie Kandidaten mit sehr schwachen Kopplungen an Standardmodell-Fermionen, die durch einen dunklen Skalar im TeV-Massenbereich vermittelt werden. Der Skalar besitzt Standardmodell-Quantenzahlen, was einen beträchtlichen Wirkungsquerschnitt für die Produktion neuer Physik am LHC ermöglicht. Bei der Analyse der Produktion von Dunkler Materie über den Freeze-In- und SuperWIMP-Mechanismus entdecken wir eine signifikante Unterdrückung der Ausbeute an Dunkler Materie durch nicht-perturbative Effekte, die höhere Massen für den skalaren Mediator begünstigen. Wir kommen daher zu dem Schluss, dass die Testung dieses Szenarios, selbst nach dem HL-LHC-Upgrade, eine größere Herausforderung darstellt als vorher angenommen wurde.

In unserer zweiten Studie konzentrieren wir uns auf die indirekten Nachweis-Eigenschaften eines Dunkle Materie Kandidaten im TeV-Massenbereich. Dieser besitzt skalare und pseudoskalare Kopplungen zu einem massiven dunklen Mediator, welcher die Verbindung zum Standardmodell herstellt. Skalare Wechselwirkungen induzieren ein attraktives Yukawa-Potential im dunklen Sektor, das nicht-perturbative Effekte ermöglicht. Wir diskutieren ihre Auswirkungen auf die Reliktdichte Dunkler Materie und ihren Einfluss auf den indirekten Nachweis. In Bezug auf Letzteres untersuchen wir die aktuellen Grenzen für indirekte Nachweissignale von Planck und Fermi-LAT sowie die Aussichten für CTA. Wir stellen fest, dass große Teile des Parameterraums des Modells in naher Zukunft getestet werden können.

There are many people who have helped, supported and believed in me on this journey throughout the last couple of years. Words cannot express how grateful I am to have crossed paths with each and every one of you in one way or the other. However, to quote here a probably famous (or not so famous) person: Let me at least try!

First and foremost, I deeply want to thank my supervisor, JProf.Dr.Stefan Vogl, who has not only given me this chance in the first place but also courageously supported me at each step along the way. His deep understanding of the subject matter that he shared with me on numerous occasions and the advice he gave me, substantially let me grow as a scientist. On this note, I also thank Dr.Simone Biondini for a fruitful collaboration over the past years.

Further, I want to give credit to my research training group, in particular Prof. Dr. Markus Schumacher and my second supervisor, Prof. Dr. Stefan Dittmaier, not only for granting me funding and enabling me to enjoy conferences and workshops around the world but especially for maintaining a scientific community of fellow PhD students and Postdocs in Freiburg, I could share my experiences with.

Scientific work usually does not happen in a void, and it needs good colleagues to foster an (occasionally) productive environment. Therefore, my special thanks go to Maria Dias and Selina Machnitzky for cheering up my everyday and also bearing my grumpy moments. Moreover, I'd like to thank the PhD students and Postdocs from the Dittmaier working group, in particular Jan Schwarz, Yann Stoll, Tim Engel, Sebastian Schumacher, Jonas Rehberg, Max Reyer and José Lüis Hernando, for many joyful moments and memorable discussions. Out of the ones mentioned above, a shout-out goes to Maria Dias and Yann Stoll for accepting the ingrateful task of proofreading my first draft, I do owe you one!

Outside of the scientific context, I would like to thank my friends, which supported me in the last years and which I hold very dear. The deep connections I am grateful to have made with you, are my pillars in life. Sebastian Ochs, Elias Eulig, Felix Wolf, Thomas Pfeil, Felix Bitzer, Alexander Prill, Elisabeth Alexander, Florian Staudt and Alexander Holler: Thank you very much for the past years and the years to come.

Finally, I want to thank my family, in particular my parents and my grandmother. The unconditional love and support you gave me helped me to overcome all the hurdles life has confronted me with so far. I could have really not done it without you!

Contents

1	Preface	1
2	Introduction to cosmology	3
2.1	A very short history of the Universe	3
2.2	The Friedmann-Robertson-Walker Universe	4
2.3	The thermal history of the early Universe	7
3	Introduction to dark matter	11
3.1	Discovery and experimental evidence	11
3.2	Characteristics and possible candidates	14
3.3	Detection methods	16
4	Dark matter production in the early Universe	19
4.1	The Boltzmann equation – a general discussion	19
4.1.1	The Liouville operator in the FRW Universe	20
4.1.2	The integrated collision term	21
4.2	The Boltzmann equations for freeze-in and freeze-out	24
4.3	The thermally averaged cross section	27
5	Non-perturbative effects in dark matter interactions	29
5.1	Sommerfeld enhancement in particle annihilation and bound state decay	31
5.1.1	Schrödinger equations for scattering and bound states	31
5.1.2	Sommerfeld enhancement in particle annihilations	33
5.1.3	Sommerfeld enhancement in bound state decays	35
5.2	Non-perturbative effects from the Bethe-Salpeter approach	36
5.2.1	The Bethe-Salpeter wave equation	37
5.2.2	The bound state formation cross section	43
5.3	Non-perturbative effects from EFT	48
5.3.1	Non-relativistic EFT	49
5.3.2	Potential non-relativistic EFT	53
6	Non-perturbative effects in non-thermal dark matter production	59
6.1	The t -channel mediator model with feeble couplings	60
6.2	Non-thermal production mechanisms	61
6.3	Non-perturbative effects in dark matter production	65
6.3.1	Dark matter annihilation cross section and bound state decay rate	66
6.3.2	Bound state formation cross section and ionization rate	68
6.4	Dark matter abundance in the superWIMP mechanism	74
6.5	Model constraints from colliders and cosmological observations	78
6.6	The parameter space for non-thermal production	82

7	Non-perturbative effects in dark matter indirect detection	87
7.1	The dark matter model and energy scales	88
7.2	Dark matter production from pNREFT	91
7.2.1	Heavy pair annihilation and decay	91
7.2.2	Bound state formation and ionization	94
7.2.3	The relic density	100
7.3	Indirect detection	102
7.3.1	The dark matter distribution function f_χ	105
7.3.2	Generalized J -factors	109
7.3.3	The photon spectrum	112
7.3.4	Indirect detection bounds and prospects	117
7.4	Complementary searches	122
7.4.1	Direct detection and BBN limits	122
7.4.2	Electric dipole moments	123
7.4.3	Thermalization of the dark sector	124
7.5	The parameter space of thermal dark matter	125
8	Conclusion	129
	Appendices	131
A	Special functions	133
B	Partial wave analysis	139
C	The non-relativistic potential for different mediator interactions	142
D	Sommerfeld enhancement from the Bethe-Salpeter approach	147
E	Overlap integrals	151
F	BSF in thermal freeze-out from the Bethe-Salpeter approach	154
G	Higher bound states	156

List of Figures

2.1	The scaling of the energy density with the scale factor a	7
2.2	The evolution of the effective number of relativistic energy and entropy degrees of freedom.	9
3.1	Circular velocity of an exemplary galaxy as a function of the radius.	12
3.2	Temperature power spectrum of the CMB.	13
4.1	The yield of a particle species χ evolving over time for a typical freeze-in and freeze-out scenario.	26
5.1	Feynman-like diagrams for particle antiparticle annihilation and a BSF process of an interacting $\bar{\chi}\chi$ pair with SE present.	30
5.2	Decomposition of the 5-point Green's function.	44
5.3	The diagrams contributing to the imaginary part of the 4-point Green's function for EFT matching.	50
5.4	Matching of the 4-fermion Lagrangians between the NRY $_{\gamma_5}$ and pNRY $_{\gamma_5}$ theory via the off-shell 4-point Green's functions.	55
6.1	Contributions to the FI yield of DM from the most relevant production processes in the top-philic mediator model.	63
6.2	Leading order diagrams to $\mathcal{C}_{g\text{-amp}}^{(5)}$ in the top-philic mediator model.	69
6.3	Mediator mass scaling of the strong couplings arising in the top-philic mediator model.	71
6.4	Contributions to the overall annihilation cross section when considering non-perturbative effects.	75
6.5	The evolution of the mediator yield in the top-philic mediator model as a function of $x \equiv m_{\tilde{t}}/T$	77
6.6	Lower limits on the decay temperature and decay length of the mediator as a function of its mass in the top-philic and lepto-philic mediator model for various couplings λ_χ	79
6.7	The parameter space of non-thermal production in the top-philic and lepto-philic mediator model.	83
6.8	The parameter space for non-thermal production in the top-philic and lepto-philic mediator model, where the values of the Yukawa-like coupling λ_χ as well as the FI fraction p have been highlighted.	85
7.1	Hierarchy of the relevant energy scales in the model employed in Section 7.	90
7.2	The localized scattering state and BS self energy diagrams in pNRY $_{\gamma_5}$	91
7.3	The SE factors of s- and p-wave scattering states in $\bar{\chi}\chi$ pair annihilation for finite mediator masses.	93
7.4	The leading order self-energy contributions to the scattering state of a heavy $\bar{\chi}\chi$ pair from quadrupole and derivative interactions in pNRY $_{\gamma_5}$	95
7.5	The SE factor for BSF into the ground state for a finite mediator mass.	98
7.6	The SE factor for BSF into the ground state as well as its thermal average for selected values of ξ	98

7.7	The DM relic abundance in a FO scenario considering non-perturbative effects for different benchmark points.	101
7.8	Velocity dependence of the leading order contributions to the total DM annihilation cross section from s-wave and p-wave annihilation as well as BSF.	103
7.9	Generalized J -factors for the leading order s-wave and p-wave contributions as well as for BSF into the ground state.	111
7.10	Branching ratios of the mediator ϕ decaying into SM particles in the high mediator mass range.	114
7.11	Indirect detection limits on the perturbative cross section in s-wave and p-wave dominated DM annihilation scenarios.	120
7.12	Thermalization limits on the quartic $\lambda_{\phi h}$ coupling for different scenarios.	125
7.13	Slices through the cosmologically preferred parameter space in the m_χ - m_ϕ/m_χ plane for four benchmark values of α_5/α	127
C.1	Interaction kernel of a $2 \rightarrow 2$ scattering process exchanging an arbitrary number of mediators φ	143
D.1	Decomposition of the two-particle annihilation / BS decay Green's function into N final states.	148
F.1	Leading order diagrams to $\mathcal{C}_{\phi\text{-amp}}^{(5)}$ in the (pseudo-)scalar mediator model.	155
G.1	The SE factor of BSF into the n -th BS compared to the ground state as a function of ζ in the Coulomb limit.	160

List of Tables

6.1	Summary of all dark sector fields introduced in the simplified models considered in Section 6.	61
7.1	Astrophysical parameters of the DM halos for dSphs and the GC.	107
C.1	Potentials and fine structure constants from top-philic and lepto-philic mediator interactions with SM particles.	145

1 Preface

The existence of dark matter is one of the most pressing problems of modern physics. Despite our precise knowledge regarding its gravitational properties and abundance in the Universe, its fundamental particle nature remains elusive. Consequently, it also represents a severe shortcoming in the otherwise highly successful Standard Model of particle physics, lacking to provide us with a viable dark matter candidate. The specifics of its spin, interactions with itself, the Standard Model, or potential new particles in an extended dark sector remain unknown, and its possible mass ranges over fifty orders of magnitude [1–3].

Over recent decades, myriad efforts have been dedicated to shedding light on dark matter, both theoretically and experimentally. With numerous theoretical models proposing various dark matter signatures across a multitude of experimental setups, the experimental quest nowadays resembles searching for a needle in a haystack. Although searches in some piles of the hay have become quite advanced, so far no clear evidence for the needle has been found. Going forward with this strategy, it is essential that the straw that has been meticulously trawled through, can be thrown away, i. e. it is imperative to discard theories contradicting experimental observations. This necessitates robust predictions of dark matter observables from theoretical models when confronted with experimental data. Yet, due to the highly complex environments in which dark matter interacts across the cosmic epochs, accurate predictions still pose serious challenges in dark matter model building. When first proposing a viable parameter space for a certain model to be tested, typically a variety of different assumptions have to be imposed to enable analytical calculations or reach numerical conclusions with limited computing power. This inevitably increases the risk that significant effects, which could substantially influence the model's parameter space, are inadvertently being overlooked, because they are mistakenly estimated to be subleading.

In recent years, a particular set of previously overlooked effects has received a considerable amount of attention among the dark matter community (see Ref. [4] for a comprehensive overview and the references therein). This thesis aims to explore certain aspects of these effects in dark matter modelling and detection. The effects in question stem from non-perturbative self-interactions among dark matter particles in the non-relativistic regime, mediated by light bosonic particles with strong couplings to the dark matter candidates. Alongside Sommerfeld enhancement, our focus lies on the intriguing prospect of dark matter particles forming metastable bound states, potentially catalyzing dark matter annihilations and significantly influencing dark matter observables. These effects not only impact the overall dark matter abundance by altering production rates in the early Universe but also affect potential dark matter signals at late times.

To this end, we conducted two studies examining these effects within a class of dark matter models. These models were chosen for their sensitivity to these effects and their testability by upcoming experiments, rendering them particularly intriguing subjects for investigation. Both studies outlined in this thesis have been published and are accessible in Refs. [5, 6]. The first study delves into the influence of non-perturbative effects on dark

matter production rates in the early Universe, focusing on a non-thermal dark matter model with feeble couplings to the Standard Model heat bath. The second study also considers these effects on dark matter production but concentrates on their implications for indirect detection. This study employs a model featuring thermal dark matter with no direct couplings to the Standard Model, but rather interactions with a thermalized dark mediator.

We start with a concise overview on the principles of cosmology in Section 2, encompassing a short history of the Universe, its main properties at its earliest stages, and its thermal evolution. Moving forward to Section 3, we introduce the concept of dark matter, including experimental evidence, its primary characteristics, potential dark matter candidates, and methods for dark matter detection. Section 4 elaborates on quantifying the evolution of dark matter and introduces fundamental concepts for calculating its present-day observed abundance. In Section 5, we present two approaches to address the non-perturbative effects examined in this thesis. Sections 6 and 7 encompass two studies conducted by the author, focusing on non-perturbative effects in dark matter production and detection, which form the core of this thesis. We wrap up with concluding remarks in Section 8.

Conventions and notation:

In this thesis, we will adopt natural units, denoted as $c = \hbar = k_B \equiv 1$, unless explicitly stated otherwise. Additionally, 4-vector operations will adhere to the metric signature $(+, -, -, -)$. Greek lower case letters, such as $\mu, \nu = 0, 1, 2, 3$, will serve as indices for 4-vectors, while Latin lower case letters, like $i, j = 1, 2, 3$, will denote spatial indices. Bold variables, such as \mathbf{x} ($\hat{\mathbf{x}}$), will represent 3-dimensional (unit-)vectors, while non-bold vector quantities will either denote 4-vectors $x \equiv x^\mu$ or absolute values of 3-vectors $x \equiv |\mathbf{x}|$, as clear from the context. Time derivatives will be indicated by a dot, i.e. $\dot{y}(t, x)$, while other derivatives will be denoted as $y'(x)$ for brevity. Regarding spherical coordinates, $\Omega \equiv (\theta, \phi)$ will represent the solid angle with the measure $d\Omega = d\cos\theta d\phi$, where $\phi \in [0, 2\pi)$ denotes the azimuthal angle and $\theta \in [0, \pi)$ represents the polar angle. All values for physical constants and particle physics properties used in this work, have been extracted from the latest *Particle Data Group* review [7], if not referenced otherwise.

2 Introduction to cosmology

Starting with an introduction to cosmology, our aim is not to comprehensively cover the 13.8 billion years [8] of cosmological evolution. Instead, we aim to provide the reader with an overview of key concepts and terminologies relevant to this work. To compile this section, we have drawn inspiration primarily from Refs. [9, 10], although similar information can be found in numerous other books on modern cosmology.

We will commence with a concise overview of significant cosmological milestones in the Universe’s history in Section 2.1. Transitioning to Section 2.2, our focus will shift to elucidate the fundamental equations that govern the early Universe, providing a quantitative understanding of its expansion dynamics. Subsequently, in Section 2.3, we will introduce key variables to delineate the thermal evolution of the early Universe.

2.1 A very short history of the Universe

The *Big Bang* is defined as the time singularity of the metric used to describe the early Universe. It will serve as our temporal reference point. In its earliest stage, the Universe likely underwent a period of exceedingly rapid expansion, commonly referred to as *inflation* [11, 12]. This inflationary epoch effectively smoothed out any pre-existing spatial curvature and erased information regarding the initial particle composition. After the inflationary phase terminated, the Universe transitioned into a stage of *reheating* [13, 14]. During this phase, a substantial amount of energy was injected into the *Standard Model* (SM) sector, leading to the formation of an intensely hot and dense plasma consisting of SM and potentially *beyond Standard Model* (BSM) particles. This marks the starting point for our subsequent discussion. Although the temperature of the SM plasma after reheating can be as low as $T_{\text{rh}} \gtrsim 4 \text{ MeV}$ [15], in the remainder of this thesis, we will presume it to be well above the TeV scale. This assumption is made without specific considerations about the underlying details of the inflationary model.

As the temperature of the SM bath cools down, particles undergo a process of decoupling from the thermal plasma. This typically occurs when the expansion rate of the Universe surpasses the interaction rates of the particles in question with the surrounding plasma. As an example, neutrinos decouple at around 1 MeV. Subsequently, they become free streaming, meaning they propagate through the Universe without further scattering, and thereby constitute the *cosmic neutrino background* [16]. Detecting this background remains challenging up to present day due to the exceedingly weak interactions of neutrinos with the rest of the SM. The earliest remnants from the primordial Universe which have been observed so far, lie in the abundances of light elements, forming once the temperature drops below the binding energy of nucleons. This phenomenon, known as *Big Bang nucleosynthesis* (BBN), initiates at temperatures around $T \lesssim 1 \text{ MeV}$ [17, 18], corresponding to a cosmic age of approximately 3 min. Presently, constraints derived from these observations play a crucial role in establishing stringent bounds on the cosmological evolution of particles beyond the SM.

At the scale of approximately a few hundred keV, the thermal bath retains only a

significant abundance of protons, electrons, and photons. The enduring strong coupling between electrons and photons at these energies primarily arises from Thomson scattering ($e^- + \gamma \rightarrow e^- + \gamma$). As the temperature drops below the binding energy of hydrogen at a few eV, neutral hydrogen atoms begin to form during a phase called *recombination* [19, 20], occurring 260,000 – 380,000 years after the Big Bang. Recombination induces a sharp drop in the free electron density, rendering Thomson scattering inefficient, and thereby making the Universe transparent to photons for the first time. Subsequently, the photons from the SM bath decouple and have since traversed freely. They constitute the *cosmic microwave background* (CMB) [21, 22], a relic of this cosmological epoch occurring approximately 380,000 years following the Big Bang, which has been observed with remarkable precision. Its examination has yielded profound insights into the underlying physics governing cosmological evolution.

The great abundance of non-relativistic matter initiated a slow process of gravitational collapse, giving rise to the formation of the first stars, galaxies, and the emergence of large-scale structures. These transformative processes span durations extending from hundreds of millions to a few billion years and persist through to the present day.

2.2 The Friedmann-Robertson-Walker Universe

On cosmological scales, the Universe exhibits isotropy, meaning that its properties appear uniform in every direction. This observation leads to the inference of homogeneity, suggesting that the Universe is uniform not only as seen from Earth but at any point in space. Since the structures we see today have grown with time, cosmologists believe that at early stages, the Universe was nearly perfectly homogeneous and isotropic (apart from quantum fluctuations). This proposition is encapsulated in the *cosmological principle*, which imposes stringent constraints on the nature of space-time anticipated in the early Universe. In fact, there is just one (non-equivalent) metric which aligns with these criteria: the *Friedmann-Robertson-Walker* (FRW) metric, parametrized by

$$ds^2 = dt^2 - a(t)^2 \left[\frac{dr^2}{1 - \kappa^2 r^2} + r^2 d\Omega^2 \right] \quad (2.2.1)$$

in spherical space coordinates with $d\Omega \equiv d\cos\theta d\phi$ and κ a curvature parameter, which we subsequently set to zero in accordance with current experimental data [8].

The parameter $a(t)$ is the *scale factor* of the Universe, describing its expansion. The properties of particles in the Universe scale differently with $a(t)$. Obviously, distances grow proportional to $a(t)$, while particle momenta p scale with $1/a(t)$, which can be seen by employing the *geodesic equation* using an FRW metric. Likewise, the wavelength of massless particles like the photon $\lambda = 2\pi/p$ will scale with $a(t)$. This leads to the interesting concept of *redshift*, meaning that light emitted with a wavelength λ_1 at some point in the cosmological history will have a larger wavelength $\lambda_0 = a(t_0)/a(t_1)\lambda_1 > \lambda_1$ when it reaches us today. The redshift is usually parametrized by a parameter z , which is defined by

$$\frac{\lambda_0}{\lambda_1} \equiv 1 + z = \frac{a(t_0)}{a(t_1)}, \quad (2.2.2)$$

and can be used as an alternative measure of time to describe cosmological evolution. As a reference point, one usually sets $a(t_0) \equiv 1$ with t_0 denoting the age of the Universe today.

The dynamics of the Universe is governed by the *Einstein field equations*

$$G_{\mu\nu} = 8\pi G T_{\mu\nu}, \quad (2.2.3)$$

which relate the space-time curvature of the Universe encoded in the Einstein tensor $G_{\mu\nu}$ with its energy content parametrized by the energy-momentum tensor $T_{\mu\nu}$. Its proportionality is given by the gravitational constant G . The Einstein tensor is defined by

$$G_{\mu\nu} \equiv R_{\mu\nu} - \frac{1}{2}R g_{\mu\nu}, \quad (2.2.4)$$

where

$$R_{\mu\nu} \equiv \partial_\lambda \Gamma_{\mu\nu}^\lambda - \partial_\nu \Gamma_{\mu\lambda}^\lambda + \Gamma_{\lambda\rho}^\lambda \Gamma_{\mu\nu}^\rho - \Gamma_{\mu\lambda}^\rho \Gamma_{\nu\rho}^\lambda, \quad R \equiv R^\mu{}_\mu = g^{\mu\nu} R_{\mu\nu}, \quad (2.2.5)$$

are, respectively, the Ricci tensor and scalar, and $g_{\mu\nu} \equiv \text{diag}(1, -a(t)^2, -a(t)^2, -a(t)^2)$ denotes the FRW metric (in Cartesian spatial coordinates). The $\Gamma_{\alpha\beta}^\mu$ are called Christoffel symbols and describe a *metric connection*. They are given by

$$\Gamma_{\alpha\beta}^\mu \equiv \frac{1}{2}g^{\mu\lambda} (\partial_\alpha g_{\beta\lambda} + \partial_\beta g_{\alpha\lambda} - \partial_\lambda g_{\alpha\beta}) \quad (2.2.6)$$

and have to be calculated using the corresponding metric. The non-vanishing components of the Einstein tensor $G^\mu{}_\nu = g^{\mu\lambda} G_{\lambda\nu}$ for the FRW metric yield

$$G^0{}_0 = 3 \left(\frac{\dot{a}}{a} \right)^2, \quad G^i{}_j = \left[2 \frac{\ddot{a}}{a} + \left(\frac{\dot{a}}{a} \right)^2 \right] \delta_j^i. \quad (2.2.7)$$

From homogeneity and isotropy arguments one can argue that the energy-momentum tensor of the system must equal the one of a perfect fluid $T^\mu{}_\nu = \text{diag}(\rho, -P, -P, -P)$ in its rest frame, where the energy density ρ and pressure P are solely functions of time. They are linked through energy-momentum conservation

$$T^\mu{}_{\nu;\mu} \equiv \partial_\mu T^\mu{}_\nu + \Gamma_{\mu\lambda}^\mu T^\lambda{}_\nu - \Gamma_{\mu\nu}^\lambda T^\mu{}_\lambda = 0, \quad (2.2.8)$$

where the $\nu = 0$ component defines a continuity equation, given for the FRW metric by

$$\dot{\rho} + 3 \frac{\dot{a}}{a} (\rho + P) = 0. \quad (2.2.9)$$

The Universe is in general composed of three idealized components, which can be classified by their relation between energy density and pressure. Their difference in scaling with $a(t)$ can be deduced from Eq. 2.2.9. The first component is *matter* for which $|P| \ll \rho$ and therefore $\rho \propto a(t)^{-3}$, i. e. the dilution of energy density mirrors the expansion of the

volume $V \propto a(t)^3$. It is comprised of all non-relativistic particle species which are part of the SM and beyond at a given time. The second component is *radiation*, for which $P = \rho/3$ and thus $\rho \propto a(t)^{-4}$. For this type also the redshift of the energy $E \propto a(t)^{-1}$ has been included in the dilution. All relativistic particles such as photons and neutrinos as well as gravitational waves fall under this category. The third component is referred to as *dark energy* and has negative pressure $P \approx -\rho$ [8], which results in a constant energy density $\rho \propto a^0$. Not much is known about dark energy, except that it is needed to explain the accelerated expansion of the Universe we observe nowadays [23, 24]. The easiest way to include such a component into the cosmological picture, which is consistent with observations, is to add a cosmological constant $\Lambda g_{\mu\nu}$ to the Einstein field equations (which would exactly yield $P = -\rho$). Due to the different scaling of the energy density with $a(t)$, each of the three components has dominated the Universe for a certain period of time, as we can see in Fig. 2.1. In the beginning, the Universe has been dominated by radiation, the era we predominantly work in for the remainder of this thesis. At a redshift of $z \sim 3400$, or equivalently $a_{\text{eq}} \sim 2.9 \times 10^{-4}$, we reach matter radiation equality and the matter component takes over, approximately 60,000 years after the Big Bang. Within this era, most structure formation processes take place. Only very recently on cosmological time scales, at a redshift of $z \sim 0.4$ (or $\bar{a}_{\text{eq}} \sim 0.71$, ca. 9 billion years after the Big Bang), we have reached equality between matter and dark energy, such that today the latter is starting to dominate the overall energy density.

Combining our results for the Einstein and the energy-momentum tensor results in the *Friedmann equations*

$$\left(\frac{\dot{a}}{a}\right)^2 = \frac{8\pi G}{3}\rho, \quad (2.2.10)$$

$$\frac{\ddot{a}}{a} = -\frac{4\pi G}{3}(\rho + 3P), \quad (2.2.11)$$

where ρ and P are understood as the respective sum over the individual energy density and pressure components mentioned above. The first Friedmann equation as well as many other cosmological properties are usually written in terms of the *Hubble parameter* $H \equiv \dot{a}/a$ instead of a . This is especially convenient, because H is the expansion rate of the Universe at a given time. The first Friedmann equation can thus be recasted into the form

$$H^2(a) = H_0^2 \left[\Omega_{r,0} \left(\frac{a_0}{a}\right)^4 + \Omega_{m,0} \left(\frac{a_0}{a}\right)^3 + \Omega_{\Lambda,0} \right], \quad (2.2.12)$$

where H_0 is the *Hubble constant*, i. e. the value of the Hubble parameter measured today, $a_0 \equiv a(t_0) \equiv 1$ and the $\Omega_{X,0} = \rho_{X,0}/\rho_{\text{crit},0}$ denote the dimensionless density parameters (or *abundances*) of the different energy density components at present time, with $\rho_{\text{crit},0} = 3H_0^2/(8\pi G)$ the *critical energy density* today. Neglecting an additional component, which would arise from a non-zero curvature, $\Omega_r + \Omega_m + \Omega_\Lambda = 1$ is true at all times. The best fit values for the abundances today are $\Omega_{r,0} = 5.38(15) \times 10^{-5}$, $\Omega_{m,0} = 0.315(7)$, $\Omega_{\Lambda,0} = 0.685(7)$ with $H_0 = 100 h \text{ km s}^{-1} \text{ Mpc}^{-1}$ and $\rho_{\text{crit},0} = 2.8 \times 10^{11} h^2 M_\odot \text{ Mpc}^{-3}$, where $M_\odot = 1.988 41(4) \times 10^{30} \text{ kg}$ denotes the solar mass and $h = 0.674(5)$ [8].

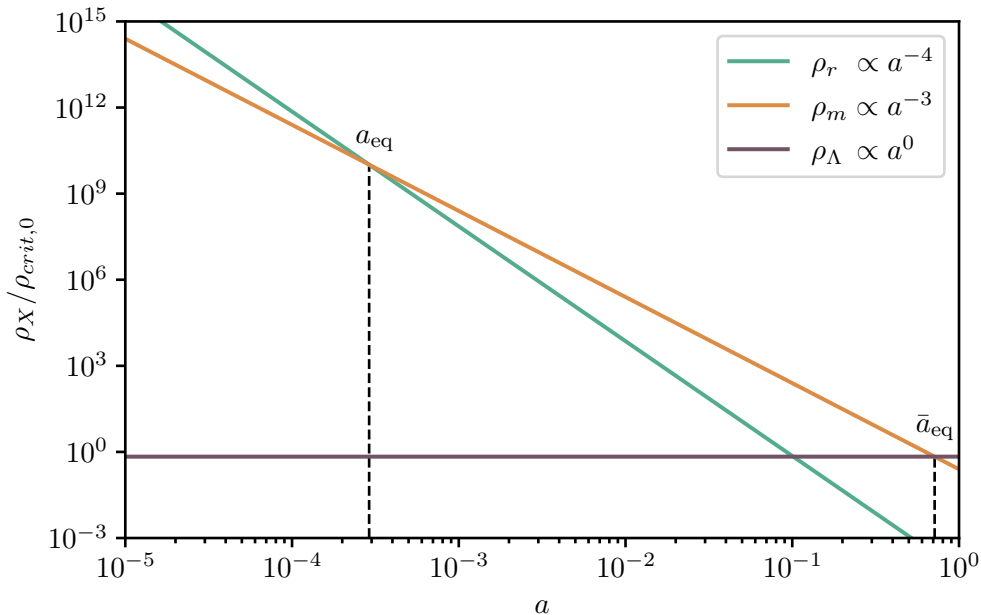


Figure 2.1: The scaling of the energy density (normalized by $\rho_{crit,0}$) with the scale factor a . Displayed are three different components: radiation (r), matter (m) and dark energy in form of a cosmological constant (Λ). Also shown are the points of matter radiation equality a_{eq} as well as dark energy matter equality \bar{a}_{eq} . The scale factor today is chosen to be $a(t_0) \equiv 1$.

2.3 The thermal history of the early Universe

From the perfect black-body spectrum of the CMB [8], we have sufficient evidence that the SM sector in the early Universe was in local *thermal equilibrium*. Thermal equilibrium (i. e. no net heat transfer) implies that two or more systems share the same temperature, which is true for the SM plasma. This allows us to use equilibrium thermodynamics in order to quantify the Universe at this stage.

We start by defining a distribution function $f(\mathbf{x}, \mathbf{p}, t)$ which quantifies how the particles and their momentum are distributed in a certain volume over time. As a consequence of homogeneity and isotropy in the early Universe, the distribution function of a bath particle should be independent of \mathbf{x} and only depend on the magnitude of the momentum $p = |\mathbf{p}|$. Leaving the time dependence implicit, we will work with $f(\mathbf{x}, \mathbf{p}, t) = f(p)$ in the following. *Kinetic equilibrium* is a statement about how efficiently energy between two or more systems can be exchanged on cosmological scales. If it is maintained, the distribution function of a particle species a with energy $E_a(p) = \sqrt{p^2 + m_a^2}$ equals a

Bose-Einstein or *Fermi-Dirac* distribution

$$f_a(p) \equiv \frac{1}{\exp \left\{ \frac{E_a(p) - \mu_a(T_a)}{T_a} \right\} \pm 1}, \quad (2.3.1)$$

depending on if the particles in question are bosons (−) or fermions (+). As we can see, the distribution function of a particle species in kinetic equilibrium depends on two macroscopic variables, its temperature T_a and its chemical potential $\mu_a(T_a)$ the latter of which characterizes the response of a system to a change in the particle number. For two or more systems in *chemical equilibrium*, there is no change in the concentration of the particles between the systems, implicating that the total chemical potential vanishes. Systems in chemical and kinetic equilibrium are also in thermal equilibrium and vice versa (see e.g. Ref. [25]). Therefore, we can replace the distribution functions for SM particles with their equilibrium values

$$f_a^{\text{eq}}(p) \equiv \frac{1}{e^{E_a(p)/T} \pm 1} \quad (2.3.2)$$

at a common temperature T , where we can safely assume all chemical potentials to be negligible at early times. For non-relativistic particles, we can reduce their distribution functions to a *Maxwell-Boltzmann* form $f_a^{\text{eq}}(p) \approx e^{-E_a(p)/T}$.

The *number density* of a particle species a , i.e. the number of particles of type a within a certain volume V , is defined as

$$n_a \equiv g_a \int \frac{d^3 p_a^3}{(2\pi)^3} f_a(p), \quad (2.3.3)$$

where g_a denotes their number of internal *degrees of freedom* (dof). The energy density and pressure of a species a can be defined likewise

$$\rho_a \equiv g_a \int \frac{d^3 p}{(2\pi)^3} f_a(p) E_a(p), \quad (2.3.4)$$

$$P_a \equiv g_a \int \frac{d^3 p}{(2\pi)^3} f_a(p) \frac{p^2}{3E_a(p)}. \quad (2.3.5)$$

Another important quantity for cosmological evolution is the entropy S of the Universe, which is conserved in thermal equilibrium. As we can neglect the insignificant enhancement of entropy from non-equilibrium processes at later stages, we can treat the expansion of the Universe as adiabatic, leading to a conservation of entropy throughout its evolution. It will be in the following more convenient to work with the *entropy density* $s \equiv S/V$ which can be related to the other thermodynamic variables via

$$s = \frac{\rho + P}{T} \quad \text{for } \mu = 0, \quad (2.3.6)$$

where a summation over all species is implicit. Its value today yields $s_0 = 2891 \text{ cm}^{-3}$.

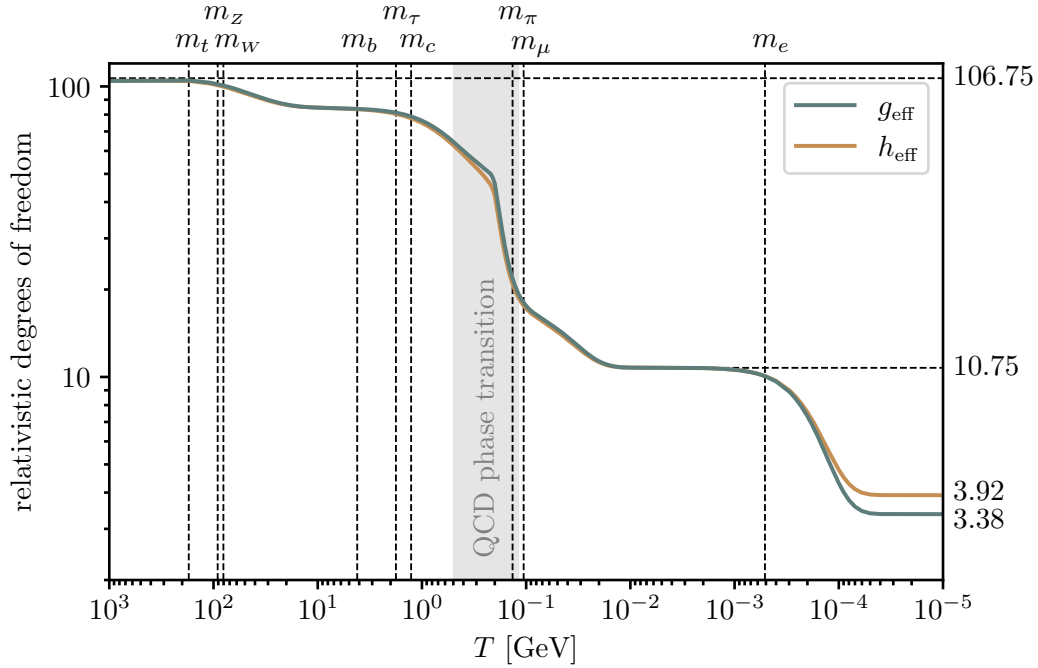


Figure 2.2: The evolution of the effective number of relativistic energy (g_{eff}) and entropy (h_{eff}) dof is depicted. Vertical lines correspond to masses of SM particles, while horizontal lines indicate important benchmark values. The temperature range at which the QCD phase transition occurs is shaded in gray. Adapted from Ref. [9] with data taken from Ref. [26].

For particles in thermal equilibrium, their number density can be determined via

$$n_a^{\text{eq}}(T) = \frac{g_a}{2\pi^2} T^3 \int_0^\infty du \frac{u^2}{e^{\sqrt{u^2 + (m/T)^2}} \pm 1}, \quad (2.3.7)$$

which is solely a function of T (as well as the particles mass) and has no analytical solution. However, we can find analytic approximations in the relativistic regime (where $m/T \ll 1$) and by using the Maxwell-Boltzmann approximation for f_a^{eq} .¹ They read

$$n_{a,\text{MB}}^{\text{eq}}(T) = \frac{g_a}{2\pi^2} m^2 T K_2\left(\frac{m}{T}\right), \quad n_{a,\text{rel}}^{\text{eq}}(T) = \frac{\zeta(3)}{\pi^2} g T^3 \begin{cases} 1 & \text{bosons} \\ \frac{3}{4} & \text{fermions} \end{cases}, \quad (2.3.8)$$

where $K_2(x)$ is the modified Bessel function of second order defined in Eq. A.8 and $\zeta(3) \approx 1.202$. Collecting contributions from all species (assuming a common temperature), the

¹In the subsequent sections, the Maxwell-Boltzmann ansatz will be used even in situations where particles are not necessarily non-relativistic. However, as long as the particles are not strictly massless, the differences with respect to the full relativistic treatment are expected to be small.

total energy and entropy density can be written as

$$\rho(T) = \sum_j \rho_j(T) = \frac{\pi^2}{30} g_{\text{eff}}(T) T^4, \quad (2.3.9)$$

$$s(T) = \sum_j \frac{\rho_j(T) + P_j(T)}{T} = \frac{2\pi^2}{45} h_{\text{eff}}(T) T^3, \quad (2.3.10)$$

where $g_{\text{eff}}(T)$ and $h_{\text{eff}}(T)$ are labelled the relativistic energy and entropy dof (see Ref. [27] for a detailed overview). Their name arises because they effectively count how many particles are still relativistic at a given temperature T and thus contribute to the total energy and entropy density in a radiation-dominated Universe. The evolution of $g_{\text{eff}}(T)$ and $h_{\text{eff}}(T)$ with the SM bath temperature is depicted in Fig. 2.2. At very high temperatures, when all SM bath particles are relativistic, they take on a value of 106.75, which is simply the sum of all bosonic dof ($g_b = 28$) plus the sum of all fermionic dof ($g_f = 90$), where the latter is multiplied by a factor of $7/8$. When a particle species a becomes non-relativistic around $m_a \gtrsim T$, its contribution to $g_{\text{eff}}(T)$ and $h_{\text{eff}}(T)$ gets suppressed by a factor $e^{-m_a/T}$. A severe drop in the relativistic dof happens around the confinement scale of *quantum chromodynamics* (QCD), $\Lambda_{\text{QCD}} \sim 400 \text{ MeV}$, when the quarks left in the plasma combine into hadrons, which are all non-relativistic (except pions) below the temperature of the QCD phase transition. After the decoupling of pions and muons, we are left with photons, electrons, and neutrinos in the SM bath, constituting a value of 10.75 at the onset of BBN around 1 MeV. The gap between $g_{\text{eff}}(T)$ and $h_{\text{eff}}(T)$ at very low temperatures is a result of their different scaling with T_ν/T , where T_ν denotes the neutrino temperature after decoupling.

We can combine Eqs. 2.2.10 and 2.3.9 to obtain an expression for the Hubble rate during the radiation dominated era, which is then given by

$$H(T) = \sqrt{\frac{4\pi^3}{45 M_{\text{Pl}}^2} g_{\text{eff}}^{1/2}(T) T^2}, \quad (2.3.11)$$

where we substituted the gravitational constant with the Planck mass via $M_{\text{Pl}} = G^{-1/2}$.

3 Introduction to dark matter

In the era of precision cosmology, it is possible to measure the baryonic content of the Universe, i. e. the amount of visible non-relativistic matter like hydrogen, helium etc. to percent level accuracy. Its measured value is $\Omega_{b,0} = 0.0493(6)$ [8], which constitutes about a fifth of the total energy density allocated to matter, today (cf. Section 2.2). The immediate question regarding the nature of the remaining matter content, which is not contained in visible objects, has puzzled cosmologists and particle physicists for almost a century. It has been given the name *dark matter* (DM) but up to the present day, it remains unclear, what this additional and very abundant matter contribution actually is.

While the structure and content of this section is based on Refs. [1, 3], the information presented about DM is also available in various other references. We will begin by providing a brief historical overview on the discovery of dark matter as well as its experimental evidence up to present day in Section 3.1. In Section 3.2, we will elaborate on the known properties of DM and classify different DM candidates. Finally, we will discuss the different detection methods for particle DM in Section 3.3.

3.1 Discovery and experimental evidence

The first evidence of DM has been observed in galaxy clusters. In 1933, the astronomer Fritz Zwicky studied the redshift of various galaxy clusters [28] using an analysis, which had been published two years prior by Edwin Hubble and Milton Humason [29]. He took particular interest in the Coma Cluster, for which he calculated the average velocity dispersion of the ≈ 800 galaxies within it by applying the *virial theorem*.² By making additional assumptions about the average masses of the galaxies obtained from visible matter sources as well as the physical size of the gravitationally bound system, he obtained an average velocity dispersion of ~ 80 km/s, which was in great contrast to the averaged observed dispersion of ~ 1000 km/s along the *line of sight* (LoS). He deduced from this comparison a large abundance of non-luminous matter within the cluster.

Although similar observations were made in other clusters in the following years, it would take over three decades, until the idea of missing mass in the Universe had been established among cosmologists. A game changer, which convinced many physicists that the DM problem was real, had been measurements of galaxy rotation curves performed by Vera Rubin and Kent Ford in the 1970's [30, 31]. Ken Freeman soon realized that the shape of these rotation curves cannot be explained by luminous matter alone [32], an argument which was later extended and linked to the missing mass problem in galaxy clusters by Jaan Einasto, Jim Peebles and others [33, 34]. The circular velocity of a

²The virial theorem connects the average kinetic energy of a particle system bound by a conservative force (like gravity) with its average potential energy. It can be applied to galaxy clusters, since the diameter of the galaxies within the cluster (~ 100 kpc) is much smaller than the diameter of the cluster itself (~ 10 Mpc).

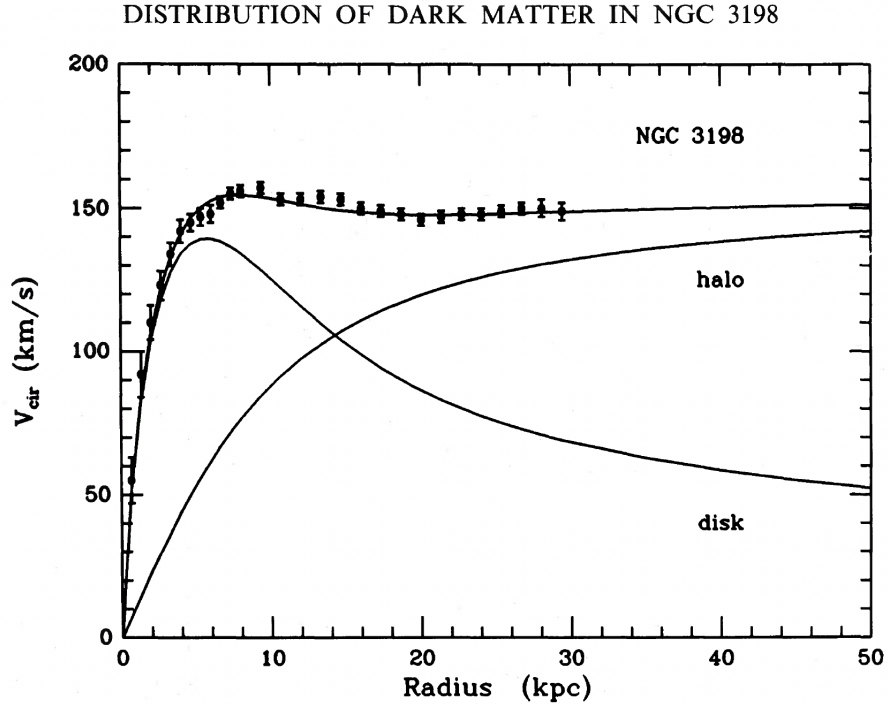


Figure 3.1: Circular velocity of an exemplary galaxy as a function of the radius. Displayed are the theoretical expectations from a luminous galactic disk, a DM halo and a combination of both. Experimental data is shown as dots with respective error bars. Taken from Ref. [35].

galactic object is given by

$$v_{\text{cir}}^2(r) = \frac{GM(r)}{r}, \quad (3.1.1)$$

with $M(r)$ being the enclosed mass in a spherical volume with radius r . As sketched in Fig. 3.1 for an exemplary galaxy, the circular velocity of a galactic disk of luminous matter is expected to rise linearly $v(r) \propto r$ in the inner part, where the matter density is approximately constant. This rise would then be followed by a $v(r) \propto r^{-1/2}$ decay in the outer parts of the galaxy, where luminous matter becomes dilute. However, the measurements strongly indicate a plateau outside of the galactic disk, hinting towards a spherical and invisible matter halo with a density $\rho(r) \propto r^{-2}$ accompanying it and thus greatly extending the size of the galaxy.

Another strong evidence for DM, which is particularly important for a better understanding of its nature, has been observed in a collision of two galaxy clusters, nowadays famously known as the *bullet cluster* [36]. The ionized gas within the two colliding systems interacts through SM processes and thus experiences a drag force. It would remain behind as the accompanying DM halos passed through each other without collision. Exactly this behaviour has been observed in the bullet cluster. The the location of the

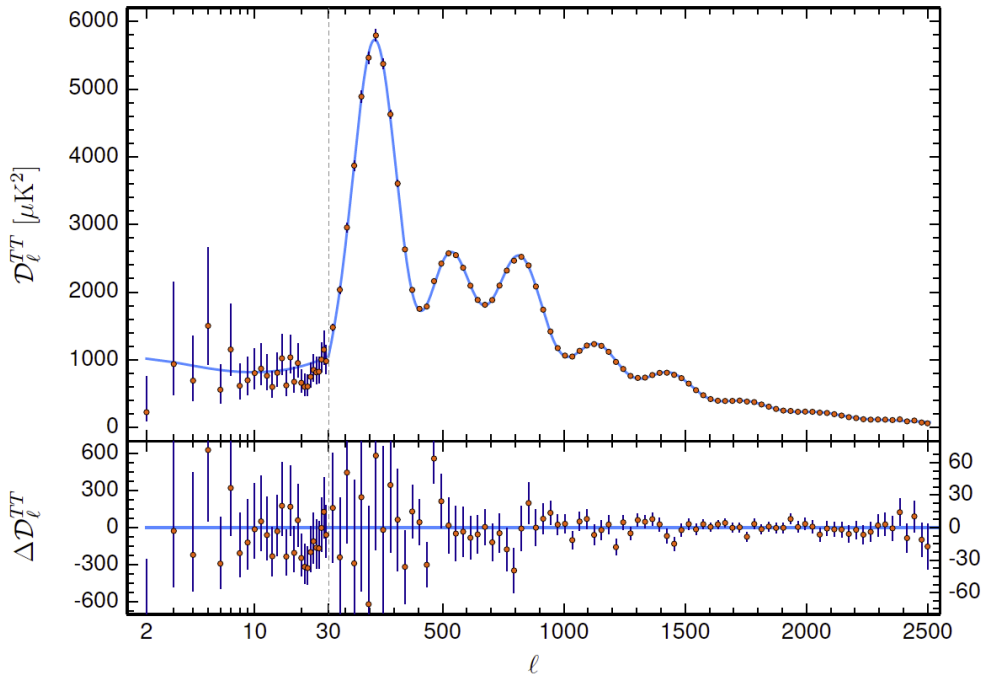


Figure 3.2: Temperature fluctuations of the CMB in terms of the two-point correlation functions expanded in spherical harmonics with angular modes l (also sometimes called *CMB power spectrum*). The continuous line represent the best-fit function from the Λ -cold dark matter (Λ CDM) model. Taken from Ref. [8].

heated gas was measured there by X-ray surveys, whereas the DM concentration could be determined through *gravitational lensing*.³

The most precise measurements of the different energy components in the Universe, including the matter content observed today, stem from the cosmological model describing the temperature fluctuations of the CMB [8].⁴ The so-called Λ CDM model, represented by the continuous line in Fig. 3.2, has been a huge success in describing these primordial deviations. It requires a total of six input parameters, which have been fitted to the data collected by various surveys over the last decades. The figure itself contains measurements of the two-point correlation function of the temperature fluctuations expanded in spherical harmonics. The height and width of the peaks of the function contain information about the values of the different abundances which have been stated in the

³Gravitational lensing is a powerful method to observe mass concentrations, in particular of matter which does not emit photons and, thus, cannot be easily be detected otherwise. It is agnostic to possible SM interactions of the matter in question, as it relies on the bending of light through massive objects within the LoS.

⁴Other important observations to constrain the cosmological abundances of certain energy components, on which we will not comment on further, come from supernovae measurements [37] and *baryon acoustic oscillations* [38].

beginning of this section as well as in Section 2.2. Its prediction for the present day DM abundance yields $\Omega_{\text{DM},0} = 0.265(7)$ [8]. The Λ CDM model, also known as *Standard Model of Cosmology*, conflates our modern understanding of the Universe with DM as a necessary but yet poorly understood component.

3.2 Characteristics and possible candidates

Over the years, it has been possible to derive certain characteristics, DM should possess. To sum it up, a viable DM candidate needs to be dark, cold, stable, collisionless, and non-baryonic. What is meant by these terms will be discussed in the following. First and foremost, it should be *dark*, meaning that its couplings to SM particles should be small. Particularly, this implies that DM must be (almost) electrically neutral. This is necessary to avoid detection and to allow it to form halos around galaxies without collapsing into disk-like structures, as is true for baryonic matter (see, for example, Ref. [39]). Further, DM must be sufficiently *cold*, i. e. it must be non-relativistic during the epoch of structure formation. This constraint comes from the observation of large scale structures, which prefer theoretical results computed using cold (non-relativistic) over hot (relativistic) DM already in the regime, where linear perturbation theory can be applied. These observations are reflected in CMB data, which requires non-relativistic DM to account for the growth of small perturbations in the power spectrum. At smaller scales, probed usually by galaxy surveys, numerical N-body simulations are needed to accurately describe the formation of structure. Here, the mismatch for hot DM becomes even more apparent (see e. g. Ref. [40]), leading to robust constraints on the velocity of DM at late times. For thermally produced DM (cf. Section 4), it is also possible to put a stringent constraint of $\gtrsim \mathcal{O}(\text{keV})$ on its mass (see e. g. Ref. [41]). Since the effects of DM have been observed on a variety of different time scales (from the CMB up to present day), it must be sufficiently *stable*. This means that DM annihilation or conversion processes into SM (and potential BSM) particles had to become inefficient at early times and DM decay rates must be very slow on cosmological time scales. Stringent limits on metastable DM are very model dependent. As mentioned in the discussion of the bullet cluster in Section 3.1, DM needs also to be *collisionless*, meaning that its self-interactions and the dissipation of kinetic energy into other particles must be small. This also ensures, that DM halos are almost spherical. Current bounds on the DM self-interaction cross section are $\sigma/m_{\text{DM}} \lesssim 1 \text{ cm}^2/\text{g}$ [4]. Finally, DM must be of *non-baryonic* nature. This requirement is clear from the previous discussion of CMB constraints but it is also imposed by BBN, as DM cannot play a measurable role in the formation of light elements.

In the discussion above, we have implicitly assumed that DM has a particle nature, i. e. that it consists of one (or more) elementary or composite particles, which we have not yet discovered. Although this possibility is by far the most accepted within the cosmology and (astro-)particle physics community (and also the one we will consider throughout this thesis), we will briefly highlight two other options, which have gained some attention. The first one is known under the label of *modified Newtonian dynamics* (MOND) [42–44]. The original idea is that in opposition to Newtons second law, the gravitational force

scales as $F = ma^2/a_0$ in the limit of very low accelerations ($a \ll a_0 \sim 1.2 \times 10^{-10} \text{ m/s}^2$). This would give an explanation for the observed motion of stars and gas within a galaxy without additional matter, meaning that this theory gets by without the need of DM. While successful in predicting the correct rotation curves of galaxies, no implementation of MOND to date can fully account for all the phenomena caused by DM on different cosmological scales. Even the so far most elaborate theory of MOND, known as *Tensor-Vector-Scalar gravity* [45] has yet to explain the observations of DM made in the bullet cluster. Although not entirely impossible, this explanation for DM seems highly unlikely, as it requires modifying the well-tested theory of *general relativity*, a challenge in itself.

The second alternative to particle DM has been historically the first plausible candidate for DM entertained among the astrophysics community. It comprises *massive astrophysical compact halo objects* (MACHOs) such as planets, brown dwarfs, red dwarfs, white dwarfs, neutron stars and black holes, i. e. astronomical objects which are much fainter than ordinary stars. As these are made of baryonic matter, it has been ruled out by CMB and also BBN measurements alongside surveys which measured *microlensing* events in galaxies (see e. g. Ref. [46]), that MACHOs which formed during structure formation could account for a considerable amount of the mass missing in galaxies. There is however one caveat which still allows for one specific type of these objects, namely black holes which have formed prior to BBN, so-called *primordial black holes* [47, 48]. If light enough, they can evade bounds from microlensing surveys and would not be considered as classical baryonic matter, which clustered into macroscopic objects at a much later stage. Up to present day, there is an active community exploring primordial black holes as DM candidates as well as their implications on the physics of the early Universe.

As mentioned above, for the remainder of this thesis, we will assume that DM has a particle nature. Armed with knowledge about the criteria that DM candidates must meet, we can start to categorize them. As there are numerous possibilities from a model building perspective, we will restrict ourselves here to the most prominent solutions to the DM problem (see e. g. Refs. [1, 49] for a broader overview). The most intuitive approach to start with is to look for a DM candidate within the SM of particle physics. The only viable option at first glance are SM neutrinos, as they are stable, electrically neutral and weakly interacting. However, it has been shown, that SM neutrinos cannot account for a considerable amount of DM as they are too light and therefore too hot to explain the large scale structures in the Universe. Nevertheless, if there were an additional neutrino species with a mass in the keV range or higher, it could realistically make up for DM. This viable DM candidate offers a rich phenomenology and has become widely known as *sterile neutrino* [50–52].

Another possibility to introduce a new particle which can account for DM emerged from the hunt for solutions to the *strong CP-problem* of QCD. At heart, this problem is related to a CP-violating term in the QCD Lagrangian. The relevance of this term is related to a quantity $\bar{\theta}$, which can, in principle, be of $\mathcal{O}(1)$ but has been found to be smaller than $\lesssim 2 \times 10^{-10}$ from measurements of the electric dipole moment of the neutron [53]. A popular theoretical explanation for this “unnatural” small value, is the proposal of a spontaneously broken global $U(1)$ symmetry (the *Peccei–Quinn symmetry*), which drives

$\bar{\theta}$ dynamically towards zero [54, 55]. This introduces a Nambu-Goldstone boson, the so-called *axion*, which acquires a small mass through an explicit breaking of the symmetry [56, 57]. Within a mass range of $m_a \sim 10^{-6} - 10^{-4}$ eV, those metastable particles could have been produced in the early Universe through the *vacuum misalignment* mechanism in a sufficient amount to constitute for DM. A relaxation of the requirement to solve the strong CP-problem, led to an even richer phenomenology of *axion-like particles* (ALPs), which together with the original QCD-axion have become one of the most studied DM candidates so far [58, 59].

In the 1990s it had been realized, that an electrically neutral self-annihilating particle with a cross section of $\sim 10^{-26}$ cm³/s undergoing thermal freeze-out (cf. Section 4) can precisely account for the DM content observed today. As this cross section is very close to cross sections arising in weak interactions, it was assumed that DM could consist of new stable particles with masses in the MeV – TeV regime that interact on the electroweak scale. These *weakly interacting massive particles* (WIMPs) have become subject to countless theoretical studies and experimental searches over the last few decades [60, 61]. The term WIMP itself is quite generic and encompasses a broad range of more refined theories. In many studies, WIMPs have been implemented into theoretically complete extensions of the SM such as *supersymmetric theories*, where the lightest supersymmetric partners are WIMP DM candidates [62]. In the era of particle colliders which can probe physics up to the TeV scale, it will become clear whether the WIMP paradigm proves successful, requires modification, or declines in favor of other DM models.

With so many different options to choose from, the model building community has in recent years shifted from DM candidates embedded in *ultraviolet* (UV) complete theories like supersymmetry, towards *simplified models* [63–65]. Within these models it has become easier to study certain characteristics of DM candidates, like their self-interacting properties as well as a variety of different couplings to SM particles that DM might possess. Also extensions to the dark sector which comprise more than one new particle can now be studied with considerably less effort. From the cosmological evolution of these particles as well as their detection signatures, one can draw conclusions about the nature of particle DM without relying on a specific theory. In Sections 6 and 7 we will employ simplified models to study the impact of non-perturbative effects on DM observables.

3.3 Detection methods

The quest for DM continues as there has been, so far, no clear evidence for a signal which can be traced back to particles beyond the SM. Considering a thermally or non-thermally (cf. Section 4) produced WIMP-like particle in the MeV – TeV mass range, there are three fundamentally different ways to search for DM, namely collider signals, direct and indirect detection.⁵ All of them will be used in the following to constrain

⁵There is the additional option to search for DM through its gravitational interactions. However, as valuable as they have been to explore general characteristics of DM, these experiments will usually not reveal information about its particle content. As an exception, there are very recent proposals to search for DM using *gravitational wave* signals (see e. g. Ref. [66]).

the phenomenology of our simplified models (cf. Sections 6 and 7), which is why we will comment on them briefly in the subsequent discussion (see e. g. Refs. [61, 67–70] for more comprehensive overviews).

If DM or other particles in the dark sector possess non-negligible couplings with SM particles, they are produced in collider experiments provided that they are light enough. The most prominent collider experiments at the moment to search for BSM particles are ATLAS [71] and CMS [72] at the *Large Hadron Collider* (LHC). Both are able to probe new physics up to the TeV scale. How to search for a new particle in collider experiments highly depends on its properties, i. e. what its interactions with SM particles are, what the expected mass range is, which charges and spin it possesses and if it is stable on collider scales. A collection of various searches for WIMP-like DM and BSM particles with different properties conducted by both experiments can be found in Refs. [73, 74]. For our study in Section 6, we will restrict ourselves to charged scalars in the TeV mass range, which do not decay inside of the experiment.

There is a large class of DM candidates (e. g. WIMPs) which can undergo scattering with atomic nuclei or their accompanying electrons via either spin-independent or spin-dependent couplings. One can look for these scattering processes in *direct detection* experiments [67, 75]. Although there are many different working principles of direct detection experiments, there are also commonalities among most of them: Firstly, they are “passive” experiments, i. e. they take advantage of the large abundance of DM around us and wait, until a DM particle scatters with the detector material. The energy deposited in the material can then be detected. From the absence of a signal, they can put upper limits on the DM-nucleus cross section. In order to detect these extremely rare scattering events, direct detection experiments require an extremely low background. They are typically situated deep underground to shield them from cosmic radiation, and they use highly purified materials for both the detector medium and supporting scaffold. The three leading direct detection experiments today for DM masses above 1 GeV all operate with liquid xenon. They are called PandaX [76], XENONnT [77], and LZ [78]. We will employ direct detection constraints in Section 7 to determine the maximally allowed coupling of dark sector particles to the SM.

The third possibility to search for DM is through *indirect detection* [79–81]. This type of experiments can probe DM which annihilates or decays into SM particles. The ways to search for indirect detection signals are quite diverse. One can, for example look for effects on the anisotropies in the CMB caused by late time energy injection from the dark sector into the SM. This can be achieved with microwave telescopes. Notably, for the upcoming discussion, emphasis will be placed on the results from the *Planck satellite* [82]. Another possibility is to search for cosmic signals from decaying or annihilating DM in overdense regions.⁶ Prominent candidates to detect by these experiments are cosmic rays (highly energetic ionized particles like antiprotons [83–85] or positrons [86–88]), X- or gamma-rays (highly energetic photons) [89–94], and neutrinos [95–97]. Searching for

⁶These annihilations or decays must be inefficient enough not to alter the DM abundance observed today in a detectable amount to match the stability criterion.

each of these remnants possesses unique strengths and limitations. The relative simplicity of detection, along with the unimpeded travel of photons from their source to Earth, renders gamma-rays particularly intriguing. Concretely, we will be interested in results from surveys of DM dominated satellite galaxies of the Milky Way and the Andromeda Galaxy [98]. Of great importance in the following will therefore be the *Fermi Large Area Telescope* (Fermi-LAT), which is installed on the Fermi gamma-ray Space Telescope [99], and the *Cherenkov Telescope Array* (CTA) [100], a next-generation ground-based gamma-ray experiment, which is currently under construction and will be commissioned in the near future. We will use existing gamma-ray data on dwarf spheroidal galaxies from Fermi-LAT as well as prospect data on the galactic center of the Milky Way provided by the CTA collaboration, alongside with Planck data on CMB anisotropies, for our phenomenological discussion in Section 7.

4 Dark matter production in the early Universe

The change in the abundance of DM in the early Universe depends on the initial DM abundance after reheating as well as its interactions with the SM bath. The latter also determine whether DM is initially in thermal equilibrium with the SM heat bath and how long chemical and kinetic equilibrium with the SM can be maintained (cf. Section 2.3).

We will focus in the following on two scenarios which are important for the subsequent discussion, namely *freeze-out* (FO) and *freeze-in* (FI). In FO, DM particles are initially in thermal equilibrium with the SM heat bath. When annihilation or, more generally, conversion processes into SM particles become slow compared to the expansion rate of the Universe, i. e. the conversion rate $\Gamma_{\text{conv}} \ll H$, they drop out of chemical equilibrium and the DM abundance becomes constant. This commonly happens when DM particles become non-relativistic ($m_{\text{DM}} \gg T$). Further assuming no (asymmetric) energy injection into the two now chemically decoupled sectors, they will maintain the same temperature until kinetic decoupling, which typically happens much later. In FI, DM never reaches thermal equilibrium with the SM and the initial DM abundance is assumed to be negligible. DM gets produced through SM conversion processes, which typically leave the momentum distributions of the particles involved thermal. Therefore, also here, a common temperature is approximately retained. When the DM production processes become inefficient, the DM abundance again levels off.

We will start by introducing the set of equations that, for our purpose, sufficiently describe the evolution of DM in the early Universe in Section 4.1. In Sections 4.1.1 and 4.1.2, we calculate both sides of the equations separately and merge them for typical FI and FO scenarios in Section 4.2. Section 4.3 deals with the calculation of the thermally averaged cross section, a quantity needed to describe the $2 \rightarrow 2$ processes governing FO and FI for our scenarios of interest.

4.1 The Boltzmann equation – a general discussion

The evolution of DM in the early Universe is commonly described using a semi-classical approach, known as the *Boltzmann equation* (BE), which models DM as a homogeneous and isotropic particle fluid in an expanding background. This approach is applicable to particle species with de Broglie wavelengths much shorter than the size of the Universe.⁷ For our subsequent calculation of the DM number density to describe its evolution, we will follow the discussion in Kolb and Turner’s book [25] together with the improved analysis by Gondolo and Gelmini [101]. In doing so, we will adopt the BE as it offers a convenient framework. A detailed derivation of the BE using kinetic theory can be found, for example, in Ref. [102].

The BE for a species a with a distribution function f_a in its most general form can be written as

$$\hat{L}[f_a] = C[f_a], \quad (4.1.1)$$

⁷This condition holds for most particle DM models, particularly for non-relativistic DM with masses well above the keV range, which is our main focus.

where \hat{L} is the *Liouville operator* encapsulating the space-time effects of the background metric and $C[f_a]$ denotes the *collision term*, which specifies all interactions of the species with the other particles present in the plasma. Note that, in principle, the *right-hand side* (RHS) of the BE contains all possible kinematic processes of species a involving an arbitrary number of particles. However, we will focus in the following on $1 \rightarrow 2$ and $2 \rightarrow 2$ processes only. Since we are usually interested in the whole species a at a certain time t , we integrate over the full Lorentz invariant momentum space

$$g_a \int \frac{d^3 p_a}{(2\pi)^3 E_a} \hat{L}[f_a] = 2g_a \int d\Pi_a C[f_a] \equiv \sum_i \mathcal{C}_i, \quad (4.1.2)$$

where we introduced the Lorentz-invariant phase-space measure as

$$d\Pi_a \equiv \frac{d^3 p_a}{(2\pi)^3 2E_a}, \quad (4.1.3)$$

with g_a being the internal degrees of freedom of species a and $E_a = \sqrt{p_a^2 + m_a^2}$ its energy given by the usual energy momentum relation. The *integrated collision term* $\sum_i \mathcal{C}_i$ contains all interaction processes i involving the target species. We will calculate both sides of Eq. 4.1.2 for our models of interest in the following.

4.1.1 The Liouville operator in the FRW Universe

The Liouville operator is defined as

$$\hat{L}[f_a] \equiv p_a^\alpha \frac{\partial f_a}{\partial x_a^\alpha} - \Gamma_{\beta\gamma}^\alpha p_a^\beta p_a^\gamma \frac{\partial f_a}{\partial p_a^\alpha}, \quad (4.1.4)$$

where the Christoffel symbols $\Gamma_{\beta\gamma}^\alpha$ in our case are calculated using the FRW metric (cf. Section 2.2). Relabelling $x_a^0 = t$, $p_a^0 = E_a$, $|\mathbf{p}_a| = p_a$ and accounting for homogeneity ($\partial f_a / \partial x_a^i = 0$) and isotropy ($\mathbf{p}_a \cdot \nabla f_a = 0$), i.e. $f_a = f_a(p_a, t) = f(E_a, t)$, the Liouville operator yields

$$\hat{L}[f_a] = E_a \frac{\partial f_a}{\partial t} - H p_a^2 \frac{\partial f_a}{\partial E_a}, \quad (4.1.5)$$

with H the Hubble parameter defined in Eq. 2.3.11. Recalling the definition of the number density n_a of a species a from Eq. 2.3.3 and inserting \hat{L} into the *left-hand side* (LHS) of Eq. 4.1.2, we obtain

$$(\text{LHS}) = \frac{\partial}{\partial t} \left(g_a \int \frac{d^3 p_a}{(2\pi)^3} f_a(p_a, t) \right) - H g_a \int \frac{d^3 p_a}{(2\pi)^3} \frac{p_a^2}{E_a} \frac{\partial f_a}{\partial E_a} = \dot{n}_a + 3H n_a, \quad (4.1.6)$$

where we used $\partial E_a / \partial p_a = E_a / p_a$ to rewrite the respective derivative of f_a and then partially integrated the second term.

It is favorable to re-express the LHS in terms of the yield $Y_a \equiv n_a/s$, a quantity which is (unlike $n_a \propto a(t)^{-3}$) independent of the expansion of the Universe. This can

be seen easily because the total entropy of a unit volume $S = s(t)a(t)^3$ in the Universe is approximately conserved throughout its history (cf. Section 2.3) and thus the entropy density $s(t) \propto a(t)^{-3}$ at all times. Assuming entropy conservation, we can use $ds/dt = -3Hs$ to check that

$$s \frac{dY_a}{dt} = s \frac{d(n_a/s)}{dt} = \frac{dn_a}{dt} - \frac{n_a}{s} \frac{ds}{dt} = \dot{n}_a + 3Hn_a. \quad (4.1.7)$$

We also want to switch from a time to a (thermal bath) temperature dependence of Y_a , since it is the more natural variable to work with in this context. The relation between time and temperature can also be obtained from entropy conservation. Since $s \propto h_{\text{eff}}(T)T^3$ (cf. Eq. 2.3.10), from $dS/dt = 0$ we obtain [103]

$$\frac{dT}{dt} = -HT \left(1 + \frac{1}{3} \frac{T}{h_{\text{eff}}} \frac{dh_{\text{eff}}}{dT} \right)^{-1} = -HT \frac{h_{\text{eff}}}{g_{\text{eff}}^{1/2}} g_{\star}^{-1/2}, \quad (4.1.8)$$

where we have defined the modified relativistic effective dof

$$g_{\star}^{1/2} \equiv \frac{h_{\text{eff}}}{g_{\text{eff}}^{1/2}} \left(1 + \frac{1}{3} \frac{T}{h_{\text{eff}}} \frac{dh_{\text{eff}}}{dT} \right) \quad (4.1.9)$$

with respect to the relativistic energy and entropy dof (cf. Fig. 2.2) for later convenience.⁸ Combining Eqs. 4.1.6 to 4.1.8, the LHS of the integrated BE yields

$$(\text{LHS}) = s \frac{dY_a}{dt} = s \frac{dT}{dt} \frac{dY_a}{dT} = -sHT \frac{h_{\text{eff}}}{g_{\text{eff}}^{1/2}} g_{\star}^{-1/2} \frac{dY_a}{dT}. \quad (4.1.10)$$

4.1.2 The integrated collision term

The RHS of Eq. 4.1.2 highly depends on the form of interactions the target species participates in. In all generality, for a process $a + b + \dots \rightarrow i + j + \dots$ the integrated collision term is given by

$$\begin{aligned} \mathcal{C}_{a+b+\dots \rightarrow i+j+\dots} &= - \sum_{\text{dof}} \int d\Pi_a d\Pi_b \dots d\Pi_i d\Pi_j \dots \\ &\quad (2\pi)^4 \delta^{(4)}(p_a + p_b + \dots - p_i - p_j - \dots) \\ &\quad \left[|\mathcal{M}|_{a+b+\dots \rightarrow i+j+\dots}^2 f_a f_b \dots (1 \pm f_i)(1 \pm f_j) \dots \right. \\ &\quad \left. - |\mathcal{M}|_{i+j+\dots \rightarrow a+b+\dots}^2 f_i f_j \dots (1 \pm f_a)(1 \pm f_b) \dots \right]. \quad (4.1.11) \end{aligned}$$

The $|\mathcal{M}|_{a+b+\dots \leftrightarrow i+j+\dots}^2$ denote the squared matrix elements of the process and its respective inverse, the f_a, f_b, \dots describe the distribution functions of the particles involved and the $(1 \pm f_a)(1 \pm f_b) \dots$ are quantum statistical factors. The sum for a single process

⁸Note, however, that for most bath temperatures T , the physical values of g_{eff} , h_{eff} and g_{\star} will be almost the same.

is taken over the internal dof of all initial and final state particles. Interactions that do not change the particle species with up to four particles involved (i. e. scattering processes) vanish upon integration of the BE. The remaining processes under consideration are $1 \rightarrow 2$ and $2 \rightarrow 2$ FI as well as $2 \rightarrow 2$ FO processes, denoted as $\mathcal{C}_{1 \rightarrow 2}^{\text{FI}}$, $\mathcal{C}_{2 \rightarrow 2}^{\text{FI}}$, and $\mathcal{C}_{2 \rightarrow 2}^{\text{FO}}$, respectively, which we will calculate in the following. We want to emphasize here that for both FI processes, we will derive the integrated collision term with respect to a particle species a that is not the DM candidate. The reason for this is that the DM candidate will only appear as a final state in FI processes, which would make a direct calculation inconvenient. However, we will make contact with the equations describing the evolution of DM in Section 4.2.

The $1 \rightarrow 2$ freeze-in processes

For a particle decay process $a \rightarrow b + \chi$, where χ denotes the DM candidate, the RHS of the integrated BE reduces to

$$\mathcal{C}_{1 \rightarrow 2}^{\text{FI}} = - \sum_{\text{dof}} \int d\Pi_a d\Pi_b d\Pi_\chi (2\pi)^4 \delta^{(4)}(p_a - p_b - p_\chi) \left[|\mathcal{M}|_{a \rightarrow b\chi}^2 f_a (1 \pm f_b)(1 \pm f_\chi) - |\mathcal{M}|_{b\chi \rightarrow a}^2 (1 \pm f_a) f_b f_\chi \right], \quad (4.1.12)$$

where for the FI scenario we can ignore the second term because we expect $f_\chi \approx 0$. Furthermore, we assume for simplicity a Maxwell-Boltzmann statistic for all other particles and neglect the statistical factors $(1 \pm f_X) \approx 1$. Absorbing the sum over all dof as well as a factor $1/g_a$ of the initial state in the summed and averaged squared matrix element $|\mathcal{M}|_{a \rightarrow b\chi}^2$, the term can be simplified into

$$\mathcal{C}_{1 \rightarrow 2}^{\text{FI}} = - \int d\Pi_a g_a f_a \underbrace{\int d\Pi_b d\Pi_\chi (2\pi)^4 \delta^{(4)}(p_a - p_b - p_\chi) \overline{|\mathcal{M}|_{a \rightarrow b\chi}^2}}_{(I)}. \quad (4.1.13)$$

The integral over the final state particles yields $(I) = 2m_a \Gamma_{a \rightarrow b\chi}$, where

$$\Gamma_{a \rightarrow b\chi} \equiv \frac{f_s}{32\pi^2 m_a^2} p^* \int d\Omega \overline{|\mathcal{M}|_{a \rightarrow b\chi}^2} \quad (4.1.14)$$

denotes the usual definition of the (partial) decay rate of a particle a with $f_s = 1/2$ (1) for (non-)identical final states. In this context, $p^* = |\mathbf{p}_b| = |\mathbf{p}_\chi| = \sqrt{\lambda(m_a^2, m_b^2, m_\chi^2)}/(2m_a)$ yields the absolute momentum of the final state particles in the rest frame of a with $\lambda(x, y, z) \equiv (x - (\sqrt{y} + \sqrt{z})^2)(x - (\sqrt{y} - \sqrt{z})^2)$ being the Källén function. Thus, the integrated collision term can be written as

$$\mathcal{C}_{1 \rightarrow 2}^{\text{FI}} = -\Gamma_{a \rightarrow b\chi} \int \frac{d^3 p_a}{(2\pi)^3} g_a f_a \frac{m_a}{E_a} = -n_a^{\text{eq}} \Gamma_{a \rightarrow b\chi} \left\langle \frac{m_a}{E_a} \right\rangle \equiv -n_a^{\text{eq}} \langle \Gamma_{\text{dec}} \rangle_{a \rightarrow b\chi}, \quad (4.1.15)$$

where we assumed $f_a = f_a^{\text{eq}} \propto e^{-E_a/T}$ to follow a Maxwell-Boltzmann distribution in equilibrium (with $\mu_a \approx 0$). Further,

$$\left\langle \frac{m_a}{E_a} \right\rangle \equiv \frac{\int dn_a \frac{m_a}{E_a}}{\int dn_a} = \frac{\int_0^\infty dp_a p_a^2 e^{-E_a/T} \frac{m_a}{E_a}}{\int_0^\infty dp_a p_a^2 e^{-E_a/T}} = \frac{\int_1^\infty dy \sqrt{y^2 - 1} e^{-xy}}{\int_1^\infty dy \sqrt{y^2 - 1} y e^{-xy}} = \frac{K_1(x)}{K_2(x)} \quad (4.1.16)$$

denotes the average of the corresponding quantity with respect to the number density measure $dn_a \equiv g_a f_a d^3 p_a / (2\pi)^3$ of species a , where we have substituted $y \equiv E_a/m_a$ and $x \equiv m_a/T$. In the last step we formulated the integrals in terms of modified Bessel functions of second kind (cf. Eq. A.8). Together with $\Gamma_{a \rightarrow b\chi}$ they define a thermally averaged decay rate

$$\langle \Gamma_{\text{dec}} \rangle_{a \rightarrow b\chi} \equiv \frac{K_1(x)}{K_2(x)} \Gamma_{a \rightarrow b\chi}. \quad (4.1.17)$$

We will briefly discuss the two limiting cases from the definitions of the modified Bessel functions given in Eqs. A.8 and A.9. At later times, for large $x \gg 1$, $K_1(x)/K_2(x) \approx 1$, such that $\langle \Gamma_{\text{dec}} \rangle_{a \rightarrow b\chi} \approx \Gamma_{a \rightarrow b\chi}$ for the thermal average. For $x \ll 1$ at early times, especially relevant for FI, the thermal average suppresses the decay rate via $K_1(x)/K_2(x) = x/2 + \mathcal{O}(x^2)$, such that in this regime, $2 \rightarrow 2$ processes are expected to dominate (cf. Fig. 6.1 for a concrete example).

The $2 \rightarrow 2$ freeze-in processes

Following similar steps as for the $1 \rightarrow 2$ case (also assuming $f_\chi \approx 0$, $(1 \pm f_\chi) \approx 1$), the collision term of an interaction $a + b \rightarrow c + \chi$ producing DM in a FI scenario can be written as

$$\begin{aligned} \mathcal{C}_{2 \rightarrow 2}^{\text{FI}} &= - \sum_{\text{dof}} \int d\Pi_a d\Pi_b d\Pi_c d\Pi_\chi (2\pi)^4 \delta^{(4)}(p_a + p_b - p_c - p_\chi) \\ &\quad \left[|\mathcal{M}|_{ab \rightarrow c\chi}^2 f_a f_b (1 \pm f_c) (1 \pm f_\chi) - |\mathcal{M}|_{c\chi \rightarrow ab}^2 (1 \pm f_a) (1 \pm f_b) f_c f_\chi \right] \\ &= - \int d\Pi_a d\Pi_b g_a f_a g_b f_b \underbrace{\int d\Pi_c d\Pi_\chi (2\pi)^4 \delta^{(4)}(p_a + p_b - p_c - p_\chi) |\mathcal{M}|_{ab \rightarrow c\chi}^2}_{(II)}, \end{aligned} \quad (4.1.18)$$

where the integral $(II) = 4F(s)\sigma_{ab \rightarrow c\chi}$ matches the common definition of the $2 \rightarrow 2$ cross section of the process times a prefactor $F(s) \equiv \sqrt{(p_a \cdot p_b)^2 - m_a^2 m_b^2} = \sqrt{\lambda(s, m_a^2, m_b^2)}/2$, which is a function of the squared *center of momentum* (COM) energy $s = (p_a + p_b)^2$ alone. A more convenient way to write $F(s) = v_{\text{Møll}} E_a E_b$ is using the Møller velocity, which has the useful property that $v_{\text{Møll}} n_a n_b$ is invariant under Lorentz transformations. In terms of the individual particle velocities $\mathbf{v}_a = \mathbf{p}_a/E_a$ and $\mathbf{v}_b = \mathbf{p}_b/E_b$, the Møller velocity is defined as

$$v_{\text{Møll}} = \sqrt{|\mathbf{v}_a - \mathbf{v}_b|^2 - |\mathbf{v}_a \times \mathbf{v}_b|^2} \quad (4.1.19)$$

and reduces to the relative velocity $v_{\text{rel}} \equiv |\mathbf{v}_a - \mathbf{v}_b|$ in the COM frame (where $\mathbf{v}_a \parallel \mathbf{v}_b$). The integrated BE then simplifies to

$$\mathcal{C}_{2 \rightarrow 2}^{\text{FI}} = - \int \frac{d^3 p_a}{(2\pi)^3} \frac{d^3 p_b}{(2\pi)^3} g_a f_a g_b f_b \sigma_{ab \rightarrow c\chi} v_{\text{M}\phi} = -n_a^{\text{eq}} n_b^{\text{eq}} \langle \sigma v_{\text{M}\phi} \rangle_{ab \rightarrow c\chi}, \quad (4.1.20)$$

where we have again assumed that $f_{a,b} = f_{a,b}^{\text{eq}}$ follow equilibrium Maxwell-Boltzmann statistics. We have further defined the thermally averaged cross section

$$\langle \sigma v_{\text{M}\phi} \rangle_{ab \rightarrow c\chi} \equiv \frac{\int dn_a dn_b \sigma_{ab \rightarrow c\chi} v_{\text{M}\phi}}{\int dn_a \int dn_b} = \frac{\int dn_a^{\text{eq}} dn_b^{\text{eq}} \sigma_{ab \rightarrow c\chi} v_{\text{M}\phi}}{\int dn_a^{\text{eq}} \int dn_b^{\text{eq}}}, \quad (4.1.21)$$

which will be calculated in Section 4.3. We want to emphasize here that the last equality of Eq. 4.1.21 also holds for distributions outside of chemical equilibrium, since the momentum-independent chemical potentials cancel.

The $2 \rightarrow 2$ freeze-out processes

The FO scenario for a particle species a considering a $2 \rightarrow 2$ process $a + b \rightarrow c + d$ starts equivalently to the FI case with SM particles in the final state. In models with only one additional particle accounting for DM (e.g. classical WIMP models), the DM candidate χ coincides with the species a in our discussion. However, in the following we will employ exclusively models with more than one particle in the dark sector. Within those, the species a undergoing FO can also refer to another particle in the dark sector and not the DM candidate directly, which is why we keep the label a for generality. We still assume Maxwell-Boltzmann statistics for all particle species and neglect statistical factors, but we can neither disregard any distribution functions nor assume all initial state particles to be in thermal equilibrium. However, since $2 \rightarrow 2$ processes need to efficiently exchange energy between the SM and the dark sector to be relevant for FO, we can assume the final state particles to be part of, and therefore in thermal equilibrium with, the SM bath, i.e. $f_c f_d = f_c^{\text{eq}} f_d^{\text{eq}}$, and that the *principle of detailed balance* holds, implying $f_c^{\text{eq}} f_d^{\text{eq}} = f_a^{\text{eq}} f_b^{\text{eq}}$ (see e.g. Ref. [25]). Further, we require the system to exhibit a CP or T symmetry, such that $|\mathcal{M}|_{ab \rightarrow cd}^2 = |\mathcal{M}|_{cd \rightarrow ab}^2$. Going through similar steps as before, we arrive at

$$\begin{aligned} \mathcal{C}_{2 \rightarrow 2}^{\text{FO}} &= - \int \frac{d^3 p_a}{(2\pi)^3} \frac{d^3 p_b}{(2\pi)^3} g_a g_b (f_a f_b - f_a^{\text{eq}} f_b^{\text{eq}}) \sigma_{ab \rightarrow cd} v_{\text{M}\phi} \\ &= - \langle \sigma v_{\text{M}\phi} \rangle_{ab \rightarrow cd} (n_a n_b - n_a^{\text{eq}} n_b^{\text{eq}}). \end{aligned} \quad (4.1.22)$$

4.2 The Boltzmann equations for freeze-in and freeze-out

With the information gathered above, we are now well-equipped to determine the BEs for typical FI and FO scenarios. We employ for this purpose a dimensionless quantity $x = m_*/T$ with m_* being a mass scale commonly set to the mass m_a of a species in the

initial state of the interaction processes (but not necessarily). Furthermore, we define (cf. Eqs. 2.3.8 and 2.3.10)

$$Y_i^{\text{eq}}(x) \equiv \frac{n_i^{\text{eq}}(x)}{s(x)} = \frac{45g_i\eta(m_i, x)}{2\pi^4 m_*^3 h_{\text{eff}}(x)}, \quad \eta(m_i, x) = \begin{cases} \frac{1}{2} m_* m_i^2 x^2 K_2\left(\frac{m_i}{m_*} x\right) & \text{for } m_i > 0 \\ \zeta(3) m_*^3 & \text{for } m_i = 0 \end{cases} \quad (4.2.1)$$

to be the equilibrium yield of any particle species i .⁹ Starting with FI, we can combine Eqs. 4.1.15 and 4.1.20 with Eq. 4.1.10 and use the relation $dY_a^{\text{FI}}/dx = -dY_\chi^{\text{FI}}/dx$, to arrive at the corresponding BEs for χ considering $1 \rightarrow 2$ and $2 \rightarrow 2$ processes

$$\frac{dY_{\chi,1\rightarrow 2}^{\text{FI}}}{dx} = \sqrt{\frac{45}{4\pi^3}} \frac{M_{\text{Pl}} g_*^{1/2}}{m_*^2 h_{\text{eff}}} \langle \Gamma_{\text{dec}} \rangle_{a \rightarrow b\chi} Y_a^{\text{eq}}, \quad (4.2.2)$$

$$\frac{dY_{\chi,2\rightarrow 2}^{\text{FI}}}{dx} = \sqrt{\frac{\pi}{45}} \frac{M_{\text{Pl}} m_* g_*^{1/2}}{x^2} \langle \sigma v_{\text{Mø}} \rangle_{ab \rightarrow c\chi} Y_a^{\text{eq}} Y_b^{\text{eq}}, \quad (4.2.3)$$

where we note that the K_n within the definitions of the thermal averages are in general functions of $(m_a/m_*)x$ rather than x alone. To obtain the total DM yield Y_χ^{FI} from these equations, we can simply add up the yields from the individual contributions, which can be extracted by integrating the equations above from 0 to x (assuming $Y_\chi^{\text{FI}}(0) = 0$). We have sketched Y_χ^{FI} for a typical FI process from particle decay of a species a in Fig. 4.1 (dashed lines) alongside with the equilibrium yield Y_a^{eq} (black solid line), where we set the mass scale $m_* = m_a$. It is apparent from Eq. 4.2.2 that the DM yield scales linearly with the decay rate, which in turn depends on the coupling strength between DM and the decaying species. The efficiency of this process drastically decreases when the species a becomes non-relativistic ($x \gg 1$) due to an exponential suppression of the equilibrium yield

$$Y_a^{\text{eq}}(x) \xrightarrow{x \gg 1} \frac{45g_a}{4\sqrt{2}\pi^{7/2} h_{\text{eff}}(x)} x^{3/2} e^{-x}, \quad (4.2.4)$$

rendering Y_χ^{FI} constant for $x \gtrsim 10$. Including other kinematic processes (like $2 \rightarrow 2$ production) will complicate the FI dynamics but the general picture of Fig. 4.1 together with the efficiency statements will remain.

To calculate the yield of a species a in a FO process, we first set $m_* = m_a$ and drop the label FO for convenience. We then combine Eqs. 4.1.10 and 4.1.22, which results in a first order differential equation

$$\frac{dY_a}{dx} = -\sqrt{\frac{\pi}{45}} \frac{M_{\text{Pl}} m_a g_*^{1/2}}{x^2} \langle \sigma v_{\text{Mø}} \rangle_{ab \rightarrow cd} (Y_a Y_b - Y_a^{\text{eq}} Y_b^{\text{eq}}). \quad (4.2.5)$$

This differential equation usually has to be solved numerically assuming thermal equilibrium at the starting point, i. e. $Y_a(x_s) = Y_a^{\text{eq}}(x_s)$. We depicted a typical FO process

⁹Note that we have taken for a massless (massive) bosonic particle the relativistic (Maxwell-Boltzmann) approximation of the number density. If one considers a massless fermion, a factor of 7/8 must be added.

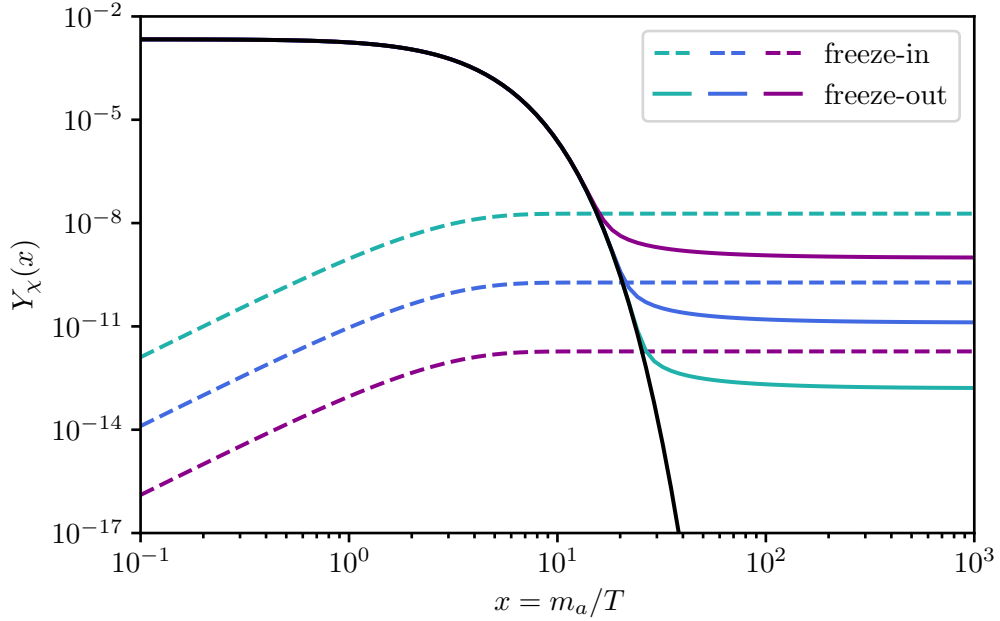


Figure 4.1: The yield of a particle species χ evolving over time as a function of $x \equiv m_a/T$ for a typical FI (dashed) and FO (solid) scenario, where m_a is either the mass of the particle χ itself with $a = \chi$ (for FO) or the mass of a particle a involved in the production of χ (for FI), respectively. Lighter colors correspond to higher values of the interaction rates which govern the FI and FO processes. The solid black line refers to the equilibrium yield Y_a^{eq} of species a .

governed by Eq. 4.2.5 in Fig. 4.1 (solid lines) as well, assuming a constant thermally averaged cross section and setting $Y_a \equiv Y_b$.¹⁰ We observe that, at early times until $x \gtrsim 15$, the yield of species a closely follows its equilibrium value. This can be explained by the efficiency of the exchange processes encapsulated in $\langle \sigma v_{\text{Mol}} \rangle_{ab \rightarrow cd} / x^2$, which quickly drive the system back to Y_a^{eq} whenever it experiences a small departure. As the efficiency of these processes decreases for $x \gg 1$ and Y_a^{eq} becomes exponentially suppressed, the RHS of Eq. 4.2.5 vanishes and the yield becomes constant.¹¹ The larger the cross sections of the processes under consideration, the longer equilibrium will be maintained and the smaller the final FO yield will be (cf. Fig. 4.1). Typical values for the FO temperature, i. e. the temperature at which Y_a departs from equilibrium, are $x_{\text{FO}} \sim 25$.

The produced DM abundance $\Omega_{\text{DM},0}$ from either of the two mechanisms up to the

¹⁰This is the case, when either species a and b are the same, or particle b is the antiparticle of a in a theory where processes that could create an asymmetry between a and b are absent.

¹¹Defining the rate of the $2 \rightarrow 2$ exchange processes as $\Gamma_a \sim n_a^{\text{eq}} \langle \sigma v_{\text{Mol}} \rangle_{ab \rightarrow cd}$, one can cast the FO equation into the form $dY_a/dx \propto -\Gamma_a/H(Y_a^2/Y_a^{\text{eq}2} - 1)$. Here, it is apparent that FO happens when $\Gamma_a \ll H$ as expected from the naïve picture.

present day (t_0) can be calculated via

$$\Omega_{\text{DM},0} \equiv \Omega_{\text{DM}}(t_0) = \frac{\rho_\chi(t_0)}{\rho_{\text{crit},0}} = \frac{m_\chi s_0 Y_{\chi,\infty}}{\rho_{\text{crit},0}}, \quad (4.2.6)$$

where we used the approximation $\rho_\chi(t) = m_\chi n_\chi(t)$ for a non-relativistic particle species and $Y_{\chi,\infty} \equiv Y_\chi(x \rightarrow \infty)$ denotes the DM yield after number changing processes have stopped.

4.3 The thermally averaged cross section

The cross section itself has to be computed individually for each particle physics process, however, the kinematics of the thermal average can be derived on a more generic level. Assuming Maxwell-Boltzmann statistics for all incoming particles¹², the thermally averaged cross section, which is only a function of the (squared) COM energy s , yields

$$\langle \sigma v_{\text{Møll}} \rangle_{ab \rightarrow cd} = \frac{\int dn_a^{\text{eq}} dn_b^{\text{eq}} \sigma_{ab \rightarrow cd}(s) v_{\text{Møll}}}{\int dn_a^{\text{eq}} \int dn_b^{\text{eq}}} = \frac{\int d^3 p_a d^3 p_b e^{-E_a/T} e^{-E_b/T} \sigma_{ab \rightarrow cd}(s) v_{\text{Møll}}}{\int d^3 p_a e^{-E_a/T} \int d^3 p_b e^{-E_b/T}}. \quad (4.3.1)$$

To simplify the calculation, we switch to a more convenient set of variables comprising [104]

$$E_+ = E_a + E_b, \quad E_- = E_a - E_b, \quad s = m_a^2 + m_b^2 + 2E_a E_b - 2p_a p_b \cos \theta, \quad (4.3.2)$$

with θ denoting the angle between the initial state particles a and b , and $p_i = |\mathbf{p}_i|$. With $\det J = 1/(4p_a p_b)$, the differentials in the new parametrization (for unpolarized initial states) are given by

$$d^3 p_a d^3 p_b = 4\pi p_a E_a dE_a 4\pi p_b E_b dE_b \frac{1}{2} d\cos \theta = 2\pi^2 E_a E_b dE_+ dE_- ds, \quad (4.3.3)$$

and the integration boundaries change from $\{E_a \geq m_a, E_b \geq m_b, |\cos \theta| \leq 1\}$ to

$$\left\{ s \geq (m_a + m_b)^2, E_+ \geq \sqrt{s}, \left| E_- + E_+ \frac{m_a^2 - m_b^2}{s} \right| \leq \frac{2F(s)}{s} \sqrt{E_+^2 - s} \right\}. \quad (4.3.4)$$

Using $\int d^3 p_i e^{-E_i/T} = 8\pi x^{-3} \eta(m_i, x)$ to calculate the denominator of Eq. 4.3.1 ($x = m_*/T$) and inserting the definition of the Møller velocity $v_{\text{Møll}} = F(s)/(E_a E_b)$, the thermally averaged cross section reads

$$\langle \sigma v_{\text{Møll}} \rangle_{ab \rightarrow cd} = \frac{x^6}{32\eta(m_a, x)\eta(m_b, x)} \int ds F(s) \sigma_{ab \rightarrow c\chi}(s) \int dE_+ e^{-E_+/T} \int dE_- . \quad (4.3.5)$$

¹²This is a simplification made in order to obtain analytic results. Being justified in the non-relativistic limit, for relativistic initial state particles (e. g. massless gauge bosons), one, in principle, needs to employ the proper statistical distributions. However, as these corrections are usually small, we neglect them in the following.

Since $\sigma_{ab \rightarrow c\chi}(s)$ is a function of s alone, we can perform the integrals over E_- and E_+ directly

$$\int dE_- = 4 \frac{F(s)}{s} \sqrt{E_+^2 - s^2}, \quad \int dE_+ e^{-E_+/T} \sqrt{E_+^2 - s} = \sqrt{s} \frac{m_*}{x} K_1 \left(\sqrt{s} \frac{x}{m_*} \right). \quad (4.3.6)$$

This leaves us with only one integral

$$\langle \sigma v_{\text{Mø}} \rangle_{ab \rightarrow cd} = \frac{m_* x^5}{32 \eta(m_a, x) \eta(m_b, x)} \int_{s_{\min}}^{\infty} ds \frac{\lambda(s, m_a^2, m_b^2)}{\sqrt{s}} K_1 \left(\sqrt{s} \frac{x}{m_*} \right) \sigma_{ab \rightarrow cd}(s), \quad (4.3.7)$$

where $s_{\min} = \max\{(m_a + m_b)^2, (m_c + m_d)^2\}$ denotes the minimal possible energy transfer. The cutoff for processes where $(m_c + m_d)^2 > (m_a + m_b)^2$ is also encoded in the kinematic phase space of the cross section. Therefore, we use $s_{\min} = (m_a + m_b)^2$ for further calculations. The $2 \rightarrow 2$ cross section in the COM frame as an integral over the solid angle is given by

$$\sigma_{ab \rightarrow cd} = \frac{f_s}{64 \pi^2 s} \frac{p_c^*}{p_a^*} \int d\Omega \overline{|\mathcal{M}|^2}_{ab \rightarrow cd}, \quad (4.3.8)$$

with $f_s = 1/2$ (1) for (non-)identical final states. The initial and final state momenta are defined here as

$$p_a^* \equiv \sqrt{\frac{\lambda(s, m_a^2, m_b^2)}{4s}}, \quad p_c^* \equiv \sqrt{\frac{\lambda(s, m_c^2, m_d^2)}{4s}}. \quad (4.3.9)$$

The thermally averaged cross section for a specific process calculated with Eq. 4.3.7 exhibits in general a complicated dependence on x . For a FO scenario, we are interested in processes happening at $x \sim 20$ or higher, such that it is usually sufficient to expand the thermally averaged cross section with respect to large x and only consider the leading order term. Although confusing, in the literature this treatment is referred to as a *partial wave expansion*.¹³ Accordingly, we will denote the x^0 term as the *s-wave* contribution, the x^{-1} term as the *p-wave* contribution and so on. For massive initial particles, we start by expressing σv_{rel} in terms of v_{rel} (instead of s) and perform a *velocity expansion* of the cross section around $v_{\text{rel}} = 0$, yielding

$$\sigma v_{\text{rel}} = \sum_{l=0}^{\infty} \sigma_l v_{\text{rel}}^{2l} \quad (4.3.10)$$

for an analytic function with expansion coefficients σ_l . Applying Eq. A.9 for large arguments to $K_n(x)$ in Eq. 4.3.7, we can, in fact, expand the whole expression for $x \rightarrow \infty$. After doing so, we can integrate analytically order by order over v_{rel} and group the contributions in powers of x^{-n} . Only considering the s-wave contribution yields $\langle \sigma v_{\text{Mø}} \rangle_{ab \rightarrow cd} \approx \sigma_0$ for all initial mass configurations considered in the following.

¹³Let us emphasise here, that an actual expansion in partial waves happens at the level of the matrix element, where its angular dependence is expanded in Legendre polynomials $P_l(\cos \theta)$, which are then matched to an expansion of the scattering amplitude that one would obtain from a non-relativistic approach using the Schrödinger equations. See App. B and App. D for a detailed discussion.

5 Non-perturbative effects in dark matter interactions

In DM models with two or more particles populating the dark sector, new interactions of the dark particles with the SM and among themselves can occur, which are typically less constrained by current observations. Consequently, macroscopic observables such as the total DM abundance or DM distributions in galaxies might differ if these interactions are taken into account properly, possibly also changing the valid parameter space of the models under consideration when confronted with experimental data. This work is dedicated to study the impact of effects arising from interactions within the dark sector on cosmological and astrophysical observables in a variety of different models. More concretely, we will focus on two effects, namely *Sommerfeld enhancement* (SE) [105] and the presence of *bound states* (BS) within the dark sector. Both concepts alone have been known for a very long time in the SM [106–119] but only recently, they have been applied in the context of DM models as well [120–143]. These effects are referred to as non-perturbative because they cannot be fully calculated in the framework of a perturbative *quantum field theory* (QFT). However, since both effects occur when the particles are non-relativistic, they can be met with a quantum mechanical treatment. For our derivation of cross sections, decay rates etc. including the aforementioned effects, switching between both pictures will be advantageous in order to address the high energy (*hard*) and low energy (*soft*) momentum transfer processes within the interactions.

SE occurs when a heavy particle antiparticle pair $\bar{\chi}\chi$ interacts with a light bosonic mediator φ , which has a Compton wavelength $\propto m_\varphi^{-1}$ longer than the Bohr radius of the particle pair $\propto (\alpha m_\chi)^{-1}$ (see e.g. Ref. [123]), where α denotes the strength of the interaction.¹⁴ This is equivalent to the statement that the potential which is generated by φ and acting on the $\bar{\chi}\chi$ pair is sufficiently *long-ranged*. The condition above is naturally fulfilled for massless mediators, whereas for massive mediators it highly depends on the mass ratio between the mediator and the interacting pair. If in processes like particle antiparticle annihilation, the interaction length of the process $\propto (v_{\text{rel}} m_\chi)^{-1}$ is much larger than the Bohr radius, the incoming particle wave functions cannot be considered as free anymore at the origin and the corresponding annihilation amplitude will receive corrections. These corrections will be larger, the smaller the relative velocity between the annihilating particles is compared to the strength of the potential ($v_{\text{rel}} \ll \alpha$). Moreover, if the potential generated by φ is attractive, BS can form.

For illustration purposes, we have sketched a typical particle antiparticle annihilation process with SE as well as a *bound state formation* (BSF) process in Fig. 5.1. The cross section of the hard annihilation process of a $\bar{\chi}\chi$ pair into arbitrary final states in the left diagram, depicted as a hatched circle, can be calculated with typical methods of perturbative QFT, where the results depend on the underlying model. The corrections due to SE, which can be described in the QFT framework as a resummation of soft φ exchanges, are more model-independent due to their non-relativistic nature and solely depend on the form of the potential generated by φ (given that the potential strength

¹⁴SE can also occur for two particles with non-identical masses. This general case, however, will not be important for the subsequent discussion.

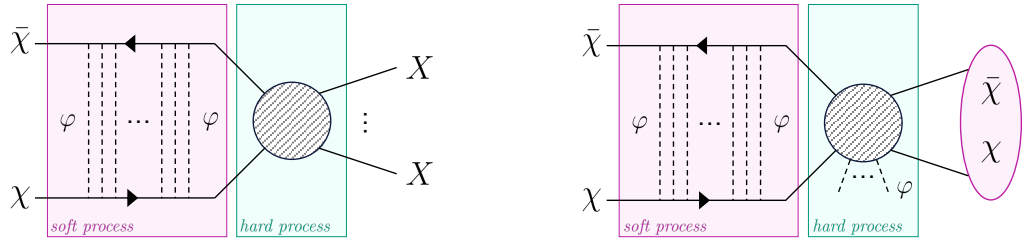


Figure 5.1: Feynman-like diagrams for particle antiparticle annihilation (left) and a BSF process (right) of an interacting $\bar{\chi}\chi$ pair. The influence of the potential inducing SE is pictured by infinite exchanges of the mediator φ . Processes featuring high momentum transfer are shaded in cyan while processes of continuous low momentum transfer (including BS) are colored in magenta.

α has already been extracted from the QFT Lagrangian). Thus, they can be derived using a quantum mechanical approach by utilizing the scattering wave functions of the corresponding Schrödinger equation. We will assume in the following that the soft and hard processes of the interaction are well separable, i. e. that we can compute the hard annihilation cross section and the SE factor independently from each other.¹⁵ In the right diagram of Fig. 5.1, a BSF process $\bar{\chi} + \chi \rightarrow \mathcal{B}(\bar{\chi}\chi) + n \cdot \varphi$ is sketched ($n = 1, 2, \dots$). The hard process can again be calculated with methods of perturbative QFT but this time a clear separation from the soft processes in order to calculate the BSF cross section cannot be reached due to the off-shellness of the outgoing states. The SE correction to the BS decay rate (not depicted) can in turn be calculated in analogy to the annihilation cross section.

In Section 5.1, we will start by establishing a quantum mechanical treatment of SE corrections within particle antiparticle annihilations and BS decay. We will further give insight on how to calculate the SE factors numerically in case an analytic treatment is not possible. Moving on, in Section 5.2 we introduce an approach to calculate the BSF rate by leveraging methods from QFT within the non-relativistic limit. Finally, we present a different approach resorting to *effective field theory* (EFT) in order to recalculate all observables in Section 5.3. We discuss the merits of each method and compare their advantages.

¹⁵This standard treatment can, however, fail in certain regimes, e. g. when BS with zero energy appear in the Schrödinger equation or when the hard cross section is already so large that adding the SE factor would violate unitarity bounds at finite velocity. We direct the reader to Ref. [127] for an in-depth discussion of these cases.

5.1 Sommerfeld enhancement in particle annihilation and bound state decay

We will now calculate the SE factor for the most typical case of an annihilating $\bar{\chi}\chi$ pair alongside with the SE factor for the decay rate of a $\mathcal{B}(\bar{\chi}\chi)$ BS into two final states. As mentioned earlier, we will assume the SE factor to be separable from the hard matrix element, such that the cross section and decay rate can be written as [124, 125, 129]

$$\sigma_{\text{ann}} v_{\text{rel}} = \sum_{l=0}^{\infty} (\sigma_{\text{ann}} v_{\text{rel}})_l = \sum_{l=0}^{\infty} \sigma_l v_{\text{rel}}^{2l} S_{\text{ann},l}, \quad (5.1.1)$$

$$\Gamma_{\text{dec}}^{(n)} = \sum_{l=0}^{\infty} \Gamma_{\text{dec},l}^{(n)} = \sum_{l=0}^{\infty} \sigma_l S_{\text{dec},l}^{(n)}, \quad (5.1.2)$$

with l indicating an expansion in partial waves (cf. App. B) where $S_{\text{ann},0}$ denotes the s-wave enhancement factor, $S_{\text{ann},1}$ the p-wave etc., and analogously for $S_{\text{dec},l}^{(n)}$, where $(n) \equiv \{nl^{(l)}m\}$ covers all quantum numbers of the bound state.¹⁶ The σ_l encapsulate the l -wave contributions to the hard cross section within this expansion where the partial matrix elements are stripped from their angular dependencies. Their definition together with a careful derivation of the equations for SE, which are stated in the following subsections, can be found in App. D. For now, we will continue by setting up the Schrödinger equations for the scattering and BS wave functions in Section 5.1.1, which are needed to derive the corresponding SE factors in Sections 5.1.2 and 5.1.3 for the potentials created by a massless and massive mediator φ .

5.1.1 Schrödinger equations for scattering and bound states

The Schrödinger equations for a two-particle scattering state $\phi_{\mathbf{k}}(\mathbf{r})$ and a BS $\psi_{nlm}(\mathbf{r})$ in a spherically symmetric potential $V(\mathbf{r}) = V(|\mathbf{r}|)$ take the form (see i. e. Ref. [144])

$$\left[-\frac{1}{2\mu} \nabla^2 + V(\mathbf{r}) \right] \phi_{\mathbf{k}}(\mathbf{r}) = \mathcal{E}_{\mathbf{k}} \phi_{\mathbf{k}}(\mathbf{r}), \quad (5.1.3)$$

$$\left[-\frac{1}{2\mu} \nabla^2 + V(\mathbf{r}) \right] \psi_{nlm}(\mathbf{r}) = \mathcal{E}_{nl} \psi_{nlm}(\mathbf{r}), \quad (5.1.4)$$

with $\mathcal{E}_{\mathbf{k}} = k^2/(2\mu)$, $\mathcal{E}_{nl} = -\gamma_{nl}^2 \kappa^2/(2\mu)$ the scattering and BS energies. The scale $k = \mu v_{\text{rel}}$ hereby denotes the typical momentum transfer between the scattering particles (inversely proportional to their interaction length) and $\kappa = \mu\alpha$ is the Bohr momentum of the BS, where $\mu = m_{\chi}/2$ indicates the reduced mass of the system. While $\phi_{\mathbf{k}}$ depends on the particles momentum transfer \mathbf{k} , ψ_{nlm} is parametrized by the main and orbital

¹⁶We want to emphasize here that the partial wave expansion number l needs, in principle, to be distinguished from the orbital quantum number l' of the bound state for $S_{\text{dec},l}^{(n)}$. However, we will see that an $\{nl'm\}$ bound state will only exhibit an l -wave contribution to the SE factor of the BS, such that we will drop the distinguishing mark unless we want to emphasize it explicitly.

quantum numbers n and l, m of the corresponding BS, respectively. They obey the normalization

$$\int d^3r \phi_{\mathbf{q}}^*(\mathbf{r}) \phi_{\mathbf{k}}(\mathbf{r}) = (2\pi)^3 \delta^{(3)}(\mathbf{q} - \mathbf{k}), \quad (5.1.5)$$

$$\int d^3r \psi_{nlm}^*(\mathbf{r}) \psi_{n'l'm'}(\mathbf{r}) = \delta_{nn'} \delta_{ll'} \delta_{mm'}, \quad (5.1.6)$$

and completeness conditions

$$\int d^3k \phi_{\mathbf{k}}^*(\mathbf{r}) \phi_{\mathbf{k}}(\mathbf{r}') = (2\pi)^3 \delta^{(3)}(\mathbf{r} - \mathbf{r}'), \quad (5.1.7)$$

$$\sum_{n,l,m} \psi_{nlm}^*(\mathbf{r}) \psi_{nlm}(\mathbf{r}') = \delta^{(3)}(\mathbf{r} - \mathbf{r}'). \quad (5.1.8)$$

The function γ_{nl} parameterizes the energy splitting between different BS on which we will comment on later. We want to emphasize here that the spin structure of the interacting particles plays no role for the subsequent discussion, and it is thus irrelevant if the particles involved are bosons or fermions. What will be important in the following, however, is if the mediator creating the potential $V(\mathbf{r})$ has a mass. Therefore, we will distinguish between a *Yukawa potential* $V_Y(\mathbf{r}) = -\alpha/r \exp(-m_\varphi r)$ for a massive φ and a *Coulomb potential* $V_C(\mathbf{r}) = -\alpha/r$ for the massless case.

Due to the spherical symmetry of the potentials under consideration, we can expand $\phi_{\mathbf{k}}$ in partial waves (see App. B) and write ψ_{nlm} in terms of spherical harmonics $Y_{lm}(\Omega_{\mathbf{r}})$ (see App. A). The wave functions then yield

$$\phi_{\mathbf{k}}(\mathbf{r}) = \sum_{l=0}^{\infty} (2l+1) \left[\frac{\chi_{\mathbf{k},l}(\kappa r)}{\kappa r} \right] P_l(\hat{\mathbf{k}} \cdot \hat{\mathbf{r}}), \quad (5.1.9)$$

$$\psi_{nlm}(\mathbf{r}) = \kappa^{3/2} \left[\frac{\chi_{nl}(\kappa r)}{\kappa r} \right] Y_{lm}(\Omega_{\mathbf{r}}). \quad (5.1.10)$$

The radial parts of the scattering and BS wave functions $\chi_{\mathbf{k},l}$ and χ_{nl} depend on the exact form of the potential. Starting with a Yukawa potential, they are solutions to the radial Schrödinger equations

$$\chi_{\mathbf{k},l}''(x) + \left(\frac{1}{\zeta^2} - \frac{l(l+1)}{x^2} + \frac{2}{x} e^{-\frac{x}{\xi}} \right) \chi_{\mathbf{k},l}(x) = 0, \quad (5.1.11)$$

$$\chi_{nl}''(x) + \left(-\gamma_{nl}^2(\xi) - \frac{l(l+1)}{x^2} + \frac{2}{x} e^{-\frac{x}{\xi}} \right) \chi_{nl}(x) = 0, \quad (5.1.12)$$

which can be obtained by inserting Eqs. 5.1.9 and 5.1.10 into Eqs. 5.1.3 and 5.1.4 and employing Eqs. A.17 and A.30 to cancel the angular dependencies. The equations above were reparameterized in terms of $x \equiv \kappa r$ and we introduced the dimensionless variables

$$\zeta \equiv \frac{\kappa}{k} = \frac{\alpha}{v_{\text{rel}}}, \quad \xi \equiv \frac{\kappa}{m_\varphi} = \frac{\alpha m_\chi}{2m_\varphi}, \quad (5.1.13)$$

which we will use throughout this work. This choice is convenient because the previous discussions regarding the significance of the SE and its relative importance as a correction to the annihilation cross-section can be easily expressed by requiring $\xi \gg 1$ and $\zeta \gg 1$, respectively. The Coulomb case can be obtained from Eqs. 5.1.11 and 5.1.12 by taking the asymptotic limit $\xi \rightarrow \infty$ (or $m_\varphi \rightarrow 0$). Utilizing Eqs. A.20, A.23, A.24, A.27 and A.44, the normalization and completeness conditions for the radial wave functions can be derived from the full expressions. They are given by

$$\frac{4}{\kappa^3} \int_0^\infty dx \chi_{\mathbf{q},l}^*(x) \chi_{\mathbf{k},l}(x) = \frac{(2\pi)}{k^2} \delta(q - k), \quad (5.1.14)$$

$$\int_0^\infty dx \chi_{nl}^*(x) \chi_{n'l}(x) = \delta_{nn'}, \quad (5.1.15)$$

$$\frac{4}{\kappa^3} \int_0^\infty dk k^2 \chi_{\mathbf{k},l}^*(x) \chi_{\mathbf{k},l}(x') = (2\pi) \delta(x - x'), \quad (5.1.16)$$

$$\sum_n \chi_{nl}^*(x) \chi_{nl}(x') = \delta(x - x'). \quad (5.1.17)$$

Their form as a solution to the radial Schrödinger equations are well known for the Coulomb limit and yield in this parametrization (see e. g. App. A of Ref. [142])

$$\chi_{\mathbf{k},l}(x) = \frac{|\Gamma(1 + l - i\zeta)| e^{\pi\zeta/2} e^{i\delta_l}}{(2l + 1)!} \left(\frac{2ix}{\zeta} \right)^l x e^{-ix/\zeta} {}_1F_1 \left(1 + l + i\zeta; 2l + 2; \frac{2ix}{\zeta} \right) \quad (5.1.18)$$

$$\chi_{nl}(x) = \frac{2}{n^2} \sqrt{\frac{(n - l - 1)!}{(n + l)!}} \left(\frac{2x}{n} \right)^l x e^{-x/n} L_{n-l-1}^{(2l+1)} \left(\frac{2x}{n} \right) \quad (5.1.19)$$

with $\delta_l = \arg(\Gamma(1 + l - i\zeta))$ and where $\Gamma(x)$, ${}_1F_1(a; c; x)$ and $L_n^{(\alpha)}(x)$ denote the gamma function, the confluent hypergeometric function and the associated Laguerre polynomial, respectively (see App. A). The solutions for radial wave equations using a Yukawa potential have to be found numerically. Methods for this, which we will use in the following, were discussed in Refs. [124, 145].

5.1.2 Sommerfeld enhancement in particle annihilations

The l -wave SE factor for particle annihilation is given by [125] (cf. also App. D)

$$S_{\text{ann},l} = \left[\frac{(2l + 1)!!}{l!} \zeta^l \frac{d^l}{dx^l} \left(\frac{\chi_{\mathbf{k},l}(x)}{x} \right) \right]_{x=0}^2. \quad (5.1.20)$$

For a massless mediator creating a Coulomb potential, we can simply plug in Eq. 5.1.18 and use Eqs. A.2 and A.36 to arrive at

$$S_{\text{ann},l}(\zeta) = S_{\text{ann},0}(\zeta) \prod_{s=1}^l \left(1 + \frac{\zeta^2}{s^2} \right), \quad \text{with} \quad S_{\text{ann},0}(\zeta) = \frac{2\pi\zeta}{1 - e^{-2\pi\zeta}}. \quad (5.1.21)$$

We can easily see that the SE vanishes, i. e. $S_{\text{ann},l}(\zeta) \rightarrow 1$, for high relative velocities of the interacting particles and/or low couplings ($\zeta \rightarrow 0$), as expected. For low velocities, $S_{\text{ann},l}(\zeta) \propto 1/v_{\text{rel}}^{1+2l}$, such that the cross section will be $\propto 1/v_{\text{rel}}$ and, therefore, diverges for $v_{\text{rel}} \rightarrow 0$. Usually this does not pose a problem since only the thermally averaged quantities are physical observables but it can lead to violation of unitarity for certain coupling strengths as explored e. g. in Refs. [128, 146, 147]. We will implicitly check for these limitations in the considered models but will not discuss them further as they turn out to play no role for the subsequent analyses in our parameter regimes of interest.

In case of a massive mediator, corresponding to a Yukawa potential in the Schrödinger equations, the SE factor can only be extracted numerically [124]. Without loss of generality, we can take $\chi_{\mathbf{k},l}$ to be real because the phase of the scattering wave function does not enter Eq. 5.1.20. The normalization chosen corresponds at leading order to an asymptotic behavior of (cf. Eq. B.13)

$$\tilde{\chi}_{\mathbf{k},l}(x) \xrightarrow{x \rightarrow \infty} C_{s,l} \sin\left(\frac{x}{\zeta} - \frac{l\pi}{2} + \delta_l\right), \quad (5.1.22)$$

where we have defined $\chi_{\mathbf{k},l}(x) = \zeta/C_{s,l} \tilde{\chi}_{\mathbf{k},l}(x)$ for later convenience, with $C_{s,l}$ being the difference in amplitude between the wave function with and without SE. Requiring the solution to Eq. 5.1.11 as well as its first derivative to be regular at the origin, we can define the initial conditions as

$$\tilde{\chi}_{\mathbf{k},l}(x) \xrightarrow{x \rightarrow 0} \left(\frac{x}{\zeta}\right)^{l+1}, \quad \tilde{\chi}'_{\mathbf{k},l}(x) \xrightarrow{x \rightarrow 0} \frac{l+1}{\zeta} \left(\frac{x}{\zeta}\right)^l - \frac{1}{l+1} \left(\frac{x}{\zeta}\right)^{l+1}. \quad (5.1.23)$$

These choices significantly simplify Eq. 5.1.20 to

$$S_{\text{ann},l} = \left| \frac{(2l+1)!!}{C_{s,l}} \right|^2. \quad (5.1.24)$$

The constant $C_{s,l}$ for an s-wave ($l = 0$) can be extracted best by defining the function $F_0(y) \equiv \tilde{\chi}_{\mathbf{k},0}(y)^2 + \tilde{\chi}_{\mathbf{k},0}(y - \pi/2)^2$ which yields $\lim_{y \rightarrow \infty} F_0(y) = C_{s,0}^2$ at sufficiently high values for $y \equiv x/\zeta$. While this procedure works perfectly fine for $l = 0$, for $l = 1$ it is necessary to increase the precision of the asymptotic expansion up to sub-leading order to obtain a good result. Starting with [124]

$$\tilde{\chi}_{\mathbf{k},1}(y) \xrightarrow{y \rightarrow \infty} C_{s,1} \left(\sin\left(y - \frac{\pi}{2} + \delta_1\right) + \frac{\cos\left(y - \frac{\pi}{2} + \delta_1\right)}{y} \right), \quad (5.1.25)$$

we can obtain $C_{s,1}^2$ by defining $F_1(y) \equiv \tilde{\chi}_{\mathbf{k},1}(y)$,

$$k(y) \equiv \frac{(\pi^2 - 16y^2)^2}{8\pi(\pi^2 - 16y^2)} (F_1(y + \pi/4)^2 - F_1(y - \pi/4)^2), \quad (5.1.26)$$

$$h(y) \equiv (\pi^3 - 4\pi y^2)(k(y + \pi/4) + k(y - \pi/4)), \quad (5.1.27)$$

$$j(y) \equiv -8 \frac{(h(y + \pi/4) + h(y - \pi/4))}{(\pi^2 - 16y^2)(3\pi^2 + 16(1 + y^2))}, \quad (5.1.28)$$

and taking $\lim_{y \rightarrow \infty} j(y) = C_{s,1}^2$. Numerically, we implemented the second method with a relative error of $\varepsilon_{\text{rel}} < 10^{-3}$ as a breaking condition for the convergence algorithm.

5.1.3 Sommerfeld enhancement in bound state decays

Bound states can only form when the corresponding potential is sufficiently long-ranged. This is always the case for potentials generated by massless particles (e. g. Coulomb potentials). For Yukawa potentials, which are created by massive mediators, this statement is less obvious. A rough estimate for the existence of a BS is $\xi \gtrsim n^2$ but one might want to do better. Considering BSF by radiating off one massive mediator, a stronger criterion to create a bound state is $\mathcal{E}_{\mathbf{k}} - \mathcal{E}_{nl} > m_\varphi$ which translates in dimensionless coordinates to

$$\xi > \frac{2}{\alpha(\gamma_{nl}^2(\xi) + 1/\zeta^2)} \xrightarrow{\zeta \rightarrow \infty} \frac{2}{\alpha\gamma_{nl}^2(\xi)} \gg n^2 \quad (5.1.29)$$

in the static limit ($v_{\text{rel}} \rightarrow 0$), if the function $\gamma_{nl}(\xi)$ is known. BSF will become effective, once the Yukawa potential can get resolved by the wavelength of the incoming state, i. e. $k \gtrsim m_\varphi$ or $\xi \gtrsim \zeta$. A criterion to determine, if a potential is long-ranged enough, is then to demand that the *screening length* D which corresponds to m_φ^{-1} for a Yukawa potential should be above a critical value D_0 [148]. For a bound state to exist, we demand $\xi > \xi_c = 0.8399$ for $n = 1$ ($l = 0$), which will be reflected in the Schrödinger equation (cf. Eq. 5.1.12) by $\gamma_{nl}^2(\xi) \rightarrow 0$ as $\xi \rightarrow \xi_c$ ¹⁷. In the Coulomb limit ($\xi \rightarrow \infty$) there is no screening and $\gamma_{nl}^2(\xi) \rightarrow 1/n^2$, where n states of different l are degenerate.

The l' -wave SE factor for bound state decay into two final states is given by Ref. [129] (cf. also App. D)

$$S_{\text{dec},l}^{(n)} = \frac{\kappa^3}{4\pi} \frac{\delta_{l'l} \delta_{m_0}}{2l+1} \left[\frac{(2l+1)!!}{l!} \alpha^l \frac{d^l}{dx^l} \left(\frac{\chi_{nl}(x)}{x} \right) \right]_{x=0}^2, \quad (5.1.30)$$

where $\delta_{l'l}$ projects out the correct angular momentum state and δ_{m_0} results from the azimuthal symmetry of the potential. Using Eq. 5.1.19 for a Coulomb potential, the SE factor for BS decay simplifies to

$$S_{\text{dec},l}^{(n)} = \frac{\kappa^{3+2l}}{\pi\mu^{2l}} \frac{\delta_{l'l} \delta_{m_0}}{2l+1} \frac{(n+l)!}{n^{2(l+2)}(n-l-1)!(l!)^2}. \quad (5.1.31)$$

In order to find the correct bound state wave function for a given ξ in a Yukawa potential, we follow the procedure in Ref. [145] where we start by substituting $\rho \equiv 2x\gamma_{nl}(\xi)$ as well as $\chi_{nl}(\rho) \equiv \tilde{\chi}_{nl}(\rho)/C_{b,nl}$ in Eq. 5.1.12 yielding

$$\tilde{\chi}_{nl}''(\rho) + \left(-\frac{1}{4} - \frac{l(l+1)}{\rho^2} + \frac{e^{-\rho/(2\xi\gamma_{nl}(\xi))}}{\rho\gamma_{nl}(\xi)} \right) \tilde{\chi}_{nl}(\rho) = 0, \quad (5.1.32)$$

¹⁷The critical value ξ_c for the $n = 1$ and other bound states can be extracted from Table 4 in Ref. [148].

with $C_{b,nl}$ being the BS equivalent to $C_{s,l}$ for scattering state solutions. Apart from determining regular solutions to this equation using the corresponding initial conditions

$$\tilde{\chi}_{nl}(\rho) \xrightarrow{\rho \rightarrow 0} \left(\frac{\rho}{2\gamma_{nl}(\xi)} \right)^{l+1}, \quad \tilde{\chi}'_{nl}(\rho) \xrightarrow{\rho \rightarrow 0} \frac{(l+1)}{2\gamma_{nl}(\xi)} \left(\frac{\rho}{2\gamma_{nl}(\xi)} \right)^l, \quad (5.1.33)$$

we also have to resolve $\gamma_{nl}(\xi)$ by requiring that the BS solutions have to be localized wave packages, i. e.

$$\lim_{\rho \rightarrow \infty} \tilde{\chi}_{nl}(\rho) = 0. \quad (5.1.34)$$

For this purpose we guess an initial $\gamma_{nl}^{(0)}$ using the approximate formula $\gamma_{nl}^{(0)} \simeq 1/n(1 - n^2\xi_c/\xi)^b$ (where the values for b for a given $\{n, l\}$ pair can be extracted from Ref. [145]) and perform an iterative shooting method demanding $\tilde{\chi}_{nl}(\rho_\infty) = 0$, with a finite ρ_∞ for numerical feasibility ($\rho_\infty \simeq 60$ was checked to be sufficient for our purpose). After we have determined the correct $\gamma_{nl}(\xi)$ up to the desired precision and changed the variables back to x , we can use the normalization condition (cf. Eq. 5.1.15)

$$\int_0^\infty dx |\tilde{\chi}_{nl}(x)|^2 = C_{b,nl}^2 \quad (5.1.35)$$

to determine $C_{b,nl}$ and thus the full BS wave function $\chi_{nl}(x)$. Plugging in Eq. 5.1.33 into Eq. 5.1.30, the SE factor for BS decay into two final states within this parametrization yields

$$S_{\text{dec},l}^{(n)} = \frac{\kappa^{3+2l}}{\pi\mu^{2l}} \frac{\delta_{ll'}\delta_{m0}}{2l+1} \left(\frac{(2l+1)!!}{2C_{b,nl}} \right)^2. \quad (5.1.36)$$

5.2 Non-perturbative effects from the Bethe-Salpeter approach

Now, we know how to explicitly calculate the SE factors for particle antiparticle annihilation and BS decay utilizing the Schrödinger equations for non-relativistic scattering and BS. This was made possible because we could clearly separate soft and hard momentum exchange processes within these interactions. By inserting the corrected rates into a set of Boltzmann equations as described in Section 4, treating the free $\bar{\chi}\chi$ pair as well as each $\mathcal{B}(\bar{\chi}\chi)$ bound state as a separate species, we can track the evolution of their yield, which eventually leaves us with a corrected DM abundance. This, we can then compare to the abundance we would have obtained without taking them into account in order to quantify their relative importance. However, so far one important link is still missing: we have to find a way to describe the production of BS, i. e. we need a suitable method to calculate processes like the one pictured in Fig. 5.1 (right). This task is significantly more challenging because the aforementioned naïve separation between soft and hard scales cannot be applied anymore. In this and in the next subsection, we will present two independent methods to achieve this goal, each of them having different advantages but an equivalent outcome. The first one has been adapted to the DM problem initially in Ref. [129] and was later extended in various ways (see e. g. Refs. [133, 136, 138–140, 142, 145, 149–152]).

The main idea starts by utilizing *Bethe-Salpeter wave equations*, which we rederive and connect to the Schrödinger equations in Section 5.2.1 to build up the scaffold and nomenclature of the method. Using common techniques from QFT as well as appropriate approximations for the non-relativistic limit, we will derive the desired BSF cross section in Section 5.2.2. Note that we will highlight in the following only the pivotal steps and most important derivations from Ref. [129]. For a detailed and in-depth discussion, the reader is referred to the original paper and the references therein (most importantly Refs. [153, 154]).

5.2.1 The Bethe-Salpeter wave equation

We first want to derive the Bethe-Salpeter wave equations, which in simplified terms can be seen as a relativistic extension of the Schrödinger equations. They can be utilized to characterize a BS of a two-particle quantum system, incorporating concepts such as spin, which the Schrödinger equations do not encompass. For simplicity, we employ a general system of two scalar particles χ_1 and χ_2 with momenta $\mathbf{q}_{1,2}$ and (not necessarily equal) masses $m_{1,2}$ interacting via a mediator φ being either a scalar or vector boson. We will later discuss what changes in the derivation if χ_1 and χ_2 were fermions instead.

The Bethe-Salpeter wave functions

We define $|\mathcal{U}_{\mathbf{Q},\mathbf{q}}\rangle$ to be a two-particle $\chi_1\chi_2$ scattering state with total and relative momentum $\mathbf{Q} = \mathbf{q}_1 + \mathbf{q}_2$ and $\mathbf{q} = \eta_2\mathbf{q}_1 - \eta_1\mathbf{q}_2 = \mu\mathbf{v}_{\text{rel}}$, respectively, where $m = m_1 + m_2$, $\mu = m_1m_2/m$ denote the total and reduced mass of the system, and $\eta_{1,2} = m_{1,2}/m$ (with $\eta_1 + \eta_2 = 1$).¹⁸ The total energy of the scattering state is then given by $\omega_{\mathbf{Q},\mathbf{q}}$. Further, we denote the one-particle BS as $|\mathcal{B}_{\mathbf{Q},n}\rangle$ with energy $\omega_{\mathbf{Q},n}$, where $n \equiv \{nlm\}$ takes into account all its quantum numbers. Within this notation, we can define the scattering and BS *Bethe-Salpeter wave functions* (first introduced in Ref. [155])

$$\Phi_{\mathbf{Q},\mathbf{q}}(x_1, x_2) \equiv \langle \Omega | T \chi_1(x_1) \chi_2(x_2) | \mathcal{U}_{\mathbf{Q},\mathbf{q}} \rangle, \quad (5.2.1)$$

$$\Psi_{\mathbf{Q},n}(x_1, x_2) \equiv \langle \Omega | T \chi_1(x_1) \chi_2(x_2) | \mathcal{B}_{\mathbf{Q},n} \rangle, \quad (5.2.2)$$

which represent, roughly speaking, a covariant extension of the Schrödinger wave functions into the relativistic regime, with T denoting the time-ordering operator and $|\Omega\rangle$ represents the vacuum state of the interacting theory.¹⁹ Further, we define

$$\Phi_{\mathbf{Q},\mathbf{q}}^*(x_1, x_2) \equiv \langle \Omega | \bar{T} \chi_1(x_1) \chi_2(x_2) | \mathcal{U}_{\mathbf{Q},\mathbf{q}} \rangle^* = \langle \mathcal{U}_{\mathbf{Q},\mathbf{q}} | T \chi_1^\dagger(x_1) \chi_2^\dagger(x_2) | \Omega \rangle, \quad (5.2.3)$$

$$\Psi_{\mathbf{Q},n}^*(x_1, x_2) \equiv \langle \Omega | \bar{T} \chi_1(x_1) \chi_2(x_2) | \mathcal{B}_{\mathbf{Q},n} \rangle^* = \langle \mathcal{B}_{\mathbf{Q},n} | T \chi_1^\dagger(x_1) \chi_2^\dagger(x_2) | \Omega \rangle, \quad (5.2.4)$$

with \bar{T} the anti-time-ordering operator and asterisk denoting the complex conjugate of a quantity. We will use these functions in the following to derive the BSF cross section as

¹⁸Unless stated otherwise, capital and small unindexed roman letters appearing in the subsequent discussion will always refer to total and relative 3- or 4-momenta of a two-body system as defined above.

¹⁹For a particle antiparticle pair as often used throughout this work, we can substitute $\chi_1(x_1) \rightarrow \chi(x_1)$ and $\chi_2(x_2) \rightarrow \chi^\dagger(x_2)$.

well as the SE factors used in Sections 5.1.2 and 5.1.3 by connecting them to the usual Schrödinger wave functions in the non-relativistic limit.

For later convenience, we want to separate the COM from the relative motion of the particles. To do so, we first switch to a more suitable coordinate system in position space $X = \eta_1 x_1 + \eta_2 x_2$ and $x = x_1 - x_2$. Using the 4-momentum operator \hat{P} to rewrite

$$\chi_1(x_1) = e^{i\hat{P}X} \chi_1(\eta_2 x) e^{-i\hat{P}X}, \quad \chi_2(x_2) = e^{i\hat{P}X} \chi_2(-\eta_1 x) e^{-i\hat{P}X}, \quad (5.2.5)$$

we obtain after a few steps

$$\Phi_{\mathbf{Q},\mathbf{q}}(x_1, x_2) = e^{-iQX} \langle \Omega | T \chi_1(\eta_2 x) \chi_2(-\eta_1 x) | \mathcal{U}_{\mathbf{Q},\mathbf{q}} \rangle \equiv e^{-iQX} \Phi_{\mathbf{Q},\mathbf{q}}(x), \quad (5.2.6)$$

where $\Phi_{\mathbf{Q},\mathbf{q}}(x)$ only depends on the distance between the two particles, and analogously for the other wave functions. Their Fourier transforms can then be defined accordingly

$$\tilde{\Phi}_{\mathbf{Q},\mathbf{q}}^{(*)}(p) \equiv \int d^4x \Phi_{\mathbf{Q},\mathbf{q}}^{(*)}(x) e^{\pm ipx}, \quad \tilde{\Psi}_{\mathbf{Q},n}^{(*)}(p) \equiv \int d^4x \Psi_{\mathbf{Q},n}^{(*)}(x) e^{\pm ipx}, \quad (5.2.7)$$

with p denoting a relative momentum coordinate defined analogously to q .²⁰

The 4-point Green's function

The 4-point Green's (or correlation) function including the mediator exchange between χ_1 and χ_2 is defined as

$$G^{(4)}(x_1, x_2; y_1, y_2) \equiv \langle \Omega | T \chi_1(y_1) \chi_2(y_2) \chi_1^\dagger(x_1) \chi_2^\dagger(x_2) | \Omega \rangle, \quad (5.2.8)$$

evaluated at arbitrary space-time points $x_{1,2}$ and $y_{1,2}$. It satisfies the *Dyson-Schwinger equation* [156–158]

$$G^{(4)}(x_1, x_2; y_1, y_2) = S_1(x_1 - y_1) S_2(x_2 - y_2) + \int d^4z_1 d^4z_2 d^4z'_1 d^4z'_2 S_1(x_1 - z_1) S_2(x_2 - z_2) W(z_1, z_2; z'_1, z'_2) G^{(4)}(z'_1, z'_2, y_1, y_2), \quad (5.2.9)$$

with $S_{1,2}$ being the full $\chi_{1,2}$ propagators and W describes the perturbative 4-point interaction kernel between χ_1 and χ_2 .²¹ Switching to COM coordinates does neither alter $G^{(4)}$ nor W due to their translational invariance. Their Fourier transforms can thus be defined as

$$\tilde{G}^{(4)}(p, p'; Q) \equiv \int d^4x d^4y d^4(X - Y) G^{(4)}(x, y; X - Y) e^{i(px - p'y)} e^{iQ(X - Y)}, \quad (5.2.10)$$

$$\tilde{W}(p, p'; Q) \equiv \int d^4x d^4y d^4(X - Y) W(x, y; X - Y) e^{i(px - p'y)} e^{iQ(X - Y)}, \quad (5.2.11)$$

²⁰More concretely we define $P \equiv p_1 + p_2$, $p \equiv \eta_2 p_1 - \eta_1 p_2$ such that the Fourier transform $\tilde{\Phi}_{\mathbf{Q},\mathbf{q}}(p_1, p_2) = \int d^4x_1 d^4x_2 \Phi_{\mathbf{Q},\mathbf{q}}(x_1, x_2) e^{ip_1 x_1} e^{ip_2 x_2} = \delta^{(4)}(P - Q) \tilde{\Phi}_{\mathbf{Q},\mathbf{q}}(p)$ reflects the desired momentum separation.

²¹The kernel W involves all truncated 4-fermion diagrams that cannot be disconnected by cutting two fermion lines (see e. g. Ref. [153]).

which we can use to recast the Dyson-Schwinger equation in momentum space

$$\tilde{G}^{(4)}(p, p'; Q) = (2\pi)^4 \delta^{(4)}(p - p') S(p; Q) + S(p; Q) \int \frac{d^4 k}{(2\pi)^4} \tilde{W}(p, k; Q) \tilde{G}^{(4)}(k, p'; Q), \quad (5.2.12)$$

where we further defined for convenience

$$S(p; Q) \equiv \tilde{S}_1(\eta_1 Q + p) \tilde{S}_2(\eta_2 Q - p) \quad \text{with} \quad \tilde{S}_j(p) \equiv \int d^4 z S_j(z) e^{ipz}. \quad (5.2.13)$$

We will employ Eq. 5.2.12 later to derive the wave equations for the Bethe-Salpeter wave functions. Before we can do this, we need to decompose the 4-point Green's function into contributions from bound and scattering states, such that $G^{(4)}$ can be linked to $\Phi_{\mathbf{Q}, \mathbf{q}}$ and $\Psi_{\mathbf{Q}, n}$, separately. This can be attained by applying the one- and two-particle completeness relation

$$\sum_n \int \frac{d^3 Q}{(2\pi)^3 2\omega_{\mathbf{Q}, n}} |\mathcal{B}_{\mathbf{Q}, n}\rangle \langle \mathcal{B}_{\mathbf{Q}, n}| + \int \frac{d^3 Q}{(2\pi)^3 2\omega_{\mathbf{Q}, q}} \frac{d^3 q}{(2\pi)^3 2\varepsilon_{\mathbf{Q}, q}} |\mathcal{U}_{\mathbf{Q}, q}\rangle \langle \mathcal{U}_{\mathbf{Q}, q}| = \mathbb{1} \quad (5.2.14)$$

to $G^{(4)}$ directly, with $\varepsilon_{\mathbf{Q}, q}$ denoting the energy of q . This enables us to split up

$$G^{(4)}(x, y; X - Y) = \sum_n G_n^{(4)}(x, y; X - Y) + G_{\mathcal{U}}^{(4)}(x, y; X - Y), \quad (5.2.15)$$

$$\tilde{G}^{(4)}(p, p'; Q) = \sum_n \tilde{G}_n^{(4)}(p, p'; Q) + \tilde{G}_{\mathcal{U}}^{(4)}(p, p'; Q), \quad (5.2.16)$$

with $G_n^{(4)}$ and $G_{\mathcal{U}}^{(4)}$ denoting the separated Green's functions for the bound and scattering state, respectively.²² After a few steps, we arrive at

$$\tilde{G}_n^{(4)}(p, p'; Q) = i \int d^4 x d^4 y e^{i(px - p'y)} \frac{\Psi_{\mathbf{Q}, n}(x) \Psi_{\mathbf{Q}, n}^*(y) e^{-i[Q^0 - \omega_{\mathbf{Q}, n}][h_-(x^0) - h_+(y^0)]}}{2\omega_{\mathbf{Q}, n}[Q^0 - \omega_{\mathbf{Q}, n} + i\epsilon]} \quad (5.2.17)$$

$$\xrightarrow{Q^0 \rightarrow \omega_{\mathbf{Q}, n}} \frac{i \tilde{\Psi}_{\mathbf{Q}, n}(p) \tilde{\Psi}_{\mathbf{Q}, n}^*(p')}{2\omega_{\mathbf{Q}, n}[Q^0 - \omega_{\mathbf{Q}, n} + i\epsilon]}, \quad (5.2.18)$$

$$\tilde{G}_{\mathcal{U}}^{(4)}(p, p'; Q) = i \int \frac{d^3 q}{(2\pi)^3} \int d^4 x d^4 y e^{i(px - p'y)} \frac{\Phi_{\mathbf{Q}, \mathbf{q}}(x) \Phi_{\mathbf{Q}, \mathbf{q}}^*(y) e^{-i[Q^0 - \omega_{\mathbf{Q}, \mathbf{q}}][h_-(x^0) - h_+(y^0)]}}{2\omega_{\mathbf{Q}, \mathbf{q}} 2\varepsilon_{\mathbf{Q}, \mathbf{q}} [Q^0 - \omega_{\mathbf{Q}, \mathbf{q}} + i\epsilon]} \quad (5.2.19)$$

$$\xrightarrow{Q^0 \rightarrow \omega_{\mathbf{Q}, \mathbf{q}}} \int \frac{d^3 q}{(2\pi)^3} \frac{i \tilde{\Phi}_{\mathbf{Q}, \mathbf{q}}(p) \tilde{\Phi}_{\mathbf{Q}, \mathbf{q}}^*(p')}{2\omega_{\mathbf{Q}, \mathbf{q}} 2\varepsilon_{\mathbf{Q}, \mathbf{q}} [Q^0 - \omega_{\mathbf{Q}, \mathbf{q}} + i\epsilon]}, \quad (5.2.20)$$

²²We used here the standard normalization of one-particle momentum eigenstates, namely $\langle \mathbf{p}_j | \mathbf{k}_j \rangle = 2E_j(\mathbf{p}; \mathbf{Q}) (2\pi)^3 \delta^{(3)}(\mathbf{p}_j - \mathbf{k}_j)$, with $E_j(\mathbf{p}; \mathbf{Q})$ denoting the energy of state $|\mathbf{p}_j\rangle$. To leading order in the interaction strength, we can assume the two-particle state $|\mathcal{U}_{\mathbf{Q}, \mathbf{q}}\rangle$ to yield just the outer product of the two composing one-particle states. Thus, $2\omega_{\mathbf{Q}, \mathbf{q}} 2\varepsilon_{\mathbf{Q}, \mathbf{q}} \simeq 2E_1(\mathbf{q}; \mathbf{Q}) E_2(\mathbf{q}; \mathbf{Q})$.

for the Fourier transformed entities, where Eqs. 5.2.18 and 5.2.20 describe their behavior close to their poles. The functions

$$h_{\pm}(z^0) \equiv \frac{1}{2}(\eta_2 - \eta_1)z^0 \pm \frac{1}{2}|z^0| \quad (5.2.21)$$

are introduced through time ordering and exponentiated after employing the integral representation of the Heavyside Θ function (cf. Eq. A.45). A detailed calculation as well as the corresponding expressions for $G_{n/\mathcal{U}}^{(4)}(x, y; X - Y)$ can be found in Ref. [129].

The Bethe-Salpeter wave equation

With the definition of the operator

$$A(p, p'; Q) \equiv (2\pi)^4 \delta^{(4)}(p - p') S^{-1}(p; Q) - \tilde{W}(p, p'; Q), \quad (5.2.22)$$

we can recast the Dyson Schwinger equation (cf. Eq. 5.2.12) into

$$\int \frac{d^4 k}{(2\pi)^4} A(p, k; Q) \tilde{G}^{(4)}(k, p'; Q) = (2\pi)^4 \delta^{(4)}(p - p'). \quad (5.2.23)$$

In this form, we can see that the 4-point Green's function possesses the general solution

$$\tilde{G}^{(4)}(p, p'; Q) = \sum_n c_n^{-1}(Q) C_n(p; Q) C_n^\dagger(p'; Q) + \int \frac{d^3 q}{(2\pi)^3} f_q^{-1}(Q) F_q(p; Q) F_q^\dagger(p'; Q), \quad (5.2.24)$$

where C_n and F_q denote here the discrete and continuous eigenfunctions of A with eigenvalues c_n and f_q left to be determined. Comparing the expression above to the separated Green's functions, given in Eqs. 5.2.17 and 5.2.19, we can easily extract their structure²³

$$C_n(p; Q) \propto \int d^4 x \Psi_{\mathbf{Q}, n}(x) e^{ipx} e^{-i[Q^0 - \omega_{\mathbf{Q}, n}]h_-(x^0)}, \quad (5.2.25)$$

$$C_n^\dagger(p'; Q) \propto \int d^4 y \Psi_{\mathbf{Q}, n}^*(y) e^{-ip'y} e^{i[Q^0 - \omega_{\mathbf{Q}, n}]h_+(y^0)}, \quad (5.2.26)$$

$$F_q(p; Q) \propto \int d^4 x \Phi_{\mathbf{Q}, q}(x) e^{ipx} e^{-i[Q^0 - \omega_{\mathbf{Q}, q}]h_-(x^0)}, \quad (5.2.27)$$

$$F_q^\dagger(p'; Q) \propto \int d^4 y \Phi_{\mathbf{Q}, q}^*(y) e^{-ip'y} e^{i[Q^0 - \omega_{\mathbf{Q}, q}]h_+(y^0)}, \quad (5.2.28)$$

$$c_n(Q) \propto 1 - \omega_{\mathbf{Q}, n}/Q^0, \quad f_q(Q) \propto 1 - \omega_{\mathbf{Q}, q}/Q^0. \quad (5.2.29)$$

Inserting these quantities into the eigenvalue equations

$$\int \frac{d^4 k}{(2\pi)^4} A(p, k; Q) C_n(k; Q) = c_n(Q) C_n(p; Q), \quad (5.2.30)$$

$$\int \frac{d^4 k}{(2\pi)^4} A(p, k; Q) F_q(k; Q) = f_q(Q) F_q(p; Q), \quad (5.2.31)$$

²³The following relations are fixed since the eigenvalues must not depend on the momenta p, p' and we demand that the eigenfunctions are free of singularities.

and putting them on-shell (i. e. $Q^0 \rightarrow \omega_{\mathbf{Q},n}$ and $Q^0 \rightarrow \omega_{\mathbf{Q},q}$, respectively), we arrive at the Bethe-Salpeter wave equations

$$\tilde{\Psi}_{\mathbf{Q},n}(p) = S(p; Q) \int \frac{d^4k}{(2\pi)^4} \tilde{W}(p, k; Q) \tilde{\Psi}_{\mathbf{Q},n}(k), \quad (5.2.32)$$

$$\tilde{\Phi}_{\mathbf{Q},q}(p) = S(p; Q) \int \frac{d^4k}{(2\pi)^4} \tilde{W}(p, k; Q) \tilde{\Phi}_{\mathbf{Q},q}(k), \quad (5.2.33)$$

which aim to describe scattering and bound states in a relativistic and covariant formalism.²⁴ By taking appropriate limits and approximations, we can revive the usual Schrödinger equation from them, as we will see in the next paragraph.

The Schrödinger equations from the instantaneous approximation

The Bethe-Salpeter wave equations, given in Eqs. 5.2.32 and 5.2.33, lack exact solutions in their general form. Nevertheless, through specific assumptions, one can simplify these equations in order to obtain analytic results. One prevalent simplification method is the *instantaneous approximation* (see e. g. Ref. [159]). It is used in the non-relativistic regime, where the energy exchange between two bound or unbound particles is $q^0 \sim |\mathbf{q}|^2 / (2\mu) \ll |\mathbf{q}|$. Under these circumstances, we can ignore the p^0 and p'^0 dependence of the interaction kernel $\tilde{W}(p, p'; Q)$ to leading order in α and v_{rel} . Moreover, for all cases of interest in the following, \tilde{W} will only depend on $|\mathbf{p} - \mathbf{p}'|$ and neither on \mathbf{p}, \mathbf{p}' nor Q alone. Therefore, we will assume $\tilde{W}(p, p'; Q) \simeq \mathcal{W}(|\mathbf{p} - \mathbf{p}'|)$ throughout this work. By doing so, we can see from the Bethe-Salpeter wave equations that the quantities $S^{-1}(p; Q) \tilde{\Psi}_{\mathbf{Q},n}(p)$ and $S^{-1}(p; Q) \tilde{\Phi}_{\mathbf{Q},q}(p)$ do not depend on p^0 any longer. We will account for that by redefining

$$\tilde{\psi}_{\mathbf{Q},n}(\mathbf{p}) \equiv \sqrt{2\mathcal{N}_{\mathbf{Q}}(\mathbf{p})} \mathcal{S}_0(\mathbf{p}; Q) S^{-1}(p; Q) \tilde{\Psi}_{\mathbf{Q},n}(p), \quad (5.2.34)$$

$$\tilde{\phi}_{\mathbf{Q},q}(\mathbf{p}) \equiv \sqrt{\frac{2\mathcal{N}_{\mathbf{Q}}(\mathbf{p})}{2\varepsilon_{\mathbf{Q},q}}} \mathcal{S}_0(\mathbf{p}; Q) S^{-1}(p; Q) \tilde{\Phi}_{\mathbf{Q},q}(p), \quad (5.2.35)$$

with $\mathcal{S}_0(\mathbf{p}; Q) \equiv \int \frac{dp^0}{2\pi} S(p; Q)$ and $\mathcal{N}_{\mathbf{Q}}(\mathbf{p})$ a normalization factor. The $\tilde{\psi}_{\mathbf{Q},n}(\mathbf{p})$ and $\tilde{\phi}_{\mathbf{Q},q}(\mathbf{p})$ can then be associated with the Fourier transforms of the scattering and bound state Schrödinger wave functions as defined in Section 5.1.1.²⁵ Choosing

$$\mathcal{N}_{\mathbf{Q}}(\mathbf{p}) \equiv \frac{E_1(\mathbf{p}; Q) E_2(\mathbf{p}; Q)}{E_1(\mathbf{p}; Q) + E_2(\mathbf{p}; Q)} \quad (5.2.36)$$

will recover the usual normalization conditions for the Schrödinger wave functions as given in Eqs. 5.1.5 and 5.1.6 (see Ref. [129] for further insight). Employing Eqs. 5.2.34

²⁴The homogeneous Bethe-Salpeter wave equations do not contain information about the normalization of the wave functions. For a detailed discussion about their derivation, the reader is referred to Ref. [129].

²⁵One can show that in position space, the Schrödinger wave functions are connected to the Bethe-Salpeter wave functions at equal times (i. e. $x_1^0 = x_2^0$, cf. Eqs. 5.2.1 and 5.2.2). Therefore, $\tilde{\psi}_{\mathbf{Q},n}^*(\mathbf{p}) = \tilde{\psi}_{\mathbf{Q},n}^*(\mathbf{p})$ and analogously for $\tilde{\phi}_{\mathbf{Q},q}$.

and 5.2.35 to the Bethe-Salpeter wave equations, given in Eqs. 5.2.32 and 5.2.33, yields

$$\frac{\mathcal{S}_0^{-1}(\mathbf{p}; Q)}{\sqrt{2\mathcal{N}_Q(\mathbf{p})}} \tilde{\psi}_{\mathbf{Q},n}(\mathbf{p}) = \int \frac{d^3k}{(2\pi)^3} \frac{\mathcal{W}(|\mathbf{p}-\mathbf{k}|)}{\sqrt{2\mathcal{N}_Q(\mathbf{k})}} \tilde{\psi}_{\mathbf{Q},n}(\mathbf{k}) \quad \text{with} \quad Q^0 = \omega_{\mathbf{Q},n}, \quad (5.2.37)$$

$$\frac{\mathcal{S}_0^{-1}(\mathbf{p}; Q)}{\sqrt{2\mathcal{N}_Q(\mathbf{p})}} \tilde{\phi}_{\mathbf{Q},q}(\mathbf{p}) = \int \frac{d^3k}{(2\pi)^3} \frac{\mathcal{W}(|\mathbf{p}-\mathbf{k}|)}{\sqrt{2\mathcal{N}_Q(\mathbf{k})}} \tilde{\phi}_{\mathbf{Q},q}(\mathbf{k}) \quad \text{with} \quad Q^0 = \omega_{\mathbf{Q},q}. \quad (5.2.38)$$

Since we are already in the non-relativistic regime, we might as well continue by making further non-relativistic approximations. Assuming $|\mathbf{P}|, |\mathbf{p}| \ll P^0, m_1, m_2$, we expand

$$E_1(\mathbf{p}, \mathbf{P}) \simeq \eta_1 \left(m + \frac{\mathbf{P}^2}{2m} \right) + \frac{\mathbf{P} \cdot \mathbf{p}}{m} + \frac{\mathbf{p}^2}{2m_1}, \quad (5.2.39)$$

$$E_2(\mathbf{p}, \mathbf{P}) \simeq \eta_2 \left(m + \frac{\mathbf{P}^2}{2m} \right) - \frac{\mathbf{P} \cdot \mathbf{p}}{m} + \frac{\mathbf{p}^2}{2m_1}, \quad (5.2.40)$$

$$E_1(\mathbf{p}, \mathbf{P}) + E_2(\mathbf{p}, \mathbf{P}) \simeq m + \frac{\mathbf{P}^2}{2m} + \frac{\mathbf{p}^2}{2\mu}, \quad (5.2.41)$$

up to second order in the momenta. This enables us to also approximate (cf. App. C of Ref. [129] for the derivation)

$$\mathcal{S}_0^{-1}(\mathbf{p}; Q) = -\frac{i2E_1(\mathbf{p}, \mathbf{Q})E_2(\mathbf{p}, \mathbf{Q}) [(Q^0)^2 - (E_1(\mathbf{p}, \mathbf{Q}) + E_2(\mathbf{p}, \mathbf{Q}))^2]}{E_1(\mathbf{p}, \mathbf{Q}) + E_2(\mathbf{p}, \mathbf{Q})} \quad (5.2.42)$$

$$\simeq -i4m\mu \left(Q^0 - m - \frac{\mathbf{P}^2}{2m} - \frac{\mathbf{p}^2}{2\mu} \right) = -i4m\mu \left(\mathcal{E} - \frac{\mathbf{p}^2}{2\mu} \right) \quad (5.2.43)$$

to the same order, where we conveniently defined

$$Q^0 \equiv m + \frac{\mathbf{Q}^2}{2m} + \mathcal{E}, \quad (5.2.44)$$

with $\mathcal{E} \in \{\mathcal{E}_n, \mathcal{E}_q\}$ denoting the BS and scattering state energies for $Q^0 = \omega_{\mathbf{Q},n}$ and $Q^0 = \omega_{\mathbf{Q},q}$, respectively. The normalization coefficients cancel on both sides if expanded to leading order in \mathbf{p} and \mathbf{k} , such that we can now write Eqs. 5.2.37 and 5.2.38 as

$$\left(-\frac{\mathbf{p}^2}{2\mu} + \mathcal{E}_n \right) \tilde{\psi}_n(\mathbf{p}) = -\frac{1}{i4m\mu} \int \frac{d^3k}{(2\pi)^3} \mathcal{W}(|\mathbf{p}-\mathbf{k}|) \tilde{\psi}_n(\mathbf{k}), \quad (5.2.45)$$

$$\left(-\frac{\mathbf{p}^2}{2\mu} + \mathcal{E}_q \right) \tilde{\phi}_q(\mathbf{p}) = -\frac{1}{i4m\mu} \int \frac{d^3k}{(2\pi)^3} \mathcal{W}(|\mathbf{p}-\mathbf{k}|) \tilde{\phi}_q(\mathbf{k}). \quad (5.2.46)$$

Note that we have dropped the index \mathbf{Q} in the labelling of the wave functions since we have eliminated its explicit dependence in the equations. Fourier transforming the quantities above, we arrive at the usual Schrödinger equations as defined in Eqs. 5.1.3 and 5.1.4 with

$$V(\mathbf{r}) \equiv -\frac{1}{i4m\mu} \int \frac{d^3p}{(2\pi)^3} \mathcal{W}(|\mathbf{p}|) e^{i\mathbf{p} \cdot \mathbf{r}} \quad (5.2.47)$$

being the non-relativistic potential, which we can now derive from the interaction kernel of the theory. For the models under consideration, this has been done in App. C.

For the case that $\chi_{1,2}$ are fermions, the derivation of the Bethe-Salpeter equations (and its solutions) becomes much more involved due to the spin structure of the particles. A full treatment, which can be reviewed e.g. in Ref. [160], goes beyond the scope of this work. However, as we are only interested in a leading order approximation in the involved momenta, it suffices in the following to use the equations for scalar particles with only a few modifications. First, we have to account for the difference in mass dimensionality of the fermions between relativistic spinors with mass dimension $3/2$ and non-relativistic fields, which are agnostic to the spin properties and have a mass dimension of 1. Thus, we introduce a mapping factor for the Schrödinger wave functions $\tilde{\psi}_n^f(\mathbf{p}) \rightarrow \sqrt{2m_1}\sqrt{2m_2}\tilde{\psi}_n(\mathbf{p})$ and analogously for $\tilde{\phi}_q^f(\mathbf{p})$, which can easily be extracted from the normalization of a single spinor in the Dirac representation $\sqrt{E_i(\mathbf{p}; \mathbf{Q}) + m_i} \simeq \sqrt{2m_i}$. This additional factor has no direct impact on the Schrödinger equations derived from Eqs. 5.2.45 and 5.2.46 due to cancellation on both sides but it will become important in the next section. Moreover, a fermionic propagator in the non-relativistic regime differs by a factor $2m_i$ from a scalar propagator, such that we further take $\tilde{S}_i^f(p_i) \rightarrow 2m_i\tilde{S}_i(p_i)$ in this limit. The additional factor $S^f(p; Q) \rightarrow 4m\mu S(p; Q)$ from the Bethe-Salpeter wave equations then cancels the corresponding factor in the definition of the non-relativistic potential $V(\mathbf{r})$ (cf. Eq. 5.2.47) for a fermionic particle antiparticle pair.

5.2.2 The bound state formation cross section

We are now ready to calculate the cross section for the formation of a BS as sketched in Fig. 5.1 (right). Using the framework we employed in the previous section, to leading order in the coupling α this process can be sufficiently described by

$$\chi_1(k_1) + \chi_2(k_2) \rightarrow \mathcal{B}(\chi_1(p_1)\chi_2(p_2)) + \varphi(P_\varphi), \quad (5.2.48)$$

where $\mathcal{B}(\chi_1\chi_2)$ denotes a bound state with quantum numbers $n \equiv \{nlm\}$. The S-matrix element we want to calculate is, thus,

$${}_{\text{out}}\langle \mathcal{B}_{\mathbf{P},n}; \varphi_{\mathbf{P}_\varphi} | \mathcal{U}_{\mathbf{K},\mathbf{k}} \rangle_{\text{in}} = \langle \mathcal{B}_{\mathbf{P},n}; \varphi_{\mathbf{P}_\varphi} | S | \mathcal{U}_{\mathbf{K},\mathbf{k}} \rangle, \quad (5.2.49)$$

with \mathbf{K}, \mathbf{P} the total and \mathbf{k}, \mathbf{p} the relative 3-momenta of the scattering and BS defined in analogy to Section 5.2.1. The state of the mediator which gets radiated off during a BSF process has 4-momentum $P_\varphi = K - P$ and is denoted in the following by $|\varphi_{\mathbf{P}_\varphi}\rangle$.

The 5-point Green's function

As a first step to determine the S-matrix element for BSF we consider the 5-point Green's function, which is given by

$$G^{(5)}(x_1, x_2; y_1, y_2, X_\varphi) \equiv \langle \Omega | T \varphi(X_\varphi) \chi_1(y_1) \chi_2(y_2) \chi_1^\dagger(x_1) \chi_2^\dagger(x_2) | \Omega \rangle. \quad (5.2.50)$$

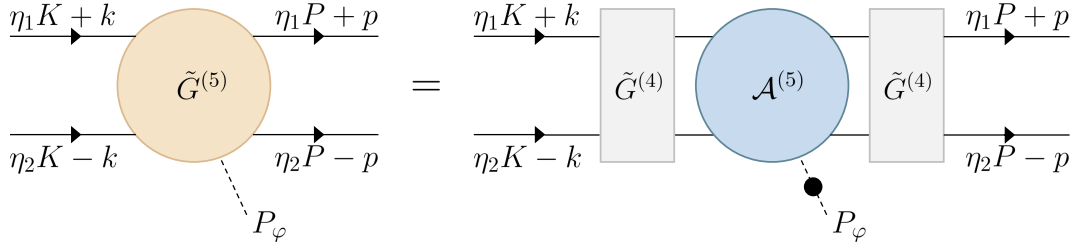


Figure 5.2: Decomposition of the 5-point Green's function $\tilde{G}^{(5)}$ of a $\bar{\chi}\chi$ pair and a bosonic mediator φ according to Eq. 5.2.52. The black filled dot refers to the full propagator of the bosonic mediator φ , whereas the gray boxes on the right denote the 4-point Green's function $\tilde{G}^{(4)}$. The momenta of the incoming (outgoing) particles are also displayed in terms of total and relative momenta of the system. A definition of $\mathcal{A}^{(5)}$ is given in the text. Adapted from Ref. [129].

Due to its translational invariance, we can switch to COM coordinates X, Y and x, y , which are equivalent to the ones used for the 4-point Green's function (cf. Section 5.2.1), and define the Fourier transform as

$$\begin{aligned} \tilde{G}^{(5)}(\eta_1 K + k, \eta_2 K - k; \eta_1 P + p, \eta_2 P - p, P_\varphi) &\equiv \int d^4 X_\varphi d^4 X d^4 Y d^4 x d^4 y \\ &e^{i(KX + kx - PY - py + P_\varphi X_\varphi)} G^{(5)}(X + \eta_2 x, X - \eta_1 x; Y + \eta_2 y, Y - \eta_1 y, X_\varphi), \end{aligned} \quad (5.2.51)$$

where the conjugate momenta of X, x and Y, y are K, k and P, p , respectively. As pictured in Fig. 5.2, the 5-point Green's function in momentum space can be decomposed into

$$\begin{aligned} \tilde{G}^{(5)}(\eta_1 K + k, \eta_2 K - k; \eta_1 P + p, \eta_2 P - p, P_\varphi) &= \tilde{S}_\varphi(P_\varphi) \int \frac{d^4 p'}{(2\pi)^4} \frac{d^4 k'}{(2\pi)^4} \tilde{G}^{(4)}(k', k; K) \\ \tilde{G}^{(4)}(p, p'; P) (2\pi)^4 \delta^{(4)}(K - P - P_\varphi) &i\mathcal{A}^{(5)}(\eta_1 K + k', \eta_2 K - k'; \eta_1 P + p', \eta_2 P - p', P_\varphi), \end{aligned} \quad (5.2.52)$$

where $\mathcal{A}^{(5)}$ can be defined via $\mathcal{C}^{(5)}$, the sum of all connected diagrams²⁶

$$i\mathcal{C}^{(5)}(k_1, k_2; p_1, p_2, P_\varphi) \equiv \tilde{S}_\varphi(P_\varphi) \tilde{S}_1(k_1) \tilde{S}_2(k_2) \tilde{S}_1(p_1) \tilde{S}_2(p_2) i\mathcal{A}^{(5)}(k_1, k_2; p_1, p_2, P_\varphi), \quad (5.2.53)$$

and $\tilde{S}_\varphi(P_\varphi)$ denotes the propagator of a scalar φ , which is given by

$$\tilde{S}_\varphi(P_\varphi) \equiv \frac{iZ_\varphi(\mathbf{P}_\varphi)}{P_\varphi^2 - m_\varphi^2 + i\varepsilon}, \quad \text{with} \quad Z_\varphi(\mathbf{P}_\varphi) = |\langle \Omega | \varphi(0) | \varphi_{\mathbf{P}_\varphi} \rangle|^2 \quad (5.2.54)$$

²⁶We want to emphasize here that $\mathcal{C}^{(5)}$ does also contain diagrams which are not fully connected. Otherwise, $\mathcal{A}^{(5)}$ would just be the sum of all fully connected and amputated diagrams.

its field strength renormalization. For later convenience, we also define $\mathcal{C}_{\varphi\text{-amp}}^{(5)}$, the sum of all connected and φ -amputated diagrams, via

$$i\mathcal{C}^{(5)}(k_1, k_2; p_1, p_2, P_\varphi) \equiv \tilde{S}_\varphi(P_\varphi) i\mathcal{C}_{\varphi\text{-amp}}^{(5)}(k_1, k_2; p_1, p_2, P_\varphi), \quad (5.2.55)$$

such that we can cast $\mathcal{A}^{(5)}$ in a more convenient form

$$i\mathcal{A}^{(5)}(\eta_1 K + k, \eta_2 K - k; \eta_1 P + p, \eta_2 P - p, P_\varphi) = S^{-1}(k; K) S^{-1}(p; P) i\mathcal{C}_{\varphi\text{-amp}}^{(5)}(\eta_1 K + k, \eta_2 K - k; \eta_1 P + p, \eta_2 P - p, P_\varphi) \quad (5.2.56)$$

with $S(p; P)$ defined as in Eq. 5.2.13.

The BSF matrix element

We now want to link the 5-point Green's function to the S-matrix element. This can be achieved by employing the *Lehmann-Symanzik-Zimmermann* (LSZ) reduction formula (see e. g. Ref. [161]). Close to on-shell, i. e. $P_\varphi^0 \rightarrow \omega_\varphi(\mathbf{P}_\varphi)$, $P^0 \rightarrow \omega_{\mathbf{P},n}$, $K^0 \rightarrow \omega_{\mathbf{K},k}$, the LSZ formula is given by

$$\begin{aligned} & \int d^4 X_\varphi e^{iP_\varphi X_\varphi} \int d^4 X e^{iKX} \int d^4 Y e^{-iPY} G^{(5)}(X + \eta_2 x, X - \eta_1 x; Y + \eta_2 y, Y - \eta_1 y, X_\varphi) \\ & \sim \left[\frac{i \langle \Omega | \varphi(0) | \varphi_{\mathbf{P}_\varphi} \rangle}{2\omega_\varphi(\mathbf{P}_\varphi) (P_\varphi^0 - \omega_\varphi(\mathbf{P}_\varphi) + i\varepsilon)} \right] \left[\frac{i \langle \Omega | T \chi_1(\eta_2 x) \chi_2(-\eta_1 x) | \mathcal{B}_{\mathbf{P},n} \rangle}{2\omega_{\mathbf{P},n} (P^0 - \omega_{\mathbf{P},n} + i\varepsilon)} \right] \\ & \int \frac{d^3 k'}{(2\pi)^3 2\varepsilon_{\mathbf{K},k'}} \frac{i \langle \mathcal{U}_{\mathbf{K},k'} | T \chi_1^\dagger(\eta_2 y) \chi_2^\dagger(-\eta_1 y) | \Omega \rangle}{2\omega_{\mathbf{K},k'} (K^0 - \omega_{\mathbf{K},k'} + i\varepsilon)} \langle \mathcal{B}_{\mathbf{P},n}; \varphi_{\mathbf{P}_\varphi} | S | \mathcal{U}_{\mathbf{K},k'} \rangle, \end{aligned} \quad (5.2.57)$$

where \sim means that both sides share the same singularities in this limit. In order to equate them, we need to extract the residues of the singularities from this relation. We start by Fourier transforming both sides with respect to x and y . This yields on the LHS just the definition of $\tilde{G}^{(5)}$. On the RHS it enables us to exchange the two-point correlator functions with the Bethe-Salpeter wave functions in momentum space (cf. Eqs. 5.2.2, 5.2.3 and 5.2.7). Hence, we arrive at

$$\begin{aligned} & \tilde{G}^{(5)}(\eta_1 K + q, \eta_2 K - q; \eta_1 P + p, \eta_2 P - p, P_\varphi) \\ & \sim \left[\frac{i \sqrt{Z_\varphi(\mathbf{P}_\varphi)}}{2\omega_\varphi(\mathbf{P}_\varphi) (P_\varphi^0 - \omega_\varphi(\mathbf{P}_\varphi) + i\varepsilon)} \right] \left[\frac{i \tilde{\Psi}_{\mathbf{P},n}(p)}{2\omega_{\mathbf{P},n} (P^0 - \omega_{\mathbf{P},n} + i\varepsilon)} \right] \\ & \int \frac{d^3 k'}{(2\pi)^3 2\varepsilon_{\mathbf{K},k'}} \frac{i \tilde{\Phi}_{\mathbf{K},k'}^*(q)}{2\omega_{\mathbf{K},k'} (K^0 - \omega_{\mathbf{K},k'} + i\varepsilon)} \langle \mathcal{B}_{\mathbf{P},n}; \varphi_{\mathbf{P}_\varphi} | S | \mathcal{U}_{\mathbf{K},k'} \rangle, \end{aligned} \quad (5.2.58)$$

which we can compare with Eq. 5.2.52 in the on-shell limit (cf. Eqs. 5.2.18 and 5.2.20)

$$\begin{aligned} \tilde{G}^{(5)}(\eta_1 K + q, \eta_2 K - q; \eta_1 P + p, \eta_2 P - p, P_\varphi) &\sim \frac{iZ_\varphi(\mathbf{P}_\varphi)}{P_\varphi^2 - m_\varphi^2 + i\epsilon} \\ &\int \frac{d^4 p'}{(2\pi)^4} \frac{d^4 q'}{(2\pi)^4} \frac{i\tilde{\Psi}_{\mathbf{P},n}(p)\tilde{\Psi}_{\mathbf{P},n}^*(p')}{2\omega_{\mathbf{P},n}(P^0 - \omega_{\mathbf{P},n} + i\epsilon)} \int \frac{d^3 k'}{(2\pi)^3} \frac{i\tilde{\Phi}_{\mathbf{K},k'}(q')\tilde{\Phi}_{\mathbf{K},k'}^*(q)}{2\varepsilon_{\mathbf{K},k'}(K^0 - \omega_{\mathbf{K},k'} + i\epsilon)} \\ &(2\pi)^4 \delta^{(4)}(K - P - P_\varphi) i\mathcal{A}^{(5)}(\eta_1 K + q', \eta_2 K - q'; \eta_1 P + p', \eta_2 P - p', P_\varphi). \end{aligned} \quad (5.2.59)$$

We can extract the residues from $P_\varphi^0 \rightarrow \omega_\varphi(\mathbf{P}_\varphi)$ and $P^0 \rightarrow \omega_{\mathbf{P},n}$ right away. To determine the leading singularity in $K^0 \rightarrow \omega_{\mathbf{K},k}$ a few more steps are in order. First, we multiply both sides by $\tilde{N}_k(q, q''; \mathbf{K})\tilde{\Phi}_{\mathbf{K},k}(q'')$ with \tilde{N}_k being the normalization of $\tilde{\Phi}_{\mathbf{K},k}$. In a second step, we integrate over q and q'' and use the normalization condition (cf. Ref. [129])

$$\int \frac{d^4 q}{(2\pi)^4} \frac{d^4 q''}{(2\pi)^4} \tilde{\Phi}_{\mathbf{K},k'}^*(q)\tilde{N}_{k'}(q, q''; K)\tilde{\Phi}_{\mathbf{K},k}(q'') = 2\omega_{\mathbf{K},k}2\varepsilon_{\mathbf{K},k}(2\pi)^3 \delta^{(3)}(\mathbf{k} - \mathbf{k}') \quad (5.2.60)$$

to match the singularity. Relabelling $p' \rightarrow p$, $q' \rightarrow q$ we can eventually equate

$$\begin{aligned} \langle \mathcal{B}_{\mathbf{P},n}; \varphi_{\mathbf{P}_\varphi} | S | \mathcal{U}_{\mathbf{K},k'} \rangle &= \sqrt{Z_\varphi(\mathbf{P}_\varphi)} \int \frac{d^4 p}{(2\pi)^4} \frac{d^4 q}{(2\pi)^4} \tilde{\Psi}_{\mathbf{P},n}^*(p)\tilde{\Phi}_{\mathbf{K},k}(q)(2\pi)^4 \delta^{(4)}(K - P - P_\varphi) \\ &i\mathcal{A}^{(5)}(\eta_1 K + q, \eta_2 K - q; \eta_1 P + p, \eta_2 P - p, P_\varphi). \end{aligned} \quad (5.2.61)$$

Conventionally defining $\langle \mathcal{B}_{\mathbf{P},n}; \varphi_{\mathbf{P}_\varphi} | S | \mathcal{U}_{\mathbf{K},k'} \rangle \equiv (2\pi)^4 \delta^{(4)}(K - P - P_\varphi) \mathcal{M}_{\mathbf{k} \rightarrow n}$ and switching to $\mathcal{C}_{\varphi\text{-amp}}^{(5)}$, the matrix element of the BSF cross section is given by

$$\mathcal{M}_{\mathbf{k} \rightarrow n} = \sqrt{Z_\varphi(\mathbf{P}_\varphi)} \int \frac{d^4 p}{(2\pi)^4} \frac{d^4 q}{(2\pi)^4} S^{-1}(p, P)\tilde{\Psi}_{\mathbf{P},n}^*(p)S^{-1}(q, K)\tilde{\Phi}_{\mathbf{K},k}(q)\mathcal{C}_{\varphi\text{-amp}}^{(5)} \quad (5.2.62)$$

for a scalar mediator. For a vector mediator, one would redefine $\mathcal{M}_{\mathbf{k} \rightarrow n} = \varepsilon_\mu \mathcal{M}_{\mathbf{k} \rightarrow n}^\mu$ and $\mathcal{C}_{\varphi\text{-amp}}^{(5)} = \varepsilon_\mu (\mathcal{C}_{\varphi\text{-amp}}^{(5)})^\mu$ with ε_μ the polarization vector of φ .

The BSF cross section in the non-relativistic limit

Processes which enable the formation of BS happen deep in the non-relativistic regime with momentum exchanges typically of the order of the binding energy $\mathcal{E}_n \propto \mu\alpha^2$. Thus, it is justified to employ the instantaneous approximation in order to rewrite Eq. 5.2.62 in terms of the Schrödinger wave functions (cf. Eqs. 5.2.34 and 5.2.35)

$$\mathcal{M}_{\mathbf{k} \rightarrow n} \simeq \sqrt{2\varepsilon_{\mathbf{K},k}} \int \frac{d^3 p}{(2\pi)^3} \frac{d^3 q}{(2\pi)^3} \frac{\tilde{\psi}_{\mathbf{P},n}^*(\mathbf{p})\tilde{\phi}_{\mathbf{K},k}(\mathbf{q})}{\sqrt{2\mathcal{N}_{\mathbf{P}}(\mathbf{p})2\mathcal{N}_{\mathbf{K}}(\mathbf{q})}} \mathcal{M}_{\text{trans}}(\mathbf{q}, \mathbf{p}), \quad (5.2.63)$$

where we assumed $Z_\varphi(\mathbf{P}_\varphi) \simeq 1$ to leading order in α . The transition matrix element on the RHS of the equation has been defined as

$$\begin{aligned} \mathcal{M}_{\text{trans}}(\mathbf{p}, \mathbf{q}) &\equiv \mathcal{S}_0^{-1}(\mathbf{q}, K)\mathcal{S}_0^{-1}(\mathbf{p}, P) \\ &\int \frac{dp^0}{2\pi} \frac{dq^0}{2\pi} \mathcal{C}_{\varphi\text{-amp}}^{(5)}(\eta_1 K + q, \eta_2 K - q; \eta_1 P + p, \eta_2 P - p, P_\varphi). \end{aligned} \quad (5.2.64)$$

Making use of Eqs. 5.2.36, 5.2.39 and 5.2.40, we can approximate

$$\frac{1}{\sqrt{2\mathcal{N}_{\mathbf{P}}(\mathbf{p})2\mathcal{N}_{\mathbf{K}}(\mathbf{q})}} \simeq \frac{1}{2\mu} \left(1 - \frac{\mathbf{p}^2 + \mathbf{q}^2}{4\mu^2} \left(1 - \frac{3\mu}{m} \right) \right) \quad (5.2.65)$$

to first order in $\mathbf{p}^2, \mathbf{q}^2$ which will be proportional to α^2 and v_{rel}^2 , respectively. Consequently, we also need to expand the Schrödinger wave functions as well as $\mathcal{M}_{\text{trans}}(\mathbf{p}, \mathbf{q})$ to the same order when computing the matrix element. Corrections from the total initial and final state momenta \mathbf{K} and \mathbf{P} are of $\mathcal{O}(\alpha^2 + v_{\text{rel}}^2)$ and can thus be neglected (i. e. we will only expand them to leading order). Further, we take $\varepsilon_{\mathbf{K}, \mathbf{k}} \simeq \mu$ to leading order in $k^2 \propto v_{\text{rel}}^2$ for the same reasons. Dropping all indices of the total momenta we arrive at

$$\mathcal{M}_{\mathbf{k} \rightarrow n} \simeq \frac{1}{\sqrt{2\mu}} \int \frac{d^3 p}{(2\pi)^3} \frac{d^3 q}{(2\pi)^3} \left(1 - \frac{\mathbf{p}^2 + \mathbf{q}^2}{4\mu^2} \left(1 - \frac{3\mu}{m} \right) \right) \tilde{\psi}_n^*(\mathbf{p}) \tilde{\phi}_{\mathbf{k}}(\mathbf{q}) \mathcal{M}_{\text{trans}}(\mathbf{q}, \mathbf{p}) \quad (5.2.66)$$

for the BSF matrix element, where the concrete dependence on the particle physics model is hidden in $\mathcal{M}_{\text{trans}}$.

The differential BSF cross section into the n -th BS in the COM frame (i. e. $\mathbf{K} = 0$, $\mathbf{P} = -\mathbf{P}_\varphi$) is given by

$$\frac{d\sigma_{\text{BSF}}^{(n)}}{d\Omega} = \frac{1}{2\sqrt{\lambda(s, m_1^2, m_2^2)}} \frac{|\mathbf{P}|}{16\pi^2 \sqrt{s}} \overline{|\mathcal{M}_{\mathbf{k} \rightarrow n}|^2}, \quad (5.2.67)$$

in accordance with Eq. 4.3.8. Using $s = \omega_{\mathbf{K}=0, \mathbf{k}}^2 = (m + \mathcal{E}_{\mathbf{k}})^2$ (see Eq. 5.2.44) as well as $M_n = m + \mathcal{E}_n$ for the bound state mass, to leading order in $\alpha^2, v_{\text{rel}}^2$ we obtain

$$|\mathbf{P}| = \sqrt{\frac{\lambda(s, M_n^2, m_\varphi^2)}{4s}} \simeq (\mathcal{E}_{\mathbf{k}} - \mathcal{E}_n) \left(1 - \frac{m_\varphi^2}{(\mathcal{E}_{\mathbf{k}} - \mathcal{E}_n)^2} \right)^{1/2}, \quad (5.2.68)$$

where we also assumed $m_\varphi \ll m$. Further, $2\sqrt{\lambda(s, m_1^2, m_2^2)} \simeq 4mk = 4m\mu v_{\text{rel}}$ to leading order in k , such that the BSF cross section can be written as

$$\sigma_{\text{BSF}}^{(n)} v_{\text{rel}} = \frac{(\mathcal{E}_{\mathbf{k}} - \mathcal{E}_n)}{64\pi^2 m^2 \mu} \left(1 - \frac{m_\varphi^2}{(\mathcal{E}_{\mathbf{k}} - \mathcal{E}_n)^2} \right)^{1/2} \int d\Omega \overline{|\mathcal{M}_{\mathbf{k} \rightarrow n}|^2}. \quad (5.2.69)$$

A full derivation of the matrix element for the BSF cross section considering a fermionic particle antiparticle system is beyond the scope of this work. However, at leading order in the corresponding momenta we can still use Eq. 5.2.66 together with the appropriate non-relativistic modifications for fermionic entities (cf. Section 5.2.1) to obtain the correct result.

5.3 Non-perturbative effects from EFT

A complementary approach exists for describing SE and the presence of BS within a theoretical model. While this method has long been established for computing the effects of non-perturbative SM processes [162–168], its application to the context of DM is relatively recent [141, 169–172]. This approach leverages the framework of EFT, which naturally facilitates the separation of scales required to compute these phenomena. Analogous to the Bethe-Salpeter approach outlined in Section 5.2, this method heavily depends on the symmetries and particle content of the UV Lagrangian to which the EFT is matched.²⁷ The computations required to determine the necessary observables are generally more extensive than in the UV theory, as the EFT Lagrangian incorporates a greater number of interaction terms that must be considered. However, once computed, many of the obtained results can be applied to different contexts, as EFTs at lower energies are often more analogous to each other than their UV counterparts. Additionally, one enjoys better control over the size of corrections at higher orders due to the clear hierarchy of scales, making it more straightforward to include thermal corrections (or justify their neglect). For these reasons, we will employ this method to ascertain the leading-order processes for the model presented in Section 7, which features a much more intricate structure than the one discussed in Section 6, for which the approach outlined in the previous section suffices. The calculations of the non-perturbative observables for the model in Section 7 will also be conducted within the EFT framework and later cross-checked using the Bethe-Salpeter approach discussed earlier.

Within systems which experience SE and the presence of BS, there are usually three important energy scales to consider. The first one is the *hard* scale, which is set to the mass of the interacting (anti)particle m_χ . The second one, labelled as the *soft* scale, is proportional to the relative momentum exchange $p \propto m_\chi v_{\text{rel}}$ of the interacting $\bar{\chi}\chi$ pair. As non-perturbative effects become important in the regime where $v_{\text{rel}} \sim \alpha$, the soft scale is commonly set to $m_\chi \alpha$. The third scale is denoted as *ultra-soft* and lives at the binding energies of the BS or the kinetic energy of the scattering state, respectively. It is thus conveniently set to $m_\chi \alpha^2$. These three energy scales are hierarchically ordered as follows: $m_\chi \gg m_\chi \alpha \gg m_\chi \alpha^2$. In principle, more energy scales can be relevant, like the mass of the mediator particle m_φ or thermal scales which can arise from interactions of the particles in question with a surrounding plasma. The construction of the EFT for the problem at hand highly depends on where these additional scales are situated with respect to the hard, soft and ultra-soft scales. We will assume in the following that the mass of the mediator particle is at most as large as the soft scale and treat the temperature scale as if it always lives below the ultra-soft scale.²⁸

The method to construct the desired EFT is a two-step procedure [164–166]. Starting

²⁷In the following, we refer to the theory applicable at the highest energy scales considered as the “UV Lagrangian” or “full Lagrangian”. This theory may itself be an EFT, but it must be power-counting renormalizable, i. e. all operators must have mass dimension $d \leq 4$.

²⁸The latter statement is not true in general when describing an evolving Universe, as the temperature runs over all scales of the EFTs. A justification for this choice is given when applying the approach to the model in Section 7.1.

from the full Lagrangian, first all energy and momentum modes of the order of the hard scale are integrated out, resulting in a so-called *non-relativistic EFT* (NREFT). Within this theory, the soft and ultra-soft modes are still intertwined, which is why in a second step, the soft modes are integrated out. Apart from the soft momentum exchanges between the non-relativistic particle pairs, this also includes the mediator mass from our previous assumptions. This procedure yields the *potential NREFT* (pNREFT), which we will use to calculate the relevant cross sections and decay widths. We will highlight in the following how such a pNREFT is constructed using the UV Lagrangian of Section 7 as a concrete example. The derivation of the corresponding EFTs can be found in Refs. [141, 162, 170, 171, 173] in greater detail.

5.3.1 Non-relativistic EFT

We will consider in the following a $\bar{\chi}\chi$ (Dirac) fermion pair which has scalar and pseudo-scalar interactions with a massive real scalar mediator ϕ . The corresponding couplings are denoted as g and g_5 where we assume that $g \gg g_5$ (see Eq. 7.1.1 for the full Lagrangian). This assumption ensures that $\alpha \equiv g^2/(4\pi)$ sets the dynamical scales of the EFTs, while $\alpha_5 \equiv g_5^2/(4\pi)$ remains subleading. After integrating out the hard scale modes, we are left with the NREFT labelled as NRY_{γ_5} , which contains only non-relativistic fermions and antifermions apart from the scalars which have energy and momenta below m_χ . The idea behind the construction of the NRY_{γ_5} Lagrangian (as for any NREFT) is to use Pauli spinor fields ζ, η representing the non-relativistic fermionic fields, where ζ annihilates a fermion and η^\dagger an antifermion, whereas the scalar field ϕ is retained from the UV Lagrangian. The effective Lagrangian is then given as an expansion in terms of the inverse of the hard scale $1/m_\chi$ reading

$$\mathcal{L}_{\text{NRY}_{\gamma_5}} \equiv \sum_{i,n} c_i \frac{\mathcal{O}_i^{(d)}}{m_\chi^n}. \quad (5.3.1)$$

The effective operators $\mathcal{O}_i^{(d)}$ with mass dimension $d = 4 + n$ can be constructed from the present fields ζ, η and ϕ along with time and space differentials ∂_0, ∇ as well as the three vector of Pauli matrices $\boldsymbol{\sigma}$ to account for spin flipping interactions. Viable operators have to respect certain properties of the effective Lagrangian, which are in our case only C and CPT invariance, rotational as well as translational invariance and hermiticity.²⁹ Using field redefinitions and other EFT methods, at each order in $1/m_\chi$ we are able to reduce the amount of effective operators to a minimal and unique number (whereas the operators itself are, in general, not unique). The matching coefficients c_i can then be determined partly using the Lorentz invariance of the full theory and through explicit matching calculations. For examples on how to construct an NREFT, the reader is directed to earlier works on the non-relativistic effective SM theories NRQED and NRQCD [163, 174–176].

²⁹Depending on the underlying full Lagrangian, also other symmetries have to be respected such as gauge invariance or invariance with respect to other discrete symmetries like P and T .

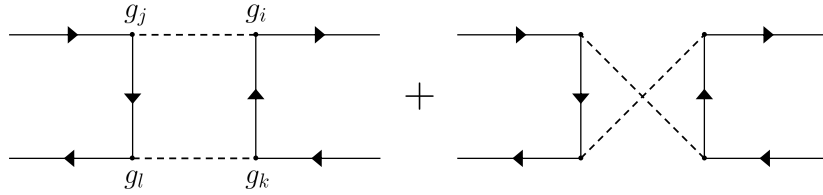


Figure 5.3: The diagrams contributing to the imaginary part of the 4-point Green's function, which can be matched to the NRY_{γ_5} . The couplings $g_{i,j,k,l}$ between the DM fermion and the scalar mediator can either be g or g_5 .

The contributions to the NRY_{γ_5} Lagrangian which will become important in the following can be split up into four sectors, reading

$$\mathcal{L}_{\text{NRY}_{\gamma_5}} \supset \mathcal{L}_{\text{bilinear}}^{\zeta} + \mathcal{L}_{\text{bilinear}}^{\eta} + \mathcal{L}_{4\text{-fermions}} + \mathcal{L}_{\text{scalar}}. \quad (5.3.2)$$

The scalar sector of the effective Lagrangian remains formally unaltered when compared to the full one, since it comprises only of mediator interactions which are at scales lower than the hard scale.³⁰ The interaction vertices between the (anti)fermion and the mediator are contained in the bilinear Lagrangians. With the matching coefficients set to their tree level values, the bilinear parts up to $\mathcal{O}(1/m_\chi)$ yield [141]

$$\mathcal{L}_{\zeta}^{\text{bilinear}} = \zeta^\dagger \left(i\partial_0 - g\phi + g_5 \frac{\boldsymbol{\sigma} \cdot [\nabla\phi]}{2m_\chi} - g_5^2 \frac{\phi^2}{2m_\chi} + \frac{\nabla^2}{2m_\chi} \right) \zeta, \quad (5.3.3)$$

$$\mathcal{L}_{\eta}^{\text{bilinear}} = \eta^\dagger \left(i\partial_0 + g\phi + g_5 \frac{\boldsymbol{\sigma} \cdot [\nabla\phi]}{2m_\chi} + g_5^2 \frac{\phi^2}{2m_\chi} - \frac{\nabla^2}{2m_\chi} \right) \eta, \quad (5.3.4)$$

(see App. A of Ref. [170] for different construction methods) where $[\nabla\phi]$ indicates that the derivative acts solely on the scalar field. We can see that the leading order (and parity violating) pseudo-scalar interaction is accompanied by a factor p/m_χ , which for the present soft and ultra-soft momenta leads to a suppression of at least α when compared to the purely scalar interactions.

The 4-fermion Lagrangian includes annihilations of fermion antifermion pairs into light mediators [163]. These processes have been integrated out in the NREFT because they happen at a scale $2m_\chi$. Employing the optical theorem, the pair annihilation process $\bar{\chi} + \chi \rightarrow 2\phi$ corresponds to the leading order term in the imaginary part of the 4-point Green's function, which is used for the matching procedure (see Ref. [171]). The latter arises from the box diagrams of the UV Lagrangian displayed in Fig. 5.3. It will be most convenient in the following to adopt the notation from NRQED and NRQCD [163, 164] to classify the different 4-fermion operators. The labelling of the operators and matching

³⁰We will ignore in the following the scalar Higgs portal couplings present in Eq. 7.1.1, as they are irrelevant for the subsequent discussion due to their small values.

coefficients is therefore spectroscopic, i. e. they inherit the structure ${}^{2S+1}L_J$ with S the total spin of the annihilating pair and L, J their relative and total angular momentum. This will turn out to be particularly useful when assigning the SE factors. At dimension 6, there are just two independent effective operators [163]

$$\mathcal{O}({}^1S_0) \equiv \varsigma^\dagger \eta \eta^\dagger \varsigma, \quad \mathcal{O}({}^3S_1) \equiv \varsigma^\dagger \boldsymbol{\sigma} \eta \cdot \eta^\dagger \boldsymbol{\sigma} \varsigma, \quad (5.3.5)$$

which contribute to the 4-fermion Lagrangian

$$(\mathcal{L}_{4\text{-fermions}})_{d=6} = \frac{f({}^1S_0)}{m_\chi^2} \mathcal{O}({}^1S_0) + \frac{f({}^3S_1)}{m_\chi^2} \mathcal{O}({}^3S_1), \quad (5.3.6)$$

with $f({}^1S_0)$ and $f({}^3S_1)$ the spin singlet and triplet matching coefficients. As apparent from the operator structure, they take part in the velocity independent s-wave contributions of the annihilation cross section. At dimension 8, one finds 7 independent effective operators [163]

$$\mathcal{O}({}^1P_1) \equiv \varsigma^\dagger \left(-\frac{i}{2} \overleftrightarrow{\nabla} \right) \eta \cdot \eta^\dagger \left(-\frac{i}{2} \overleftrightarrow{\nabla} \right) \varsigma, \quad (5.3.7)$$

$$\mathcal{O}({}^3P_0) \equiv \frac{1}{3} \varsigma^\dagger \left(-\frac{i}{2} \overleftrightarrow{\nabla} \cdot \boldsymbol{\sigma} \right) \eta \eta^\dagger \left(-\frac{i}{2} \overleftrightarrow{\nabla} \cdot \boldsymbol{\sigma} \right) \varsigma, \quad (5.3.8)$$

$$\mathcal{O}({}^3P_1) \equiv \frac{1}{3} \varsigma^\dagger \left(-\frac{i}{2} \overleftrightarrow{\nabla} \times \boldsymbol{\sigma} \right) \eta \cdot \eta^\dagger \left(-\frac{i}{2} \overleftrightarrow{\nabla} \times \boldsymbol{\sigma} \right) \varsigma, \quad (5.3.9)$$

$$\mathcal{O}({}^3P_2) \equiv \varsigma^\dagger \left(-\frac{i}{2} \overleftrightarrow{\nabla}^{(i\sigma^j)} \right) \eta \eta^\dagger \left(-\frac{i}{2} \overleftrightarrow{\nabla}^{(i\sigma^j)} \right) \varsigma, \quad (5.3.10)$$

$$\mathcal{P}({}^1S_0) \equiv \frac{1}{2} \left[\varsigma^\dagger \eta \eta^\dagger \left(\frac{i}{2} \overleftrightarrow{\nabla} \right)^2 \varsigma + \text{h.c.} \right], \quad (5.3.11)$$

$$\mathcal{P}({}^3S_1) \equiv \frac{1}{2} \left[\varsigma^\dagger \boldsymbol{\sigma} \eta \cdot \eta^\dagger \boldsymbol{\sigma} \left(\frac{i}{2} \overleftrightarrow{\nabla} \right)^2 \varsigma + \text{h.c.} \right], \quad (5.3.12)$$

$$\mathcal{P}({}^3S_1, {}^3D_1) \equiv \frac{1}{2} \left[\varsigma^\dagger \sigma^i \eta \cdot \eta^\dagger \sigma^j \left(\frac{i}{2} \overleftrightarrow{\nabla} \right)^2 \overleftrightarrow{\nabla}^{(i\overleftrightarrow{\nabla}^j)} \varsigma + \text{h.c.} \right], \quad (5.3.13)$$

contributing to the 4-fermion Lagrangian

$$\begin{aligned} (\mathcal{L}_{4\text{-fermions}})_{d=8} &= \frac{f({}^1P_1)}{m_\chi^4} \mathcal{O}({}^1P_1) + \frac{f({}^3P_0)}{m_\chi^4} \mathcal{O}({}^3P_0) + \frac{f({}^3P_1)}{m_\chi^4} \mathcal{O}({}^3P_1) + \frac{f({}^3P_2)}{m_\chi^4} \mathcal{O}({}^3P_2) \\ &+ \frac{g({}^1S_0)}{m_\chi^4} \mathcal{P}({}^1S_0) + \frac{g({}^3S_1)}{m_\chi^4} \mathcal{P}({}^3S_1) + \frac{g({}^3S_1, {}^3D_1)}{m_\chi^4} \mathcal{P}({}^3S_1, {}^3D_1), \end{aligned} \quad (5.3.14)$$

where $\eta^\dagger \overleftrightarrow{\nabla} \varsigma \equiv \eta^\dagger (\nabla \varsigma) - (\nabla \eta)^\dagger \varsigma$ and the notation $T^{(ij)}$ for a rank 2 tensor represents its traceless symmetric components, i. e. $T^{(ij)} \equiv (T^{ij} + T^{ji})/2 - T^{kk} \delta^{ij}/3$. The dimension

8 operators all contain spatial derivatives which contribute to the velocity dependent parts of the annihilation cross section. We denote in Eq. 5.3.14 the leading order p-wave operators and matching coefficients with \mathcal{O} and f , respectively, whereas the v_{rel}^2 contributions to the s-wave are labelled with \mathcal{P} and g .

The calculations of the matching coefficients are performed while maintaining the dependence of the results on the mass ratio $\tilde{R} \equiv m_\phi/m_\chi$.³¹ At leading order in both couplings, the imaginary parts of the matching coefficients yield [6]

$$\text{Im} \{f(^1S_0)\} = 2\pi\alpha\alpha_5 \mathcal{F}(\tilde{R}), \quad (5.3.15)$$

$$\text{Im} \{g(^1S_0)\} = -\frac{8\pi\alpha\alpha_5}{3} \frac{\left(1 - \frac{13}{8}\tilde{R}^2 + \frac{5}{8}\tilde{R}^4 - \frac{3}{32}\tilde{R}^6\right)}{(1 - \tilde{R}^2/2)^2(1 - \tilde{R}^2)} \mathcal{F}(\tilde{R}), \quad (5.3.16)$$

$$\text{Im} \{f(^3P_0)\} = \frac{\pi}{6} \left[3\alpha \left(2 - \frac{\mathcal{G}(\tilde{R})}{3} \right) - \alpha_5 \mathcal{G}(\tilde{R}) \right]^2 \mathcal{F}(\tilde{R}), \quad (5.3.17)$$

$$\text{Im} \{f(^3P_2)\} = \frac{\pi}{15} (\alpha + \alpha_5)^2 \mathcal{G}(\tilde{R})^2 \mathcal{F}(\tilde{R}), \quad (5.3.18)$$

with contributions from $f(^3S_1)$, $f(^1P_1)$, $f(^3P_1)$, $g(^3S_1)$ and $g(^3S_1, ^3D_1)$ vanishing. We introduced in the equations above the auxiliary functions

$$\mathcal{F}(\tilde{R}) = \frac{\sqrt{1 - \tilde{R}^2}}{(1 - \tilde{R}^2/2)^2}, \quad \mathcal{G}(\tilde{R}) = \frac{1 - \tilde{R}^2}{1 - \tilde{R}^2/2}, \quad (5.3.19)$$

for a more compact notation. The matching coefficients are calculated by computing the matrix elements of the UV box diagrams in Fig. 5.3, splitting up the 4-fermion spinors into their Pauli spinor components

$$u(\mathbf{p}) \equiv \sqrt{\frac{E_{\mathbf{p}} + m_\chi}{2E_{\mathbf{p}}}} \begin{pmatrix} \zeta \\ \frac{\mathbf{p} \cdot \boldsymbol{\sigma}}{E_{\mathbf{p}} + m_\chi} \zeta \end{pmatrix}, \quad v(\mathbf{p}) \equiv \sqrt{\frac{E_{\mathbf{p}} + m_\chi}{2E_{\mathbf{p}}}} \begin{pmatrix} \frac{\mathbf{p} \cdot \boldsymbol{\sigma}}{E_{\mathbf{p}} + m_\chi} \eta \\ \eta \end{pmatrix}, \quad (5.3.20)$$

and expanding around \mathbf{p}/m_χ to (next to) leading order to compare their structure with the dimension 6 (8) operators of the NREFT. The fermion propagators are expanded as well, whereas the scalar mediator propagators can be put on-shell, since we are only interested in the imaginary parts. We can explain the vanishing 3S_1 and 1P_1 components using C symmetry arguments. The fermion antifermion pair has $C = (-1)^{L+S}$ whereas $C = 1^n$ for n scalar final states. Therefore, only $C = 1$ states are allowed for the initial pair which selects 1S_0 and 3P_J with $J = 0, 1, 2$.

³¹This generalizes the results of Ref. [141]. Although the effect is modest, because the mediator mass is at most of the order of $m_\chi\alpha$, the result is useful for future studies, if one considers higher mediator masses. Note however, that in this case the construction of the NREFT would change, as the mediator scale has to be integrated out together with the fermion mass at the hard scale.

5.3.2 Potential non-relativistic EFT

We can use NREFT to calculate the annihilation cross sections but it is not sufficient, yet, to describe SE or properly account for BS dynamics. We strive for a theory, where the equations of motion have the form of a Schrödinger equation and the dof are bound and scattering states rather than fermions and antifermions. Moreover, we want a unique power-counting, as the soft and ultra-soft scales in the NREFT are still intertwined. To achieve this, we switch to another effective theory by integrating out the soft scale $m_\chi\alpha$, which corresponds to the inverse relative distance $1/r$ between a $\bar{\chi}\chi$ pair. In our case, the mediator mass m_ϕ also needs to be integrated out simultaneously, as it is allowed to be of the order of the soft scale, whereas thermal scales can be set to zero due to the assumption $T \lesssim m_\chi\alpha^2$. The resulting theory is a pNREFT, which for our example case is labelled pNRY $_{\gamma_5}$. It contains as dof only $\bar{\chi}\chi$ pairs as well as mediators ϕ of energies at the order of the ultra-soft scale $m_\chi\alpha^2$.³² These fermion pairs can easily translate to the scattering and BS governed by a Schrödinger equation in the quantum mechanical picture and the power counting is unique as there is only one dynamical scale present.

The Lagrangian of a pNREFT is organized as an expansion in $1/m_\chi$, \mathbf{p} and α which is inherited from the NREFT together with an expansion in $r \sim (m_\chi\alpha)^{-1}$ specific to the pNREFT.³³ The matching coefficients of a pNREFT, which are functions of r , are called *potentials* for reasons which will become clear in a moment. The first thing to notice is that the structure of the Lagrangians of the scalar and bilinear sectors does not change when moving from NRY $_{\gamma_5}$ to pNRY $_{\gamma_5}$ because they do not depend on $1/r$ and are therefore insensitive to the scale which is integrated out, i. e.

$$\mathcal{L}_{\text{scalar}}^{\text{pNRY}_{\gamma_5}} = \mathcal{L}_{\text{scalar}}^{\text{NRY}_{\gamma_5}}, \quad (5.3.21)$$

$$\mathcal{L}_{\text{bilinear}}^{\text{pNRY}_{\gamma_5}} = \mathcal{L}_{\text{bilinear}}^{\zeta, \text{NRY}_{\gamma_5}} + \mathcal{L}_{\text{bilinear}}^{\eta, \text{NRY}_{\gamma_5}}. \quad (5.3.22)$$

However, the actual size of each term is not yet explicit from the NRY $_{\gamma_5}$ Lagrangian and it is also not clear, that the mediator fields are only dependent on ultra-soft scales. Therefore, we project the pNRY $_{\gamma_5}$ Hamiltonian onto the Fock subspace

$$\int d^3x_1 d^3x_2 \varphi_{ij}(\mathbf{x}_1, \mathbf{x}_2, t) \zeta_i^\dagger(\mathbf{x}_1, t) \eta_j(\mathbf{x}_2, t) |\phi_{\text{us}}\rangle, \quad (5.3.23)$$

where the state $|\phi_{\text{us}}\rangle$ contains an arbitrary number of scalar mediators with energies much smaller than the soft scale and no heavy (anti-)fermions, i. e. $\zeta(\mathbf{x}) |\phi_{\text{us}}\rangle = \eta^\dagger(\mathbf{x}) |\phi_{\text{us}}\rangle = 0$. The scattering and bound states of the $\bar{\chi}\chi$ pair are represented by the bilocal wave function field $\varphi_{ij}(\mathbf{x}_1, \mathbf{x}_2, t)$, where i, j are Pauli spinor indices, which we will suppress in the following. The Pauli spinor fields satisfy the equal time anti-commutation relations

$$\{\zeta_i(\mathbf{x}), \zeta_j^\dagger(\mathbf{y})\} = \delta_{ij} \delta^{(3)}(\mathbf{x} - \mathbf{y}), \quad \{\eta_i^\dagger(\mathbf{x}), \eta_j(\mathbf{y})\} = \delta_{ij} \delta^{(3)}(\mathbf{x} - \mathbf{y}), \quad (5.3.24)$$

³²Note that the fermion antifermion pair can still have momenta up to the soft scale, as they appear only as $\mathbf{p}^2/m_\chi \sim m_\chi\alpha^2$ in the observables, whereas the mediator momenta must be ultra-soft.

³³In general, there is an additional expansion in α at the soft scale due to its running. However, we will neglect this for now and justify our decision in Section 7.2 for the specific cases of NRY $_{\gamma_5}$ and pNRY $_{\gamma_5}$.

with all other combinations vanishing. Performing this projection in the bilinear sector yields [141, 170]

$$\mathcal{L}_{\text{bilinear}}^{\text{pNRY}_{\gamma_5}} \supset \int d^3r \varphi^\dagger(\mathbf{r}, \mathbf{R}, t) \left\{ i\partial_0 + \frac{\nabla_{\mathbf{r}}^2}{m_\chi} + \frac{\nabla_{\mathbf{R}}^2}{4m_\chi} + \frac{\nabla_{\mathbf{r}}^4}{4m_\chi^3} - 2g\phi(\mathbf{R}) - g\frac{r^i r^j}{4} \left[\nabla_{\mathbf{R}}^i \nabla_{\mathbf{R}}^j \phi(\mathbf{R}) \right] - g\phi(\mathbf{R}) \frac{\nabla_{\mathbf{r}}^2}{m_\chi^2} \right\} \varphi(\mathbf{r}, \mathbf{R}, t), \quad (5.3.25)$$

where we also switched to COM coordinates $\mathbf{r} \equiv \mathbf{x}_1 - \mathbf{x}_2$, $\mathbf{R} \equiv (\mathbf{x}_1 + \mathbf{x}_2)/2$ and only kept terms up to order $m_\chi \alpha^4$ in the power counting of pNRY $_{\gamma_5}$ for reasons which will become apparent later.³⁴ To see the scaling of the different terms, however, we need to know the power counting rules for the different quantities in the equation [162, 170, 173]. We already know that inverse relative distance together with the corresponding derivative scale as r^{-1} , $\nabla_{\mathbf{r}} \sim m_\chi \alpha$. The time derivative, the scalar field and the inverse COM coordinate as well as its derivative scale as $\partial_0, g\phi, R^{-1}, \nabla_{\mathbf{R}} \sim m_\chi \alpha^2 (\sim T)$, which also self-consistently leads to $r \ll R$ as needed for the expansion. The first line of Eq. 5.3.25 can then be determined easily, where the first two terms are of $m_\chi \alpha^2$ and the last two follow an $m_\chi \alpha^4$ scaling behaviour. Note that the last term had to be added from the $\nabla^4/(8m_\chi^3)$ contributions at $\mathcal{O}(1/m_\chi^3)$ in the mass expansion (not displayed in Eqs. 5.3.3 and 5.3.4) due to these power counting rules. The terms in the second line emerge after a *multipole expansion* of the mediator field in terms of \mathbf{r}

$$\phi(\mathbf{x}_{1,2}) = \phi\left(\mathbf{R} \pm \frac{\mathbf{r}}{2}\right) = \phi(\mathbf{R}) \pm \frac{\mathbf{r}}{2} \cdot \nabla_{\mathbf{R}} \phi(\mathbf{R}) + \frac{1}{8} r^i r^j \nabla_{\mathbf{R}}^i \nabla_{\mathbf{R}}^j \phi(\mathbf{R}) + \mathcal{O}(r^3) \quad (5.3.26)$$

in order to disentangle the different scales induced by \mathbf{r} and \mathbf{R} . We can see that the first two terms in the second line of Eq. 5.3.25 correspond to the monopole and quadrupole of the expansion, whereas the dipole terms cancel. Note that the quadrupole term is needed in the following to capture the leading non-trivial dynamics among the scattering and bound states. The last term is added from the $\pm g\{\nabla, \{\nabla, \phi\}\}/(8m_\chi^2)$ contributions to the bilinear Lagrangians at $\mathcal{O}(1/m_\chi^2)$ in the mass expansion, as it is of the same order as the quadrupole term. In the purely scalar part of the pNRY $_{\gamma_5}$ Lagrangian, we only keep the $\phi(\mathbf{R})$ terms of the multipole expansion. The resulting structure is the same as for the underlying full theory and therefore not displayed.

The 4-fermion sector of the pNRY $_{\gamma_5}$ Lagrangian features new terms when compared to the NRY $_{\gamma_5}$. After projection onto the low energy subspace using Eq. 5.3.23, its Lagrangian reads

$$\mathcal{L}_{4\text{-fermion}}^{\text{pNRY}_{\gamma_5}} = - \int d^3r \varphi^\dagger(\mathbf{r}, \mathbf{R}, t) V(\mathbf{r}, \mathbf{p}, \boldsymbol{\sigma}_1, \boldsymbol{\sigma}_2) \varphi(\mathbf{r}, \mathbf{R}, t), \quad (5.3.27)$$

with matching coefficients $V(\mathbf{r}, \mathbf{p}, \boldsymbol{\sigma}_1, \boldsymbol{\sigma}_2)$, where the $\boldsymbol{\sigma}_1(\boldsymbol{\sigma}_2)$ denotes the spin matrix of the (anti)fermion field in the bilinear NRY $_{\gamma_5}$ Lagrangian. This *potential* comprises a

³⁴Note that the integration over \mathbf{R} is missing since the displayed quantity is actually the Lagrangian density. The spatial derivatives in the new coordinate system yield $\nabla_{\mathbf{x}_{1,2}} = \nabla_{\mathbf{R}}/2 \pm \nabla_{\mathbf{r}}$.

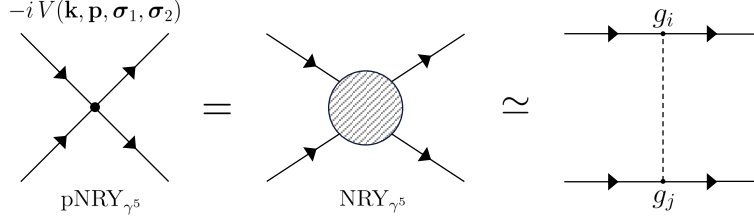


Figure 5.4: Matching of the 4-fermion Lagrangians between the NRY_{γ_5} and pNRY_{γ_5} theory via the off-shell 4-point Green's functions. Solid lines denote (anti)fermions, whereas dashed lines refer to scalar mediator propagators. At leading order, the 4-point Green's function of NRY_{γ_5} consists only of one-boson exchange diagrams with vertex couplings $g_{i,j} \in \{g, g_5\}$. The matching coefficients of the pNRY_{γ_5} are contained in $V(\mathbf{k}, \mathbf{p}, \boldsymbol{\sigma}_1, \boldsymbol{\sigma}_2)$ (in momentum space), where \mathbf{k} is the momentum transfer between the $\bar{\chi}\chi$ pair and thus also the momentum of the mediator propagator in the leading order diagrams.

real and imaginary part, where the latter again corresponds to the annihilation process $\bar{\chi} + \chi \rightarrow 2\phi$. The potential, given by

$$V(\mathbf{r}, \mathbf{p}, \boldsymbol{\sigma}_1, \boldsymbol{\sigma}_2) = V^{(0)} + \frac{V^{(1)}}{m_\chi} + \frac{V^{(2)}}{m_\chi^2}, \quad (5.3.28)$$

is organized as an expansion in α , $1/r$, and $1/m_\chi$ and can be calculated by matching the off-shell 4-point Green's function of NRY_{γ_5} onto pNRY_{γ_5} (see Fig. 5.4). At leading order, the NRY_{γ_5} Green's function corresponds to one boson exchange diagrams. Calculating the purely scalar contribution gives rise to $V(\mathbf{k}, \mathbf{p}, \boldsymbol{\sigma}_1, \boldsymbol{\sigma}_2)|_{g^2} = -4\pi\alpha/(\mathbf{k}^2 - m_\phi^2)$ which after a Fourier transform yields the static Yukawa potential, matching

$$V^{(0)} = -\frac{\alpha}{r} e^{-m_\phi r} \quad (5.3.29)$$

in the expansion of the potential. From the mixed scalar-pseudo-scalar and pure pseudo-scalar diagrams one obtains [141]

$$V(\mathbf{r}, \mathbf{p}, \boldsymbol{\sigma}_1, \boldsymbol{\sigma}_2)|_{gg_5, g_5^2} = -\frac{gg_5}{4\pi m_\chi} \frac{\mathbf{r} \cdot \boldsymbol{\sigma}_1 - \mathbf{r} \cdot \boldsymbol{\sigma}_2}{r^3} + \frac{\pi\alpha_5}{m_\chi^2} \left[-\frac{\boldsymbol{\sigma}_1 \cdot \boldsymbol{\sigma}_2}{3} \delta^{(3)}(\mathbf{r}) + \frac{3\boldsymbol{\sigma}_1 \cdot \hat{\mathbf{r}} \boldsymbol{\sigma}_2 \cdot \hat{\mathbf{r}} - \boldsymbol{\sigma}_1 \cdot \boldsymbol{\sigma}_2}{4\pi r^3} \right], \quad (5.3.30)$$

which enter the m_χ suppressed $V^{(1)}$ and $V^{(2)}$ terms. From power counting arguments, where $\delta^{(3)}(\mathbf{r}) \sim (m_\chi \alpha)^3$, we can see that these terms are of order $(g/g_5)m_\chi \alpha^3$ and $(g/g_5)^2 m_\chi \alpha^4$, respectively, and thus suppressed compared to the purely scalar term, which scales as $m_\chi \alpha^2$. As we will work later with moderate couplings $\alpha < 0.25$ and

already assumed $g_5 < g$, we can therefore neglect mixed and pure pseudo-scalar contributions and only retain the Yukawa term $V^{(0)}$. Collecting all leading $m_\chi \alpha^2$ terms in the pNRY $_{\gamma_5}$ Lagrangian, we are left with

$$\mathcal{L}^{\text{pNRY}_{\gamma_5}} \supset \int d^3r \varphi^\dagger(\mathbf{r}, \mathbf{R}, t) \left[i\partial_0 + \frac{\nabla_{\mathbf{r}}^2}{m_\chi} - V^{(0)} - 2g\phi(\mathbf{R}) \right] \varphi(\mathbf{r}, \mathbf{R}, t). \quad (5.3.31)$$

The corresponding equation of motion for $\varphi(\mathbf{r}, \mathbf{R}, t)$ yields a Schrödinger equation

$$\left(-\frac{\nabla_{\mathbf{r}}^2}{m_\chi} + V^{(0)} + 2g\phi(\mathbf{R}) \right) \varphi(\mathbf{r}, \mathbf{R}, t) = i\partial_0 \varphi(\mathbf{r}, \mathbf{R}, t) \quad (5.3.32)$$

featuring a Yukawa potential.³⁵ Assuming the equation to be independent of \mathbf{R} with no constant background field (i. e. $\phi(\mathbf{R}) \rightarrow 0$) and the Hamiltonian to be independent of time, we obtain the stationary Schrödinger equations given in Eqs. 5.1.3 and 5.1.4. This also relates the bilocal field to the non-relativistic scattering and bound state wave functions $\phi_{\mathbf{k}}$ and ψ_{nlm} , which can be computed with the methods displayed in Section 5.1.1.

As mentioned before, pair annihilations into scalar mediators are encoded in the imaginary part of the matching coefficients in pNRY $_{\gamma_5}$. The Lagrangian of these terms does not discriminate if the bilocal fields $\varphi(\mathbf{r}, \mathbf{R}, t)$ represent scattering or BS. Therefore, in pNRY $_{\gamma_5}$, BS decays can be computed from the same Lagrangian as annihilations cross sections. In NRY $_{\gamma_5}$, annihilations are described by local 4-fermion operators. The same is true for pNRY $_{\gamma_5}$, where the 4-fermion operators of NRY $_{\gamma_5}$ create local terms in the imaginary part of the potential $V(\mathbf{k}, \mathbf{p}, \boldsymbol{\sigma}_1, \boldsymbol{\sigma}_2)$. The relevant terms for annihilation, including s-wave and p-wave contributions up to v_{rel}^2 , are given by [141, 167, 168]

$$\begin{aligned} \mathcal{L}_{\text{ann}}^{\text{pNRY}_{\gamma_5}} &= \frac{i}{m_\chi^2} \int d^3r \varphi^\dagger(\mathbf{r}) \delta^{(3)}(\mathbf{r}) [2\text{Im} \{f^{(1)S_0}\} - \mathbf{S}^2 (\text{Im} \{f^{(1)S_0}\} - \text{Im} \{f^{(3)S_0}\})] \varphi(\mathbf{r}) \\ &\quad - \frac{i}{m_\chi^4} \int d^3r \varphi^\dagger(\mathbf{r}) \mathcal{T}_{S_J}^{ij} \nabla_{\mathbf{r}}^i \delta^{(3)}(\mathbf{r}) \nabla_{\mathbf{r}}^j \text{Im} \{f^{(2S+1)P_J}\} \varphi(\mathbf{r}) \\ &\quad - \frac{i}{2m_\chi^4} \int d^3r \varphi^\dagger(\mathbf{r}) \Omega_{S_J}^{ij} \left\{ \delta^{(3)}(\mathbf{r}), \nabla_{\mathbf{r}}^i \nabla_{\mathbf{r}}^j \right\} \text{Im} \{g^{(2S+1)S_J}\} \varphi(\mathbf{r}), \end{aligned} \quad (5.3.33)$$

where $\mathbf{S} = (\boldsymbol{\sigma}_1 + \boldsymbol{\sigma}_2)/2$ denotes the total spin matrix of the pair³⁶ and $\mathcal{T}_{S_J}^{ij}, \Omega_{S_J}^{ij}$ are spin projection operators, which read [168]

$$\begin{aligned} \mathcal{T}_{01}^{ij} &= \delta^{ij}(2 - \mathbf{S}^2), \quad \mathcal{T}_{10}^{ij} = \frac{1}{3} S^i S^j, \quad \mathcal{T}_{11}^{ij} = \frac{1}{2} \varepsilon^{kil} \varepsilon^{kjm} S^l S^m, \\ \mathcal{T}_{12}^{ij} &= \left(\frac{\delta^{ik} S^l + \delta^{il} S^k}{2} - \frac{\delta^{kl} S^i}{3} \right) \left(\frac{\delta^{jk} S^l + \delta^{jl} S^k}{2} - \frac{\delta^{kl} S^j}{3} \right) \end{aligned} \quad (5.3.34)$$

$$\Omega_{00}^{ij} = \delta^{ij}(2 - \mathbf{S}^2), \quad \Omega_{11}^{ij} = \delta^{ij} \mathbf{S}^2. \quad (5.3.35)$$

³⁵Since $T \lesssim m_\chi \alpha^2$, no thermal contributions will enter the potential at any order.

³⁶Note that \mathbf{S} is an operator which is properly defined as $\mathbf{S} = \boldsymbol{\sigma}_1/2 \otimes \mathbb{1}_2 + \mathbb{1}_1 \otimes \boldsymbol{\sigma}_2/2$ and acts on the $\mathbf{1}/2 \otimes \mathbf{1}/2$ spin space (where $\mathbb{1} = \mathbb{1}_1 \otimes \mathbb{1}_2$ is the unity operator). We will mostly project it on total spin states, where $\mathbf{S}^2|S, m_S\rangle = S(S+1)|S, m_S\rangle$ with $S = 0$ ($S = 1$) for a total spin singlet (triplet).

Note that we have suppressed the \mathbf{R} and t dependence of the $\varphi(\mathbf{r}, \mathbf{R}, t)$ to favor a more compact notation, whereas the \mathbf{r} dependence contributes only at $\mathbf{r} = 0$ due to the contact nature of the 4-fermion interactions already at NRY $_{\gamma_5}$. The NRY $_{\gamma_5}$ matching coefficients in Eq. 5.3.34 are given in Eqs. 5.3.15 to 5.3.18.

When projected onto a total spin state, we can define the expectation value of the bilocal field as

$$\begin{aligned} \varphi_{ij}^{(S)}(t, \mathbf{r}, \mathbf{R}) &\equiv \langle S, m_S | \varphi_{ij}(t, \mathbf{r}, \mathbf{R}) | S, m_S \rangle \\ &= \int \frac{d^3 P}{(2\pi)^3} \left[\sum_n e^{-i\mathcal{E}_n t + i\mathbf{P} \cdot \mathbf{R}} \psi_n(\mathbf{r}) \tilde{S}_{ij}^{(S)} a_n(\mathbf{P}) \right. \\ &\quad \left. + \int \frac{d^3 p}{(2\pi)^3} e^{-i\mathcal{E}_p t + i\mathbf{P} \cdot \mathbf{R}} \phi_p(\mathbf{r}) \tilde{S}_{ij}^{(S)} a_p(\mathbf{P}) \right], \end{aligned} \quad (5.3.36)$$

with $\tilde{S}_{ij}^{(0)} = \delta_{ij}/\sqrt{2}$ the spin matrix elements for a singlet ($S = 0$) and $\tilde{S}_{ij}^{(1)} = (\boldsymbol{\sigma} \cdot \boldsymbol{\epsilon})_{ij}/\sqrt{2}$ for a triplet state ($S = 1$), where $\boldsymbol{\epsilon}$ denotes the spin polarization vector. The matrix elements are already normalized, such that $(\tilde{S}_{ji}^{(S)})^* \tilde{S}_{ij}^{(S)} = 1$ and $(\tilde{S}_{ji}^{(0)})^* \tilde{S}_{ij}^{(1)} = 0$. The $a_{\mathbf{p}}(\mathbf{P})$ and $a_n(\mathbf{P})$ are the ladder operators of the scattering and BS of the $\bar{\chi}\chi$ pair, respectively, where $|\mathbf{p}, \mathbf{P}\rangle = a_{\mathbf{p}}^\dagger(\mathbf{P}) |\Omega\rangle$ creates a scattering and $|n, \mathbf{P}\rangle = a_n^\dagger(\mathbf{P}) |\Omega\rangle$ a bound state. They fulfill the commutation relations

$$\left[a_n(\mathbf{P}), a_{n'}^\dagger(\mathbf{P}') \right] = (2\pi)^3 \delta_{nn'} \delta^{(3)}(\mathbf{P} - \mathbf{P}'), \quad (5.3.37)$$

$$\left[a_{\mathbf{p}}(\mathbf{P}), a_{\mathbf{p}'}^\dagger(\mathbf{P}') \right] = (2\pi)^6 \delta^{(3)}(\mathbf{p} - \mathbf{p}') \delta^{(3)}(\mathbf{P} - \mathbf{P}'), \quad (5.3.38)$$

where we note that n comprises all quantum numbers of the bound state.

The two approaches outlined in Sections 5.2 and 5.3 together with the treatment of the SE factors discussed in Section 5.1 will be extensively used in the following two sections to account for non-perturbative effects in the DM observables for the explicit models under consideration. Whereas the Bethe-Salpeter method is sufficient to describe non-perturbative effects in Section 6, in Section 7 we will resort to the EFT approach for a better handling of the various scales involved, and use the Bethe-Salpeter method only for cross checking.

6 Non-perturbative effects in non-thermal dark matter production

Now that we have gained an understanding of the theoretical and experimental challenges posed by DM, have developed tools to delineate its evolutionary dynamics and address non-perturbative effects in DM interactions, our focus shifts towards practical application. In the following two sections, we explore two distinct theoretical models of DM, each heavily influenced by non-perturbative effects. The primary research topic of this thesis revolves around conducting a comprehensive investigation into the phenomenology of DM within these models, with a particular emphasize on SE and the existence of BS.

Examining the production of DM in the early Universe offers a path towards a clearer understanding of its fundamental nature. Within this area of research, theoretical predictions of experimental signals for DM candidates produced by thermal FO attained a high degree of refinement within the past decades (see e.g. Refs. [1, 61] and references therein). Non-thermal production mechanisms, such as FI, which involve DM that does not thermalize with the SM heat bath (cf. Section 4), have received significantly less recognition to date [177–179]. Nevertheless, these mechanisms, by generating potentially long-lived states within the dark sector, can lead to markedly different collider signatures, rendering them intriguing subjects for study.

We will consider in this section a minimal class of DM models which allow for non-thermal production and can be tested with collider experiments. More concretely, we focus on so-called t -channel mediator models with feeble couplings to the SM, as they have been adopted frequently in DM searches at the LHC [70, 180–187]. These models usually comprise a very weakly interacting DM candidate as well as a mediator with SM quantum numbers. Besides a testable production rate of the mediator particle at colliders for mediator masses below $\mathcal{O}(1 \text{ TeV})$, the mediator interactions with SM gauge bosons give rise to potentially large non-perturbative effects as discussed in Section 5. We compute in the following the two non-thermal production mechanisms relevant for the parameter choices of our model, namely FI and *superWIMP* (sW), with a particular emphasize on SE and BSF. The results will be compared to collider and astrophysical bounds to determine the viable parameter space of the model.

We start by introducing our t -channel mediator model(s) in Section 6.1. In Section 6.2, we explain the two non-thermal production mechanisms mentioned above and set up the BEs for our specific applications. Subsequently, in Section 6.4, we modify the BEs to include non-perturbative effects after computing their impact on the corresponding production rates in Section 6.3. Then, in Section 6.5, we discuss various astrophysical, cosmological, and collider constraints, which we combine to obtain a complete picture of the open parameter space in Section 6.6.

The work presented in this section has been published in Ref. [5]. It appeared as a preprint on the arXiv around the same time as Ref. [188], which also studied the impact of bound state effects on the sW mechanism in the same mediator model but focused more on the astrophysical limits of non-thermal DM. The latter is hence complementary

to our analysis. A later paper by Binder et al. [172] provided a more comprehensive study on BSF within this class of models by taking into account a large number of higher BS as well as BS transitions. Their results will not be considered in the following analysis.

6.1 The t -channel mediator model with feeble couplings

The simplified model under consideration consists of two new particles in the dark sector. First, a DM candidate χ , which is taken to be a singlet under the SM gauge group to allow for non-thermal production. In order to also avoid a direct coupling to the SM via a Higgs portal, we assume it to be of fermionic nature. More concretely, we (arbitrarily) choose χ to be a Majorana fermion, but the outcome for a Dirac fermion is comparable. Furthermore, we assume a \mathbb{Z}_2 symmetry under which all (non-)SM particles are considered even (odd). This guarantees the stability of the DM candidate and prevents a direct coupling to the SM via the neutrino portal. Secondly, we introduce a scalar mediator φ in the \mathcal{O} (TeV) mass regime, eventually linking χ to the SM via a Yukawa-type interaction $\mathcal{L} \subset \lambda_\chi \bar{f} \varphi \chi$, with f a SM fermion and λ_χ the coupling which gatekeeps the connection between the DM candidate and the SM heat bath. Due to the gauge invariance of the Lagrangian, the quantum numbers of the mediator must match the quantum numbers of the SM fermion, but conceptually, interactions with all SM fermions are possible. To simplify things, we assume the mediator to be a singlet under the weak gauge group. Therefore, only interactions with right-handed quarks or leptons are allowed. Disregarding further differences in flavor because they will not alter the features of our model on a qualitative level, we will consider only interactions with the heaviest quarks and leptons. This leaves us with two possible choices: 1) a color-charged *top-philic* mediator denoted by \tilde{t} , which interacts with the right-handed top quark, and 2) a *lepto-philic* mediator $\tilde{\tau}$, carrying only hypercharge while interacting with the right-handed τ -lepton.³⁷ An overview of the introduced dark sector particles is given in Table 6.1.

For the top-philic mediator \tilde{t} , the Lagrangian reads

$$\mathcal{L}_{\text{DS}}^{\tilde{t}} = \frac{i}{2} \bar{\chi} \gamma^\mu \partial_\mu \chi - \frac{1}{2} m_\chi \bar{\chi} \chi - m_{\tilde{t}}^2 \tilde{t}^* \tilde{t}, \quad (6.1.1)$$

$$\mathcal{L}_{\text{int}}^{\tilde{t}} = |D_\mu \tilde{t}|^2 + \lambda_\chi \bar{t}_R \tilde{t} \chi + \lambda_H \tilde{t}^* \tilde{t} (H^\dagger H) + h.c., \quad (6.1.2)$$

and likewise for $\tilde{\tau}$ (exchanging \bar{t}_R with τ_R^\dagger). Here, D_μ denotes the covariant derivative, and H is the SM Higgs doublet present due to an additional Higgs portal of the mediator. Together with the DM and mediator masses m_χ , $m_{\tilde{t}}$ ($m_{\tilde{\tau}}$) as well as the DM mediator coupling λ_χ , its coupling strength λ_H represents one of the four free parameters of our theory. We assume in the following $m_{\tilde{t}}$ ($m_{\tilde{\tau}}$) $\geq m_\chi$, since an inverted mass hierarchy would lead to a stable (color-)charged relic and thus a vastly different phenomenology. For readability, we will continue our discussion using only the top-philic mediator model. Calculations for the lepto-philic mediator are analogous unless stated otherwise.

³⁷The notation is borrowed from supersymmetry, but we want to emphasize that the gauge theory employed is not supersymmetric, and neither are the introduced fields.

Table 6.1: Summary of all dark sector fields introduced in the simplified models considered in Section 6. Note that all of these particles are odd under an additional \mathbb{Z}_2 symmetry.

new particles	type	$SU(3)_c \times SU(2)_L \times U(1)_Y$
\tilde{t}	bosonic scalar	$(\mathbf{3}, \mathbf{1}, 4/3)$
$\tilde{\tau}$	bosonic scalar	$(\mathbf{1}, \mathbf{1}, -2)$
χ	Majorana fermion	$(\mathbf{1}, \mathbf{1}, 0)$

6.2 Non-thermal production mechanisms

As already discussed in Section 4 for the case of FI, we require for non-thermal production the initial number density of DM after reheating to be negligible. Therefore, we set $n_\chi(T_{\text{rh}}) = 0$ in the following. Moreover, DM shall never reach thermal equilibrium with the SM, which is why we further demand the processes driving the production of DM to be slow on cosmological time-scales throughout the entire evolution of the Universe. This means that

$$\left. \frac{\langle \Gamma \rangle_{\text{tot}}}{H} \right|_{T_{\text{max}}} \ll 1, \quad (6.2.1)$$

with $\langle \Gamma \rangle_{\text{tot}}$ being the total thermally averaged production rate and T_{max} the temperature at which the production of χ reaches its maximum. Since all DM production processes relevant for FI within our model scale $\propto \lambda_\chi^2$, Eq. 6.2.1 imposes tight upper limits on the DM mediator coupling. If the two-particle decay of the mediator is kinematically allowed, we can roughly estimate the constraint on λ_χ by taking $\langle \Gamma \rangle_{\text{tot}} \approx \Gamma_{\tilde{t} \rightarrow t_R \chi}$ with

$$\Gamma_{\tilde{t} \rightarrow t_R \chi} = \lambda_\chi^2 \frac{\sqrt{\lambda(m_{\tilde{t}}^2, m_{\tilde{t}}^2, m_\chi^2)}(m_{\tilde{t}}^2 - m_\chi^2 - m_t^2)}{16\pi m_{\tilde{t}}^3}, \quad (6.2.2)$$

and $T_{\text{max}} \approx 0.3 m_{\tilde{t}}$.³⁸ Given a strong mass hierarchy between m_χ and $m_{\tilde{t}}$, Eq. 6.2.1 yields $\lambda_\chi \ll 2 \times 10^{-9} \sqrt{m_{\tilde{t}}/\text{GeV}}$ for $m_{\tilde{t}} \gtrsim 500 \text{ GeV}$. For $T \gtrsim m_{\tilde{t}}$, the mediator is in thermal equilibrium with the SM bath due to its gauge couplings with SM bosons, which results in production and annihilation rates much faster than the expansion of the Universe.

The evolution of DM and the mediator can in general be described by a system of coupled BEs [189]. For FI, the complexity of the system can be drastically reduced (cf. Section 4.2), resulting in a DM yield given by

$$Y_\chi^{\text{FI}}(x) = 2 \left[Y_{\chi, 1 \rightarrow 2}^{\text{FI}}(x) + \sum_{2 \rightarrow 2} Y_{\chi, 2 \rightarrow 2}^{\text{FI}}(x) \right], \quad (6.2.3)$$

³⁸For the top-philic mediator, contributions from $2 \rightarrow 2$ processes can overtake the production rate from $1 \rightarrow 2$ mediator decay for certain mass configurations as we will see in the following (cf. Fig. 6.1). In these cases, a more detailed analysis is in order.

where $x \equiv m_{\tilde{t}}/T$, and an additional factor 2 arises from the summation over equal contributions from \tilde{t} and \tilde{t}^* . Equation 6.2.3 can be derived by integrating over Eqs. 4.2.2 and 4.2.3 with

$$Y_{\chi,1 \rightarrow 2}^{\text{FI}}(x) \equiv \xi_1^{\text{FI}} \int_0^x dx' \frac{g_\star^{1/2}(x')}{h_{\text{eff}}(x')} Y_{\tilde{t}}^{\text{eq}}(x') x' \langle \Gamma_{\text{dec}} \rangle_{\tilde{t} \rightarrow t_R \chi}, \quad (6.2.4)$$

$$Y_{\chi,2 \rightarrow 2}^{\text{FI}}(x) \equiv \xi_2^{\text{FI}} \int_0^x dx' g_\star^{1/2}(x') \frac{Y_a^{\text{eq}}(x') Y_b^{\text{eq}}(x')}{x'^2} \langle \sigma v_{\text{rel}} \rangle_{ab \rightarrow c \chi}, \quad (6.2.5)$$

where the equilibrium yields Y_i^{eq} are given in Eq. 4.2.1, and the prefactors are defined as $\xi_1^{\text{FI}} \equiv \sqrt{45/(4\pi^3)} M_{\text{Pl}}/m_{\tilde{t}}^2$ and $\xi_2^{\text{FI}} \equiv \sqrt{\pi/45} M_{\text{Pl}} m_{\tilde{t}}$. In the color-charged mediator model we take into account the $1 \rightarrow 2$ decay process $\tilde{t} \rightarrow t_R + \chi$ alongside the $2 \rightarrow 2$ processes $\tilde{t} + \bar{t}_R \rightarrow g + \chi$, $\tilde{t} + g \rightarrow t_R + \chi$, and $t_R + g \rightarrow \tilde{t} + \chi$, which are also relevant due to the relative size of the strong coupling $\alpha_s(T)$. For the lepto-philic mediator model, only the $\tilde{\tau} \rightarrow \tau_R^- + \chi$ decay process needs to be considered, because $2 \rightarrow 2$ processes are suppressed by the coupling strength of electromagnetic interactions.

The thermally averaged matrix elements for the $2 \rightarrow 2$ processes $\langle \sigma v_{\text{rel}} \rangle_{ab \rightarrow c \chi}$ can be calculated numerically using Eq. 4.3.7. In the course of the procedure, the integration over s in the $\tilde{t} + g \rightarrow t_R + \chi$ channel requires some additional care due to its infrared divergence at tree level. Calculating the loop diagrams cancelling this divergence goes beyond the scope of this work, which is why we follow Ref. [190] and set a minimal bound of $\sqrt{s_{\text{min}}} = (1 + \epsilon)m_{\tilde{t}}$ with $\epsilon = 0.1$ instead. Analogously, one could also introduce a thermal mass for the gluon. We checked that the results do not change with the cutoff scheme and that they also remain constant upon variation of ϵ . Further, we neglect thermal corrections to the DM yield, which are estimated to give an $\mathcal{O}(10\%)$ correction to the relic density [191].

Contributions from different processes to the FI yield in the top-philic mediator model are depicted in Fig. 6.1 for two different choices of the mediator and DM mass. We can see that DM production through FI is most efficient for $T \sim m_{\tilde{t}}$ (or $x \sim 1$) and levels off swiftly for $T \ll m_{\tilde{t}}$ due to the exponential suppression by the equilibrium yields (cf. Eq. 4.2.4). Additionally, we notice that the $2 \rightarrow 2$ processes become important at early times and for mass configurations where the mediator decay is phase-space suppressed. For $T \lesssim m_{\tilde{t}}/10$ (or $x \gtrsim 10$), the FI contributions become negligible, allowing us to safely consider $Y_{\chi,\infty}^{\text{FI}} \equiv Y_{\chi}^{\text{FI}}(x = 100)$ as the final yield from this production mechanism. If the Yukawa coupling λ_χ is very small, the amount of DM produced from FI (which can be calculated via Eq. 4.2.6) is insufficient to account for the complete amount of DM observed today. In this regime, another production mechanism becomes important, and as λ_χ decreases, it becomes dominant: the so-called superWIMP mechanism.

Up to $T \gtrsim m_{\tilde{t}}/10$ (or $x \lesssim 10$), the mediator maintains thermal equilibrium with the SM heat bath through sufficiently fast interactions with the SM gauge bosons. However, for $T \ll m_{\tilde{t}}$ (or $x \gg 1$) these processes become ineffective, and the mediator eventually freezes out (cf. Section 4.2). Assuming further mediator decays to proceed long after the FO process has been completed, the BE for a $\tilde{t} \tilde{t}^*$ pair is described by Eq. 4.2.5 in this

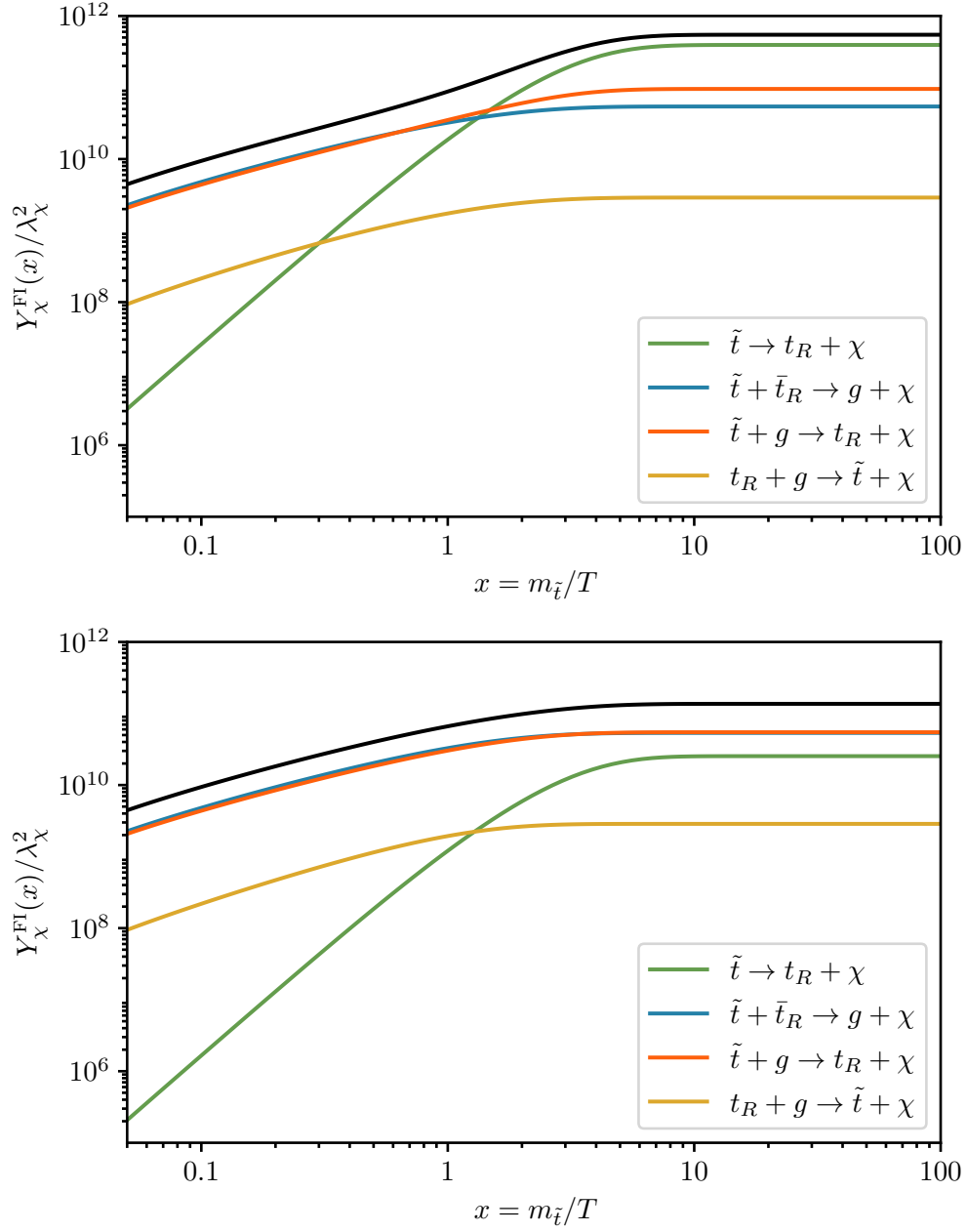


Figure 6.1: Contributions to the FI yield of DM from the most relevant production processes in the top-philic mediator model as a function of $x \equiv m_{\tilde{t}}/T$. The yields on the top (bottom) are stripped of their λ_{χ}^2 dependence and calculated for exemplary masses of $m_{\tilde{t}} = 1 \text{ TeV}$, $m_{\chi} = 100 \text{ GeV}$ ($m_{\chi} = 800 \text{ GeV}$). The black line depicts the total DM yield from FI production.

regime and reads

$$\frac{dY_{\tilde{t}\tilde{t}^*}}{dx} = -\frac{1}{2}\xi_1(x)\langle\sigma_{\text{ann}}v_{\text{rel}}\rangle_0\left(Y_{\tilde{t}\tilde{t}^*}^2 - Y_{\tilde{t}\tilde{t}^*}^{\text{eq}2}\right), \quad (6.2.6)$$

where $Y_{\tilde{t}\tilde{t}^*} = Y_{\tilde{t}} + Y_{\tilde{t}^*}$ (resulting in the additional factor of 1/2), and the prefactor is given by $\xi_1(x) \equiv \sqrt{\pi/45}M_{\text{Pl}}m_{\tilde{t}}g_*^{1/2}(x)x^{-2}$. The thermally averaged annihilation cross section $\langle\sigma_{\text{ann}}v_{\text{rel}}\rangle_0$ incorporates all relevant $\tilde{t} + \tilde{t}^* \rightarrow \text{SM} + \text{SM}$ depletion processes of the mediator and the index 0 indicates that we have not taken into account non-perturbative corrections yet. For the top-philic mediator, assuming $\lambda_H = 0$, the s-wave annihilation cross section reads

$$\langle\sigma_{\text{ann}}v_{\text{rel}}\rangle_0^{\tilde{t}} \approx \sigma_0^{\tilde{t}} = \frac{14\pi\alpha_{s,\text{ann}}^2}{27m_{\tilde{t}}^2} + \frac{64\pi\alpha_{\text{em}}\alpha_{s,\text{ann}}}{81m_{\tilde{t}}^2} \left[1 + \left(1 - \frac{m_Z^2}{4m_{\tilde{t}}^2} \right) \tan^2\theta_W \right], \quad (6.2.7)$$

with contributions from $g + g$, $g + \gamma$ and $g + Z$ final states.³⁹ Allowing for $\lambda_H > 0$, the annihilation channels $t + \bar{t}$, $W^+ + W^-$ and $h + h$ can become sizeable. We have taken here the electromagnetic coupling $\alpha_{\text{em}} \equiv \alpha_{\text{em}}(m_Z) \approx 1/128$ measured at the Z pole and evaluate the strong coupling $\alpha_{s,\text{ann}} \equiv \alpha_s(m_{\tilde{t}})$ at the mediator mass scale (assuming the annihilating particles to be non-relativistic). In the lepto-philic mediator model, the dominant final states for $\lambda_H = 0$ are $\gamma + \gamma$, $\gamma + Z$ and $Z + Z$, resulting in an s-wave cross section of

$$\begin{aligned} \langle\sigma_{\text{ann}}v_{\text{rel}}\rangle_0^{\tilde{\tau}} \approx \sigma_0^{\tilde{\tau}} &= \frac{2\pi\alpha_{\text{em}}^2}{m_{\tilde{\tau}}^2} + \left(1 - \frac{m_Z^2}{4m_{\tilde{\tau}}^2} \right) \frac{4\pi\alpha_{\text{em}}^2}{m_{\tilde{\tau}}^2} \tan^2\theta_W \\ &+ \sqrt{1 - \frac{m_Z^2}{m_{\tilde{\tau}}^2}} \frac{8m_{\tilde{\tau}}^4 - 8m_{\tilde{\tau}}^2m_Z^2 + 3m_Z^4}{(m_Z^2 - 2m_{\tilde{\tau}}^2)^2} \frac{\pi\alpha_{\text{em}}^2}{m_{\tilde{\tau}}^2} \tan^4\theta_W. \end{aligned} \quad (6.2.8)$$

For sizable $\lambda_H > 0$, the channels $W^+ + W^-$, $h + h$, and $t + \bar{t}$ become accessible at tree-level, with the first two potentially dominating. The co-annihilation processes which have been important for FI production of DM, do not play a role here because they are suppressed by the very small coupling λ_χ .

After FO, the relic abundance of the mediator has to be depleted to avoid constraints from BBN. For a Yukawa coupling $\lambda_\chi > 0$, this is achieved through its decay, opening up another production mode for DM, known as superWIMP mechanism [177, 178, 192]. In this mechanism, one DM particle χ is produced for each frozen out mediator, resulting in a total dark matter yield given by $Y_{\chi,\infty}^{\text{sW}} \equiv Y_{\tilde{t}\tilde{t}^*}^{\text{sW}}(x_p)$, where x_p refers to a temperature regime after FO where the mediator yield is stable and before decay processes take place. As long as the mediator abundance is fully depleted before BBN, this mechanism is agnostic to the size of the coupling λ_χ .

The final DM yield is then given by a combination of FI and sW production, $Y_{\chi,\infty} = Y_{\chi,\infty}^{\text{FI}} + Y_{\chi,\infty}^{\text{sW}}$, where the relative importance of the two mechanisms is moderated by the value of the Yukawa coupling. When establishing the valid parameter space for our

³⁹Contributions from e. g. $\gamma + \gamma$ or $Z + Z$ (for $\lambda_H = 0$) have been neglected since they are suppressed by α_{em}^2 .

model in Section 6.6, this will enable us to fix one of the four free model parameters by comparing the calculated abundance (cf. Eq. 4.2.6) to its experimental value observed today. Before proceeding, we investigate the influence of non-perturbative effects, which can affect the FO process of the mediator and thus influence the sW contribution to the overall dark matter abundance.

6.3 Non-perturbative effects in dark matter production

The long-ranged interactions of the mediator with the SM gauge fields give rise to non-perturbative effects in DM production (cf. Section 5). Since FO typically happens in the non-relativistic regime where $\zeta \gg 1$, these effects can lead to sizeable corrections to the mediator yield after FO (and therefore to the DM abundance). Following the discussion in App. C, the potentials entering the Schrödinger equations (cf. Eqs. 5.1.3 and 5.1.4)

$$\begin{aligned} \left[-\frac{1}{2\mu} \nabla^2 + V(\mathbf{r}) \right] \phi_{\mathbf{k}}(\mathbf{r}) &= \mathcal{E}_{\mathbf{k}} \phi_{\mathbf{k}}(\mathbf{r}), \\ \left[-\frac{1}{2\mu} \nabla^2 + V(\mathbf{r}) \right] \psi_{nlm}(\mathbf{r}) &= \mathcal{E}_{nl} \psi_{nlm}(\mathbf{r}), \end{aligned}$$

are given by

$$V_{\tilde{t}}(\mathbf{r}) = -\frac{\alpha_g}{r}, \quad V_{\tilde{\tau}}(\mathbf{r}) = -\frac{1}{r} (\alpha_\gamma + \alpha_Z e^{-m_Z r} + \alpha_H e^{-m_H r}), \quad (6.3.1)$$

for both mediator models. The form of the individual contributions and their couplings can be extracted from Table C.1. For the top-philic mediator model, we will only consider the dominating gluon potential, which is Coulomb-like in the perturbative regime, for both scattering and bound states [193]. In the lepto-philic mediator model, we will also employ the Z boson and Higgs potential for the scattering states as they can be sizeable for certain mass configurations of the DM and mediator particle. For the BS Schrödinger equation within this model, only the Coulomb potential is taken into account, which we justify in App. C.

The energy eigenstates of the Schrödinger wave functions are given by $\mathcal{E}_{\mathbf{k}} = k^2/(2\mu)$ for scattering and $\mathcal{E}_n = -\kappa^2/(2\mu n^2)$ for BS, where n denotes the principal quantum number and l is degenerate. The reduced mass is given by $\mu = m_{\tilde{t}}/2$ and $k \equiv |\mathbf{k}| = \mu v_{\text{rel}}$ denotes the average momentum transfer in scattering processes. The Bohr momentum of the bound state is defined as $\kappa = \mu \alpha_g^B$, where α_g^B denotes the interaction strength of the gluon potential (cf. Table C.1) evaluated at κ .⁴⁰ Starting with a $\tilde{t} \tilde{t}^*$ pair in the (anti)fundamental representation, from group theoretical arguments ($\mathbf{3} \otimes \bar{\mathbf{3}} = \mathbf{8} \oplus \mathbf{1}$) we can see that the resulting final state can either be in a color singlet or octet configuration. For a scattering state, both representations are possible, while for a BS only the singlet state is populated since the color octet creates a repulsive potential, making it impossible for BS to form. Therefore, $\alpha_g^B \equiv \alpha_{g,[1]}^B = 4/3 \alpha_{s,[1]}^B$ with $\alpha_{s,[1]}^B \equiv \alpha_s(\mu \alpha_{g,[1]}^B)$.

⁴⁰In case of the lepto-philic mediator the running of α_{em} can be neglected.

In the top-philic mediator model, the SE factors and the BSF cross section can be calculated using analytical solutions for $\phi_{\mathbf{k}}(\mathbf{r})$ and $\psi_{nlm}(\mathbf{r})$ as given in Eqs. 5.1.9, 5.1.10, 5.1.18 and 5.1.19. For the lepto-philic mediator model, this is also possible for the BSF cross section (as we neglect the Z and Higgs contributions), for the SE factors, however, a numerical solution has to be employed (cf. Sections 5.1.2 and 5.1.3). Since this is a qualitative study on the impact of non-perturbative effects, we will restrict ourselves calculating only the dominating s-wave contributions to the corresponding quantities. With respect to BS, we will for simplicity take into account only the ground state ($\{nlm\} \rightarrow \{100\}$) and neglect excited states as well as bound-to-bound transitions. For a quantitative study on higher bound state effects, the reader is referred to Ref. [172].

By taking into account these non-perturbative effects, the BE, given in Eq. 6.2.6, for mediator FO is modified in two ways. Firstly, the thermally averaged annihilation cross section $\langle\sigma_{\text{ann}}v_{\text{rel}}\rangle_0 \rightarrow \langle\sigma_{\text{ann}}v_{\text{rel}}\rangle$ receives corrections from SE. Secondly, we employ a separate BE for each bound state and couple it to Eq. 6.2.6 through BSF and ionization processes. The new system of BEs is then given by (cf. e. g. Ref. [142])

$$\frac{dY_{\tilde{t}\tilde{t}^*}}{dx} = -\frac{1}{2}\xi_1(x) \langle\sigma_{\text{ann}}v_{\text{rel}}\rangle \left(Y_{\tilde{t}\tilde{t}^*}^2 - Y_{\tilde{t}\tilde{t}^*}^{\text{eq}2}\right) - \frac{1}{2}\xi_1(x) \langle\sigma_{\text{BSF}}v_{\text{rel}}\rangle Y_{\tilde{t}\tilde{t}^*}^2 + 2\xi_2(x) \langle\Gamma_{\text{ion}}\rangle Y_B, \quad (6.3.2)$$

$$\frac{dY_B}{dx} = -\xi_2(x) \langle\Gamma_{\text{dec}}\rangle (Y_B - Y_B^{\text{eq}}) + \frac{1}{4}\xi_1(x) \langle\sigma_{\text{BSF}}v_{\text{rel}}\rangle Y_{\tilde{t}\tilde{t}^*}^2 - \xi_2(x) \langle\Gamma_{\text{ion}}\rangle Y_B, \quad (6.3.3)$$

with Y_B the bound state yield of the ground state and $\xi_2(x) \equiv \xi_1(x)/s(x)$ denoting a second prefactor. The equilibrium yields in the non-relativistic regime ($x \gg 1$) are given by (cf. Eq. 4.2.4)

$$Y_{\tilde{t}\tilde{t}^*}^{\text{eq}}(x) = \frac{45g_{\tilde{t}}}{2\sqrt{2}\pi^{7/2}h_{\text{eff}}(x)} x^{3/2} e^{-x}, \quad (6.3.4)$$

$$Y_B^{\text{eq}}(x) = \frac{g_B}{2g_{\tilde{t}}} \frac{h_{\text{eff}}\left(\frac{m_B}{m_{\tilde{t}}}x\right)}{h_{\text{eff}}(x)} Y_{\tilde{t}\tilde{t}^*}^{\text{eq}}\left(\frac{m_B}{m_{\tilde{t}}}x\right), \quad (6.3.5)$$

where $m_B = 2m_{\tilde{t}} + \mathcal{E}_1$ is the mass of the ground state and $\mathcal{E}_1 = -4/9 m_{\tilde{t}}(\alpha_{s,[1]}^B)^2$ denotes its binding energy. The internal dof are $g_{\tilde{t}} = 3$ ($g_{\tilde{\tau}} = 1$) for the individual mediator particles and $g_B = 1$ for the bound ground state. In the regime where $x \gtrsim 1$, we can set $h_{\text{eff}}(m_B/m_{\tilde{t}}x)/h_{\text{eff}}(x) \approx 1$. In the following subsections, we will calculate $\langle\sigma_{\text{ann}}v_{\text{rel}}\rangle$ as well as the thermally averaged BSF cross section $\langle\sigma_{\text{BSF}}v_{\text{rel}}\rangle$, the bound state ionization rate $\langle\Gamma_{\text{ion}}\rangle$ and its decay rate $\langle\Gamma_{\text{dec}}\rangle$ for the top- and lepto-philic mediator model.

6.3.1 Dark matter annihilation cross section and bound state decay rate

Following the decomposition in Eq. 5.1.1, the SE corrected s-wave contribution to the thermally averaged annihilation cross section in the top-philic mediator model is given by

$$\langle\sigma_{\text{ann}}v_{\text{rel}}\rangle \approx \sum_i \sigma_0^i \left\langle S_{\text{ann},0}^{[\tilde{\mathbf{R}}_i]} \right\rangle, \quad (6.3.6)$$

where σ_0^i are the s-wave contributions to the annihilation cross section (cf. Eq. 6.2.7) split up by the color representation of their two-particle final state $\hat{\mathbf{R}}_i$ and the

$$\left\langle S_{\text{ann},0}^{[\hat{\mathbf{R}}_i]} \right\rangle \equiv \frac{x^{3/2}}{2\sqrt{\pi}} \int_0^\infty dv_{\text{rel}} v_{\text{rel}}^2 e^{-\frac{x}{4}v_{\text{rel}}^2} S_{\text{ann},0}^{[\hat{\mathbf{R}}_i]} \quad (6.3.7)$$

denote the thermally averaged s-wave SE factors. This distinction of representations is necessary because particles in different initial representations (which have to match the final state representations due to color conservation) will experience different potentials. Therefore, also the SE factor for a Coulomb potential as given in Eq. 5.1.21 depends on $\hat{\mathbf{R}}_i$ through $\alpha_{g,[\hat{\mathbf{R}}_i]}^S$. Mediator annihilations into the final states $Z + Z$, $h + h$, $W^+ + W^-$ can only happen in the singlet configuration due to the lack of color-charge in the final state. Therefore, they have $\alpha_{g,[1]}^S = 4/3 \alpha_s^S$ with $\alpha_s^S \equiv \alpha_s(k)$ being evaluated at k . Annihilations into $\bar{t} + t$ are also approximated color singlets because the gluon mediated interactions are p-wave suppressed. The final states $g + Z$ and $g + \gamma$ are color octets and therefore possess a coupling of $\alpha_{g,[8]}^S = -1/6 \alpha_s^S$. The SE factors for pure singlet and octet potentials are given by

$$S_{\text{ann},0}^{[1]} = S_0 \left(\frac{4}{3} \zeta \right), \quad S_{\text{ann},0}^{[8]} = S_0 \left(-\frac{1}{6} \zeta \right), \quad (6.3.8)$$

with $\zeta \equiv \alpha_s^S/v_{\text{rel}}$, here. For the annihilation process $\tilde{t} + \tilde{t}^* \rightarrow g + g$, both color configurations are possible. One has to correct here for the treatment of the initial states in the computation of the matrix elements that enter σ_0^i by weighting the SE factors [126, 194]

$$S_{\text{ann},0}^{[1]+[8]} = \frac{2}{7} S_0 \left(\frac{4}{3} \zeta \right) + \frac{5}{7} S_0 \left(-\frac{1}{6} \zeta \right). \quad (6.3.9)$$

The lepto-philic mediator model just features one SE factor for all contributions σ_0^i (cf. Eq. 6.2.8) to the annihilation cross sections. However, in this case the SE factor has to be calculated numerically due to the Yukawa potentials from Higgs and Z boson exchange (cf. Eq. 6.3.1). To accomplish this, we employ the technique presented in Section 5.1.2 using the differential equation for the radial part of the s-wave scattering wave function (cf. Eq. 5.1.11)

$$\tilde{\chi}_{\mathbf{k},0}''(y) + \left(1 + \frac{2}{y} \left[\zeta_\gamma + \zeta_Z e^{-b_Z y} + \zeta_H e^{-b_H y} \right] \right) \tilde{\chi}_{\mathbf{k},0}(y) = 0, \quad (6.3.10)$$

with $y = kr$, $b_i = m_i/k$, where we employ the initial conditions $\tilde{\chi}_{\mathbf{k},0}(y) \xrightarrow{y \rightarrow 0} y$, $\tilde{\chi}_{\mathbf{k},0}'(y) \xrightarrow{y \rightarrow 0} 1 - (\zeta_\gamma + \zeta_Z + \zeta_H)y$.⁴¹

For BS decays, we can approximate the thermal average $\langle \Gamma_{\text{dec}} \rangle \approx \Gamma_{\text{dec}}$ for $x \gtrsim 10$. In the top-philic mediator model we require the BS to be a color singlet for reasons explained above. Applying the decomposition given in Eq. 5.1.2, we then obtain

$$\Gamma_{\text{dec}} \approx \frac{g_t^2}{g_B} S_{\text{dec},0}^{\{100\}} \sum_i w_{[1]}^i \sigma_0^i, \quad (6.3.11)$$

⁴¹The same parametrization as in Eq. 5.1.11 is not feasible here, due to the different coupling strengths of the potentials. However, this choice does not affect Eq. 5.1.24.

with $S_{\text{dec},0}^{\{100\}} = \kappa^3/\pi = 8m_{\tilde{t}}^3(\alpha_{s,[1]}^B)^3/(27\pi)$ being the SE factor for the ground state decay rate when applying a Coulomb potential and σ_0^i contains all contributions to the annihilation cross section where a singlet final state is possible. The factor $g_{\tilde{t}}^2/g_B$ corrects for the difference in dof between the scattering and the BS in the cross section due to color-charge, while $w_{[1]}^i$ is a singlet weighting factor, which yields 2/7 for mixed [1] + [8] contributions (cf. Eq. 6.3.9), 1 for the purely [1] final states and 0 for the pure [8] representations. In the lepto-philic mediator model, where BS are only mediated by the Coulomb potential (see App. C), the picture is very similar with $g_{\tilde{\tau}}^2/g_B = 1$, $S_{\text{dec},0}^{\{100\}} = \kappa^3/\pi = \alpha_{\tilde{\gamma}}^3 m_{\tilde{\tau}}^3/(8\pi)$ (and no weighting factor).

6.3.2 Bound state formation cross section and ionization rate

To calculate the BSF cross section for the top-philic mediator model, we will use the results obtained in Section 5.2.2 (or Ref. [129]) and from there on revise the derivation in Ref. [136] for non-abelian theories. First, we need to calculate the transition matrix element (cf. Eq. 5.2.64)

$$[\mathcal{M}_{\text{trans}}(\mathbf{p}, \mathbf{q})]_{ii',jj'}^{\nu,a} \equiv \mathcal{S}_0^{-1}(\mathbf{p}, P)\mathcal{S}_0^{-1}(\mathbf{q}, K) \int \frac{d^3p^0}{2\pi} \frac{d^3q^0}{2\pi} \left[\mathcal{C}_{g\text{-amp}}^{(5)}(q, p; K, P, P_g) \right]_{ii',jj'}^{\nu,a}$$

of the process $(\tilde{t} + \tilde{t}^*)_{[8]} \rightarrow \mathcal{B}(\tilde{t} \tilde{t}^*)_{[1]} + g_{[8]}$, where the color representation of the initial state has been fixed by the final state demands. $\mathcal{C}_{g\text{-amp}}^{(5)}$ denotes the sum of all connected diagrams contributing to the process

$$\chi_{1,i}(\eta_1 K + q) + \chi_{2,j}(\eta_2 K - q) \rightarrow \chi_{1,i'}(\eta_1 P + p) + \chi_{2,j'}(\eta_2 P - p) + g^a(P_g) \quad (6.3.12)$$

where we relabelled $\tilde{t} \rightarrow \chi_1$, $\tilde{t}^* \rightarrow \chi_2$ for better comparability with Section 5.2. The incoming and outgoing scalars $\chi_{1,2}$ are off-shell and carry color-charge indices i, i', j and j' . The radiated gluon with momentum P_g and color-charge a is on-shell and amputated, and the total and relative momenta K, P, p and q are defined equivalently to the ones in Section 5.2.2. To leading order in the strong coupling, the diagrams contributing to

$$\left[\mathcal{C}_{g\text{-amp}}^{(5)} \right]_{ii',jj'}^{\nu,a} = [\mathcal{C}_0]_{ii',jj'}^{\nu,a} + [\mathcal{C}_1]_{ii',jj'}^{\nu,a} + [\mathcal{C}_2]_{ii',jj'}^{\nu,a} \quad (6.3.13)$$

are sketched in Fig. 6.2. They yield

$$\begin{aligned} i [\mathcal{C}_0]_{ii',jj'}^{\nu,a} = & \tilde{S}_1(\eta_1 P + p) [-ig_s^{\text{NA}}(T_1^b)_{ii'}(\eta_1 K + \eta_1 P + q + p)_\rho] \tilde{S}_1(\eta_1 K + q) \frac{-i}{(\eta_1 K + q - \eta_1 P - p)^2} \\ & \tilde{S}_2(\eta_2 P - p) [-ig_s^{\text{NA}}(T_2^c)_{jj'}(\eta_2 K + \eta_2 P - q - p)_\mu] \tilde{S}_2(\eta_2 K - q) \frac{-i}{(\eta_2 K - q - \eta_2 P + p)^2} \\ & (-ig_s^{\text{BSF}} f^{abc}) \{g^{\rho\mu}[(\eta_1 K + q - \eta_1 P - p) - (\eta_2 K - q - \eta_2 P + p)]^\nu \\ & -g^{\nu\rho}[(\eta_1 K + q - \eta_1 P - p) + P_g]^\mu + g^{\mu\nu}[(\eta_2 K - q - \eta_2 P + p) + P_g]^\rho\}, \quad (6.3.14) \end{aligned}$$

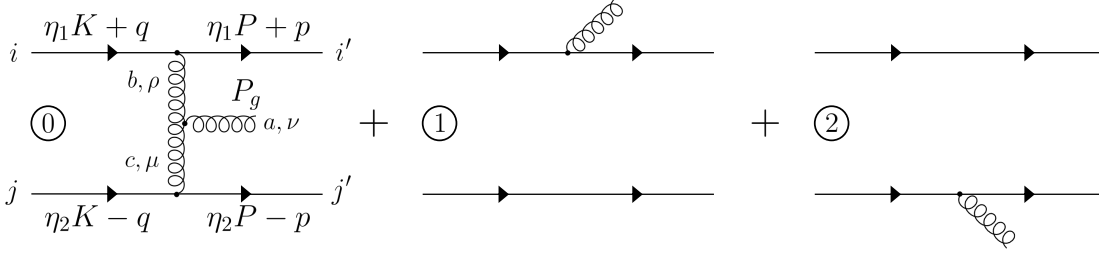


Figure 6.2: Leading order diagrams to $\mathcal{C}_{g\text{-amp}}^{(5)}$ in the top-philic mediator model. All three diagrams share the same color and Lorentz indices. The momenta of the incoming (outgoing) particles are displayed in terms of total and relative momenta of the system. In the lepto-philic mediator model (where we exchange the gluon with photon lines), the leftmost diagram is absent in the calculation of $\mathcal{C}_{\gamma\text{-amp}}^{(5)}$ due to the abelian nature of $U(1)_{\text{em}}$. Adapted from Ref. [136].

$$i [\mathcal{C}_1]_{ii',jj'}^{\nu,a} = \tilde{S}_1(\eta_1 P + p) [-ig_s^{\text{BSF}}(T_1^a)_{ii'}(\eta_1 K + \eta_1 P + q + p)^\nu] \tilde{S}_2(\eta_1 K + q) \tilde{S}_2(\eta_2 K - q) \delta_{jj'} (2\pi)^4 \delta^{(4)}(\eta_1 K + q - \eta_1 P - p - P_g), \quad (6.3.15)$$

$$i [\mathcal{C}_2]_{ii',jj'}^{\nu,a} = \tilde{S}_1(\eta_2 P - p) [-ig_s^{\text{BSF}}(T_2^a)_{jj'}(\eta_2 K + \eta_2 P - q - p)^\nu] \tilde{S}_2(\eta_2 K - q) \tilde{S}_1(\eta_1 K + q) \delta_{ii'} (2\pi)^4 \delta^{(4)}(\eta_2 K - q - \eta_2 P + p - P_g), \quad (6.3.16)$$

where g_s^{BSF} refers to the coupling involved in gluon emission and g_s^{NA} is the coupling between $\chi_{1,2}$ and an internal gluon in the first diagram.⁴² Following the approximations performed in Section 5.2.2, we can estimate the expressions above to leading order in α_s and v_{rel} in the COM frame. To obtain the squared matrix element later, we need to consider the sum over the polarisation states of the radiated gluon

$$\begin{aligned} \sum_{\text{pol.}} |\epsilon_\mu \mathcal{M}_{\mathbf{k}\rightarrow n}^\mu|^2 &= \mathcal{M}_{\mathbf{k}\rightarrow n}^{\mu*} \mathcal{M}_{\mathbf{k}\rightarrow n}^\nu \sum_{\text{pol.}} \epsilon_\mu^* \epsilon_\nu = -g_{\mu\nu} \mathcal{M}_{\mathbf{k}\rightarrow n}^{\mu*} \mathcal{M}_{\mathbf{k}\rightarrow n}^\nu \\ &= |\mathcal{M}_{\mathbf{k}\rightarrow n}|^2 - |\hat{\mathbf{P}}_g \cdot \mathcal{M}_{\mathbf{k}\rightarrow n}|^2. \end{aligned} \quad (6.3.17)$$

The contribution coming from the $\mu, \nu = 0$ component cancels the components parallel to $\hat{\mathbf{P}}_g$, such that we can express the final result in terms of the spatial entities only. Therefore, we can disregard the time-like $\nu = 0$ component in the computation of $\mathcal{C}_{g\text{-amp}}^{(5)}$. The spatial parts simplify to

$$[\mathcal{C}_0]_{ii',jj'}^a \simeq + i f^{abc} (T_1^b)_{ii'} (T_2^c)_{jj'} 8g_s^{\text{BSF}} (g_s^{\text{NA}})^2 m\mu \frac{(\mathbf{q} - \mathbf{p})}{(\mathbf{q} - \mathbf{p})^4} S(q; K) S(p; P), \quad (6.3.18)$$

⁴²One would expect \mathcal{C}_0 to be of higher order in the strong coupling. However, this is not the case due to the scaling of the relative momenta with α_s and v_{rel} as will become clear in the following.

$$[\mathcal{C}_1]_{ii',jj'}^a \simeq -\delta_{jj'}(T_1^a)_{ii'}g_s^{\text{BSF}}(\mathbf{q}+\mathbf{p})S(q;K)\tilde{S}_1(\eta_1 P+p)(2\pi)^4\delta^{(4)}(q-p-\eta_2 P_g), \quad (6.3.19)$$

$$[\mathcal{C}_2]_{ii',jj'}^a \simeq +\delta_{ii'}(T_2^a)_{jj'}g_s^{\text{BSF}}(\mathbf{q}+\mathbf{p})S(q;K)\tilde{S}_2(\eta_2 P-p)(2\pi)^4\delta^{(4)}(q-p+\eta_1 P_g), \quad (6.3.20)$$

where we used the on-shell relation $K = P + P_g$ for the expressions in the δ -distribution.⁴³ Using the approximations [129]

$$\int \frac{dp^0}{2\pi} \frac{dq^0}{2\pi} S(q;K)\tilde{S}_1(\eta_1 P+p)(2\pi)\delta(q^0-p^0-\eta_2 P_g^0) \simeq 2m_2 \mathcal{S}_0(\mathbf{p}, P)\mathcal{S}_0(\mathbf{q}, K), \quad (6.3.21)$$

$$\int \frac{dp^0}{2\pi} \frac{dq^0}{2\pi} S(q;K)\tilde{S}_2(\eta_2 P-p)(2\pi)\delta(q^0-p^0+\eta_1 P_g^0) \simeq 2m_1 \mathcal{S}_0(\mathbf{p}, P)\mathcal{S}_0(\mathbf{q}, K), \quad (6.3.22)$$

at $\mathbf{q} - \mathbf{p} - \eta_2 \mathbf{P}_g = 0$ (or $\mathbf{q} - \mathbf{p} + \eta_1 \mathbf{P}_g = 0$, respectively), the transition matrix element in the COM frame (i. e. $\mathbf{K} = 0$) can be written as

$$[\mathcal{M}_{\text{trans}}(\mathbf{p}, \mathbf{q})]_{ii',jj'}^a \simeq -4m\sqrt{4\pi\alpha_{s,[1]}^{\text{BSF}}}\left\{ -if^{abc}(T_1^b)_{ii'}(T_2^c)_{jj'}8\pi\mu\alpha_{s,[1]}^{\text{NA}}\frac{(\mathbf{q}-\mathbf{p})}{(\mathbf{q}-\mathbf{p})^4} \right. \\ \left. +\eta_2(T_1^a)_{ii'}\delta_{jj'}\mathbf{p}(2\pi)^3\delta^{(3)}(\mathbf{q}-\mathbf{p}-\eta_2\mathbf{P}_g) \right. \\ \left. -\eta_1\delta_{ii'}(T_2^a)_{jj'}\mathbf{p}(2\pi)^3\delta^{(3)}(\mathbf{q}-\mathbf{p}+\eta_1\mathbf{P}_g) \right\}. \quad (6.3.23)$$

Note that we set $(\mathbf{q}+\mathbf{p})\delta^{(3)}(\mathbf{q}-\mathbf{p}\mp\eta_{2,1}\mathbf{P}_g) = (2\mathbf{p}\pm\eta_{2,1}\mathbf{P}_g)\delta^{(3)}(\mathbf{q}-\mathbf{p}\mp\eta_{2,1}\mathbf{P}_g)$ in the second and third term and neglected the $\mathbf{P}_g = \mathbf{P}$ contributions as they are of $\mathcal{O}(\alpha_s^2 + v_{\text{rel}}^2)$. For a BS in the singlet representation, the coupling strength $\alpha_{s,[1]}^{\text{BSF}} = \alpha_s(\omega)$ is evaluated at the gluon energy $\omega = \mathcal{E}_{\mathbf{k}} - \mathcal{E}_n = \mu/2[v_{\text{rel}}^2 + (\alpha_{g,[1]}^B/n)^2]$, whereas for $\alpha_{s,[1]}^{\text{NA}}$, the average momentum transfer is $|\mathbf{q} - \mathbf{p}|$, which yields $\alpha_{s,[1]}^{\text{NA}} = \alpha_s(\mu\sqrt{v_{\text{rel}}^2 + (\alpha_{g,[1]}^B)^2})$ considering $|\mathbf{q}| \sim k$ and $|\mathbf{p}| \sim \kappa$. An overview on the different scaling of the strong couplings with the mediator mass adopted in this derivation, is given in Fig. 6.3. Employing Eq. 5.2.66, the spatial matrix element in the non-relativistic limit is given by

$$[\mathcal{M}_{\mathbf{k}\rightarrow n}]_{ii',jj'}^a = -\sqrt{2^5\pi\alpha_{s,[1]}^{\text{BSF}}m^2/\mu}\left\{ -if^{abc}(T_1^b)_{ii'}(T_2^c)_{jj'}\mathcal{Y}_{\mathbf{k},n} \right. \\ \left. +\eta_2(T_1^a)_{ii'}\delta_{jj'}\mathcal{J}_{\mathbf{k},n}(\eta_2\mathbf{P}_g) -\eta_1\delta_{ii'}(T_2^a)_{jj'}\mathcal{J}_{\mathbf{k},n}(-\eta_1\mathbf{P}_g) \right\}, \quad (6.3.24)$$

where we again neglected contributions from \mathbf{p}^2 and \mathbf{q}^2 . The definition of the integrals $\mathcal{J}_{\mathbf{k},n}$ and $\mathcal{Y}_{\mathbf{k},n}$, which compute different overlaps of the scattering and BS wave functions

⁴³In \mathcal{C}_0 , the $g^{\rho\mu}$ term yields the dominant contribution. Also, the energy transfer along gluon propagators can be neglected for the same reasons as in App. D using the instantaneous approximation.

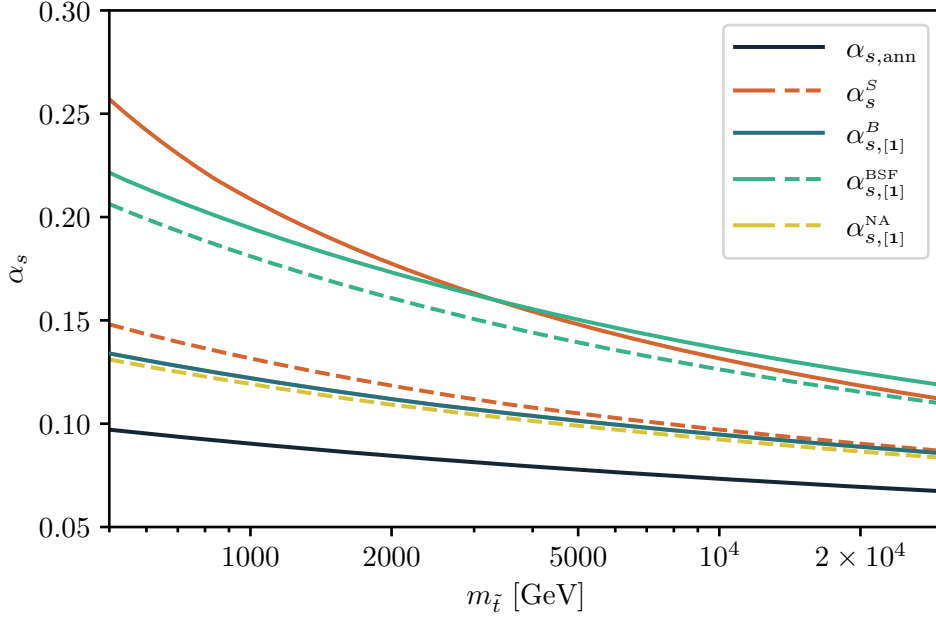


Figure 6.3: Mediator mass scaling of the strong couplings arising in the top-philic mediator model as defined in the text. Velocity dependent quantities are evaluated at $v_{\text{rel}} = 0.01$ ($v_{\text{rel}} = 0.1$), which is indicated by the solid (dashed) lines. Note that scaling for the coupling $\alpha_{s,[1]}^{\text{NA}}$ at $v_{\text{rel}} = 0.01$ is not visible as it coincides with $\alpha_{s,[1]}^B$ for small velocities. The running of α_s has been implemented up to one loop order following the prescription in Ref. [195].

over the momentum space, can be found in App. E. These integrals will depend on the color representation of the incoming scattering and outgoing BS through the different QCD couplings involved. Since for $\mathcal{J}_{\mathbf{k},n}(\mathbf{b})$, $|\mathbf{b}| \propto |\mathbf{P}_g|$, the dominating contribution will be independent of \mathbf{b} . Therefore, we can set $\mathcal{J}_{\mathbf{k},n} \equiv \mathcal{J}_{\mathbf{k},n}(\mathbf{b} = 0)$ in the following.

To gradually match this so far rather general discussion with our model, we start by assuming that the initial state particles transform under conjugate color state representations, i. e. $\mathbf{R}_1 \equiv \mathbf{R}$ and $\mathbf{R}_2 \equiv \bar{\mathbf{R}}$ (with $\mathbf{R} = \mathbf{3}$ in our case), such that $T_1^a = T^a$ and $T_2^a = -(T^a)^*$. Singling out the BS singlet configuration by setting $i' = j'$, the matrix element yields

$$[\mathcal{M}_{\mathbf{k} \rightarrow n}]_{ij}^a \equiv \delta_{i'j'} [\mathcal{M}_{\mathbf{k} \rightarrow n}]_{ii',jj'}^a = -\sqrt{\frac{2^5 \pi \alpha_{s,[1]}^{\text{BSF}} m^2}{\mu}} \left[\mathcal{J}_{\mathbf{k},n} + \frac{C_2(\mathbf{G})}{2} \mathcal{Y}_{\mathbf{k},n} \right] T_{ij}^a, \quad (6.3.25)$$

where we employed the identity $f^{abc} T^b T^c = (i/2) C_2(\mathbf{G}) T^a$ with $C_2(\mathbf{G})$ denoting the quadratic Casimir operator of the group \mathbf{G} (taken to be $\mathbf{G} = SU(3) \equiv \mathbf{3}$ later). The

squared, color-summed and averaged spatial matrix element is then given by

$$\overline{|\mathcal{M}_{\mathbf{k} \rightarrow n}|^2} = \frac{1}{d_{\mathbf{R}}^2} \sum_{i,j,a} \left| [\mathcal{M}_{\mathbf{k} \rightarrow n}]_{ij}^a \right|^2 = \left(\frac{2^5 \pi \alpha_{s,[1]}^{\text{BSF}} m^2}{\mu} \right)^2 \frac{C_2(\mathbf{R})}{d_{\mathbf{R}}^2} \left| \mathcal{J}_{\mathbf{k},n} + \frac{C_2(\mathbf{G})}{2} \mathcal{Y}_{\mathbf{k},n} \right|^2, \quad (6.3.26)$$

where $d_{\mathbf{R}}$ denotes the dimension and $C_2(\mathbf{R}) \equiv T_{ij}^a T_{ji}^a$ is the quadratic Casimir operator of a given \mathbf{R} . Employing Eq. 6.3.17, the BSF cross section reads (cf. Eq. 5.2.69)

$$\sigma_{\text{BSF}}^{(n)} v_{\text{rel}} = \frac{(\mathcal{E}_{\mathbf{k}} - \mathcal{E}_n)}{64\pi^2 m^2 \mu} \int d\Omega \left(\overline{|\mathcal{M}_{\mathbf{k} \rightarrow n}|^2} - \overline{|\hat{\mathbf{P}}_g \cdot \mathcal{M}_{\mathbf{k} \rightarrow n}|^2} \right). \quad (6.3.27)$$

Considering just the ground state $n = \{100\}$ for which $\mathcal{E}_{\mathbf{k}} - \mathcal{E}_1 = \mu/2((\alpha_{g,[1]}^B)^2 + v_{\text{rel}}^2)$, the overlap integrals in Eq. 6.3.26 are both proportional to $\hat{\mathbf{k}}$ at leading order in the expansion (cf. App. E). Therefore,

$$\overline{|\mathcal{M}_{\mathbf{k} \rightarrow \{100\}}|^2} - \overline{|\hat{\mathbf{P}}_g \cdot \mathcal{M}_{\mathbf{k} \rightarrow \{100\}}|^2} = \overline{|\mathcal{M}_{\mathbf{k} \rightarrow \{100\}}|^2} \sin^2 \theta, \quad (6.3.28)$$

where the squared spatial matrix element is independent of θ , which denotes the angle between \mathbf{k} and \mathbf{P}_g . Performing the orbital integration thus leaves us with

$$\sigma_{\text{BSF}}^{\{100\}, \tilde{t}} v_{\text{rel}} = \frac{(\alpha_{g,[1]}^B)^2 + v_{\text{rel}}^2}{48\pi m^2} \overline{|\mathcal{M}_{\mathbf{k} \rightarrow \{100\}}|^2}. \quad (6.3.29)$$

Calculating $\mathcal{J}_{\mathbf{k},\{100\}}$, $\mathcal{Y}_{\mathbf{k},\{100\}}$ to leading order (see App. E) and defining $\zeta_S \equiv \alpha_{g,[S]}^S/v_{\text{rel}}$, $\zeta_B \equiv \alpha_{g,[1]}^B/v_{\text{rel}}$, the BSF cross section into the ground state yields

$$\sigma_{\text{BSF}}^{\{100\}, \tilde{t}} v_{\text{rel}} = \frac{\pi \alpha_{s,[1]}^{\text{BSF}} \alpha_{g,[1]}^B}{\mu^2} \frac{2^7 C_2(\mathbf{R})}{3d_{\mathbf{R}}^2} \left[1 + \frac{C_2(\mathbf{G})}{2C_2(\mathbf{R})} \left(\frac{\alpha_{s,[1]}^{\text{NA}}}{\alpha_{s,[1]}^B} \right) \right]^2 S_{\text{BSF}}^{\tilde{t}}(\zeta_S, \zeta_B), \quad (6.3.30)$$

$$\implies \sigma_{\text{BSF}}^{\{100\}, \tilde{t}} v_{\text{rel}} = \frac{2^7 17^2}{3^5} \frac{\pi \alpha_{s,[1]}^{\text{BSF}} \alpha_{s,[1]}^B}{m_{\tilde{t}}^2} S_{\text{BSF}}^{\tilde{t}}(\zeta_S, \zeta_B), \quad (6.3.31)$$

where we inserted the color factors $d_{\mathbf{R}} = 3$, $C_2(\mathbf{R}) = 4/3$, $C_2(\mathbf{G}) = 3$ as well as the masses $\eta_1 = \eta_2 = 1/2$, $\mu = m_{\tilde{t}}/2$ in the last step and approximated $\alpha_{s,[1]}^{\text{NA}} \approx \alpha_{s,[1]}^B$ in our regime of interest ($v_{\text{rel}} \ll 1$; see Fig. 6.3). We also defined a SE factor for the BSF process incorporating all terms which are ζ -dependent, namely

$$S_{\text{BSF}}^{\tilde{t}}(\zeta_S, \zeta_B) \equiv S_0(\zeta_S) \frac{(1 + \zeta_S^2) \zeta_B^4}{(1 + \zeta_B^2)^3} e^{-4\zeta_S \arccot(\zeta_B)}. \quad (6.3.32)$$

As expected for $\zeta_S, \zeta_B \ll 1$, $S_{\text{BSF}}^{\tilde{t}} \rightarrow \zeta_B^4 \ll 1$ is inefficient at large velocities. Moreover, at small velocities the BSF cross section in the top-philic mediator model becomes also suppressed exponentially due to the repulsion of the scattering state, since $\zeta_S < 0$ and thus $S_0(\zeta_S) \rightarrow 0$ for $\zeta_S \ll -1$.

By taking the thermal average of the BSF cross section, we can assume that the scattering state follows a Maxwell-Boltzmann distribution. However, since the gluon is relativistic, we need to take into account its statistical factor in the calculation. Therefore, the thermal average reads

$$\begin{aligned}\langle\sigma_{\text{BSF}}v_{\text{rel}}\rangle &= \frac{x^{3/2}}{2\sqrt{\pi}} \int_0^\infty dv_{\text{rel}} v_{\text{rel}}^2 e^{-\frac{x}{4}v_{\text{rel}}^2} (1 + f_g(\omega)) \sigma_{\text{BSF}}v_{\text{rel}} \\ &= \frac{x^{3/2}}{2\sqrt{\pi}} e^{\frac{x}{4}(\alpha_{g,[1]}^B)^2} \int_0^\infty dv_{\text{rel}} v_{\text{rel}}^2 f_g(\omega) \sigma_{\text{BSF}}v_{\text{rel}},\end{aligned}\quad (6.3.33)$$

where $f_g(\omega) = 1/(e^{-\omega x/m_{\tilde{t}}} - 1)$ is the gluon distribution function in the SM plasma. The ionization rate is characterized by the reverse process $\mathcal{B}(\tilde{t} \tilde{t}^*)_{[1]} + g_{[8]} \rightarrow (\tilde{t} + \tilde{t}^*)_{[8]}$. It is related to the BSF cross section through the principle of detailed balance which is in this context also referred to as Milne relation [136, 171]. The thermal average of the ionization rate can then be written as

$$\langle\Gamma_{\text{ion}}\rangle = \frac{n_{\tilde{t}}^{\text{eq}2}}{n_B} \langle\sigma_{\text{BSF}}v_{\text{rel}}\rangle = \frac{g_{\tilde{t}}^2}{g_B} \frac{m_{\tilde{t}}^3}{(4\pi)^{3/2}} x^{-3/2} e^{-\frac{x}{4}(\alpha_{g,[1]}^B)^2} \langle\sigma_{\text{BSF}}v_{\text{rel}}\rangle.\quad (6.3.34)$$

The computation of the BSF cross section in the lepto-philic mediator model will in principle be similar to the derivation shown above. Since the contributions from radiating a Higgs or Z boson are highly suppressed (cf. App. C), we only take into account the process $\tilde{\tau} + \tilde{\tau}^* \rightarrow \mathcal{B}(\tilde{\tau} \tilde{\tau}^*) + \gamma$, where the leading order contributions are structurally the same as in Fig. 6.2 with the first diagram missing due to the abelian nature of *quantum electrodynamics* (QED). Instead of redoing the full calculation, we can simply modify Eq. 6.3.30 in the following way to obtain the correct result: First, we take $\alpha_{s,[1]}^{\text{NA}} \rightarrow 0$ to eliminate the non-abelian diagram, which is not present in the lepto-philic case. Then, we erase the effects of color-charge and the running of the strong coupling by neglecting the color-dependent factors $C_2(\mathbf{R}), d_{\mathbf{R}} \rightarrow 1$ and substituting $\alpha_{s,[1]}^{\text{BSF}}, \alpha_{g,[1]}^B \rightarrow \alpha_\gamma$ as well as $\zeta_S, \zeta_B \rightarrow \zeta_\gamma$ with $\zeta_\gamma = \alpha_\gamma/v_{\text{rel}}$. Eventually, the BSF cross section in the lepto-philic mediator model yields

$$\sigma_{\text{BSF}}^{\{100\},\tilde{\tau}} v_{\text{rel}} = \frac{2^9}{3} \frac{\pi \alpha_\gamma^2}{m_{\tilde{\tau}}^2} S_{\text{BSF}}^{\tilde{\tau}}(\zeta_\gamma),\quad (6.3.35)$$

with

$$S_{\text{BSF}}^{\tilde{\tau}}(\zeta_\gamma) \equiv S_0(\zeta_\gamma) \frac{\zeta_\gamma^4}{(1 + \zeta_\gamma^2)^2} e^{-4\zeta_\gamma \arccot(\zeta_\gamma)}.\quad (6.3.36)$$

The behaviour of $S_{\text{BSF}}^{\tilde{\tau}}$ at large velocities is the same as for the top-philic mediator model. However, since $\zeta_\gamma > 0$, at small velocities the SE factor $S_{\text{BSF}}^{\tilde{\tau}} \propto 1/v_{\text{rel}}$ and thus the BSF cross section will diverge in this limit. Since we are only considering thermally averaged quantities in our analysis, this does not pose a problem (see Section 5.1.2). By performing this matching of the results from the top-philic to the lepto-philic mediator model, we did not consider the contributions of the Higgs and Z boson within the scattering state wave

function $\phi_{\mathbf{k}}$, as they would require a numerical treatment. However, due to the mass suppression of the heavy bosons, these corrections to the $\mathcal{J}_{\mathbf{k},n}$ integral are small and can therefore be neglected. The thermal average to the BSF cross section and ionisation rate has been computed in analogy to the top-philic mediator model.

6.4 Dark matter abundance in the superWIMP mechanism

As discussed in Section 6.2, the DM abundance in the sW mechanism is obtained via the mediator yield after FO. The yield is governed by the BE (cf. Eq. 6.2.6), or, respectively, a system of coupled BE given in Eqs. 6.3.2 and 6.3.3

$$\begin{aligned}\frac{dY_{\tilde{t}\tilde{t}^*}}{dx} &= -\frac{1}{2}\xi_1(x)\langle\sigma_{\text{ann}}v_{\text{rel}}\rangle\left(Y_{\tilde{t}\tilde{t}^*}^2 - Y_{\tilde{t}\tilde{t}^*}^{\text{eq}2}\right) - \frac{1}{2}\xi_1(x)\langle\sigma_{\text{BSF}}v_{\text{rel}}\rangle Y_{\tilde{t}\tilde{t}^*}^2 + 2\xi_2(x)\langle\Gamma_{\text{ion}}\rangle Y_B, \\ \frac{dY_B}{dx} &= -\xi_2(x)\langle\Gamma_{\text{dec}}\rangle(Y_B - Y_B^{\text{eq}}) + \frac{1}{4}\xi_1(x)\langle\sigma_{\text{BSF}}v_{\text{rel}}\rangle Y_{\tilde{t}\tilde{t}^*}^2 - \xi_2(x)\langle\Gamma_{\text{ion}}\rangle Y_B,\end{aligned}$$

if the non-perturbative effects outlined in Section 6.3 are taken into account. Since these types of equations lack analytical solutions, we must resort to numerical methods to evaluate the mediator yield. Solving the coupled system numerically, in particular around the FO temperature near $x \sim 20$, poses a challenge. Fortunately, within this regime we can simplify our calculations significantly. We will employ in the following two distinct approaches to validate the accuracy of our results.

The first idea has been proposed in Ref. [196]. A more recent study has shown that its validity may persist even if its primary assumptions are relaxed [143]. It extends the method to higher BS and accounts for BS transitions, which we will disregard in this analysis. We start by presuming that at high temperatures BSF and ionization processes are very efficient, while at smaller temperatures BS decays are dominant. In both regimes, the rates are sufficiently high to assume quasi-steady state conditions for the BS, where $dY_B/dx \approx 0$. Utilizing Eq. 6.3.34, we can rewrite Eq. 6.3.3 to express the bound state yield as

$$Y_B \approx \frac{\langle\Gamma_{\text{dec}}\rangle + Y_{\tilde{t}\tilde{t}^*}^2/Y_{\tilde{t}\tilde{t}^*}^{\text{eq}2}\langle\Gamma_{\text{ion}}\rangle}{\langle\Gamma_{\text{dec}}\rangle + \langle\Gamma_{\text{ion}}\rangle} Y_B^{\text{eq}}. \quad (6.4.1)$$

Through substitution into Eq. 6.3.2, we can describe the evolution of the mediator particle using a single BE even in the presence of non-perturbative effects. The newly obtained equation is given by

$$\begin{aligned}\frac{dY_{\tilde{t}\tilde{t}^*}}{dx} &= -\frac{1}{2}\xi_1(x)\left[\langle\sigma_{\text{ann}}v_{\text{rel}}\rangle + \langle\sigma_{\text{BSF}}v_{\text{rel}}\rangle\frac{\langle\Gamma_{\text{dec}}\rangle}{\langle\Gamma_{\text{dec}}\rangle + \langle\Gamma_{\text{ion}}\rangle}\right]\left(Y_{\tilde{t}\tilde{t}^*}^2 - Y_{\tilde{t}\tilde{t}^*}^{\text{eq}2}\right) \\ &\equiv -\frac{1}{2}\xi_1(x)\left[\langle\sigma_{\text{ann}}v_{\text{rel}}\rangle + \langle\sigma_{\text{BSF}}v_{\text{rel}}\rangle_{\text{eff}}\right]\left(Y_{\tilde{t}\tilde{t}^*}^2 - Y_{\tilde{t}\tilde{t}^*}^{\text{eq}2}\right) \\ &\equiv -\frac{1}{2}\xi_1(x)\langle\sigma_{\text{ann}}v_{\text{rel}}\rangle_{\text{tot}}\left(Y_{\tilde{t}\tilde{t}^*}^2 - Y_{\tilde{t}\tilde{t}^*}^{\text{eq}2}\right),\end{aligned} \quad (6.4.2)$$

and turns out to be structurally equivalent to Eq. 6.2.6, where no non-perturbative effects are present. Under this approximation, the inclusion of SE factors and the presence of

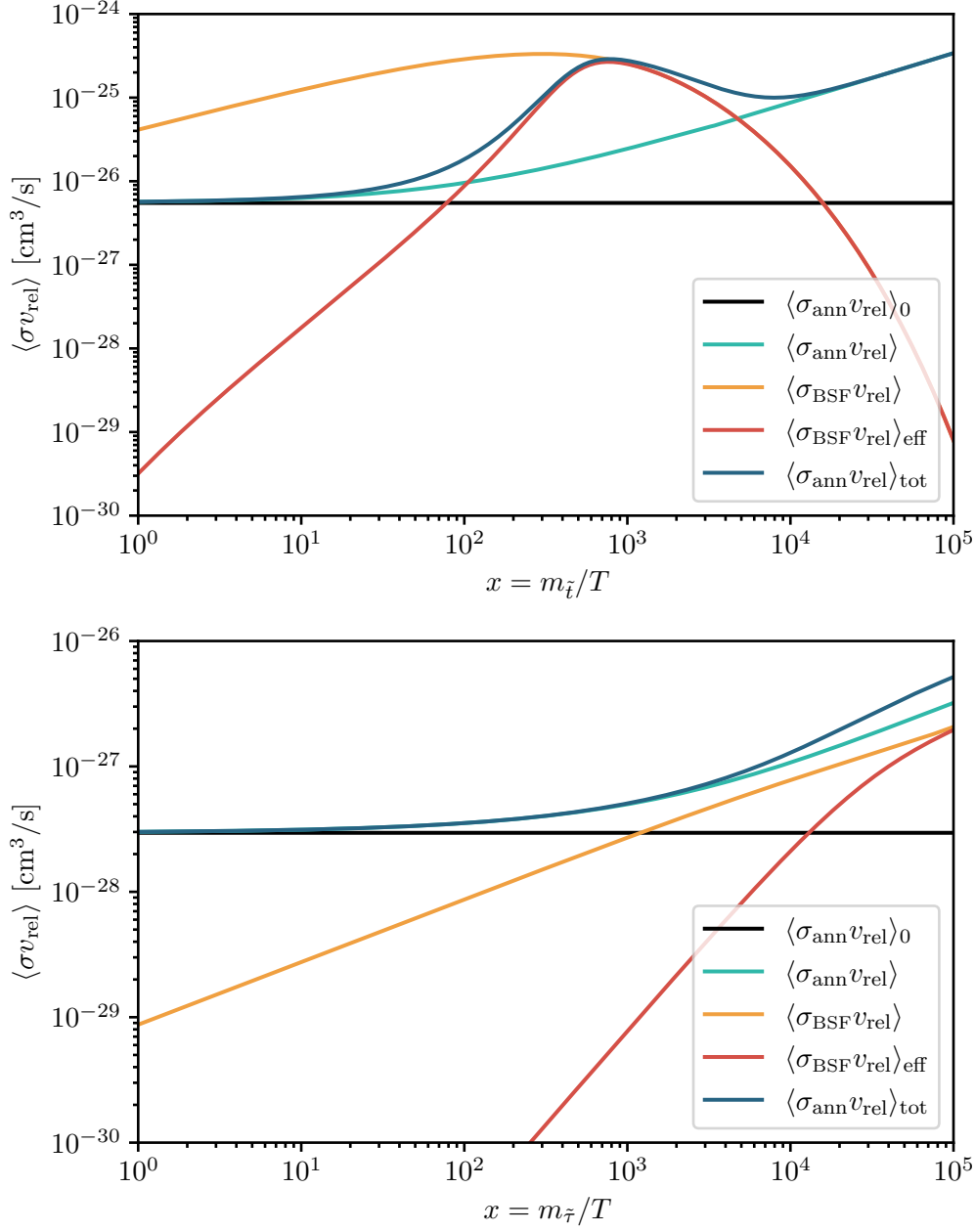


Figure 6.4: Contributions to the overall annihilation cross section, defined in Eq. 6.4.2, when considering non-perturbative effects as a function of the mediator mass over temperature. Also displayed is the perturbative cross section $\langle \sigma_{\text{ann}} v_{\text{rel}} \rangle_0$ (black) for comparison. The results are presented for a top-philic (top) and a lepto-philic (bottom) mediator model at an exemplary mediator mass of 5 TeV.

BS thus leads to a modification of the thermally averaged cross section within the framework of an ordinary BE describing FO. The *total annihilation cross section* $\langle\sigma_{\text{ann}}v_{\text{rel}}\rangle_{\text{tot}}$ consists of the sum of SE corrected annihilation and BSF contributions. The latter is weighted by a factor which accounts for the depletion of BS into the dark sector through ionization. This term suppresses the *effective BSF cross section*, denoted as $\langle\sigma_{\text{BSF}}v_{\text{rel}}\rangle_{\text{eff}}$, particularly at high temperatures when ionization processes are rapid, and tends to unity when the temperature drops below the energy of the BS. This behaviour can be observed in Fig. 6.4, where we compare the different contributions to the total annihilation cross section for the top-philic (top) and lepto-philic (bottom) mediator model at an exemplary mediator mass of 5 TeV. In the top-philic mediator model, both SE and BS corrections noticeably increase the overall cross section shortly after decoupling, potentially exerting a significant impact on the mediator yield through non-perturbative effects. In the lepto-philic mediator model, we anticipate a sizeable impact from SE corrections, whereas contributions from BSF are expected to be insignificant as they occur much later.

Another approach to simplify the coupled system of BEs is to assume Saha equilibrium (see e. g. Ref. [197] and Ref. [198] for the original paper) at the time, where the mediator starts to deviate from its equilibrium value around $x \sim 20$. This assumption posits that ionization processes are rapid enough to maintain chemical equilibrium between bound and scattering states, ensuring that their relative abundances remain constant, i. e. $n_B/n_B^{\text{eq}} = n_{\tilde{t}}^2/n_{\tilde{t}}^{\text{eq}2}$ or $Y_B = R(x)s(x)Y_{\tilde{t}\tilde{t}^*}^2$ with $R(x) \equiv n_B^{\text{eq}}/n_{\tilde{t}}^{\text{eq}2}$. We checked this condition to hold up to $x \lesssim 30$. Defining further $\bar{x} \equiv Y_B/Y_{\text{tot}}$ as the fraction of the BS yield compared to the total yield of the free mediator and BS $Y_{\text{tot}} \equiv Y_{\tilde{t}\tilde{t}^*} + Y_B$, we can use the Saha equilibrium condition to rewrite the BE for the total yield

$$\frac{dY_{\text{tot}}}{dx} = -\frac{1}{2}\xi_1(x) \langle\sigma_{\text{eff}}v_{\text{rel}}\rangle \left((1 - \bar{x})^2 Y_{\text{tot}}^2 - Y_{\tilde{t}\tilde{t}^*}^{\text{eq}2} \right), \quad (6.4.3)$$

through a combination of Eqs. 6.3.2 and 6.3.3 with $\langle\sigma_{\text{eff}}v_{\text{rel}}\rangle \equiv \langle\sigma_{\text{ann}}v_{\text{rel}}\rangle + 2R(x) \langle\Gamma_{\text{dec}}\rangle$. At early times, when $\bar{x} \ll 1$, we can safely approximate $(1 - \bar{x})^2 \approx 1$ and take $Y_{\text{tot}}(x_0) = Y_{\tilde{t}\tilde{t}^*}^{\text{eq}}(x_0)$ at $x_0 = 1$ as an initial condition. We solve Eq. 6.4.3 up to $x_1 = 30$ and subsequently transition to solving the coupled system of BEs (Eqs. 6.3.2 and 6.3.3). The initial conditions for the full system are taken to be $Y_{\tilde{t}\tilde{t}^*}(x_1) = Y_{\text{tot}}(x_1)$ and $Y_B(x_1)$ being defined through the Saha relation. The final yields obtained through this method closely match those obtained using the steady-state approximation $dY_B/dx \approx 0$, with differences of less than 1% within our range of interest. Hence, we will use the method proposed in Ref. [136] going forward, as it offers a simpler applicability.

We have presented in Fig. 6.5 the evolution of the mediator yield in the top-philic mediator model for a benchmark point of $m_{\tilde{t}} = 5 \text{ TeV}$ and $\lambda_H = 0$. Three different scenarios are compared here: 1) the solution to Eq. 6.2.6 using only the perturbative DM cross section $\langle\sigma_{\text{ann}}v_{\text{rel}}\rangle_0 \approx \sigma_0$ (red), 2) the solution taking into account the SE factors in the annihilation cross section $\langle\sigma_{\text{ann}}v_{\text{rel}}\rangle$ (green), and 3) the solution to Eq. 6.4.2 using $\langle\sigma_{\text{ann}}v_{\text{rel}}\rangle_{\text{tot}}$ with SE and BSF effects present (blue). This example illustrates the significant impact of SE and BSF effects on the mediator yield. While SE effects become significant shortly after deviation from equilibrium, BSF effects start to influence the

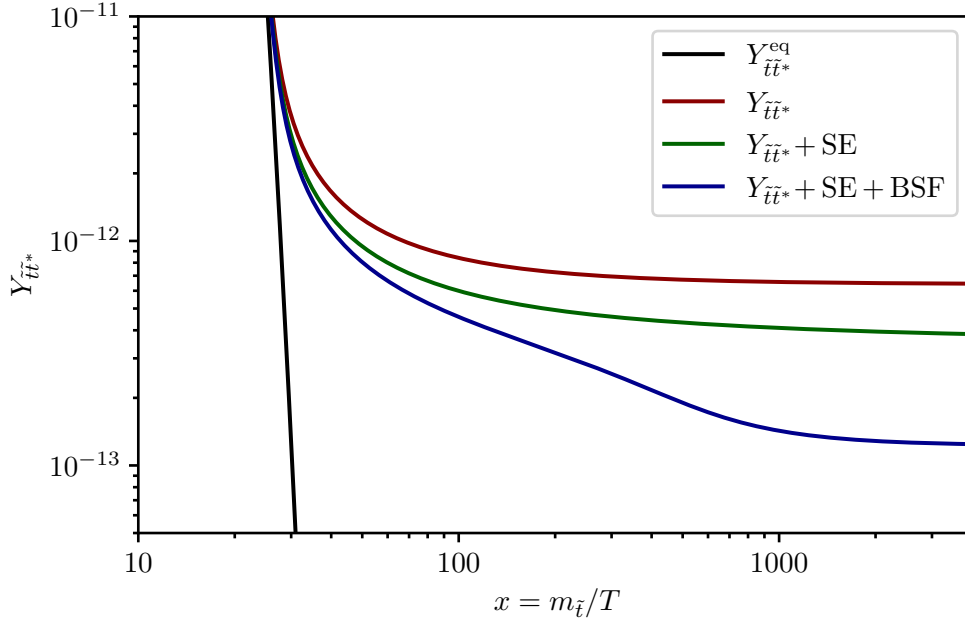


Figure 6.5: The evolution of the mediator yield in the top-philic mediator model as a function of $x = m_{\tilde{t}}/T$ for an exemplary mass of $m_{\tilde{t}} = 5 \text{ TeV}$ and $\lambda_H = 0$. For comparison, the yield of the perturbative computation (red) is displayed alongside an only SE corrected (green) and an SE and BSF corrected result (blue). The equilibrium yield is shown in black. Adapted from Ref. [5].

yield at $x \sim \mathcal{O}(10^2 - 10^3)$. This behavior aligns with our expectations when comparing it to Fig. 6.4. Both effects lead to a significant increase in the effective cross section around $x \sim 100$ which in turn depletes the yield, a behavior which has been observed previously e.g. in coannihilation scenarios [136, 137, 169]. Considering only BSF into the ground state, the mediator has frozen out at $x_p \gtrsim 1000$ which we will take as a reference point to define $Y_{\chi,\infty}^{\text{sW}}$ (cf. Sections 4.2 and 6.2).⁴⁴ By utilizing Eq. 4.2.6, we can exclude combinations of m_χ , $m_{\tilde{t}}$, and λ_H that result in abundances $\Omega_{\text{DM}}^{\text{sW}} > \Omega_{\text{DM},0}$, given that later modifications to the cosmological history of the Universe are absent (e.g. late entropy production [199, 200]). Abundances resulting from sW production yielding $\Omega_{\text{DM}}^{\text{sW}} < \Omega_{\text{DM},0}$ are acceptable as they can be supplemented with contributions from FI production. Assuming that these two mechanism make up for the entire DM abundance we observe today, we can define the required FI fraction for a given sW abundance as

⁴⁴This calculation will serve as a lower limit to BSF effects on the mediator yield since it has been shown e.g. in Ref. [172], that the inclusion of higher BS as well as BS transitions will deplete the abundance even further. However, this might lead to a scenario where FO and decay of the mediator are no longer separable, a scenario which is beyond the scope of this work.

$p \equiv 1 - \Omega_{\text{DM}}^{\text{sW}} / \Omega_{\text{DM},0}$. Given $m_{\tilde{t}}$, λ_H , and a fixed p , the required DM mass can be calculated via (cf. Eq. 4.2.6)

$$m_\chi = \frac{(1-p)\Omega_{\text{DM},0}\rho_{\text{crit},0}}{s_0 Y_{\chi,\infty}^{\text{sW}}}. \quad (6.4.4)$$

We can easily see that it is largest, if all DM is produced through the sW mechanism and decreases linearly with $p > 0$. Conversely, if a DM mass m_χ (alongside $m_{\tilde{t}}$ and λ_H) is given, we are able to determine p , which also fixes λ_χ via

$$\lambda_\chi = \sqrt{\frac{p}{(1-p)} \frac{Y_{\chi,\infty}^{\text{sW}}}{Y_{\chi,\infty}^{\text{FI}}}}. \quad (6.4.5)$$

As anticipated from Fig. 6.4, in the lepto-philic mediator model BSF plays a subordinate role compared to SE in determining the mediator yield due to the much smaller binding energy of electromagnetic interactions. Consequently, the overall corrections due to non-perturbative effects are less than 15%, and therefore, they are not explicitly shown.

6.5 Model constraints from colliders and cosmological observations

Apart from overclosing the Universe (i. e. $\Omega_{\text{DM}}^{\text{sW}} > \Omega_{\text{DM},0}$), there are a few more observations which will constrain the parameter space of our models. We will start with limits from collider searches. If the masses of the mediators are small enough, they can be produced e. g. in proton-proton collisions through Drell-Yann-like processes due to their SM gauge couplings. Production through Higgs interactions are also possible but suppressed even for sizeable values of λ_H [201]. Especially the top-philic mediator has a large production cross section of $\sigma_{\tilde{t}\tilde{t}^*} \simeq 1$ fb for $m_{\tilde{t}} \sim 1300$ GeV which make various classes of DM searches at the LHC sensitive to it.⁴⁵ Moreover, a small coupling of $\lambda_\chi \ll 10^{-8}$ as estimated from Eq. 6.2.1, corresponds to a long lifetime of the mediator, which can render it long-lived or even stable on collider scales. To test this presumption, we estimate the mediator decay length within a collider experiment via

$$\Delta x \simeq \beta \gamma \tau_{\tilde{t}}, \quad (6.5.1)$$

with $\tau_{\tilde{t}} \equiv 1/\Gamma_{\tilde{t}}$ its lifetime and β the velocity of the decaying particle (in natural units), boosted by a Lorentz factor γ . For the velocity factors, we choose a typical value of $\beta\gamma = \sqrt{1 - m_{\tilde{t}}^2/E_{\tilde{t}}^2} \sim 0.3$ for heavy particles produced at the LHC.⁴⁶ Considering only the $1 \rightarrow 2$ process as the dominant contribution and neglecting the top mass, we can set a lower limit on the lifetime of the mediator, yielding $\tau_{\tilde{t}} \geq 32\pi/(m_{\tilde{t}}\lambda_\chi^2) \equiv \tau_{\tilde{t}}^{\text{min}}$ for $m_\chi \rightarrow 0$ (and respectively larger for $m_\chi > 0$). For mediator masses of $\mathcal{O}(1 \text{ TeV})$, we observe in Fig. 6.6 (dashed lines) that within our regime of interest ($\lambda_\chi \ll 10^{-8}$), we always obtain $\Delta x \gg 10$ m in both models. For the values of λ_χ preferred by FI and a

⁴⁵Correspondingly, for the lepto-philic mediator, a cross section of $\sigma_{\tilde{\tau}\tilde{\tau}^*} \simeq 0.1$ fb for a mediator mass of $m_{\tilde{\tau}} \sim 500$ GeV can be estimated.

⁴⁶We checked the validity of this choice by estimating the range of $\beta\gamma$, applying a simplified t -channel model from MicrOMEGAs [202, 203] to a DM production simulation performed in CalcHEP [204].

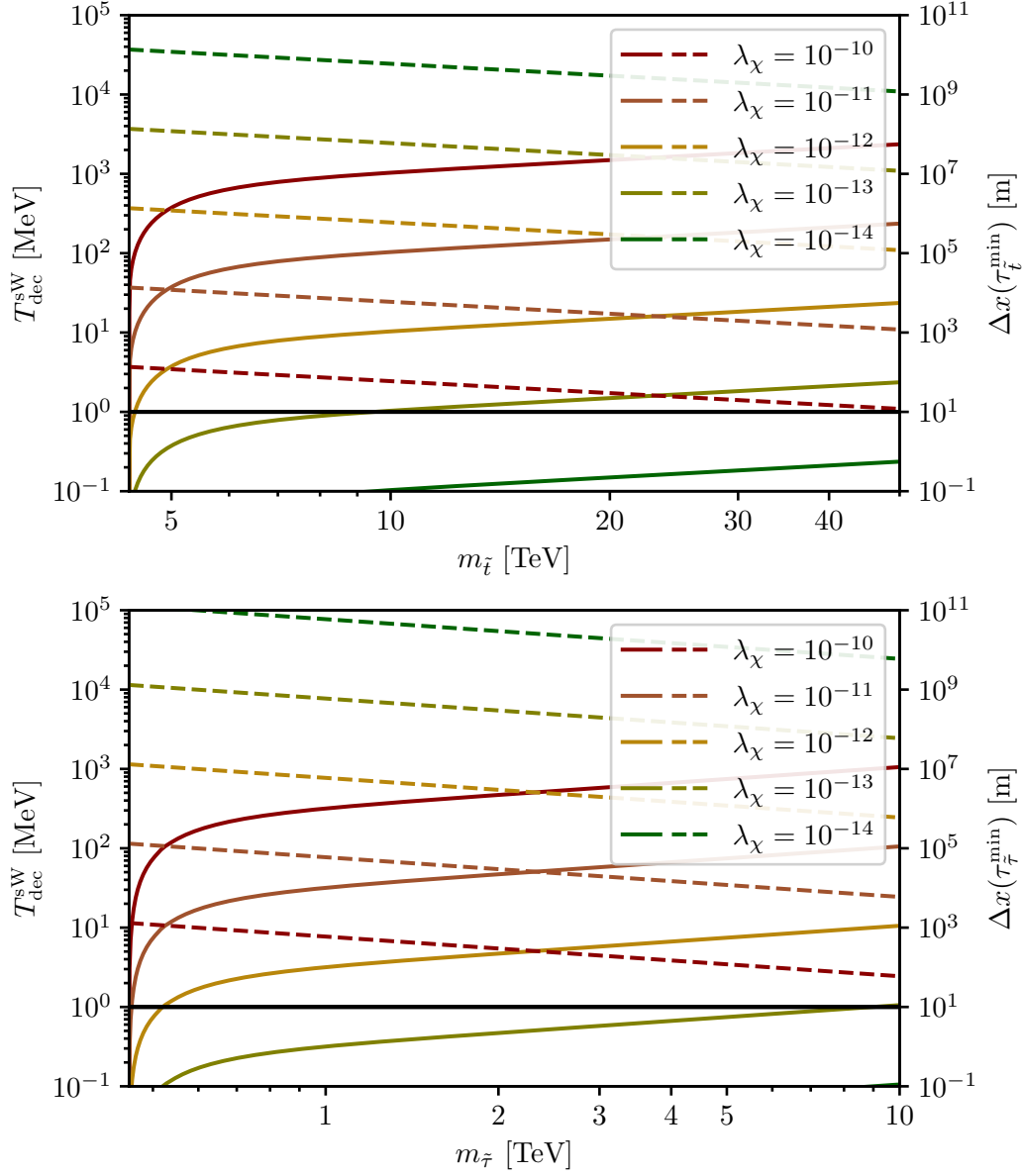


Figure 6.6: Lower limits on the decay temperature (solid lines) and decay length (dashed lines) of the mediator as a function of its mass in the top-philic (top) and lepto-philic (bottom) mediator model for various couplings λ_χ . The decay temperature $T_{\text{dec}}^{\text{sW}}$ has been calculated via Eq. 6.5.2 assuming an sW contribution only and can be compared to the bath temperature T_{BBN} at the onset of BBN (black line). The decay length after production at the LHC is given via Eq. 6.5.1 for a minimal mediator lifetime (see text) and is compared to a detector length of $\Delta x_{\text{DL}} = 10$ m (black line).

realistic distribution of $\beta\gamma$ factors, we checked that even $\Delta x \geq 100$ m throughout our parameter space, implying that we can treat the mediator to be stable on collider scales.

A heavy, non-relativistic, stable and charged mediator will leave distinct signatures at the LHC experiments ATLAS and CMS. These are characterized by an unusual energy loss in the calorimeters and a low velocity measured in the tracking system [205, 206]. We will apply in the following the most stringent limits on a stop-like R-hadron (for a top-philic mediator) as well as on a directly produced stau (for a lepto-philic mediator), imposed by an ATLAS search [205], which is based on an integrated luminosity of 36.1 fb^{-1} at a collider energy of $\sqrt{s} = 13 \text{ TeV}$. The measurements for the top-philic mediator exclude masses up to 1345 GeV at 95% *confidence level* (CL), while those for the lepto-philic mediator rule out masses above $m_{\tilde{\tau}} \gtrsim 430 \text{ GeV}$. We expect these limits to strengthen in the future up to $m_{\tilde{t}} \lesssim 1600 \text{ GeV}$ and $m_{\tilde{\tau}} \lesssim 600 \text{ GeV}$, respectively, after the *high-luminosity* (HL) upgrade of the LHC, assuming a similar efficiency as today and an integrated luminosity of 3000 fb^{-1} . The supersymmetric theoretical models employed in the analysis of Ref. [205] are very similar to our own models, although not identical. Particularly, one might worry that contributions from supersymmetric partners, which are not present in our model, lead to different results. Therefore, we performed a reevaluation of the theoretical mediator production cross section using our model with CalcHEP [204] and compared it with the predictions in Ref. [205]. The results agree well, which suggests a limited effect of the supersymmetric model on these observables. This validates the use of these results for our objectives.

Other than collider experiments, there are several constraints emerging from cosmological observations. In our parameter regime of interest, the most important ones stem from BBN. A sufficiently long-lived mediator could decay during the formation of the light elements and inject energy into the SM plasma, or form bound states with SM particles triggering unexpected nuclear reactions [207, 208]. If sufficiently effective, both processes will spoil the delicate balance of the nuclear reactions and alter the primordial abundances of the light elements. In order to avoid these kinds of complications, one usually demands the vast majority of the mediator particles to decay before the relevant stage of BBN, such that the remnants are too dilute to affect the nuclear reactions. We will therefore require the lifetime of the mediator to be shorter than $\tau_{\tilde{t}} = 1/\Gamma_{\tilde{t}} \lesssim 10 \text{ s}$ which corresponds to a bath temperature of $T_{\text{BBN}} \sim 1 \text{ MeV}$ at the time of decay [208]. Utilizing the time-temperature relation in a radiation dominated Universe as given in Eq. 4.1.8 (neglecting the slight differences in values of g_{eff} , h_{eff} , and g_{\star} , fixing them to $g_{\text{eff}} = 10.75$ at 1 MeV), we can define a corresponding decay temperature of the mediator as a function of the decay width

$$T_{\text{dec}} \simeq \sqrt{0.301 g_{\text{eff}}^{-1/2} M_{\text{Pl}} \Gamma_{\tilde{t}}(m_{\tilde{t}}, m_{\chi}, \lambda_{\chi})}, \quad (6.5.2)$$

which can be compared to T_{BBN} . If kinematically allowed, the two-body decay $\tilde{t} \rightarrow t_R + \chi$ (or $\tilde{\tau} \rightarrow \tau_R^+ + \chi$) will dominate the decay width and usually lead to a sufficiently fast decay. We have displayed its impact on the decay temperature in Fig. 6.6 (solid lines) for a variety of λ_{χ} assuming sW production only ($p = 0$), which will serve us as a lower

limit. An FI contribution ($p > 0$) will result in lower DM masses (cf. Eq. 6.4.4) which leads to higher decay rates. As we can see, for couplings $\lambda_\chi \gtrsim 10^{-12}$, bounds from BBN can be naturally avoided. If two-body decays are not kinematically allowed in the top-philic mediator model, we will consider the dominant three-body decay $\tilde{t} \rightarrow W^+ + b + \chi$, which vastly increases the lifetime of the mediator for a fixed λ_χ . This process has to be calculated numerically and we have included it in our analysis below the threshold of the two-body decay. For the lepto-philic mediator, this procedure is unnecessary for reasons explained in Section 6.6.

Another category of cosmological constraints can become important, when the velocity of DM after decoupling is high enough to affect structure formation. This occurs, when the closely related DM free-streaming length (in this context, the average distance a DM particle can travel without scattering after matter-radiation equality) becomes larger than the size of primordial density fluctuations, such that DM can escape overdensities and prevents structure on these scales to grow. In the literature, these so-called *warm dark matter* (WDM) bounds are presented in terms of the DM mass m_{WDM} assuming a thermal velocity distribution. However, for comparison with our model predictions, it will be more convenient to work with the *root-mean-square* (rms) velocity of DM today, which can be related to the mass limit via [209, 210]

$$v_{\text{rms}} \approx 0.04 \left(\frac{\Omega_{\text{DM},0} h^2}{0.12} \right)^{1/3} \left(\frac{m_{\text{WDM}}}{1 \text{ keV}} \right)^{-4/3} \frac{\text{km}}{\text{s}}. \quad (6.5.3)$$

Numerous astrophysical observations can be used to constrain m_{WDM} , typically confining it to the keV regime (see e.g. Refs. [41, 211–213]). We will employ in the following a limit from Ref. [41] of $m_{\text{WDM}} \geq 3.5 \text{ keV}$ or $v_{\text{rms}} \leq 7.5 \text{ m/s}$, respectively, which is based on a *Lyman- α forest* data analysis.

The mean velocity of a (non-relativistic) DM particle today is given by

$$v_0 = \frac{p_0}{m_\chi} = \frac{p_{\text{prod}} a_{\text{prod}}}{m_\chi a_0} = \frac{p_{\text{prod}}}{m_\chi} \left(\frac{h_{\text{eff}}(T_0)}{h_{\text{eff}}(T_{\text{prod}})} \right)^{1/3} \frac{T_0}{T_{\text{prod}}}, \quad (6.5.4)$$

with p its momentum and the subscript 0 (prod) refers to the values of the corresponding entities today (at production). Note that we assumed no efficient (self-)interaction processes of DM after its production and applied entropy conservation in the last step. Given these assumptions, Eq. 6.5.4 holds irrespective of the underlying DM model. For simplicity, we will use in the following v_0 instead of the rms velocity when calculating the WDM mass bound, since a conversion of v_0 to v_{rms} would only yield a $\mathcal{O}(10\%)$ correction. Considering DM produced by FI, the mean DM momentum at production is simply $T_{\text{prod}}/2$ (for a mediator decaying at rest) times an $\mathcal{O}(1)$ factor, given that $m_{\tilde{t}} \gg m_\chi + m_t$. Taking the proportionality factor to be 2.5 [214] and estimating $h_{\text{eff}}(T_{\text{prod}}) \sim 100$, the mean velocity of DM from FI is approximately

$$v_0^{\text{FI}} \approx 30 \left(\frac{1 \text{ keV}}{m_\chi} \right) \frac{\text{m}}{\text{s}}, \quad (6.5.5)$$

which can be translated to a lower DM mass limit of $m_\chi \gtrsim 4 \text{ keV}$.⁴⁷

For DM produced via the sW mechanism, the DM momentum is given by the kinematics of the non-relativistic frozen out mediator at its decay. For simplicity, we will model the mediator decay as instantaneous, such that we can compute the production temperature through $\Gamma_{\tilde{t}} = H|_{T_{\text{prod}}}$ (see e.g. Ref. [215]). Determining m_χ through Eq. 6.4.4 with $p = 0$ (sW production only), we can employ Eq. 6.5.4 with $p_{\text{prod}} \approx (m_{\tilde{t}}^2 - m_\chi^2)/(2m_{\tilde{t}})$, $h_{\text{eff}}(T_{\text{prod}}) \sim 10$ and $v_0 = 7.5 \text{ m/s}$ to obtain a lower limit on λ_χ as a function of the mediator mass. For our regime of interest, which encompasses mediator masses in the TeV and multi-TeV regime, we find $\lambda_\chi \gtrsim 10^{-15} - 10^{-14}$ for both models, too low to provide compatible constraints on the parameter space.

6.6 The parameter space for non-thermal production

We will now combine our findings regarding the non-perturbative corrections to the DM abundance (cf. Section 6.4) with the constraints presented in Section 6.5 to obtain a complete picture of the parameter space of our models which allows for non-thermal production. With our precise knowledge of $\Omega_{\text{DM},0} h^2 = 0.1200 \pm 0.0012$ [8], we can fix the Yukawa-like coupling λ_χ while keeping the DM and mediator masses alongside λ_H as free parameters. We expect the latter to be of no importance for non-perturbative effects from BSF for reasons explained above, but it will modify effects from SE due to its impact on the perturbative annihilation cross sections and the scattering state wave function in the lepto-philic mediator model. Therefore, we will compare in the following the two scenarios of $\lambda_H = 0$, i.e. no Higgs portal, and a sizeable value of $\lambda_H = 0.3$ to investigate its significance in the corresponding models. We are then left with a parameter scan over the mediator mass $m_{\tilde{t}}$ ($m_{\tilde{\tau}}$) as well as the DM mass, which we express through $\Delta m = m_{\tilde{t}} - m_\chi$ ($\Delta m = m_{\tilde{\tau}} - m_\chi$) to enhance the visibility of our model constraints.

The impact of non-perturbative effects on the parameter space of the top- and lepto-philic mediator model is presented in Fig. 6.7. In addition, Fig. 6.8 highlights the computed values of λ_χ for each combination of masses, along with the FI fraction to the total DM abundance p (cf. Eq. 6.4.5). From above, the parameter space is constrained by the trivial condition that Δm cannot be larger than the mediator mass (gray). Very close to this bound lies another bound stemming from WDM constraints on FI production. However, as this constraint only applies to DM masses below $\mathcal{O}(10 \text{ keV})$, it is not visible in the plots. As evident from Fig. 6.8 (bottom), even the lowest values of λ_χ , in the regime where DM production is dominated by the sW mechanism, are well above the corresponding WDM constraints of $\lambda_\chi \gtrsim 10^{-15} - 10^{-14}$ calculated in the previous section. Therefore, a pure sW scenario is possible for all mediator masses considered here. LHC searches for heavy stable particles constrain the parameter space from the left (orange), since they give a lower bound on the allowed mediator mass. We have checked that the mediator is stable on collider scales, such that the limit is independent of m_χ and thus appears as a vertical line in both figures.

⁴⁷For comparison, a limit of $m_\chi \gtrsim 15 \text{ keV}$ has been stated in [188] by performing a full modeling of the transfer function for FI.

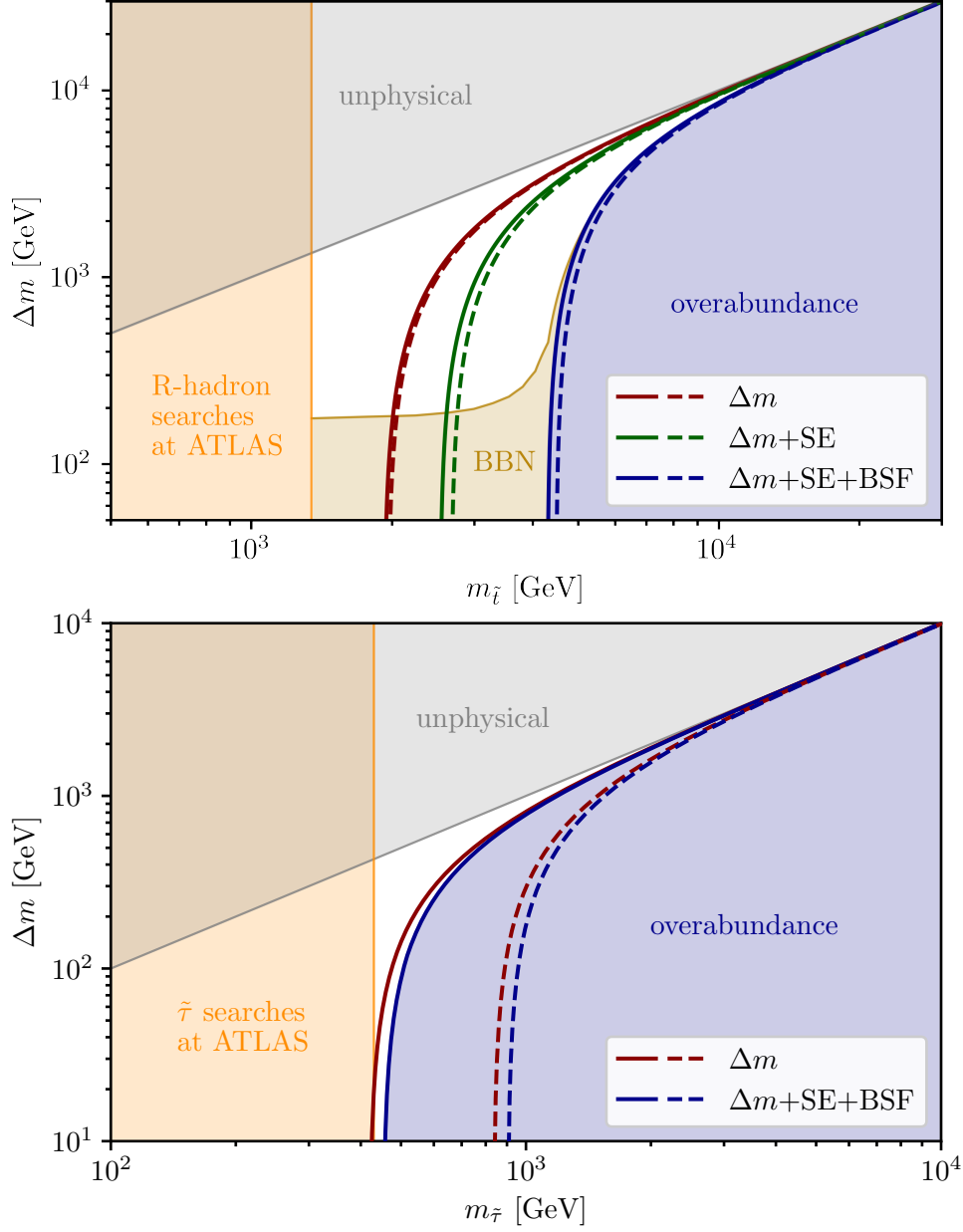


Figure 6.7: The parameter space of non-thermal production in the top-philic (top) and lepto-philic (bottom) mediator model spanned by the mediator mass $m_{\tilde{t}}$ ($m_{\tilde{\tau}}$) and the mass difference $\Delta m = m_{\tilde{t}} - m_{\chi}$ ($\Delta m = m_{\tilde{\tau}} - m_{\chi}$). For the calculation of m_{χ} considering sW production only (cf. Eq. 6.4.4), the perturbative (red), SE corrected (green) and SE+BSF corrected (blue) yields of the mediator after FO have been used, considering a Higgs portal coupling of $\lambda_H = 0$ (solid lines) and $\lambda_H = 0.3$ (dashed lines). Excluded regions are shaded (refer to text for additional information). Adapted from Ref. [5], where a former mistake in the calculation of the BBN constraints has been corrected.

From the right, the parameter space is constrained from an *overabundance* bound on DM (blue). Since sW production is independent of λ_χ , and the frozen out mediator yield scales proportional to its mass, we expect for high mediator masses an sW contribution to the total DM abundance which exceeds $\Omega_{\text{DM},0}$, i.e. the sW mechanism alone overproduces DM (cf. Eq. 4.2.6). In order to avoid this bound, one needs for a fixed mediator mass a smaller value of m_χ or a larger value of Δm , respectively. Above this threshold, the sW mechanism alone is insufficient to explain the entire DM abundance. This creates space for FI production to contribute to the remaining portion. How much production from FI is required for each configuration of masses has been displayed in Fig. 6.8 (top).

As anticipated from our discussion in Section 6.4 and evident from Fig. 6.7, non-perturbative corrections have a considerable impact on the overabundance limit. We illustrate this by displaying the surfaces where $\Omega_{\text{DM},0} = \Omega_{\text{DM}}^{\text{sW}}$, for $\lambda_H = 0$ (solid) and $\lambda_H = 0.3$ (dashed), calculated using the perturbative cross section as well as the enhanced ones from non-perturbative effects, while retaining the same color coding as in Fig. 6.5. In case of the top-philic mediator model, the highest allowed mediator mass for the lowest possible Δm , increases from 2 TeV for a perturbative cross section to over 4 TeV if SE and BS effects are taken into account. Neglecting BS effects, we still observe an enhancement of $\sim 40\%$. The influence of λ_H in the top-philic mediator model is small as expected but it still allows for a shift of the overabundance limit of $\mathcal{O}(100 \text{ GeV})$. In the context of the lepto-philic mediator model, the situation differs. Due to the significantly lower QED couplings, BSF has no real impact on the mediator yield after FO, which is why the difference between the SE only and SE+BSF scenario in both figures cannot be resolved (and is therefore not displayed). The difference in the overabundance limit using a perturbative and an SE corrected cross section is of $\mathcal{O}(10\%)$. We want to note here that for a $\lambda_H = 0$, the current collider limits from the LHC are already very close to the cosmological ones for the lowest Δm and have the prospects to rule out large DM masses within this scenario after the HL upgrade of the LHC. However, unlike the top-philic mediator model, a non-zero Higgs coupling in the lepto-philic mediator model has a large impact on the allowed parameter space, as discussed at the beginning of this section. Hence, a full exclusion of this regime is not foreseeable.

The last bound we take into account, and which constrains the parameter space from below, stems from BBN (beige). In the top-philic mediator model, for most mediator masses, this limit is approximately independent of $m_{\tilde{t}}$ and solely excludes mass differences below the top mass. This is expected as it coincides with the kinematic threshold of the two body decay, which leads to a drastic increase in the mediator lifetime beyond $\Delta m \lesssim m_t$ for a constant coupling. Being close to this threshold will also lower the contributions from the two-body decay channel to FI production. This will, in turn, lead to a preference for larger λ_χ couplings to compensate for this effect (see Fig. 6.8, bottom left). Due to sizeable contributions from the $2 \rightarrow 2$ production channels (cf. Fig. 6.1) in this regime, this effect will, however, not be sufficient to balance the suppression from the three-body decay, such that the limit remains close to the top mass in the regime where FI dominates. As we approach the regime where sW production becomes dominant (cf. Fig. 6.1, top left), the BBN constraints are strengthened due to overall smaller values of

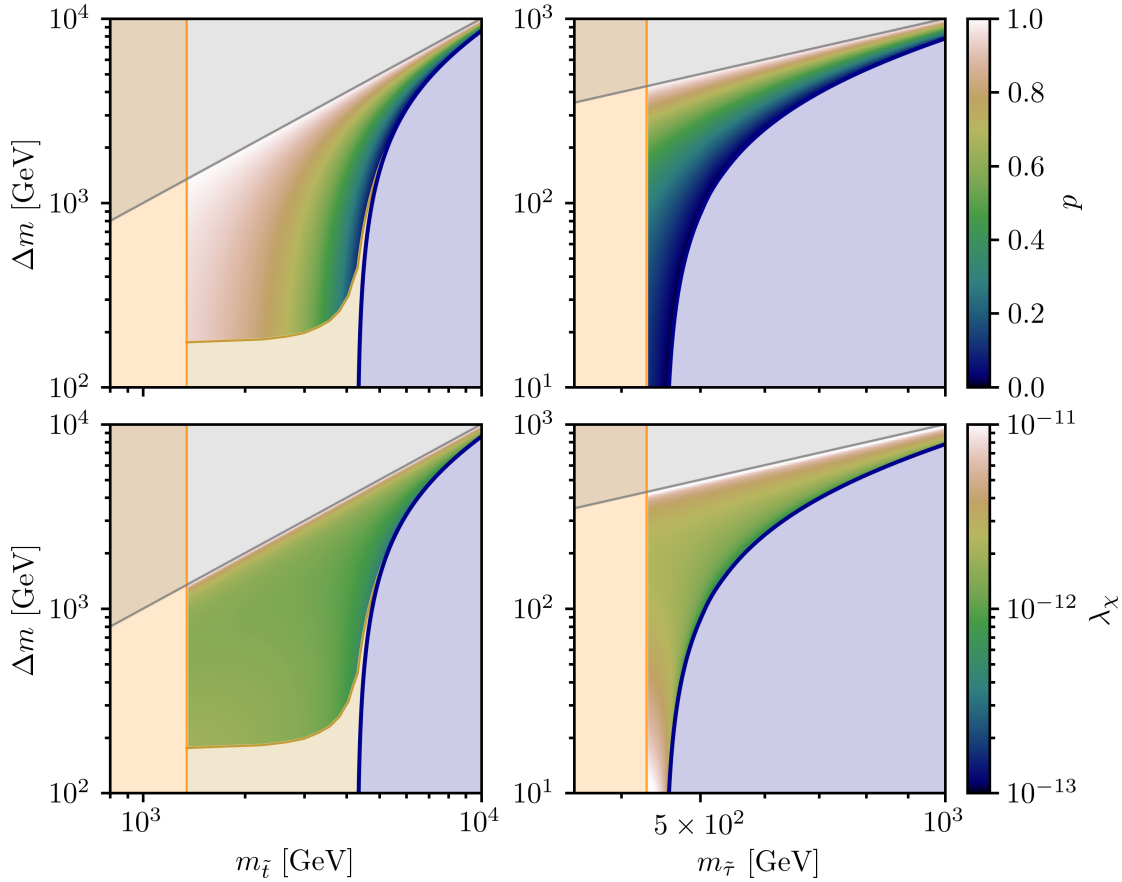


Figure 6.8: The parameter space of non-thermal production in the top-philic (left) and lepto-philic (right) mediator model, where the values of the Yukawa-like coupling λ_χ (bottom) as well as the FI fraction p (top) in the viable parameter space considering non-perturbative corrections at $\lambda_H = 0$ have been highlighted. For information on the labels and shaded areas, see Fig. 6.7. Adapted from Ref. [5].

λ_χ which will boost the lifetime of the mediator. A similar exclusion limit exists in the lepto-philic mediator model around the mass of the tau lepton. However, this is outside our primary regime of interest and is therefore not displayed.

We observe the predictions of λ_χ in both models to be roughly constant in the regime, where both FI and the sW mechanism play a role in DM production (see Fig. 6.8, bottom). This suggests that both regimes can be well separated and dominate DM production for $\lambda_\chi \gtrsim 10^{-12}$ and $\lambda_\chi \lesssim 10^{-12}$, respectively. For the largest mass splittings, DM is solely produced via FI. This can be important, since within this regime sW production might enter a phase where the mediator FO and decay are no longer separable due to the increased mediator lifetime as a consequence of larger λ_χ . Fortunately, this will have no impact on the DM abundance due to the negligible sW contribution in this regime.

Overall, we showed that a perturbative calculation of the non-thermal DM abundance within the top-philic mediator model drastically underestimates the parameter space allowed by cosmological constraints. We expect a moderate improvement up to ≈ 1.6 TeV on the exclusion limits by collider searches after the HL upgrade of the LHC, leaving us doubtful that the parameter space of this model can be tested in the foreseeable future. In the lepto-philic mediator model, where non-perturbative effects are of lesser importance, the upgrade could be sufficient to rule out large mass splittings assuming $\lambda_H = 0$. However, if a sizable Higgs portal is allowed, testing the viable regime remains a challenge for far-future colliders probing BSM physics at significantly higher energies.

7 Non-perturbative effects in dark matter indirect detection

Another intriguing avenue to explore the impact of non-perturbative effects on DM models apart from DM production is to focus on its detection properties. Among the different approaches to search for DM introduced in Section 3.3, indirect detection distinguishes itself as being the most directly linked to the production process. Given that the CTA, a cutting-edge gamma-ray telescope [100], has entered the building phase, it is now the right time to reevaluate constraints on DM imposed by current indirect detection experiments and juxtapose these bounds with the prospects forecasted by the CTA collaboration.

Having already explored non-thermal production of DM in the previous section, we will focus in this section on a typical thermal FO scenario for the DM candidate. However, in contrast to the common WIMP paradigm, DM annihilations here will not proceed into SM particles but rather into states beyond the SM. These types of models go under the name of *secluded DM* [216, 217] and they are a particularly interesting scenario for indirect detection as it facilitates the decoupling of the relic density from other observables, thereby circumventing stringent constraints imposed by direct detection experiments [218–220] and collider searches [221–224]. If the new states are light compared to the DM mass, long-range self-interactions can occur, leading to SE and, if the interactions are attractive, to the formation of BS (cf. Section 5).

Over recent years, the integration of SE has become a common practice in both calculating the relic density of DM and establishing indirect detection limits [122, 225–229], while accounting for BSF remains less established and is still under ongoing methodological development. When considering BS, most studies either focus on the DM relic density [128–143] or on experimental signatures [230–235], whereas only a limited number of works consistently integrate the influence of non-perturbative effects on both the cross sections for thermal FO and indirect detection. Relevant examples have so far scrutinized models with a vector mediator, i.e. a dark photon, which undergoes kinetic mixing with the $U(1)_Y$ gauge group of the SM [133, 236–238]. In the study of this section, our objective is to address the gap concerning a category of DM models, where the self-interaction is mediated by a scalar particle. Specifically, we investigate both scalar and pseudo-scalar interactions of the mediator with a fermionic DM candidate. Employing pNREFT, we derive the cross sections, which are crucial for determining the DM relic density as well as DM annihilations in astrophysical environments, such as the *galactic center* (GC) and *dwarf spheroidal galaxies* (dSphs). Subsequently, we utilize these results to delineate the cosmologically viable parameter space for the model, which we then integrate with existing and prospective constraints from the CMB as well as gamma-ray telescopes, namely Fermi-LAT and CTA, respectively.

In Section 7.1, we introduce the DM model and its pertinent energy scales. Subsequently, in Section 7.2, we present the cross sections and decay widths relevant for DM production within the framework of pNREFT and perform the relic density calculation including non-perturbative effects. Section 7.3 is dedicated to scrutinize the impact of SE and BSF on DM annihilation in various astrophysical and cosmological environments, including discussions on current bounds and future prospects, such as those offered by

the next-generation detector CTA. These constraints are complemented in Section 7.4 by various other searches. The parameter space currently constrained by existing bounds as well as those that can be tested by future experiments is laid out in Section 7.5.

The work presented in this section has been published in Ref. [6]. For transparency, we want to note that the analytic computation of the observables presented in Section 7.2 using pNREFT has been carried out by Simone Biondini and is added to this thesis for the sake of completeness and consistency. However, the obtained results have been cross-checked by the author through a rederivation, employing the approach introduced in Section 5.2. Due to perfect agreement, these computations have been omitted in the publication but can be found in App. F.

7.1 The dark matter model and energy scales

We will start by introducing the DM model employed in this section and discuss the relevant energy scales of our system, as we will use pNREFT (cf. Section 5.3) to compute our observables. Our DM candidate is a Dirac fermion χ which features no direct interactions with SM particles and is thus naturally a singlet under the SM gauge group. It does, however, possess Yukawa-like interactions with a real scalar mediator ϕ of an extended dark sector, which in turn couples to the SM via mixing with the Higgs boson. The Lagrangian density of the two-particle dark sector is then given by

$$\mathcal{L}_{\text{DS}} = \bar{\chi} (i\gamma_\mu \partial^\mu - m_\chi) \chi + \frac{1}{2} \partial_\mu \phi \partial^\mu \phi - \frac{1}{2} m_\phi^2 \phi^2 - \bar{\chi} (g + ig_5 \gamma_5) \chi \phi - \frac{\lambda_\phi}{4!} \phi^4 + \mathcal{L}_{\text{portal}}, \quad (7.1.1)$$

where m_χ , m_ϕ denote the DM and mediator masses and g , g_5 are the scalar and pseudo-scalar Yukawa-type couplings between the dark sector particles. The mediator self coupling λ_ϕ is chosen to be negligible such that it plays no role in the subsequent discussion. To allow for the study of non-perturbative effects, the mediator mass is chosen to be considerably smaller than the DM mass. We further require $\alpha \equiv g^2/(4\pi) \gg \alpha_5 \equiv g_5^2/(4\pi)$ to ensure that the non-perturbative effects predominantly arise from scalar-type interactions, which induce an attractive mediator potential (see App. C). This allows us to neglect mixed and pure pseudo-scalar contributions to SE and BSF effects (see Section 5.3 and Refs. [141, 239]).

Since we are chiefly interested in investigating the impact of non-perturbative effects on indirect detection, we opt for a minimal DM model [240, 241]. Consequently, the mass parameters and couplings in Eq. 7.1.1 are chosen freely, without making any assumptions about a specific UV completion.⁴⁸ We refer to Refs. [242, 243] as instances of similar simplified models, which feature gauge symmetries and spontaneous symmetry breaking in the dark sector. Technically, the mediator sector can be extended to include a richer set of interactions, as discussed in works such as Refs. [150, 239, 244]. For instance, an

⁴⁸However, it is not challenging to devise a mechanism for generating masses in our model. Assuming, for instance, a non-zero vev for the scalar mediator, we would obtain $m_\chi \simeq gv_\phi$, $m_\phi \simeq \sqrt{\lambda_\phi} v_\phi$, allowing for an arbitrary splitting between both dark sector masses $m_\phi/m_\chi \simeq \sqrt{\lambda_\phi}/g < 1$, since λ_ϕ can be tuned freely. Interestingly, this choice would also maintain a negligible thermal contribution to the mediator mass $m_\phi^{\text{th}}/m_\phi \simeq gT/m_\chi$ at FO (since $T \ll m_\chi$) largely independent of λ_ϕ .

interaction of the form $\rho_\phi\phi^3$ with a dimensionful coupling could exist, thereby facilitating additional BSF processes [138, 150].

The Higgs sector containing the Higgs portal interactions with the dark sector mediator is given by

$$\mathcal{L}_{\text{portal}} = -\mu^2 H^\dagger H - \lambda(H^\dagger H)^2 - \mu_{\phi h}\phi \left(H^\dagger H - \frac{v^2}{2} \right) - \frac{1}{2}\lambda_{\phi h}\phi^2 \left(H^\dagger H - \frac{v^2}{2} \right), \quad (7.1.2)$$

where H denotes the SM Higgs doublet with μ , λ its SM potential couplings and $v^2 \equiv -\mu^2/\lambda$ the usual Higgs *vacuum expectation value* (vev). Note that we have applied a shift to the scalar mediator field such that it does not develop a vev on its own. The quartic coupling $\lambda_{\phi h}$ is taken to be negligible in the following such that only the dimensionful coupling $\mu_{\phi h}$ induces a mixing between the mediator and the Higgs.⁴⁹ We made this choice, along with $v_\phi = 0$, to minimize the number of relevant free model parameters. An alternative choice could have been to set $\mu_{\phi h} = 0$ and retain the quartic mixing $\lambda_{\phi h}$ alongside the quartic scalar coupling λ_ϕ . Inevitably, this would introduce a vev for the scalar ($v_\phi > 0$) analogous to the SM Higgs sector. Nonetheless, the definition of the mixing angle δ and the mixing term in the Lagrangian after *electroweak symmetry breaking* (EWSB) remain the same at leading order when substituting $\mu_{\phi h} \rightarrow v_\phi\lambda_{\phi h}$. We have verified that the phenomenology of both scenarios, including the resulting dark scalar and Higgs boson masses, is mostly equivalent up to $\mathcal{O}(\sin^2\delta)$, which we will neglect in the following due to the small value of δ . However, a sizeable self-interaction of the mediator would introduce a thermal mass for the mediator $m_\phi^{\text{th}} = T\sqrt{\lambda_\phi/12}$, a complication which is not pursued further here. A discussion of the scalar mixing and its implications for indirect detection is postponed to Section 7.3.3.

The DM relic density in this model is fixed via thermal FO (cf. Section 4.2). The essential process that activates this mechanism and plays a crucial role in generating astrophysical signals for indirect detection is the annihilation of DM pairs into mediator particles, $\bar{\chi} + \chi \rightarrow \phi + \phi$. Both DM production and detection processes occur in the non-relativistic regime, where $v_{\text{rel}} \ll 1$. To study non-perturbative effects in this model, we reintroduce the dimensionless parameters from Eq. 5.1.13

$$\zeta \equiv \frac{\alpha}{v_{\text{rel}}} \quad \text{and} \quad \xi \equiv \frac{m_\chi\alpha}{2m_\phi},$$

where the criteria for large SE ($\zeta \gtrsim 1$) and BS ($\xi \gg 1$) effects have already been discussed in Section 5.1. In addition to the DM mass m_χ , there are two dynamical energy scales at $v_{\text{rel}} \sim \alpha$ that will play a major role in the subsequent discussion (cf. Section 5.3): 1) the typical momentum transfer in $\bar{\chi}\chi$ -scattering which is proportional to the Bohr momentum $\kappa \propto m_\chi\alpha$ of the BS and 2) the BS energy scale $m_\chi\alpha^2$. With decreasing α , the separation between the scales becomes more pronounced, with $m_\chi \gg m_\chi\alpha \gg m_\chi\alpha^2$.

⁴⁹By this choice, we naturally avoid sizeable contributions to the Higgs mass through mediator loops. Thermal contact between the SM and the dark sector can still be maintained with relatively small values of $\lambda_{\phi h}$ (see Section 7.4.3).

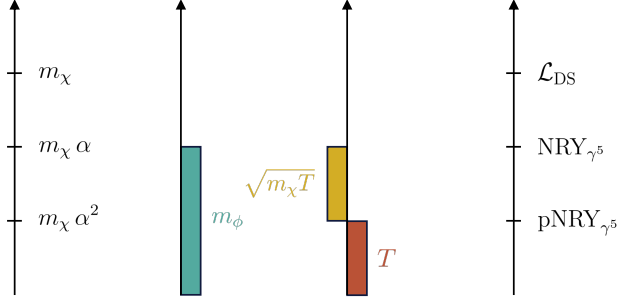


Figure 7.1: Hierarchy of the relevant energy scales in the model employed in Section 7. Besides the two mass scales, dynamically generated as well as thermal scales are depicted. Effective field theories considered in this work (cf. Section 5.3) for the DM model defined in Eq. 7.1.1 are matched with their corresponding scales. Adapted from Ref. [6].

As discussed in Section 5.3, we will refer to them as the hard, soft, and ultra-soft energy scales, respectively.

The mediator mass m_ϕ is another pertinent energy scale. We consider it to be smaller than the DM mass m_χ and, at most, as large as the soft scale $m_\chi\alpha$. A key distinction from massless mediators is the screening of DM self-interactions when the soft scale $m_\chi\alpha$ is of the order of the mediator mass m_ϕ .⁵⁰ In the case of scattering states subject to an attractive potential as produced by the scalar coupling, the SE typically levels off at low velocities (instead of further increasing $\propto v_{\text{rel}}^{-1}$). Furthermore, a characteristic resonance structure emerges due to the Yukawa potential, which depends on the ratio of mediator to DM mass characterized by ξ [121–123]. The Coulomb limit is regained for velocities significantly larger than α , i. e. $\zeta \ll 1$, and/or in the massless mediator limit $\xi \rightarrow \infty$. Phenomenologically, the latter does not occur since our primary interest lies in the regime where $m_\phi \geq 2m_\pi^0$. This is motivated by the observation that lighter mediators do not produce a substantial amount of gamma-rays, which constitute the primary observational signature examined in this study. Nonetheless, lighter mediators can impact other observables such as the positron flux or the distribution of DM mass in dense halos (see e. g. Refs. [239, 245]).

Eventually, during the FO of DM particles in the early Universe, thermal scales can become relevant. The first one to note is the temperature T of the thermal plasma, which is already $T \ll m_\chi$ at the onset of FO. Nevertheless, it can still be of the order of the soft or ultra-soft scale, which one has to account for. In this study, we incorporate thermal effects due to the medium, presuming the temperature to be approximately at the ultrasoft scale $m_\chi\alpha^2$ or smaller. This assumption implies that thermal effects do not affect

⁵⁰One might wonder, if the mediator induced DM self coupling places any bounds on the parameter space of our model. This does seem to be the case, as e. g. Ref. [239] found limits for a very similar model only at DM and mediator masses lower than considered in this study.

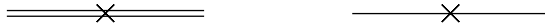


Figure 7.2: The localized ($\propto \delta^{(3)}(\mathbf{r})$) contributions to the scattering state (left) and BS (right) self energy diagrams in pNRY $_{\gamma_5}$. Their imaginary parts, given in the Lagrangian of Eq. 5.3.33, can be matched to the $\bar{\chi}\chi$ annihilation cross section and the BS decay rate, respectively, where a double solid line corresponds to a scattering state and a single solid line to a BS. The crosses denote the interaction points.

the non-relativistic potential, which we can then still assume to be the in-vacuum Yukawa one. For DM fermions in thermal equilibrium, the relative velocity is approximately $v_{\text{rel}} \sim \sqrt{T/m_\chi}$, resulting in a typical momentum of $m_\chi v_{\text{rel}} \sim \sqrt{m_\chi T} \lesssim m_\chi \alpha$, indicating $v_{\text{rel}} \lesssim \alpha$. Additionally, within the temperature range considered in this work, we have $\sqrt{m_\chi T} \gtrsim m_\chi \alpha^2$. These conditions classify $m_\chi v_{\text{rel}}$ as a soft scale, and $m_\chi v_{\text{rel}}^2 \sim T$ as an ultrasoft scale (cf. Section 5.3). Visualized in Fig. 7.1, we summarize the hierarchy of the energy scales as

$$m_\chi \gg m_\chi \alpha \gtrsim \sqrt{m_\chi T} \gg m_\chi \alpha^2 \gtrsim T, \quad (7.1.3)$$

where the mediator mass is assumed to be $m_\phi \lesssim m_\chi \alpha$. For reasons explained above, thermal masses are negligible in this setup and do not enter the scale hierarchy.

7.2 Dark matter production from pNREFT

Before we can study the indirect detection properties of our DM model, we first need to determine how much DM is produced during FO. As for the model discussed in Section 4, we will subsequently calculate the annihilation cross section with SE, the BSF cross section as well as the BS ionization and decay rate. Contrary to before, we will employ pNREFT to perform the computations, as it allows for a better control of the different scales within the model.

7.2.1 Heavy pair annihilation and decay

We will start by calculating the annihilation cross section of the heavy $\bar{\chi}\chi$ pair. This can be achieved by relating the cross section via the optical theorem to the imaginary contribution of the scattering pair self-energy as visualized in Fig. 7.2 (left). In NRY $_{\gamma_5}$, annihilation processes are encoded in local 4-fermion operators. This translates to pNRY $_{\gamma_5}$, where these operators generate local terms ($\propto \delta^{(3)}(\mathbf{r})$) in the imaginary part of the potential. The matching coefficients required for the subsequent computation, are thus the ones given in Eq. 5.3.33, which we will collectively denote as V_{ann} in the following. The

annihilation cross section can be written as

$$\sigma_{\text{ann}} v_{\text{rel}}(\mathbf{p}) = \frac{1}{4} \langle \mathbf{p}, 0 | \int d^3r \varphi^\dagger(\mathbf{r}, \mathbf{R}, t) [2\text{Im} \{-V_{\text{ann}}(\mathbf{r}, \mathbf{p}, \boldsymbol{\sigma}_1, \boldsymbol{\sigma}_2)\}] \varphi(\mathbf{r}, \mathbf{R}, t) | \mathbf{p}, 0 \rangle, \quad (7.2.1)$$

where we have considered the scattering amplitude from an initial to a final state $|\mathbf{p}, 0\rangle$ in the COM frame (with $\mathbf{P} = 0$). We sum here implicitly over all possible spin configurations of $|\mathbf{p}, 0\rangle$ and average over the initial spins which results in a prefactor $1/4$. In order to project out the spin factors, it is advantageous to insert a $\mathbb{1} = \sum_{S, m_S} |S, m_S\rangle \langle S, m_S|$, where $\sum_{m_S} \langle 1, m_S | S^i S^j | 1, m_S \rangle = 2\delta^{ij}$ and all singlet projections vanish. After inserting the definitions of $\varphi^{(S)}(\mathbf{r}, \mathbf{R}, t)$ given in Eq. 5.3.36 and decomposing the scattering state wave function $\phi_{\mathbf{p}}(\mathbf{r})$ into partial waves (cf. Eq. 5.1.9), the cross section yields

$$\begin{aligned} \sigma_{\text{ann}} v_{\text{rel}}(\mathbf{p}) &= \frac{\text{Im} \{f(^1S_0)\}}{m_\chi^2} |\mathcal{R}_{\mathbf{p},0}(r)|_{r=0}^2 + \frac{\text{Im} \{f(^3P_0)\} + 5\text{Im} \{f(^3P_2)\}}{3m_\chi^4} |\mathcal{R}'_{\mathbf{p},1}(r)|_{r=0}^2 \\ &\quad - \frac{\text{Im} \{g(^1S_0)\}}{m_\chi^4} \text{Re} \{ \mathcal{R}_{\mathbf{p},0}^*(r) \nabla_r^2 \mathcal{R}_{\mathbf{p},0}(r) \}_{r=0}. \end{aligned} \quad (7.2.2)$$

The $\mathcal{R}_{\mathbf{p},l}(r) \equiv (2l+1)\chi_{\mathbf{p},l}(\kappa r)/(\kappa r)$ denote the radial wave functions, which are related to the SE factors via $|\mathcal{R}_{\mathbf{p},0}(r)|_{r=0}^2 = S_{\text{ann},0}(\zeta, \xi)$ and $|\mathcal{R}'_{\mathbf{p},1}(r)|_{r=0}^2 = p^2 S_{\text{ann},1}(\zeta, \xi)$ (cf. Eq. 5.1.20), with $p = m_\chi v_{\text{rel}}/2$.⁵¹ The expression $\text{Re} \{ \mathcal{R}_{\mathbf{p},0}^*(r) \nabla_r^2 \mathcal{R}_{\mathbf{p},0}(r) \}$ formally diverges for $r = 0$, however, we can exchange this term with the finite expression $-p^2 |\mathcal{R}_{\mathbf{p},0}(r)|_{r=0}^2$ as explained in Ref. [167]. As we can see, by computing the annihilation cross section in pNRY $_{\gamma_5}$, the resummation of soft exchanges (i. e. SE) is naturally included because pNRY $_{\gamma_5}$ is a theory of interacting pairs. The hard dynamics is encoded in the matching coefficients of NRY $_{\gamma_5}$, whereas soft dynamics are contained in the radial wave functions. The annihilation cross section corrected for SE is then given by

$$\begin{aligned} \sigma_{\text{ann}} v_{\text{rel}} &= \frac{1}{m_\chi^2} \left\{ \left(\text{Im} \{f(^1S_0)\} + \text{Im} \{g(^1S_0)\} \frac{v_{\text{rel}}^2}{4} \right) S_{\text{ann},0}(\zeta, \xi) \right. \\ &\quad \left. + \left(\frac{\text{Im} \{f(^3P_0)\} + 5\text{Im} \{f(^3P_2)\}}{3} \right) \frac{v_{\text{rel}}^2}{4} S_{\text{ann},1}(\zeta, \xi) \right\}, \end{aligned} \quad (7.2.3)$$

where the SE factors have to be computed numerically with the methods introduced in Section 5.1.2. We have displayed them in Fig. 7.3, where we observe the aforementioned resonance structure along the ξ axis. These resonances are caused by the Yukawa potential in the Schrödinger equation, which for some mediator masses exactly cancels the kinetic and angular contributions resulting in a zero energy BS. The resonance peaks vary for the displayed partial waves due to the different angular dependencies (i. e. the $l(l+1)/x^2$ terms in the Schrödinger equation) [246]. We cross-checked Eq. 7.2.3 utilizing Eq. 5.1.1, where we calculated the s- and p-wave contributions to the hard annihilation

⁵¹We want to note here that the corresponding radial l -wave functions are projected out from the decomposition of $\phi_{\mathbf{p}}(\mathbf{r})$ because the NRY $_{\gamma_5}$ matching coefficients have a concrete angular momentum dependence (and thus come with angular projection operators), which has been left implicit in Eq. 5.3.33.

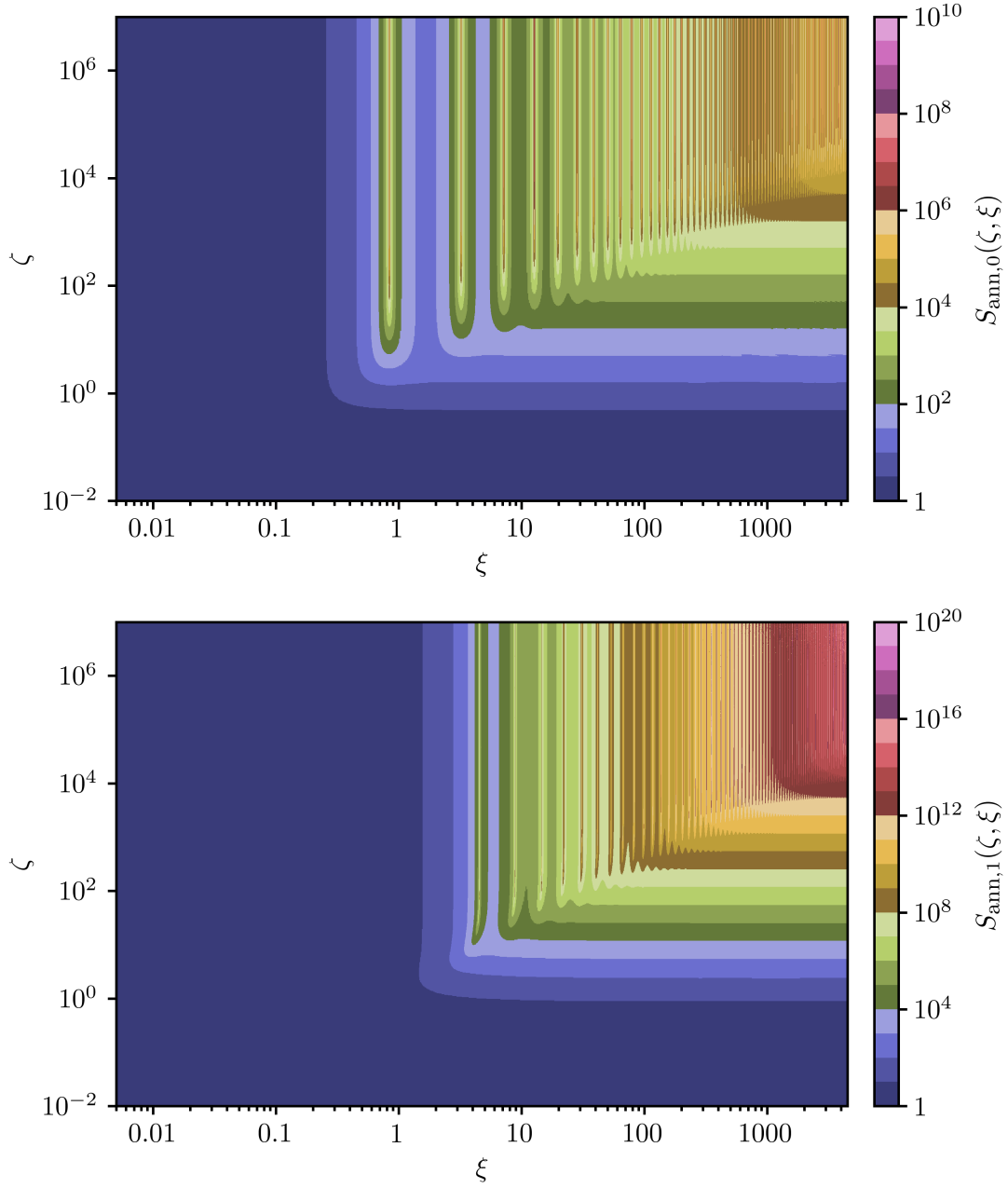


Figure 7.3: The SE factors of s-wave (top) and p-wave (bottom) scattering states in $\bar{\chi}\chi$ pair annihilation for a finite mediator mass as a function of the dimensionless variables ζ and ξ , encompassing the DM to mediator mass ratio, the scalar coupling strength and the relative DM velocity.

cross section directly from the QFT matrix element of the full theory.

The decay rate of a BS can be calculated equivalently to the annihilation cross section by relating it to its self-energy via the optical theorem (see the right diagram in Fig. 7.2). We employ again the imaginary part of the matching coefficients V_{ann} and project it onto the BS $|n, 0\rangle$ in the COM frame, yielding

$$\Gamma_{\text{dec}}^{(n)} = \frac{1}{2J+1} \langle n, 0 | \int d^3r \varphi^\dagger(\mathbf{r}, \mathbf{R}, t) [2\text{Im} \{-V_{\text{ann}}(\mathbf{r}, \mathbf{p}, \boldsymbol{\sigma}_1, \boldsymbol{\sigma}_2)\}] \varphi(\mathbf{r}, \mathbf{R}, t) |n, 0\rangle, \quad (7.2.4)$$

where we average over the degenerate states with the same total angular quantum number J .⁵² We can already see from the spin and angular momentum structure in Eq. 5.3.33, that an S -state $|nS\rangle \equiv |n00\rangle$ will project out a spin singlet, whereas for a P -state $|nP\rangle \equiv |n1m\rangle$ only a spin triplet contribution will remain. Performing similar steps as before, we obtain

$$\Gamma_{\text{dec}}^{(nS)} = \frac{\text{Im} \{f(^1S_0)\}}{\pi m_\chi^2} |\mathcal{R}_{n0}(r)|_{r=0}^2 = \frac{4\text{Im} \{f(^1S_0)\}}{m_\chi^2} S_{\text{dec},0}^{(nS)}(\xi), \quad (7.2.5)$$

$$\Gamma_{\text{dec}}^{(nP)} = \frac{\text{Im} \{f(^3P_J)\}}{\pi m_\chi^4} |\mathcal{R}'_{n1}(r)|_{r=0}^2 = \frac{\text{Im} \{f(^3P_J)\}}{3m_\chi^2} S_{\text{dec},1}^{(nP)}(\xi), \quad (7.2.6)$$

where $\mathcal{R}_{nl}(r) \equiv \kappa^{3/2} \chi_{nl}(\kappa r) / (\kappa r)$ is the radial wave function of the BS (cf. Eq. 5.1.10), which translates to the decay SE factors (cf. Eq. 5.1.30) via $|\mathcal{R}_{n0}(r)|_{r=0}^2 = 4\pi S_{\text{dec},0}^{(nS)}(\xi)$ and $|\mathcal{R}'_{n1}(r)|_{r=0}^2 = \pi/3 m_\chi^2 S_{\text{dec},1}^{(nP)}(\xi)$. Methods to compute the SE factors for BS decay have been discussed in Section 5.1.3. For reasons explained later, we will only consider the decay of the $1S$ state in the following.

7.2.2 Bound state formation and ionization

We will continue by calculating the BSF cross section as well as the BS ionization rate. The latter will only be important for FO because ionization requires a thermal population of mediator particles, which is not present in the late Universe. For BSF, we will restrict ourselves to the leading order ultra-soft transitions between a scattering and a BS, which radiate off a single scalar mediator particle, namely $\bar{\chi} + \chi \rightarrow \mathcal{B}(\bar{\chi}\chi) + \phi$.⁵³ These are given in the pNRY _{γ_5} Lagrangian by the terms in the second line of Eq. 5.3.25. The BSF cross section at finite temperature can then be calculated from the imaginary parts of the respective contributions to the self-energy of the scattering state, which are illustrated in Fig. 7.4. Note that the monopole diagrams are absent because they vanish due to

⁵²Note that a sum over the degenerate quantum states with different m is not necessary, because only the $m = 0$ state contributes due to the azimuthal symmetry of the potential (cf. Eq. 5.1.30).

⁵³Additional BSF processes can emerge from $2 \rightarrow 2$ inelastic scatterings between SM particles and the $\bar{\chi}\chi$ pair (see e. g. Refs. [137, 139, 247]). However, as they are induced in our case by the mixing between the scalar and the SM Higgs, they are strongly suppressed due to the small mixing angle and, therefore, will be neglected. Inelastic scattering processes involving the mediator are absent because we assume the trilinear mediator coupling $\rho_\phi \phi^3$ to vanish.



Figure 7.4: The leading order self-energy contributions to the scattering state (double solid line) of a heavy $\bar{\chi}\chi$ pair from quadrupole (diamond vertex) and derivative (triangle vertex) interactions in pNRY $_{\gamma_5}$ (cf. Eq. 5.3.25). Their imaginary parts can be matched to the BSF cross section. The internal propagators correspond to a BS (single solid line) and a mediator (dashed line).

the orthogonality of the scattering and BS wave functions. Therefore, the BSF processes are driven by the quadrupole as well as the derivative term. In principle, the BSF cross section in pNRY $_{\gamma_5}$ is given by an expression similar to Eq. 7.2.1. However, since none of the interaction vertices are spin dependent, we can drastically simplify the notation in this case, yielding

$$\sigma_{\text{BSF}} v_{\text{rel}}|_T = \langle \mathbf{k} | 2\text{Im} \{-\Sigma_{\text{BSF}}\} | \mathbf{k} \rangle, \quad (7.2.7)$$

with $|\mathbf{k}\rangle$ a scattering state in the COM frame and Σ_{BSF} the self energy contributions from the three diagrams in Fig. 7.4. The scattering and BS wave functions are then simply given by $\langle \mathbf{r} | \mathbf{k} \rangle = \phi_{\mathbf{k}}(\mathbf{r})$ and $\langle \mathbf{r} | n \rangle = \psi_n(\mathbf{r})$.

As an example, we will proceed by calculating the self-energy from the leftmost diagram, corresponding to the pure quadrupole contribution. In dimensional regularization with $D = 4 - 2\epsilon$, the self-energy contribution with purely quadrupole interactions is given by [141]

$$\Sigma^{\mathcal{Q}} = -i \frac{\pi\alpha}{4} \mu^{4-D} r^i r^j \int \frac{d^D q}{(2\pi)^D} \frac{i}{K^0 - q^0 - H + i\eta} q^i q^j q^m q^n \left[\frac{i}{(q^0)^2 - q^2 - m_\phi^2 + i\eta} + 2\pi\delta((q^0)^2 - q^2 - m_\phi^2) f_\phi(|q^0|) \right] r^m r^n, \quad (7.2.8)$$

where $\mu = m_\chi/2$ is the reduced mass of the system, $K^0 = \mathcal{E}_{\mathbf{k}}$ denotes the energy of the scattering state, the q^i correspond to the $\nabla_{\mathbf{R}}^i$ in momentum space and the r^i are understood as operators which act on the bound and scattering states. The terms in the brackets correspond to the scalar propagator, which splits up into an in-vacuum and a thermal part at finite temperature, where $f_\phi(x) = 1/(e^{x/T} - 1)$ is the Bose-Einstein equilibrium distribution of the scalar.⁵⁴ Note that the thermal non-relativistic propagator of a fermion antifermion pair interacting through a potential $V(r)$ as given e.g. in Ref. [250], can be replaced by its in-vacuum form, as displayed in the first line

⁵⁴The scalar propagator at finite temperature has been derived in the *real-time formalism* and can be found e.g. in Ref. [141]; see Refs. [248, 249] for further details on the construction.

of Eq. 7.2.8, when considering physical amplitudes (H denoting the Hamiltonian). To ensure that the internal loop propagator describes BS, we insert a complete set of BS

$$\frac{i}{K^0 - q^0 - H + i\eta} = \sum_n \frac{i}{\Delta\mathcal{E}_n^{\mathbf{k}} - q^0 + i\eta} |n\rangle\langle n|, \quad (7.2.9)$$

where $H|n\rangle = \mathcal{E}_n|n\rangle$ projects out the BS energy and

$$\Delta\mathcal{E}_n^{\mathbf{k}} \equiv \mathcal{E}_{\mathbf{k}} - \mathcal{E}_n = \frac{k^2}{2\mu} + \gamma_{nl}^2(\xi) \frac{\kappa^2}{2\mu} = \frac{m_\chi \alpha^2}{4} \left(\frac{1 + \gamma_{nl}^2(\xi) \zeta^2}{\zeta^2} \right) \quad (7.2.10)$$

denotes the energy difference between the scattering and the BS. Note that γ_{nl} for the massive mediator scenario must be determined simultaneously with the BS wave function (see Section 5.1.3). By applying the usual cutting rules $1/(x - q^0 + i\eta) \rightarrow -\pi i \delta(x - q^0)$ and $1/((q^0)^2 - x^2 + i\eta) \rightarrow -2\pi i \delta((q^0)^2 - x^2)$, as outlined in Ref. [161], the imaginary part of the self-energy is obtained, yielding

$$\text{Im} \{ \Sigma^{\mathcal{Q}} \} = -\frac{\alpha}{240} \sum_n \left[(\Delta\mathcal{E}_n^{\mathbf{k}})^2 - m_\phi^2 \right]^{5/2} (\mathbf{r}^2 |n\rangle\langle n| \mathbf{r}^2 + 2r^i r^j |n\rangle\langle n| r^i r^j) \left[1 + f_\phi(\Delta\mathcal{E}_n^{\mathbf{k}}) \right]. \quad (7.2.11)$$

The self-energy contributions from the other two diagrams in Fig. 7.4 can be computed in a similar manner. As evident from Eq. 7.2.11 (and also holds in general to this order), the T dependence of the BSF cross section into a BS state (n) can be factored out

$$\sigma_{\text{BSF}}^{(n)} v_{\text{rel}}|_T = \sigma_{\text{BSF}}^{(n)} v_{\text{rel}} \left[1 + f_\phi(\Delta\mathcal{E}_n^{\mathbf{k}}) \right], \quad (7.2.12)$$

with the in-vacuum cross section at $T = 0$ given by

$$\begin{aligned} \sigma_{\text{BSF}}^{(n)} v_{\text{rel}} &= \frac{\alpha}{120} \left[(\Delta\mathcal{E}_n^{\mathbf{k}})^2 - m_\phi^2 \right]^{5/2} \left[|\langle \mathbf{k} | \mathbf{r}^2 | n \rangle|^2 + 2 |\langle \mathbf{k} | r^i r^j | n \rangle|^2 \right] \\ &\quad - \frac{\alpha}{3m_\chi^2} \left[(\Delta\mathcal{E}_n^{\mathbf{k}})^2 - m_\phi^2 \right]^{3/2} \text{Re} \{ \langle \mathbf{k} | \nabla_{\mathbf{r}}^2 | n \rangle \langle n | \mathbf{r}^2 | \mathbf{k} \rangle \} \\ &\quad + \frac{2\alpha}{m_\chi^4} \left[(\Delta\mathcal{E}_n^{\mathbf{k}})^2 - m_\phi^2 \right]^{1/2} |\langle \mathbf{k} | \nabla_{\mathbf{r}}^2 | n \rangle|^2. \end{aligned} \quad (7.2.13)$$

The quantum mechanical matrix elements, sometimes also referred to as *overlap integrals*, for an operator \mathcal{O} are defined as

$$\langle \mathbf{k} | \mathcal{O} | n \rangle \equiv \int d^3r \phi_{\mathbf{k}}^*(\mathbf{r}) \mathcal{O} \psi_n(\mathbf{r}) \quad (7.2.14)$$

and have to be evaluated numerically due to the finite mediator mass. To do so, we employed the leading order Yukawa potential in the Schrödinger equations (cf. Eqs. 5.1.3 and 5.1.4) to derive the scattering and BS wave functions with the methods introduced in Section 5.1. The total BSF cross section contains in principle the sum over all possible

BS $\sigma_{\text{BSF}} v_{\text{rel}} = \sum_n \sigma_{\text{BSF}}^{(n)} v_{\text{rel}}$ which are kinematically allowed (i. e. for which $\Delta \mathcal{E}_n^{\mathbf{k}} > m_\phi$). However, we will consider in the following only BSF into the ground state $(1S) = \{100\}$ and estimate corrections of higher states in Section 7.2.3. By factoring out $\pi\alpha^4/m_\chi^2$, the BSF cross section can be expressed as

$$\sigma_{\text{BSF}} v_{\text{rel}} = \frac{\pi\alpha^4}{m_\chi^2} S_{\text{BSF}}(\zeta, \xi), \quad (7.2.15)$$

where we have suppressed the $(1S)$ superscript and defined the dimensionless SE factor for BSF into the ground state as

$$\begin{aligned} S_{\text{BSF}}(\zeta, \xi) \equiv & \frac{\sqrt{\mathcal{P}_{10}(\zeta, \xi)}}{4\pi} \left(\frac{1 + \zeta^2 \gamma_{10}^2(\xi)}{\zeta^2} \right) \\ & \left\{ \frac{\kappa^7}{240} \mathcal{P}_{10}^2(\zeta, \xi) \left(\frac{1 + \zeta^2 \gamma_{10}^2(\xi)}{\zeta^2} \right)^4 [|\langle \mathbf{k} | \mathbf{r}^2 | 1S \rangle|^2 + 2|\langle \mathbf{k} | r^i r^j | 1S \rangle|^2] \right. \\ & \left. - \frac{\kappa^3}{6} \mathcal{P}_{10}(\zeta, \xi) \left(\frac{1 + \zeta^2 \gamma_{10}^2(\xi)}{\zeta^2} \right)^2 \text{Re} \left\{ \langle \mathbf{k} | \nabla_{\mathbf{r}}^2 | 1S \rangle \langle 1S | \mathbf{r}^2 | \mathbf{k} \rangle \right\} + \frac{1}{\kappa} |\langle \mathbf{k} | \nabla_{\mathbf{r}}^2 | 1S \rangle|^2 \right\}. \end{aligned} \quad (7.2.16)$$

The quantity $\mathcal{P}_{10}(\zeta, \xi)$ denotes the phase space suppression factor and is given by

$$\mathcal{P}_{10}(\zeta, \xi) \equiv 1 - \frac{m_\phi^2}{(\Delta \mathcal{E}_{1S}^{\mathbf{k}})^2} = 1 - \frac{4\zeta^4}{\alpha^2 \xi^2 (1 + \zeta^2 \gamma_{10}^2(\xi))^2}, \quad (7.2.17)$$

yielding $\mathcal{P}_{10}(\zeta, \xi) \rightarrow 1$ in the Coulomb limit. In App. F, we verify Eq. 7.2.16 by recalculating the BSF cross section using the approach introduced in Section 5.2.

As evident from Fig. 7.5, the resonance structure in the ξ direction is also present in the BSF cross section, similar to the SE factors observed in DM annihilations. Additionally, the gray regions in the parameter space indicate where BSF is kinematically forbidden, i. e. where $\Delta \mathcal{E}_{1S}^{\mathbf{k}} < m_\phi$. When $\xi > 2/(\alpha \gamma_{10}^2(\xi))$, BSF can always occur (see Eq. 5.1.29). For $\alpha = 0.1$, this condition is approximately satisfied at $\xi_{\text{min}} \approx 22$. To better illustrate the dependence of the BSF cross section on ζ , we sliced through the parameter space at different fixed values of ξ in Fig. 7.6 (left) and also included the Coulomb case ($\xi \rightarrow \infty$). We observe a very different behaviour for various mediator to DM mass ratios. As expected, when $\xi = 20$, the SE factor drops to zero as soon as the $\bar{\chi}\chi$ pair no longer has sufficient kinetic energy to form a BS. In the cases where BSF is always possible, such as for $\xi = 75$ and $\xi = 100$, the curves flatten out towards large ζ or small v_{rel} , respectively. This behavior is attributed to the screening effect of the finite mediator mass. For $\xi = 100$, a resonance structure appears.

If we assume the non-relativistic scattering state follows a Maxwell-Boltzmann distribution, the thermal average of the BSF cross section

$$\langle \sigma_{\text{BSF}} v_{\text{rel}} \rangle \equiv \frac{x^{3/2}}{2\sqrt{\pi}} \int_0^\infty dv_{\text{rel}} v_{\text{rel}}^2 e^{-\frac{x}{4} v_{\text{rel}}^2} (1 + f_\phi(\Delta \mathcal{E}_{1S}^{\mathbf{k}})) \sigma_{\text{BSF}} v_{\text{rel}} \quad (7.2.18)$$

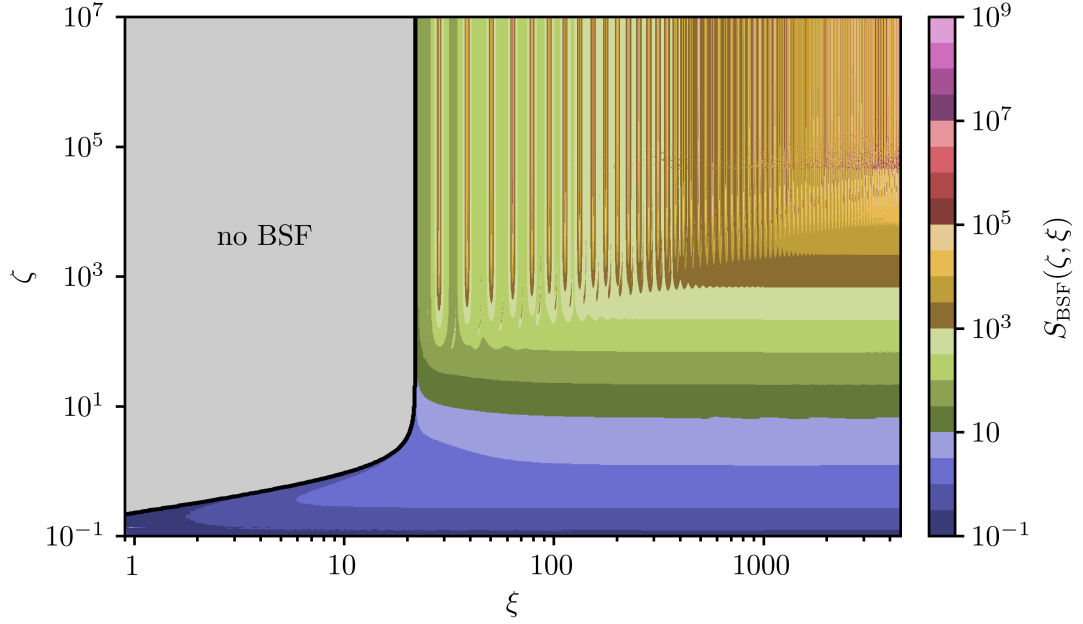


Figure 7.5: The SE factor for BSF into the ground state for a finite mediator mass and $\alpha = 0.1$ as a function of the dimensionless variables ζ and ξ , encompassing the DM to mediator mass ratio, the scalar coupling strength and the relative DM velocity. The gray area denotes the region of parameter space, where BSF is not possible.

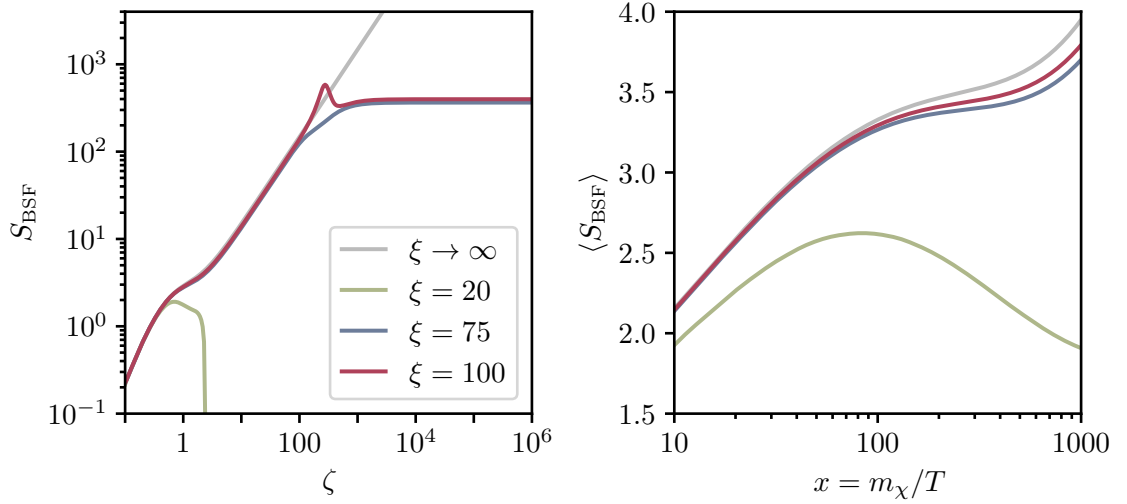


Figure 7.6: The SE factor for BSF into the ground state (left) as well as its thermal average (right) for $\alpha = 0.1$ as a function of ζ or, respectively, $x \equiv m_\chi/T$ for selected values of ξ (identical for both plots). The case $\xi \rightarrow \infty$ (or $m_\phi \rightarrow 0$) corresponds to the Coulomb limit. Adapted from Ref. [6].

with $x \equiv m_\chi/T$ is essentially the same as in Eq. 6.3.33. Note that the statistical factor for the potentially relativistic mediator arises in pNRY_{γ_5} naturally when considering finite temperature effects (cf. Eq. 7.2.12). In the right panel of Fig. 7.6, we displayed the thermal average of the SE factor of BSF, defined via $\langle \sigma_{\text{BSF}} v_{\text{rel}} \rangle \equiv \pi \alpha^4 / m_\chi^2 \langle S_{\text{BSF}} \rangle$, for the same choices of ξ as in the left panel. We observe that the resonance structures observable for $\xi = 100$ in the left panel are washed out and not visible any longer. The same is true with the drop off for $\xi = 20$, such that we find smooth enhancement factors at FO for all ξ .

The computation of the BS ionization rate can be performed in analogy to the BSF cross section. The self-energy diagrams, which must be projected onto $|n\rangle$, are the same as in Fig. 7.4 with the bound and scattering state lines exchanged (see e. g. Refs. [141, 250]). However, the ionization cross section can be also just inferred from the BSF cross section utilizing the principle of detailed balance, usually referred as Milne relation in this field of application [136, 171]

$$\sigma_{\text{ion}}(\omega) = \frac{g_\chi^2}{g_B g_\phi} \frac{m_\chi^2 v_{\text{rel}}^2}{4\omega^2} \sigma_{\text{BSF}}, \quad (7.2.19)$$

with $\omega = \Delta \mathcal{E}_n^k$ the energy of the scalar mediator and $g_\chi = 2$, $g_\phi = 1$, g_B the internal dof of the DM candidate, the mediator and the corresponding BS ($g_{1S} = 1$). The thermally averaged ionization rate is then given by

$$\langle \Gamma_{\text{ion}} \rangle \equiv g_\phi \int_{\omega_{\text{min}}}^{\infty} \frac{d\omega}{2\pi^2} \omega^2 f_\phi(\omega) \sigma_{\text{ion}}(\omega), \quad (7.2.20)$$

where $\omega_{\text{min}} = \max\{|\mathcal{E}_n|, m_\phi\}$ represents the minimum energy required for the scalar to ionize a BS. Note that for $m_\phi \rightarrow 0$ we recover the structural form of Eq. 6.3.34. For the calculation of the DM abundance we will in the following only consider BS ionization of the ground state, which is why we have suppressed the superscript (n) in the Milne relation and in the definition of $\langle \Gamma_{\text{ion}} \rangle$.

So far we have not considered the running of the scalar coupling α , on which we want to catch up on now. The scalar coupling strength appears in the hard matching coefficients of Eqs. 5.3.15 to 5.3.18, in the SE factors of Eqs. 7.2.3 and 7.2.5 describing soft processes, as well as in the BSF cross section in Eq. 7.2.13 generated via ultra-soft vertices. It therefore has to be evaluated at the hard, soft, and ultrasoft scale, resulting in different physical values one has to keep track of if its running is considered. We used two different approaches to study the running of α : 1) Taking into account DM fermion, scalar self energy, as well as vertex one-loop diagrams of the full theory and expanding the integrals according to their soft and ultra-soft momenta with respect to the mediator and DM mass scales. 2) Performing the calculations directly in NRY_{γ_5} or pNRY_{γ_5} . Both methods show that there is no significant running induced at scales below m_χ , thus α remains approximately frozen at the hard scale. The running of α_5 is neglected because it is smaller than α and does not contribute at leading order to soft and ultra-soft processes.

7.2.3 The relic density

To calculate the relic density of DM, we employ the same approach as in Section 6.4 utilizing a set of BEs for FO. We first assume a quasi steady-state for the BS yield, i. e. $dY_B/dx \approx 0$, holding if the processes governing the rate at which the BS yield changes are faster than the Hubble rate. The DM yield as a function of $x \equiv m_\chi/T$ incorporating non-perturbative effects can then be summarized in a single equation (cf. Eq. 6.4.2)

$$\frac{dY_\chi}{dx} = -\frac{1}{2}\xi_1(x)\langle\sigma_{\text{ann}}v_{\text{rel}}\rangle_{\text{tot}}(Y_\chi^2 - Y_\chi^{\text{eq}2}), \quad (7.2.21)$$

where Y_χ^{eq} is the equilibrium yield given in Eq. 4.2.1, $\xi_1(x) \equiv \sqrt{\pi/45}M_{\text{Pl}}m_\chi g_\star^{1/2}(x)x^{-2}$ and the factor 1/2 accounts for the Dirac nature of the DM candidate. The total thermally averaged cross section (neglecting bound-to-bound transitions) is given by

$$\langle\sigma_{\text{ann}}v_{\text{rel}}\rangle_{\text{tot}} \equiv \langle\sigma_{\text{ann}}v_{\text{rel}}\rangle + \sum_n \frac{\langle\Gamma_{\text{dec}}^{(n)}\rangle}{\langle\Gamma_{\text{ion}}^{(n)}\rangle + \langle\Gamma_{\text{dec}}^{(n)}\rangle} \langle\sigma_{\text{BSF}}^{(n)}v_{\text{rel}}\rangle, \quad (7.2.22)$$

where $\langle\sigma_{\text{ann}}v_{\text{rel}}\rangle$ is the thermal average of SE corrected annihilation cross section given in Eq. 7.2.3 (cf. also Eq. 4.3.7) and we sum over BS contributions with different quantum numbers (n). The factor in front of the BSF cross section serves as a weight that determines which percentage of the produced BS will actually decay and therefore effectively deplete the DM abundance. For indirect detection, the prefactor becomes 1 because the ionization rate goes to zero due to the lack of thermal mediators in the late Universe. As previously stated, we will only include the 1S BS in the following. Therefore, $\langle\sigma_{\text{BSF}}v_{\text{rel}}\rangle$ and $\langle\Gamma_{\text{ion}}\rangle$ are given by Eqs. 7.2.18 and 7.2.20, respectively. The thermal average of the ground state decay rate of Eq. 7.2.5 can be calculated from Eq. 4.1.17.

In Fig. 7.7 (left), we displayed the DM relic abundance computed from Eq. 4.2.6 as a function of ξ for the benchmark point $m_\chi = 2 \text{ TeV}$, $\alpha_5/\alpha = 0.01$ and two different values for α . Dashed lines correspond to the case where BSF effects are not taken into account, i. e. $\langle\sigma_{\text{ann}}v_{\text{rel}}\rangle_{\text{tot}} = \langle\sigma_{\text{ann}}v_{\text{rel}}\rangle$, whereas for solid lines both non-perturbative effects contribute. We can see that for large ξ , the curves flatten as the solution converges to the Coulomb limit, where non-perturbative effects become maximal (cf. also Fig. 7.6). Whereas BS effects become sizeable for $\xi \gtrsim 5$ considering this benchmark point, for $\xi \lesssim 3$ they are absent due to phase space suppression effects of BSF and the overall existence limit of the ground state $\xi > 0.84$ (cf. Section 5.1.3). For $\alpha = 0.13$, BS effects are even crucial to avoid overclosing of the Universe.

In the right panel of Fig. 7.7, we show the ratio of the DM relic density when including or disregarding BS effects. We fixed $m_\chi = 2 \text{ TeV}$ and $\alpha = 0.15$, and then varied the ratio α_5/α between the scalar and pseudo-scalar couplings over a range of values. While decreasing the coupling ratio an interesting trend can be observed. The effects from BS first become stronger for smaller pseudo-scalar couplings as visible by the orange ($\alpha_5/\alpha = 0.01$) and blue line ($\alpha_5/\alpha = 0.005$) in comparison to the red graph ($\alpha_5/\alpha = 0.1$). The reason for this is the linear dependence of the velocity-independent s-wave part of

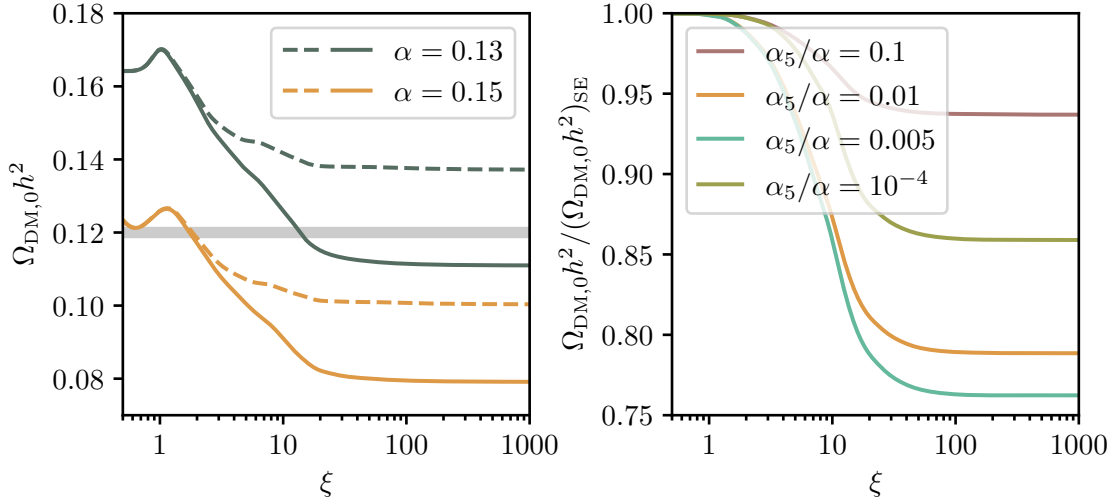


Figure 7.7: *Left:* The DM relic abundance observed today as a function of ξ for a benchmark point $m_\chi = 2 \text{ TeV}$, $\alpha_5/\alpha = 0.01$ and two different values of α . Solid lines correspond to the case where both, SE and BS effects are taken into account, whereas for the dashed lines only SE has been included. The gray area corresponds to the observed relic abundance today $\Omega_{\text{DM},0} h^2 = 0.1200 \pm 0.0012$ [8] with a 1σ uncertainty band. *Right:* The ratio of the DM abundance taking into account both non-perturbative effects with respect to the DM abundance obtained by only considering SE for a benchmark point $m_\chi = 2 \text{ TeV}$, $\alpha = 0.15$ and different values of α_5/α . Adapted from Ref. [6].

the annihilation cross section on the pseudo-scalar coupling (cf. Eq. 7.2.3), whereas BSF is independent of α_5 . For very small ratios, as for the green line ($\alpha_5/\alpha = 10^{-4}$), the trend reverses because α_5 also affects the decay rate of the ground state, therefore decreasing the weighting factor of the BSF contribution.⁵⁵ This behaviour as well as the importance of BS effects in general is rather independent of the DM mass.

As mentioned earlier, for the relic density calculations as well as for indirect detection we will only include the ground state $1S$ in our estimate of BS effects on the total annihilation cross section. In the light of recent works about the high relevance of excited states for the FO of DM [142, 143, 172], we need to justify this decision. The cited studies focus on models with massless vector mediators from an unbroken gauge symmetry. They find a large logarithmic enhancement of the total BSF cross section (i. e. in the right term in Eq. 7.2.22) considering a large number of Coulomb BS. Partly, this is caused by the enormous increase of BS with $l \leq n - 1$ for large n . The model in our work comprises of a massive scalar mediator. The resulting Yukawa potential only features a finite number

⁵⁵In fact, for $\alpha_5 \rightarrow 0$ the ground states cannot decay and $\langle \Gamma_{\text{dec}} \rangle / (\langle \Gamma_{\text{dec}} \rangle + \langle \Gamma_{\text{ion}} \rangle) \rightarrow 0$, resulting in an absence of BS effects. Allowing for three body decays, i. e. diagrams with three scalar vertices or a trilinear coupling vertex from a $\rho_\phi \phi^3$ term in the Lagrangian, would alleviate the problem by making the decay width of the ground state independent of α_5 .

of BS, such that a large enhancement from summing up to large n is not expected.⁵⁶ To estimate effects from the lowest excited states we have included in the Coulomb limit the four $n = 2$ states, namely the $2S$ singlet and $2P$ triplet, for which we have calculated the SE BSF factors in App. G. From Fig. G.1 in the same appendix, it can be observed that the inclusion of states with $n > 2$ will not substantially alter this estimate. For the $n = 2$ states we found that the corrections to the relic density always stay below 10% within our parameter regime of interest. The dominant contribution to these corrections arises from the $2S$ states for two reasons: 1) The weighting factor for the $2P$ state is significantly smaller than for the $2S$ state, because the decay rate is strongly suppressed (cf. Eq. 7.2.6). 2) Due to the missing dipole moment in the ultra-soft vertices of pNRY_{γ_5} (cf. Eq. 5.3.25), only $\Delta l = 0, 2$ transitions between BS are allowed [141, 150, 170]. Therefore, $2P$ states cannot transition into $2S$ states effectively. A more thorough study of the effects of higher BS in finite mass mediator models goes beyond the scope of this work.

7.3 Indirect detection

Within our model, DM annihilations at late times are still possible (especially in regions with a high DM density) but happen far too rarely to significantly affect the total DM abundance on cosmological scales. However, their presence can be detected by methods of indirect detection, e.g. through their effects on the flux of various cosmic rays. We will primarily focus on present and future gamma-ray telescopes in the following discussion, as they have the prospects to provide the most stringent limits in our parameter regime of interest. Specifically, we will look at data by Fermi-LAT on dSphs as well as prospects from the CTA collaboration of a future survey of the GC of the Milky Way (cf. Section 3.3). Additionally, we will take into account bounds on late time energy injection during CMB decoupling derived by the Planck collaboration.

As sketched in Fig. 7.8 (shaded regions), all three environments under consideration, namely the CMB, dSphs and the GC, feature a different velocity distribution of DM. While the characteristic DM velocities in dSphs and the GC are of $\mathcal{O}(10^{-5})$ and $\mathcal{O}(10^{-3})$, respectively, the DM velocity at times around the CMB is typically of $\mathcal{O}(10^{-8})$. Figure 7.8 depicts the leading order s- and p-wave contributions as well as the BSF cross section into the ground state for an exemplary configuration of masses and couplings, respectively.⁵⁷ It is apparent that the typical velocity dependence of $\propto 1/v_{\text{rel}}$, present for all contributions at the time of FO (cf. Sections 5.1.2 and 6.3.2), morphs into a non-trivial behaviour at lower velocities due to the finite mass of the mediator. These low-velocity regimes are relevant for indirect detection. Therefore, it is imperative to discern the dominant contributions within the aforementioned astrophysical environments. For dSphs and the GC, the cross sections associated with s-wave annihilation and BSF are enhanced due to their scaling with low velocities. This is also true for the

⁵⁶We can impose a conservative limit on the number of BS supported by a Yukawa potential by requiring that the binding energy of the BS exceeds the mediator mass. For the parameter space of interest in our model, this leads to the constraint of $n \leq 22$.

⁵⁷Due to the considerably lower velocities relevant for indirect detection as compared to FO, all higher order velocity contributions to the corresponding cross sections can be safely neglected.

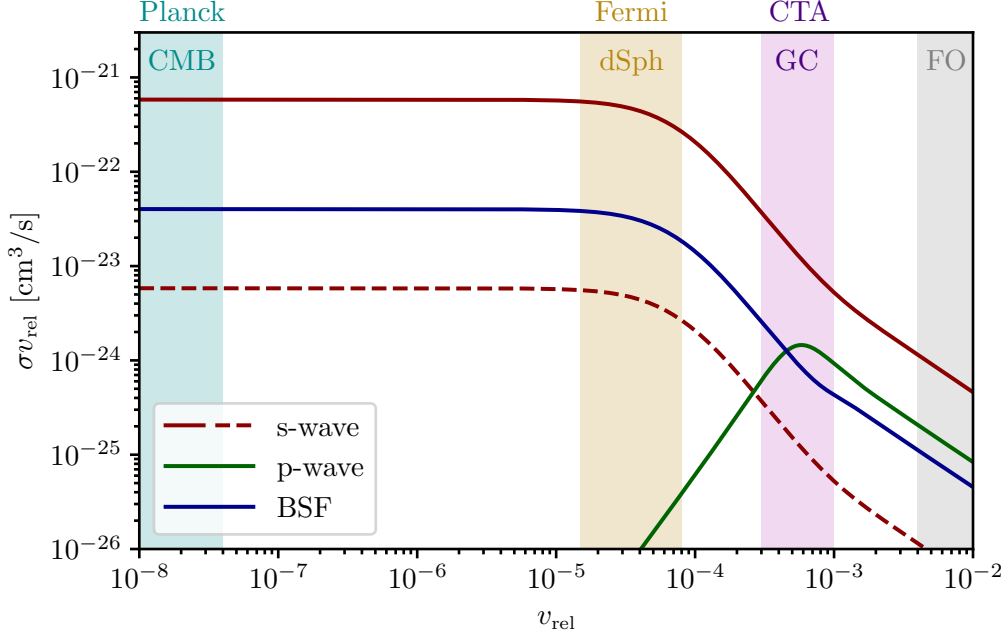


Figure 7.8: Velocity dependence of the leading order contributions to the total DM annihilation cross section from s-wave and p-wave annihilation as well as BSF into the ground state for a benchmark point of $m_\chi = 1$ TeV, $m_\phi = 1$ GeV and $\alpha = 0.1$. For the pseudo-scalar coupling, two different values of $\alpha_5 = 10^{-3}$ (solid lines) and $\alpha_5 = 10^{-5}$ (dashed lines) have been chosen and are depicted for s-wave annihilation only, since the α_5 dependence on the p-wave (BSF) contribution is subdominant (absent). We have shaded regions of typical DM velocities during FO, at times of the CMB decoupling as well as for dSphs and the GC. Adapted from Ref. [6].

p-wave cross section in the region $v_{\text{rel}} \gg m_\phi/m_\chi$, where SE is capable of compensating for the p-wave velocity suppression. The CMB is mostly influenced by the s-wave and BSF cross sections whereas their relative strength is governed by the value of α_5 . Within this regime, both contributions have flattened due to the finite size of the potential and thus their SE factors have been rendered constant. For all configurations of masses and couplings considered in this work, the p-wave annihilation cross section will have no relevance for the CMB due to its v_{rel}^2 velocity suppression.

In order to take into account the non-trivial velocity dependence of the annihilation cross section in the phenomenology of indirect detection, a few adjustments to the conventional approaches are necessary. Considering the CMB, a redefinition of the thermally averaged cross section is sufficient, on which we will comment later. In case of galactic environments, such as dSphs and the GC, the matter is more intricate. In the context of gamma-ray signals from these objects, the pivotal observable is the photon flux. The

contribution to the differential photon flux from (Dirac) DM annihilations reads (see e. g. Ref. [251])

$$\frac{d\Phi_\gamma}{dE_\gamma} = \frac{1}{16\pi m_\chi^2} \frac{dN_\gamma}{dE_\gamma} \int_{\Delta\Omega} d\Omega \int_0^\infty d\psi \int d^3v_1 \int d^3v_2 f_\chi(r(\psi, \Omega), \mathbf{v}_1) f_{\bar{\chi}}(r(\psi, \Omega), \mathbf{v}_2) \sigma v_{\text{rel}}. \quad (7.3.1)$$

Here, the *photon spectrum* $dN_\gamma/dE_\gamma \equiv \sum_f \mathcal{B}_f dN_\gamma^{(f)}/dE_\gamma$ denotes the number of photons that get produced per photon energy E_γ per annihilation, where the sum runs over all possible annihilation final states f weighted by their branching fraction \mathcal{B}_f . The (in general velocity dependent) annihilation cross section σv_{rel} is first integrated over the velocities of the initial state DM particles together with the DM phase space *distribution functions* (DFs) $f_\chi = f_{\bar{\chi}}$.⁵⁸ The remaining integration is then performed over the field of view of the gamma-ray telescope, which is usually given in galactic coordinates, namely the galactic longitude l and latitude b as well as the LoS distance ψ . For the galactic coordinates parametrization, the angular measure is given by $d\Omega = \cos b db dl$, and the distance of a DM particle from the center of the galaxy is determined by $r(\psi, \Omega) = \sqrt{D^2 + \psi^2 - 2D\psi \cos b \cos l}$, where D represents the distance of our sun to the center of the galaxy ($D = 8.5$ kpc for the GC and $\mathcal{O}(10 - 100)$ kpc for the different dSphs under consideration [252]).

In case that σv_{rel} is velocity independent, as for the leading order s-wave contribution without SE, it can be pulled out of the integration, such that the remainder yields the usual J -factor, which is defined by (see e. g. [2])

$$J_0 \equiv \int d\Omega \int_0^\infty d\psi \rho_\chi(r(\psi, \Omega))^2, \quad (7.3.2)$$

where $\rho_\chi(r) \equiv \int d^3v f_\chi(r, \mathbf{v})$ is the DM energy density. In the following, we assume that the DFs and, consequently, the energy density are spherically symmetric, which is a reasonable assumption for galactic environments and will greatly simplify our subsequent calculations. If the cross section is p-wave dominated or non-perturbative effects play a role, the non-trivial velocity dependence of σv_{rel} demands a full calculation of the velocity average which in turn requires knowledge about the behaviour of the DFs f_χ . To start with, we will in analogy to the thermally averaged total annihilation cross section in Eq. 7.2.22 assume that we can split up the total annihilation cross section into

$$\sigma v_{\text{rel}} = \sum_{l=0}^{\infty} \sigma_l v_{\text{rel}}^{2l} S_{\text{ann},l}(\zeta, \xi) + \sum_n \sigma_{\text{BSF}}^{(n)} v_{\text{rel}}, \quad (7.3.3)$$

where any weighting factors in front of the $\sigma_{\text{BSF}}^{(n)} v_{\text{rel}}$ can be neglected since the ionization rate is negligible. Since we are only considering BSF into the ground state for the same reasons as in Section 7.2.3, we will drop the sum over n in the second term and

⁵⁸This cross section includes contributions from s- and p-wave annihilations as well as BSF. The DFs here are position and velocity dependent because the astrophysical environment is neither homogeneous nor isotropic.

define $\sigma_{\text{BSF}} v_{\text{rel}} \equiv \sigma_{\text{BSF}}^0 S_{\text{BSF}}$ with $\sigma_{\text{BSF}}^0 \equiv \pi \alpha^4 / m_\chi^2$ (cf. Eq. 7.2.15). In the first term, we only consider the leading order contributions to s- and p-wave annihilation, where the perturbative cross sections, which have been stripped from their angular and velocity dependence (cf. Eq. 7.2.3), are given by

$$\sigma_0 \equiv \frac{\text{Im} \{f(^1S_0)\}}{m_\chi^2}, \quad \sigma_1 \equiv \frac{\text{Im} \{f(^3P_0)\} + 5\text{Im} \{f(^3P_2)\}}{12m_\chi^2}. \quad (7.3.4)$$

This splitting enables us to define a generalized J -factor for annihilation (and an analogous factor for BSF)

$$J_{\text{ann},l}^{(\alpha)}(\xi) \equiv \int_{\Delta\Omega} d\Omega \int_0^\infty d\psi \int d^3v_1 f_\chi(r(\psi, \Omega), \mathbf{v}_1) \int d^3v_2 f_\chi(r(\psi, \Omega), \mathbf{v}_2) v_{\text{rel}}^{2l} S_{\text{ann},l}(\zeta, \xi), \quad (7.3.5)$$

which only depends on the DM and mediator masses through ξ as well as explicitly on the scalar coupling α . We can therefore write Eq. 7.3.1 as

$$\frac{d\Phi_\gamma}{dE_\gamma} = \frac{1}{16\pi m_\chi^2} \frac{dN_\gamma}{dE_\gamma} \left(\sigma_0 J_{\text{ann},0}^{(\alpha)}(\xi) + \sigma_1 J_{\text{ann},1}^{(\alpha)}(\xi) + \sigma_{\text{BSF}}^0 J_{\text{BSF}}^{(\alpha)}(\xi) \right). \quad (7.3.6)$$

In the subsequent sections, we will derive the generalized J -factors and the photon spectra dN_γ/dE_γ separately. For the prior, however, we must first determine the distribution functions (DFs) of DM in galactic environments, with which we will start.

7.3.1 The dark matter distribution function f_χ

The DF of DM in galaxies is not directly observable through astrophysical measurements. Consequently, it is necessary to incorporate additional information to ascertain a form of f_χ that ensures consistency with observations of measurable quantities deduced from it. In the following, we will primarily employ methods developed for spherically symmetric distributions of DM in galaxies, which are applicable to collisionless systems in quasi-static equilibrium. A detailed discussion of these techniques can be found in Ref. [253], whereas Refs. [251, 252, 254] focus on their application to galactic DM structures. An alternative strategy that we do not use here is the direct sampling of the DF from numerical simulations of DM halos, as has been done e. g. in Ref. [255, 256].

Within the dSphs under consideration (or the GC), we assume a static and spherically symmetric DM density function ρ_χ . For a sufficiently isolated system, this allows us to determine the gravitational potential of the galaxy Ψ through Poisson's equation

$$\Delta\Psi = -4\pi G(\rho_\chi + \rho_b), \quad (7.3.7)$$

with G the Newtonian constant and ρ_b the local baryon density within the galaxy. We can then determine a unique and ergodic DF for DM supported by this potential via the Eddington inversion method [253]

$$f_\chi(\epsilon) = \frac{1}{\sqrt{8\pi^2}} \left(\int_0^\epsilon \frac{d^2\rho_\chi}{d\Psi^2} \frac{d\Psi}{\sqrt{\epsilon - \Psi}} - \frac{1}{\sqrt{-\epsilon}} \frac{d\rho_\chi}{d\Psi} \Big|_{\Psi=0} \right), \quad (7.3.8)$$

where $\epsilon = \Psi(r) - v^2/2$ denotes the DM energy per unit mass. Following from the isolation criterion mentioned above, we will set the gravitational potential $\Psi(r)$ to 0 at $r \rightarrow \infty$, which causes the second term to disappear.⁵⁹ Since Ψ is monotonic in r , we can rewrite Eq. 7.3.8 directly as a function of r and v [251]

$$f_\chi(r, v) = \frac{1}{\sqrt{8\pi^2}} \int_{r_{\min}}^{\infty} \frac{dr'}{\sqrt{\Psi(r) - \Psi(r') - \frac{v^2}{2}}} \left(\frac{d\Psi}{dr'} \right)^{-1} \left[\frac{d^2\rho_\chi}{dr'^2} - \left(\frac{d\Psi}{dr'} \right)^{-1} \frac{d^2\Psi}{dr'^2} \frac{d\rho_\chi}{dr'} \right], \quad (7.3.9)$$

where r_{\min} is determined by the solution to the equation $\Psi(r) - \Psi(r_{\min}) - v^2/2 = 0$.

A range of different parametrizations for the energy density ρ_χ of a DM halo have been considered in the literature (see e. g. Ref. [257] for an overview). As for dSphs, we will assume a *Navarro-Frenk-White* (NFW) profile [258–260] in the following. It is given by

$$\rho_{\text{NFW}} = \frac{\rho_0}{\frac{r}{r_s} \left(1 + \frac{r}{r_s} \right)^2}, \quad (7.3.10)$$

where r_s is the *scale radius* and ρ_0 fixes the normalization. For a better comparability with other galactic models as well as astrophysical measurements, it is advisable to establish a frame of reference for the model parameters. Following e. g. Ref. [257], we will define the scale radius via the logarithmic slope

$$\left. \frac{d \log \rho_\chi}{d \log r} \right|_{r=r_s} \equiv -2, \quad \rho_\chi(r_s) = \rho_s, \quad (7.3.11)$$

where ρ_s denotes the *scale density*, which is given by $\rho_s = \rho_0/4$ for the NFW profile. For our DM model of the GC, we employ an *Einasto profile* [261, 262] to stay comparable to the sensitivity study performed by the CTA collaboration [263]. It reads

$$\rho_{\text{Ein}} = \rho_0 \exp \left[-\frac{2}{\gamma} \left[\left(\frac{r}{r_s} \right)^\gamma - 1 \right] \right], \quad (7.3.12)$$

with $\gamma = 0.17$ and $\rho_s = \rho_0$. Note that although we will perform our study on indirect detection in dSphs and the GC using the designated DM density profiles, we will employ the respective other profile for cross-verification and to estimate potential errors. For our analysis of dSphs we will calculate the best-fit values for (r_s, ρ_s) from the parameters (r_{\max}, V_{\max}) given in Table 1 of Ref. [252], which denote the maximal circular velocity $v_{\text{cir}}(r_{\max}) = V_{\max}$ and its radius. The circular velocity (cf. Eq. 3.1.1) is defined as $v_{\text{cir}} \equiv \sqrt{GM(r)/r}$, with $M(r) = 4\pi \int_0^r dr' (r')^2 \rho_\chi(r')$ being the enclosed DM mass at radius r . The relations of the two parameter tuples for the considered density profiles are given by $r_s = r_{\max}/C_1$ and $\rho_s = (V_{\max}/C_2)^2/(16\pi G r_s^2)$ with $(C_1^{\text{NFW}}, C_2^{\text{NFW}}) = (2.163, 0.465)$ for the NFW and $(C_1^{\text{Ein}}, C_2^{\text{Ein}}) = (2.204, 0.473)$ for the Einasto profile [252]. For the GC, we

⁵⁹Technically, setting $\Psi(r) = 0$ at $r \rightarrow \infty$ is unphysical because the gravitational potential of a galaxy is naturally bounded by its neighbors. However, it was shown in Ref. [254] that the effect of a large but finite boundary compared to an infinite one is small such that we will neglect it in the following.

Table 7.1: Astrophysical parameters of the DM halos for dSphs and the GC used for subsequent computations, namely the distance D to the sun (in kpc), the concentration parameter c as well as the virial radius r_{vir} (in kpc) and the virial mass M_{vir} in units of the solar mass M_{\odot} . All model dependent parameters have been calculated for an underlying NFW and Einasto density profile from data provided in Refs. [252, 263].

galaxy	D [kpc]	c^{NFW}	c^{Ein}	$r_{\text{vir}}^{\text{NFW}}$ [kpc]	$r_{\text{vir}}^{\text{Ein}}$ [kpc]	$M_{\text{vir}}^{\text{NFW}}$ [M_{\odot}]	$M_{\text{vir}}^{\text{Ein}}$ [M_{\odot}]
Coma B.	44	44.84	44.32	7.879	7.640	5.17×10^7	4.71×10^7
Ursa Minor	76	34.55	34.59	21.09	20.71	9.91×10^8	9.39×10^8
Draco	76	37.83	37.72	15.04	14.71	3.60×10^8	3.37×10^8
Sergue 1	23	38.85	38.68	13.65	13.34	2.69×10^8	2.50×10^8
GC	8.5	11.83	12.17	236.6	243.4	1.40×10^{12}	1.52×10^{12}

set $r_s = 20$ kpc, $\rho_s = 0.081$ GeV/cm³ as suggested by the CTA prospect analysis [263].

To define the properties of a DM halo which can in turn be used to further enhance the comparability of different density models, we will define two additional parameters: the *virial radius* r_{vir} and the *virial mass* M_{vir} . The virial radius of a system is a radius within which the virial theorem can be applied (cf. Section 3.1). Roughly speaking, this is the distance at which the galaxy, including its DM halo, can still be regarded as a stable system of discrete particles bound by a gravitational force. In our context, the virial radius measures the extent of the DM halo and the virial mass is defined as the DM mass encapsulated by it, i. e. $M_{\text{vir}} \equiv M(r_{\text{vir}})$. Vice versa, equating the virial mass of a spherical DM halo with the mass of a sphere of the same size but a flat background times an overdensity parameter Δ_c (typically set to $\Delta_c = 200$), defines the virial radius

$$4\pi \int_0^{r_{\text{vir}}} dr r^2 \rho_{\chi}(r) \equiv \frac{4}{3} \pi r_{\text{vir}}^3 \Delta_c \rho_{\text{crit},0}. \quad (7.3.13)$$

Using Eq. 7.3.13, one can calculate r_{vir} and M_{vir} from other scaling parameters such as (r_s, ρ_s) . We have displayed them for the dSphs under consideration as well as for the GC in Table 7.1 considering both DM density profiles.

It will be more convenient in the following to switch to dimensionless coordinates [251]. We will define $x \equiv r/r_{\text{vir}}$ as a fractional measure of distance from the center and $c \equiv r_{\text{vir}}/r_s$ a concentration parameter which can be calculated using Eq. 7.3.13 (also displayed in Table 7.1). The density functions can be written as $\rho_{\chi} \equiv \rho_0 \tilde{\rho}_{\chi}(x, c; \dots)$ with $\tilde{\rho}_{\chi}$ its dimensionless part. We can express ρ_0 through the virial parameters $M_{\text{vir}} = 4\pi r_{\text{vir}}^3 \rho_0 g(c)$, where we further define $g(c; \dots) \equiv \int_0^{\infty} x^2 \tilde{\rho}_{\chi}(x, c; \dots)$. For the NFW and

Einasto profile this reparametrization reads

$$\rho_\chi = \frac{M_{\text{vir}}}{4\pi r_{\text{vir}}^3} \frac{1}{g(c)} \tilde{\rho}_\chi(x, c) \equiv \frac{M_{\text{vir}}}{4\pi r_{\text{vir}}^3} \begin{cases} \frac{1}{g_{\text{NFW}}(c)} \frac{1}{cx(1+cx)^2} & \text{NFW} \\ \frac{1}{g_{\text{Ein}}(c; \gamma)} \exp\left[-\frac{2}{\gamma} [(cx)^\gamma - 1]\right] & \text{Einasto} \end{cases}, \quad (7.3.14)$$

with [251]

$$g_{\text{NFW}}(c) = \frac{1}{c^3} \left[\log(1+c) - \frac{c}{1+c} \right], \quad (7.3.15)$$

$$g_{\text{Ein}}(c; \gamma) = \frac{e^{2/\gamma}}{c^3 \gamma} \left(\frac{2}{\gamma} \right)^{-3/\gamma} \left[\Gamma\left(\frac{3}{\gamma}\right) - \Gamma\left(\frac{2}{\gamma}, \frac{2}{\gamma} c^\gamma\right) \right], \quad (7.3.16)$$

where Γ denotes the (incomplete) gamma function (cf. Eq. A.1). Likewise, all other parameters within Eq. 7.3.9 can be substituted with their dimensionless counterparts

$$\Psi \equiv \frac{GM_{\text{vir}}}{r_{\text{vir}}} \tilde{\psi}, \quad \epsilon \equiv \frac{GM_{\text{vir}}}{r_{\text{vir}}} \tilde{\epsilon}, \quad v^2 \equiv \frac{GM_{\text{vir}}}{r_{\text{vir}}} \tilde{v}^2, \quad (7.3.17)$$

such that $\tilde{\epsilon} = \tilde{\psi} - \tilde{v}^2/2$. The dimensionless DF then follows as

$$\tilde{f}_\chi(x, \tilde{v}) = \int_{x_{\text{min}}}^{\infty} \frac{dx'}{\sqrt{\tilde{\psi}(x) - \tilde{\psi}(x') - \frac{\tilde{v}^2}{2}}} \left(\frac{d\tilde{\psi}}{dx'} \right)^{-1} \left[\frac{d^2 \tilde{\rho}_\chi}{dx'^2} - \left(\frac{d\tilde{\psi}}{dx'} \right)^{-1} \frac{d^2 \tilde{\psi}}{dx'^2} \frac{d\tilde{\rho}_\chi}{dx'} \right], \quad (7.3.18)$$

with x_{min} defined analogously to r_{min} . The relation to f_χ is given by

$$f_\chi(r, v) = \frac{1}{8\pi^3 \sqrt{2G^3 r_{\text{vir}}^3 M_{\text{vir}}}} \frac{1}{g(c)} \tilde{f}_\chi(x, \tilde{v}). \quad (7.3.19)$$

In the following we mostly make use of DFs which are normalized by their DM density distribution and are defined via

$$P_r(v) d^3v \equiv \frac{f_\chi(r, v)}{\rho_\chi(r)} d^3v = \frac{1}{\sqrt{8\pi^2}} \frac{\tilde{f}_\chi(x, \tilde{v})}{\tilde{\rho}_\chi(x, c)} d^3\tilde{v} \equiv P_x(\tilde{v}) d^3\tilde{v}, \quad (7.3.20)$$

such that $4\pi \int_0^{v_{\text{esc}}} dv v^2 P_r(v) = 4\pi \int_0^{\tilde{v}_{\text{esc}}} d\tilde{v} \tilde{v}^2 P_x(\tilde{v}) = 1$, where $v_{\text{esc}} = \sqrt{2\Psi(r)}$ (and analogously \tilde{v}_{esc}) denotes the *escape velocity*, i. e. the maximal velocity a particle within a gravitationally bound system can possess.

The (dimensionless) gravitational potential arising from the DM halo can be computed analytically from Eq. 7.3.7, yielding [251]

$$\tilde{\psi}_\chi^{\text{NFW}}(x) = \frac{\log(1+cx)}{c^3 g_{\text{NFW}}(c)x}, \quad (7.3.21)$$

$$\tilde{\psi}_\chi^{\text{Ein}}(x) = \frac{1}{x} \frac{\Gamma\left(\frac{3}{\gamma}\right) - \Gamma\left(\frac{3}{\gamma}, \frac{2}{\gamma}(cx)^\gamma\right)}{\Gamma\left(\frac{3}{\gamma}\right) - \Gamma\left(\frac{3}{\gamma}, \frac{2}{\gamma}c^\gamma\right)} + c \left(\frac{2}{\gamma}\right)^{1/\gamma} \frac{\Gamma\left(\frac{2}{\gamma}, \frac{2}{\gamma}(cx)^\gamma\right)}{\Gamma\left(\frac{3}{\gamma}\right) - \Gamma\left(\frac{3}{\gamma}, \frac{2}{\gamma}c^\gamma\right)}, \quad (7.3.22)$$

for the two different density profiles. In the case of dSphs, the gravitational contribution from baryonic matter can be neglected due to the dominance of DM in the dwarf galaxies under consideration [264, 265]. In the GC, however, baryonic matter plays a significant role and its influence on the overall gravitational potential must be considered. We will only model the baryonic bulge and the stellar disk in the following, since they give the largest contributions. In order to apply Eddington inversion, the gravitational potential of the baryons must also be spherically symmetric, which is certainly not the case. However, following Ref. [251], we can approximate the baryonic potentials using symmetrized models which enclose the same mass as the actual profiles. They read

$$\tilde{\psi}_{\text{bulge}}(x) = \frac{M_{\text{bulge}}}{M_{\text{vir}}} \frac{1}{x + \frac{c_0}{r_{\text{vir}}}}, \quad \tilde{\psi}_{\text{disk}}(x) = \frac{M_{\text{disk}}}{M_{\text{vir}}} \frac{1 - \exp\left[-\frac{r_{\text{vir}}}{b_{\text{disk}}} x\right]}{x}, \quad (7.3.23)$$

where $M_{\text{bulge}} = 1.5 \times 10^{10} M_{\odot}$ and $M_{\text{disk}} = 5 \times 10^{10} M_{\odot}$ denote the bulge and disk masses, respectively, whereas $b_{\text{disk}} = 4 \text{ kpc}$ and $c_0 = 0.6 \text{ kpc}$ are model parameters encoding the spatial extent of these objects.

7.3.2 Generalized J -factors

After having established a technique to compute the DFs f_{χ} , we will now determine the generalized J -factors as given in Eq. 7.3.5

$$J_{\text{ann},l}^{(\alpha)}(\xi) = \int_{\Delta\Omega} d\Omega \int_0^{\infty} d\psi \int d^3v_1 f_{\chi}(r(\psi, \Omega), \mathbf{v}_1) \int d^3v_2 f_{\chi}(r(\psi, \Omega), \mathbf{v}_2) v_{\text{rel}}^{2l} S_{\text{ann},l}(\zeta, \xi).$$

It is convenient to start with the velocity integrals in order to reduce complexity. Due to the spherical symmetry of the system we can perform three out of the six integrals trivially $d^3v_1 d^3v_2 = 4\pi v_1^2 dv_1 4\pi v_2^2 dv_2 \frac{1}{2} d\cos\phi$, where ϕ denotes the angle between \mathbf{v}_1 and \mathbf{v}_2 . In order to carry out the remaining integrals, we perform a coordinate transformation $\{v_1, v_2, \cos\phi\} \rightarrow \{v_{\text{rel}}, v_{\text{cm}}, z\}$, where $v_{\text{rel}} = |\mathbf{v}_1 - \mathbf{v}_2|$ denotes the relative velocity as usual, $v_{\text{cm}} = |\mathbf{v}_1 + \mathbf{v}_2|/2$ is the COM velocity and $z = \cos\theta$, with θ being the angle between \mathbf{v}_{cm} and \mathbf{v}_{rel} . We find $\mathbf{v}_{1,2} = \mathbf{v}_{\text{cm}} \pm \mathbf{v}_{\text{rel}}/2$, such that

$$v_{1,2} = \sqrt{v_{\text{cm}}^2 + \frac{v_{\text{rel}}^2}{4} \pm v_{\text{cm}} v_{\text{rel}} z}, \quad \cos\phi = \frac{v_{\text{cm}}^2 - \frac{v_{\text{rel}}^2}{4}}{\sqrt{v_{\text{cm}}^2 + \frac{v_{\text{rel}}^2}{4} + v_{\text{cm}} v_{\text{rel}} z} \sqrt{v_{\text{cm}}^2 + \frac{v_{\text{rel}}^2}{4} - v_{\text{cm}} v_{\text{rel}} z}}, \quad (7.3.24)$$

with $|J| = v_{\text{cm}}^2 v_{\text{rel}}^2 / (v_1^2 v_2^2)$ the Jacobian of the transformation. Therefore, we can identify $8\pi^2 v_1^2 v_2^2 dv_1 dv_2 d\cos\phi = 8\pi^2 v_{\text{cm}}^2 v_{\text{rel}}^2 dv_{\text{cm}} dv_{\text{rel}} dz$. The limits $0 \leq v_{1,2} < v_{\text{esc}}$ translate to $v_{\text{cm}} \leq v_{\text{esc}}$, $v_{\text{rel}} \leq 2v_{\text{esc}}$ and $|z| \leq z_0$ with $z_0 \equiv (v_{\text{esc}}^2 - v_{\text{cm}}^2 - v_{\text{rel}}^2/4)/(v_{\text{cm}} v_{\text{rel}})$. Employing the symmetry $z \rightarrow -z$ to restrict our integration to $0 \leq z \leq z_0$, we need to consider that for $0 \leq v_{\text{cm}} < v_{\text{esc}} - v_{\text{rel}}/2$, z would exceed 1, which is why we split up the integral and use $0 \leq z < 1$ in this regime. Moreover, for $v_{\text{cm}} > \sqrt{v_{\text{esc}}^2 - v_{\text{rel}}^2/4}$ we would obtain $z < 0$, such that we use this as an upper bound for v_{cm} instead. In the new

coordinates, we can write Eq. 7.3.5 as

$$J_{\text{ann},l}^{(\alpha)}(\xi) = \int_{\Delta\Omega} d\Omega \int_0^\infty d\psi \rho_\chi(x)^2 \Sigma^{-2l} \int_0^{2\tilde{v}_{\text{esc}}} d\tilde{v}_{\text{rel}} P_{x,\text{rel}}(\tilde{v}_{\text{rel}}) \tilde{v}_{\text{rel}}^{2l} S_{\text{ann},l}(\Sigma\alpha/\tilde{v}_{\text{rel}}, \xi), \quad (7.3.25)$$

where we switched to a dimensionless coordinate representation and introduced a unit conversion constant $\Sigma \equiv c_\gamma \sqrt{r_{\text{vir}}/(GM_{\text{vir}})}$ with c_γ the speed of light.⁶⁰ The integrals over \tilde{v}_{cm} and z have been absorbed in the definition of

$$P_{x,\text{rel}}(\tilde{v}_{\text{rel}}) \equiv \frac{2\tilde{v}_{\text{rel}}^2}{\pi^2 \tilde{\rho}_\chi(x)^2} \left\{ \int_0^{\tilde{v}_{\text{esc}} - \frac{\tilde{v}_{\text{rel}}}{2}} d\tilde{v}_{\text{cm}} \tilde{v}_{\text{cm}}^2 \int_0^1 dz + \int_{\tilde{v}_{\text{esc}} - \frac{\tilde{v}_{\text{rel}}}{2}}^{\sqrt{v_{\text{esc}}^2 - \frac{\tilde{v}_{\text{rel}}^2}{4}}} d\tilde{v}_{\text{cm}} \tilde{v}_{\text{cm}}^2 \int_0^{z_0} dz \right\} \\ \tilde{f}_\chi \left(x, \sqrt{\tilde{v}_{\text{cm}}^2 + \tilde{v}_{\text{rel}}^2/4 + \tilde{v}_{\text{cm}}\tilde{v}_{\text{rel}}z} \right) \tilde{f}_\chi \left(x, \sqrt{\tilde{v}_{\text{cm}}^2 + \tilde{v}_{\text{rel}}^2/4 - \tilde{v}_{\text{cm}}\tilde{v}_{\text{rel}}z} \right). \quad (7.3.26)$$

In slight abuse of notation, we further define a velocity averaged SE factor

$$\left\langle S_{\text{ann},l}^{(\alpha)} \right\rangle (x; \xi) \equiv \Sigma^{-2l} \int_0^{2\tilde{v}_{\text{esc}}} d\tilde{v}_{\text{rel}} P_{x,\text{rel}}(\tilde{v}_{\text{rel}}) \tilde{v}_{\text{rel}}^{2l} S_{\text{ann},l}^{(l)}(\Sigma\alpha/\tilde{v}_{\text{rel}}, \xi), \quad (7.3.27)$$

which approaches 1 for the s-wave contribution of a heavy mediator (i. e. no SE). The generalized J -factors for annihilation can then be written as

$$J_{\text{ann},l}^{(\alpha)}(\xi) = \int_{\Delta\Omega} d\Omega \int_0^\infty d\psi \rho_\chi(x(\psi, \Omega))^2 \left\langle S_{\text{ann},l}^{(\alpha)} \right\rangle (x(\psi, \Omega); \xi), \quad (7.3.28)$$

and analogously for $J_{\text{BSF}}^{(\alpha)}(\xi)$.

We are now left with an integration over the field of view. Regarding dSphs, the solid angle observed by telescopes is usually large enough to cover the entire DM halo and the distance between the galaxy and us is much larger than its extent, i. e. $D \gg r_{\text{vir}}$. This enables us to substitute the integration over the cone representing the field of view by a sphere centered around the galaxy, i. e. $\int d\Omega \int d\psi \rightarrow 4\pi/D^2 \int r^2 dr$. The dSphs considered in the subsequent computation are given in Table 7.1. Assuming an underlying NFW profile, we calculated their generalized J -factors for annihilation and BSF and displayed them for an exemplary galaxy in Fig. 7.9 (top) for a scalar coupling $\alpha = 0.1$. We observe two limits, in which the J -factors are rendered constant. One occurs for $\xi \rightarrow 0$, for which the mediator mass becomes so large that the mediator potential becomes short-ranged and the SE becomes ineffective. In this limit we recover the J_0 -factor for s-wave annihilation (cf. Eq. 7.3.2) and its p-wave equivalent. The other plateau exists for $\xi \rightarrow \infty$ where we approach the Coulomb limit. In between these limits we observe a series of peaks inherited from the SE factors of a Yukawa potential

⁶⁰The c_γ is needed here because the term $v_{\text{rel}}^{2l} S_{\text{ann},l}(\alpha/v_{\text{rel}}, \xi)$ has been given in natural units.

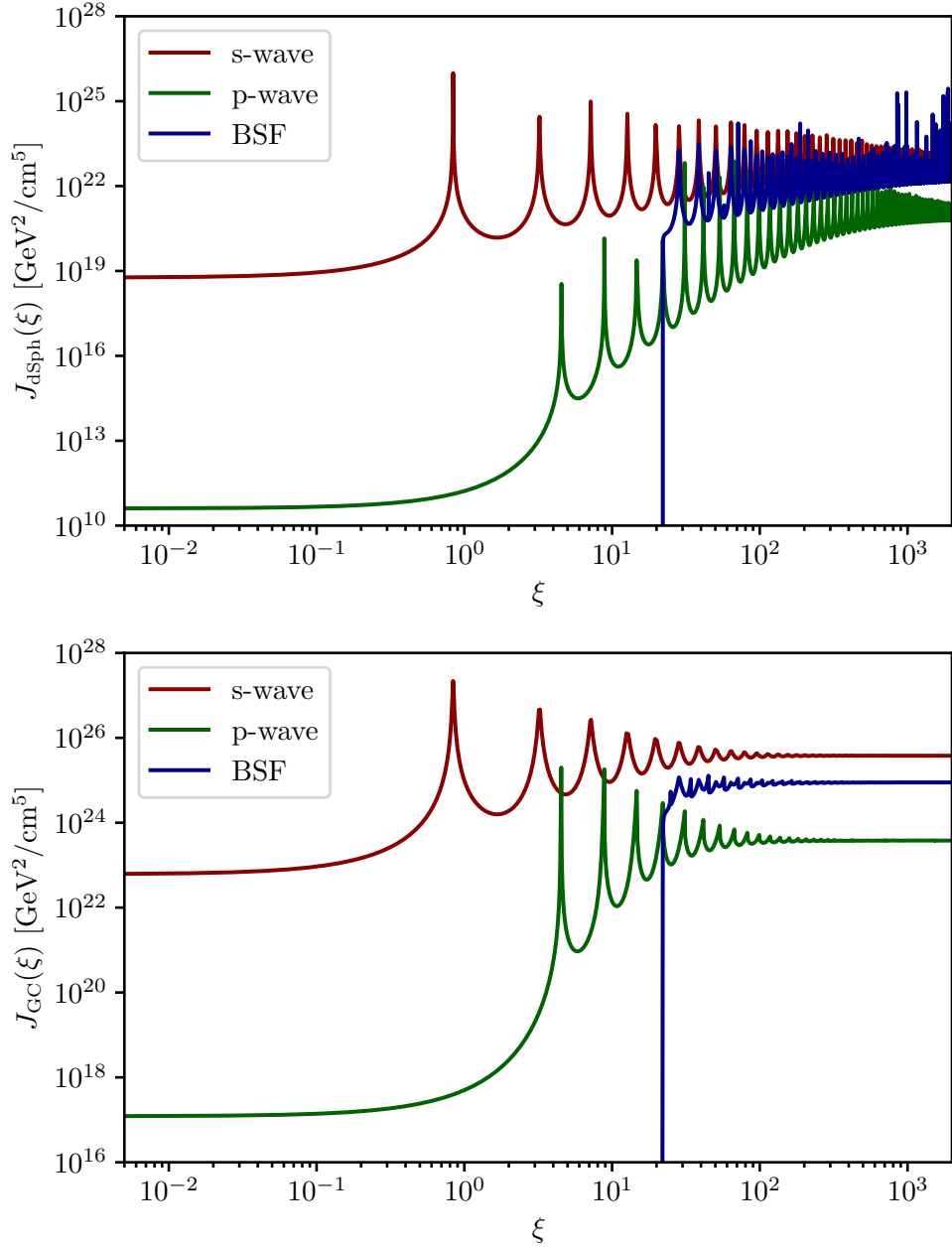


Figure 7.9: Generalized J -factors for the leading order s-wave (red) and p-wave (green) contributions as well as for BSF into the ground state with a scalar coupling $\alpha = 0.1$ as a function of ξ for the exemplary dSph *Draco* (top) and the GC (bottom), including a baryonic contribution to the gravitational potential for the latter. Adapted from Ref. [6].

as expected (cf. Section 7.2). The enhancement becomes very pronounced for large ξ and the natural hierarchy between s-wave and the p-wave contributions is significantly reduced. For $m_\phi \lesssim |E_{1S}|$, which happens around $\xi \approx 22$ for $\alpha = 0.1$, also BSF is allowed (cf. Eq. 5.1.29). For larger ξ , the BSF J -factor rises steeply and settles slightly below the s-wave and well above the p-wave contribution. This behaviour has already been anticipated from Fig. 7.8. We would like to remind the reader at this point, that due to the different behaviour of the velocity-independent factors σ_l and σ_{BSF}^0 on the masses and couplings, the J -factors alone are not sufficient to assess the relative importance of the annihilation and BSF contributions to the expected DM flux (cf. Eq. 7.3.6).

For the GC, the simplification on calculating the generalized J -factors as done for the dSphs is not possible due to $D \ll r_{\text{vir}}$. We consider in the following a region of interest of $l, b \in [-6^\circ, 6^\circ]$ motivated by the sensitivity study performed by the CTA collaboration [263]. The generalized J -factors for the GC are presented in Fig. 7.9 (bottom) for the same $\alpha = 0.1$, where we employed an Einasto profile including the impact of baryonic matter on the gravitational potential. The overall structure (as well as its origin) is comparable to the dSphs and we will only comment on the main differences. First, the absolute values of the J -factors are larger due to the higher concentration of DM in the GC and thus a much larger virial DM mass. Second, the resonance structure is more washed out due to the overall higher average velocities in comparison with dSphs (see again Fig. 7.8).

7.3.3 The photon spectrum

We define the photon spectrum dN_γ/dE_γ as the number of photons N_γ which are produced by annihilating or decaying DM per photon energy E_γ . In our case, we will deal with annihilating DM producing a pair of mediators $\bar{\chi} + \chi \rightarrow 2\phi$ at first. The mediators eventually decay into pairs of SM particles $\phi \rightarrow \bar{f}f$, which undergo further decay or hadronization processes, ultimately leaving only particles stable over astrophysical distances (e. g. photons) in the resulting spectrum. Since the decay of ϕ is mediated through mixing with the SM Higgs boson, the mediator inherits all kinematically allowed Higgs decay modes leaving us with a plethora of possible SM final states. By looking at

$$\frac{dN_\gamma}{dE_\gamma} = \sum_f \mathcal{B}_f \frac{dN_\gamma^{(f)}}{dE_\gamma}, \quad (7.3.29)$$

we can see that essentially two tasks have to be performed: 1) Determining the relevant branching ratios $\mathcal{B}_f \equiv \text{BR}(\phi \rightarrow \bar{f}f)$ of the mediator decaying into SM final states and 2) calculating the photon spectrum produced by a given SM final state while taking into account the large boosts originating from the mediator decays in the galactic rest frame. For the latter we will in the following consider two mass regimes of the mediator, namely $m_\phi \geq 10 \text{ GeV}$, denoted as *high mass range* and $2m_{\pi^0} \leq m_\phi \leq 1 \text{ GeV}$, which we label the *low mass range*). The reasons for this splitting and the avoidance for masses in between are explained below.

1) Branching ratios for $\phi \rightarrow \bar{f} + f$

After EWSB the Lagrangian containing couplings and mass terms of the physical Higgs field h and mediator ϕ reads (cf. Eqs. 7.1.1 and 7.1.2)

$$\mathcal{L} \supset -\frac{1}{2}m_\phi^2\phi^2 - \mu_{\phi h}v\phi h - \frac{1}{2}m_h^2h^2 - \frac{1}{2}\mu_{\phi h}\phi h^2 - \frac{m_h^2}{2v}h^3 - \frac{m_h^2}{8v^2}h^4, \quad (7.3.30)$$

where we have neglected the quartic couplings $\lambda_{\phi h}$ and λ_ϕ . The vev of the Higgs field is given by $v^2 = -\mu^2/\lambda$ as usual and the Higgs mass is consistently defined as $m_h^2 \equiv 2\lambda v^2$. After rotating into the mass eigenbasis $\phi \rightarrow \cos\delta\phi' - \sin\delta h'$, $h \rightarrow \sin\delta\phi' + \cos\delta h'$ and expanding around $\sin\delta$, we obtain the Lagrangian

$$\begin{aligned} \mathcal{L} \supset & -\frac{1}{2}m_\phi^2\phi'^2 - \frac{1}{2}m_h^2h'^2 - \frac{m_h^2}{2v}h'^3 - \frac{m_h^2}{8v^2}h'^4 \\ & + \left(-\frac{m_h^2}{2v^2}\phi'h'^3 - \frac{2m_h^2 + m_\phi^2}{2v}\phi'h'^2 \right) \sin\delta + \mathcal{O}(\sin^2\delta), \end{aligned} \quad (7.3.31)$$

where fields that correspond to mass eigenstates are highlighted here by $'$ for illustration purposes. This indication is dropped in the following. We observe, that if we choose a very small mixing angle δ , which is connected to the trilinear coupling via

$$\sin\delta \approx \frac{\mu_{\phi h}v}{|m_h^2 - m_\phi^2|}, \quad (7.3.32)$$

we can neglect the corrections to the mediator and Higgs masses as well as the Higgs self-interactions because they only arise at $\mathcal{O}(\sin^2\delta)$. However, we do obtain novel interactions between the mediator and the Higgs boson which are only suppressed by $\sin\delta$ and can give rise to $\phi \rightarrow hh$ and $\phi \rightarrow hhh$ decay channels if kinematically allowed. Likewise, the mediator will inherit all Higgs couplings to SM fermions and bosons, equally suppressed by a factor of $\sin\delta$ at leading order. Therefore, its decay rates will mimic the decay rates of a Higgs boson with equal mass and the branching ratios \mathcal{B}_f will be largely independent of the mixing angle. Moreover, since also for small mixing angles the mediator decays instantly on astrophysical scales, its absolute value is irrelevant for indirect detection.

Leading order approximations of the decay rates of a scalar SM Higgs boson with variable masses above $\gtrsim 2\text{ GeV}$ are taken from Ref. [266], where we have included the running of the masses and couplings through Ref. [267].⁶¹ Below the kinematic threshold of $\phi \rightarrow hh$, the branching ratios \mathcal{B}_f of the mediator will be equivalent to the branching ratios of a Higgs boson with equal mass. For $m_\phi > 2m_h$ and $m_\phi > 3m_h$, respectively, decay channels into 2 and 3 Higgs bosons open, but only the $\phi \rightarrow hh$ contribution changes the branching ratios of the mediator enough within this regime (it actually

⁶¹Older computations from an era where the Higgs mass was still unknown have been performed in e. g. Refs. [268, 269]. For an in-depth analysis and numerical results on each channel, the reader is directed to the combined studies of the *Higgs Cross Section Working Group*, exemplarily stating Refs. [270, 271] and references therein.

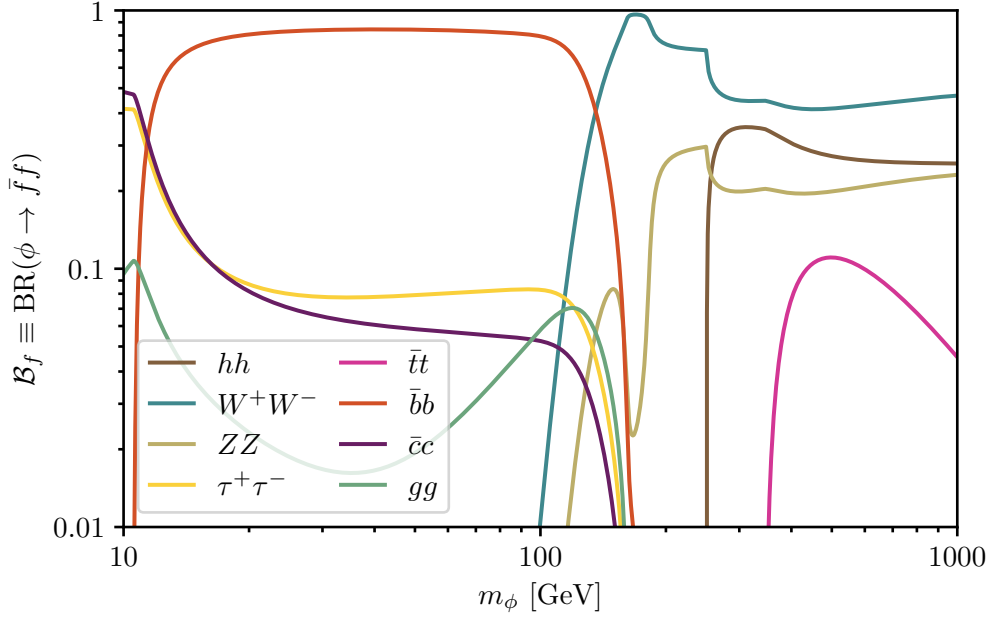


Figure 7.10: Branching ratios of the mediator ϕ decaying into SM particles in the high mediator mass range (see text). Displayed are all channels which contribute at least 1% to the total decay width in the regime of interest. Below mediator masses of $m_\phi < 2m_h$, the branching ratios of the mediator are equivalent to the ones of a Higgs boson with equal mass. Adapted from Ref. [6].

becomes comparable to the W and Z contributions) to take it into account. Its decay rate is given by

$$\Gamma_{\phi \rightarrow hh} = \frac{(v^2 + 2m_h^2)^2}{32\pi m_\phi v^2} \sqrt{1 - \frac{4m_h^2}{m_\phi^2}} \sin^2 \delta. \quad (7.3.33)$$

We display the branching ratios of all relevant channels contributing more than 1% to the total decay rate in Fig. 7.10 for a mediator mass range between 10 – 1000 GeV. In our analysis of the high mediator mass range we consider all of the depicted channels, namely $\phi \rightarrow \{hh, W^+W^-, ZZ, gg, \bar{t}t, \bar{b}b, \bar{c}c, \tau^+\tau^-\}$.

For quark and gluon final states, all methods outlined above to calculate the decay rates break down close to the confinement scale. Hence, in the low mediator mass range $m_\phi \lesssim 1$ GeV we employ the branching ratios into hadrons derived in Ref. [272]. Within this regime, we notice that below the kaon threshold around 1 GeV, most mediators ($\gtrsim 80\%$) will decay into pairs of pions with minor contributions from the muon, electron and photon decay channels. Since $\text{BR}(\pi^0 \rightarrow 2\gamma) \approx 99\%$, a large fraction of the energy in this mass range goes directly to hard gamma-rays. Therefore, it is sufficient to solely focus on the π^0 decay channel to derive limits and prospects.

2) Cascade annihilations

The photon spectrum $dN_\gamma^{(f)}/dE_\gamma$ of DM annihilation through a single mediator decay channel can be characterized by a two step process: 1) DM annihilation into two mediator particles $\bar{\chi} + \chi \rightarrow \phi + \phi$ and 2) the decay of each mediator into SM particles which in turn cascade into N photons and other stable particles $\phi \rightarrow f + \bar{f} \rightarrow \dots \rightarrow N \gamma + X$. The quantity $N_\gamma^{(f)}(E_\gamma)$ in this context is then defined as the average number of photons with an energy E_γ produced per DM annihilation process.

For mediator masses above a few GeV (i. e. well above the QCD confinement scale), the second process can and has already been simulated utilizing event generators for high-energy physics collisions like Pythia [273] or Herwig [274]. In fact, simulated data on photon spectra for DM annihilations into all relevant SM final states has been published by several groups including Refs. [202, 275] as well as Ref. [79], which we will use in the following. This public data source provides us with $dN_\gamma^{(f)}/d(\log_{10} x)$ as a function of an annihilating DM mass $m_{\text{DM}} = \sqrt{s}/2$ taken to be half the COM energy, as well as the energy of the photons produced in the COM frame of the annihilating system denoted by E_γ and parametrized as $x \equiv E_\gamma/m_{\text{DM}}$. In our case, χ does not annihilate directly to SM particles but through a one-step cascade producing mediator particles. Therefore, the data on $dN_\gamma^{(f)}/d(\log_{10} x_0)$ refers here to the number of photons produced for a decaying mediator particle in the rest frame of the mediator. The COM energy is then just $\sqrt{s} = m_\phi$ such that $m_{\text{DM}} \equiv m_\phi/2$ and $x_0 \equiv 2E_0/m_\phi$, where the index 0 emphasizes that the corresponding quantity is in the mediator rest frame. Overall, a mediator mass range of $m_\phi \in [10, 2 \times 10^5]$ GeV is covered by the data.

We are then left with translating the photon spectra of Ref. [79], given in the rest frame of the mediator, into the galactic rest frame, which is equivalent to the COM frame of the annihilating DM particles. Since the scalar mediator decays isotropically, the spectrum in the COM frame is given by [276]

$$\frac{dN_\gamma^{(f)}}{dE_\gamma} = \int_{-1}^1 d\cos\theta \int_0^{m_\phi/2} dE_0 \frac{dN_\gamma^{(f)}}{dE_0} \delta(E_\gamma - E_\gamma^*(E_0)), \quad (7.3.34)$$

with $E_\gamma^*(E_0)$ the Lorentz boost constraint which we will determine in the following. Assuming χ to be non-relativistic, the energy of the mediator in the COM frame is $E_\phi^* = E_\chi^* \approx m_\chi$ with E_χ^* the energy of the annihilating DM particles. Starting in turn from the energy of the mediator in its rest frame E_ϕ , a boost to the COM frame yields $E_\phi^* = \gamma(E_\phi - \mathbf{v} \cdot \mathbf{k}) = \gamma m_\phi$ since $\mathbf{k} = 0$ and $E_\phi = m_\phi$. Equating these two formulas leaves us with a boost factor of $\gamma = 1/\epsilon_\phi$ or $v = \sqrt{1 - \epsilon_\phi^2}$, respectively, where we defined $\epsilon_\phi \equiv m_\phi/m_\chi$. The boost of the photon energy to the COM frame is then given by $E_\gamma^*(E_0) = \gamma(E_0 + \mathbf{v} \cdot \mathbf{k}_0) = E_0/\epsilon_\phi \left(1 + \sqrt{1 - \epsilon_\phi^2} \cos\theta\right)$, where $|\mathbf{k}_0| = E_0$ and θ denotes the angle between \mathbf{v} and \mathbf{k}_0 . Redefining $x \equiv E_\gamma/m_\chi$, we can write Eq. 7.3.34 as

$$\frac{dN_\gamma^{(f)}}{dx} = 2 \int_{-1}^1 d\cos\theta \int_0^1 dx_0 \delta\left(2x - x_0 \left(1 + \sqrt{1 - \epsilon_\phi^2} \cos\theta\right)\right) \frac{dN_\gamma^{(f)}}{dx_0}, \quad (7.3.35)$$

which leaves us with

$$\frac{dN_\gamma}{dx} = 2 \int_{t_{\min}}^{t_{\max}} \frac{dx_0}{x_0 \sqrt{1 - \epsilon_\phi^2}} \frac{dN_\gamma}{dx_0}, \quad (7.3.36)$$

where $t_{\max} = \min \left\{ 1, 2x/\epsilon_\phi^2 \left(1 + \sqrt{1 - \epsilon_\phi^2} \right) \right\}$ and $t_{\min} = 2x/\epsilon_\phi^2 \left(1 - \sqrt{1 - \epsilon_\phi^2} \right)$.

If $m_\phi \lesssim 10$ GeV, the approach of calculating photon spectra via event simulation from high-energy physics collisions breaks down due to large corrections from non-perturbative QCD effects. Attempts have been made to derive photon spectra for light vector mediators [277, 278], however, they are not applicable for a scalar ϕ . Therefore, we exclude the range $1 \text{ GeV} \leq m_\phi \leq 10 \text{ GeV}$ from our subsequent analysis. In contrast, for the light mediator mass range $2m_{\pi^0} \leq m_\phi \leq 1 \text{ GeV}$, the prominent mediator decay into pions once again enables a computation of the photon spectrum.⁶² The process under consideration $\bar{\chi} + \chi \rightarrow 2\phi \rightarrow 4\pi^0 \rightarrow 8\gamma$ is a two-step cascade annihilation with a branching fraction of $\approx 50\%$. The photon spectrum in the rest frame of the pion is simply given by $dN_\gamma^{(\pi)}/dx_0 = 2\delta(x_0 - 1)$ with $x_0 \equiv 2E_0/m_{\pi^0}$. Defining further $x_1 \equiv 2E_1/m_\phi$ and $\epsilon_{\pi^0} = 2m_{\pi^0}/m_\phi$, we can use the methodology outlined in Ref. [280] to obtain (after two boosts) the photon spectrum in the COM frame of the annihilating DM

$$\frac{dN_\gamma^{(\pi)}}{dx} = 2 \int_{t_{2,\min}}^{t_{2,\max}} \frac{dx_1}{x_1 \sqrt{1 - \epsilon_\phi^2}} \left(2 \int_{t_{1,\min}}^{t_{1,\max}} \frac{dx_0}{x_0 \sqrt{1 - \epsilon_{\pi^0}^2}} \frac{dN_\gamma^{(\pi)}}{dx_0} \right), \quad (7.3.37)$$

with the integration limits

$$\begin{aligned} t_{1,\min} &= \frac{2x_1}{\epsilon_{\pi^0}^2} \left(1 - \sqrt{1 - \epsilon_{\pi^0}^2} \right), & t_{1,\max} &= \min \left\{ 1, \frac{2x_1}{\epsilon_{\pi^0}^2} \left(1 + \sqrt{1 - \epsilon_{\pi^0}^2} \right) \right\} \\ t_{2,\min} &= \frac{2x}{\epsilon_\phi^2} \left(1 - \sqrt{1 - \epsilon_\phi^2} \right), & t_{2,\max} &= \min \left\{ \frac{1}{2} \left(1 + \sqrt{1 - \epsilon_{\pi^0}^2} \right), \frac{2x}{\epsilon_\phi^2} \left(1 + \sqrt{1 - \epsilon_\phi^2} \right) \right\}. \end{aligned} \quad (7.3.38)$$

Performing the integrations over x_0 and x_1 , we are left with an analytic result

$$\frac{dN_\gamma}{dx} = \frac{8}{\sqrt{1 - \epsilon_{\pi^0}^2} \sqrt{1 - \epsilon_\phi^2}} \begin{cases} \ln \left(\frac{x}{K_+^-} \right) & K_+^- \leq x < \min\{K_+^+, K_-^-\} \\ \ln \left(\frac{\min\{K_+^+, K_-^-\}}{K_+^-} \right) & \min\{K_+^+, K_-^-\} \leq x < \max\{K_+^+, K_-^-\} \\ \ln \left(\frac{K_+^+}{x} \right) & \max\{K_+^+, K_-^-\} \leq x < K_+^+ \end{cases} \quad (7.3.39)$$

⁶²Below the pion threshold, mediators will decay predominantly into light lepton pairs. The most stringent bounds in this regime come from the positron flux [83], which has been interpreted in the context of DM e. g. in Ref. [279]. However, since we are predominantly interested in the gamma-ray flux, we will not include these final states in the following. Moreover, in this mediator mass regime it will also become challenging to avoid BBN and direct detection constraints, as we will see in Section 7.4.

and 0 elsewhere, where we have defined for convenience

$$K_{\mp}^{\pm} \equiv \frac{\left(1 \pm \sqrt{1 - \epsilon_{\pi^0}^2}\right) \epsilon_{\phi}^2}{4 \left(1 \mp \sqrt{1 - \epsilon_{\phi}^2}\right)}. \quad (7.3.40)$$

The photon spectrum of DM annihilation through pion decay is very hard. Therefore, at sufficiently high energies a dedicated analysis searching for discrete spectral features may boost the sensitivity to astrophysical observation considerably [281, 282]. However, this will be not pursued further here and is left for future work.

7.3.4 Indirect detection bounds and prospects

We have now all ingredients to calculate our model predictions of the DM photon flux and compare them with observations. To achieve this, we will in the following match bounds from the Fermi-LAT collaboration as well as prospects for the CTA. Additionally, we will consider limits from CMB anisotropies derived by the Planck collaboration.

Fermi-LAT limits

The Fermi collaboration has published a statistical analysis of a variety of different dSphs on the basis of 6 years of Fermi-LAT data [89]. They evaluated the significance of a DM hypothesis using the following *test statistics* (TS)

$$\text{TS} = -2 \log \left(\frac{\mathcal{L}(\boldsymbol{\mu}_0, \hat{\boldsymbol{\theta}} | \mathcal{D})}{\mathcal{L}(\hat{\boldsymbol{\mu}}, \hat{\boldsymbol{\theta}} | \mathcal{D})} \right), \quad (7.3.41)$$

which is based on a negative log-likelihood ratio on a data set \mathcal{D} , where \mathcal{L} denotes the likelihood function, either of an individual galaxy or as a joint likelihood of all dSphs under consideration. The $\boldsymbol{\mu}_0$ are the model parameters of the null hypothesis (no DM) and $\hat{\boldsymbol{\mu}}, \hat{\boldsymbol{\theta}}$ represent, respectively, the best fit values of $\boldsymbol{\mu}, \boldsymbol{\theta}$, the model and nuisance parameters under the DM hypothesis.⁶³ In order to derive upper limits on the DM cross section as a function of the DM mass, the collaboration performed a combined global fit of 15 dSphs for a few selected channels into pure SM final states, which is however not applicable to our situation. Fortunately, they also published the energy-bin by energy-bin likelihood as a function of the integrated photon flux $\langle \Phi_{\gamma} \rangle$ (as the only model parameter) for each dSph individually [284]. More concretely, they provided the *delta-log-likelihood ratio* (see also Refs. [285, 286])

$$\Delta_{ij}(\langle \Phi_{\gamma} \rangle_i) = \log \left(\frac{\mathcal{L}(\langle \Phi_{\gamma} \rangle, \hat{\boldsymbol{\theta}}_j | \mathcal{D}_{ij})}{\mathcal{L}(\langle \Phi_{\gamma} \rangle, \hat{\boldsymbol{\theta}}_j | \mathcal{D}_{ij})} \right), \quad (7.3.42)$$

⁶³Note that this definition of the TS departs from the conventional one by fixing both $\hat{\boldsymbol{\theta}}$ to the best-fit values of the DM hypothesis, where the signal is modelled by a $d\Phi_{\gamma}/dE_{\gamma} = -2$ power law (see Ref. [283]).

for each dSph j and energy bin i . We can derive our indirect detection limits easily from this data, by demanding that

$$\sum_{i,j} \Delta_{ij} \langle \Phi_\gamma \rangle_i + \frac{2.71}{2} > 0, \quad (7.3.43)$$

with $j = 1, \dots, 4$ (for our classical dwarfs Coma Berenices, Ursa Minor, Draco, and Serguee 1), where the maximally allowed deviation of $2.71/2$ from the extremum corresponds to a 95% CL with the factor of $1/2$ accounting for a one-sided statistical test [286, 287]. For this purpose, we integrate Eq. 7.3.6 using the same binning as in the supplementary material given, defining

$$\langle \Phi_\gamma \rangle_i \equiv \int_{E_{\min,i}}^{E_{\max,i}} dE_\gamma E_\gamma \frac{d\Phi_\gamma}{dE_\gamma}, \quad \langle N_\gamma \rangle_i \equiv \sum_f \mathcal{B}_f \int_{E_{\min,i}}^{E_{\max,i}} dE_\gamma E_\gamma \frac{dN_\gamma^{(f)}}{dE_\gamma}, \quad (7.3.44)$$

such that we can write

$$\langle \Phi_\gamma \rangle_i = \frac{1}{16\pi m_\chi^2} \left(\sigma_0 J_{\text{ann},0}^{(\alpha)}(\xi) + \sigma_1 J_{\text{ann},1}^{(\alpha)}(\xi) + \sigma_{\text{BSF}}^0 J_{\text{BSF}}^{(\alpha)}(\xi) \right) \langle N_\gamma \rangle_i, \quad (7.3.45)$$

and check the condition of Eq. 7.3.43 for each set of masses and couplings. For each dSph, the globally maximized nuisance parameters $\hat{\theta}_j$ used in the analysis of the Fermi collaboration, can be split up into best-fit parameters from the Fermi-LAT analysis $\hat{\alpha}_j$ and the corresponding J_0 -factors of the galaxy, where an NFW profile has been assumed. Uncertainties on the derived limits due to a varying J -factor by e.g. assuming a different density profile have been estimated by the collaboration to yield not more than $\sim 40\%$, mostly caused by a change in the relative importance of each dSph. We checked this for the case of generalized J -factors by recalculating them for an underlying Einasto profile and found a deviation of $\sim 30\%$. This difference is largely independent of the DM velocity, in fact, the velocity dependence changes the ratio of generalized J -factors considering an NFW and Einasto profile by $\lesssim 5\%$ for the highest ξ . As a comprehensive revision of the statistical analysis for our particular model is beyond the scope of this work, this statement reaffirms the robustness of the limits when considering non-perturbative effects. As a cross-check, we also derived limits on the perturbative cross section for the benchmark channels analyzed in Ref. [89], where we used our reduced set of dSphs as well as the J_0 -factors given by the collaboration. To accomplish this, we changed $\Delta_{ij} \langle \Phi_\gamma \rangle_i \rightarrow \Delta_{ij} \langle \sigma v_{\text{rel}} \rangle_0$ and equated the relation of Eq. 7.3.43. Good agreement with the official limits has been found.⁶⁴

Assuming that only one annihilation channel significantly contributes to the photon flux, we can employ the same approach to establish an upper limit (at 95% CL) on the individual perturbative cross section, incorporating non-perturbative effects. This

⁶⁴Note that an exact agreement cannot be expected since the statistical treatment for the energy binned data is simplified compared to the full method used by the collaboration. Moreover, we have included less dSphs.

involves considering all mediator decay channels along with the corresponding generalized J -factor. We have illustrated in Fig. 7.11 two scenarios of s-wave (top) and p-wave domination (bottom) as a function of the DM mass for a benchmark point with $m_\phi = 10 \text{ GeV}$ and $\alpha = 0.1$. It is evident that the constraint on the s-wave cross section is relatively modest when the SE is absent. It falls within a similar range as the limits for pure SM final states at the corresponding DM masses. The incorporation of the SE significantly tightens the constraints by several orders of magnitude. As expected, the most substantial impact is observed around the resonances of the J -factors, potentially lowering the limit to values even below $10^{-29} \text{ cm}^3/\text{s}$. For the p-wave case in the lower panel, the limits are notably weaker due to the velocity suppression of the annihilation rate. In the absence of SE, the limits are far from the values relevant for a thermal relic. Even with SE, only the parts resonantly enhanced around specific masses dip below $10^{-23} \text{ cm}^3/\text{s}$. The overall limit improves with higher masses since we are maintaining m_ϕ constant, leading to stronger SE as m_χ is increased.

Planck limits

Measurements of CMB properties can be quite constraining for DM models with late time annihilation. This is due to the fact that the CMB is susceptible to exotic energy injection during the cosmic dark ages (at redshifts of $z \approx 600 - 1000$). DM annihilations into SM particles around that time provide this additional energy injection into the *intergalactic medium* (IGM). The resulting increase of the residual ionization fraction will in turn broaden the last scattering surface and modify CMB anisotropies and polarization [288–290]. The Planck collaboration [8] has established the most rigorous constraints on non-standard energy injection. Under the assumption that the redshift dependence of the energy injection rate is solely governed by the variation in the DM density (implying a velocity-independent cross section) they have imposed an upper limit on

$$p_{\text{ann}} \equiv f_{\text{eff}} \frac{\langle \sigma v_{\text{rel}} \rangle}{m_\chi} \leq 3.5 \times 10^{-28} \frac{\text{cm}^3}{\text{GeV s}}, \quad (7.3.46)$$

with f_{eff} an efficiency factor controlling how much of the energy released into the visible sector due to, e. g. DM annihilation, is absorbed by the IGM.⁶⁵ Based on the findings in Refs. [292, 293], we will use in the following a conservative estimate of $f_{\text{eff}} \simeq 0.137$ for all annihilation channels. This yields a lower limit on

$$\langle \sigma v_{\text{rel}} \rangle < 2.5 \times 10^{-24} \frac{\text{cm}^3}{\text{s}} \left(\frac{m_\chi}{\text{TeV}} \right), \quad (7.3.47)$$

where $\langle \sigma v_{\text{rel}} \rangle$ is understood as the sum of contributions to the thermally averaged annihilation cross section which scale as v_{rel}^0 . By looking at Fig. 7.8, for typical DM velocities

⁶⁵The underlying assumption here is that the energy which is deposited into the IGM is proportional to the energy injected at the same redshift. In all generality, this may not be the case, since the absorption from the IGM can also happen at a much later time. To account for this, one would need to define a general function $f(z)$, which depends on the redshift as well as the underlying DM model. However, it has been shown in Ref. [291] that the impact on the CMB in contrast to employing a constant f_{eff} is negligible.

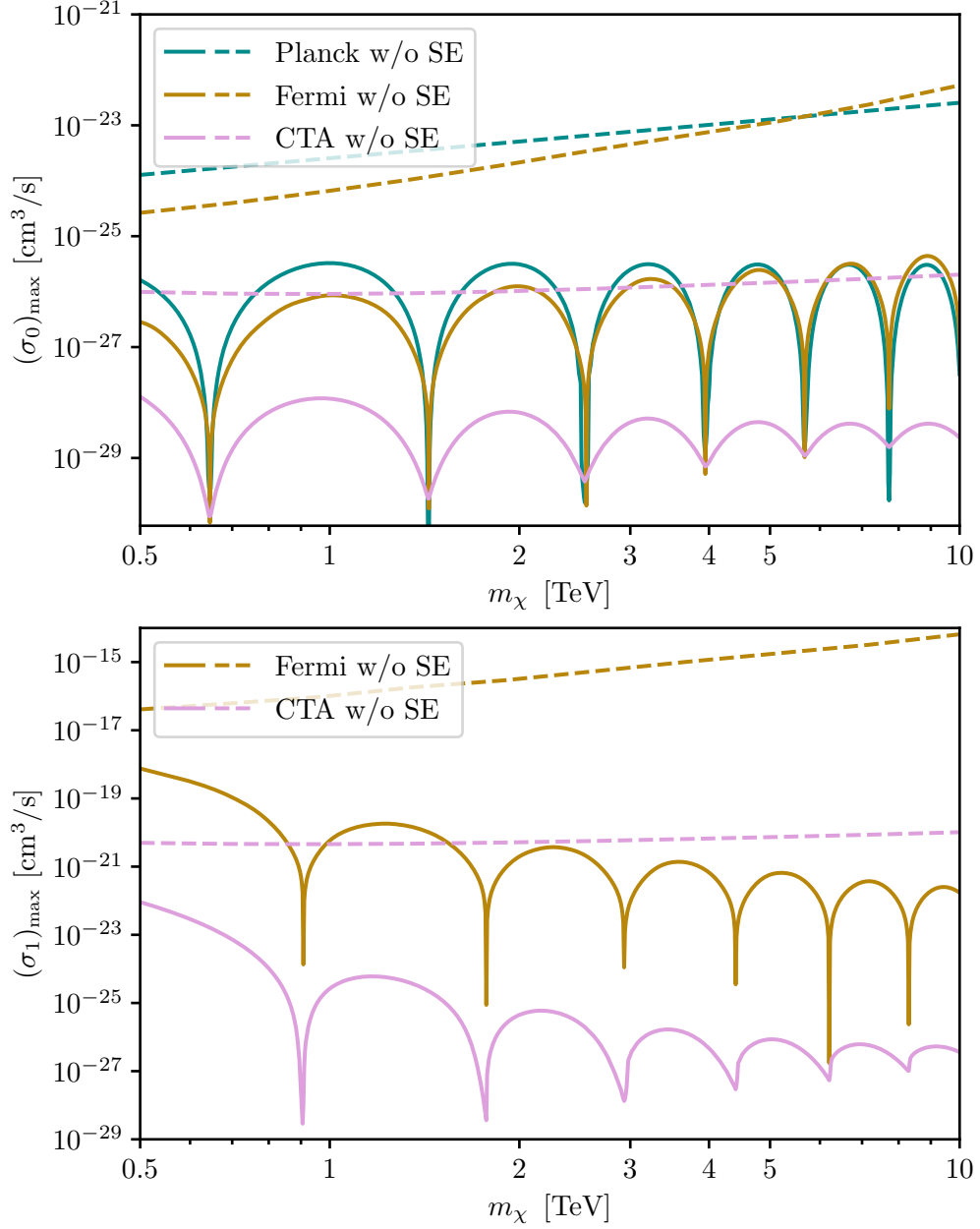


Figure 7.11: Indirect detection limits on the perturbative cross section in s-wave (top) and p-wave (bottom) dominated DM annihilation scenarios as a function of the DM mass m_χ for a benchmark point of $m_\phi = 10 \text{ GeV}$ and $\alpha = 0.1$. The turquoise lines represent current CMB limits based on Planck data (only for s-wave domination), the golden lines indicate limits from an analysis of Fermi-LAT data from dSphs, and the pink lines denote prospects for upcoming CTA measurements in the GC. Dotted lines depict the limits without accounting for SE, whereas solid lines incorporate SE into the analysis. Adapted from Ref. [6].

of $\mathcal{O}(10^{-8})$ we can see that this is the case in our model for the s-wave and BSF cross section, which both become constant in this regime due to a finite mediator mass. Note that this limit cannot be applied for p-wave annihilating DM due to its v_{rel}^2 scaling. However, p-wave contributions in this regime are highly suppressed and can be neglected.

The limits on the perturbative s-wave cross section have been displayed in Fig. 7.11 (left) for a representative set of parameters. The inclusion of the SE enhances the Planck limit on the cross section, resulting in an improvement of several orders of magnitude across the mass range. Notably, the Planck limit is relatively similar to the one derived from Fermi-LAT observations, and at high DM masses, Planck even outperforms the gamma-ray limits. This qualitative observation can be explained based on the scaling of the relevant rates with m_χ . The Fermi-LAT sensitivity is tied to the photon flux, scaling as $\langle\sigma v_{\text{rel}}\rangle\rho_\chi^2/m_\chi^2$, while the CMB is sensitive to the energy release rate, which scales as $m_\chi\langle\sigma v_{\text{rel}}\rangle\rho_\chi^2/m_\chi^2$. Consequently, the dependence on the DM mass is weaker in the CMB case.

CTA prospects

The *Cherenkov Telescope Array Consortium* has examined DM prospects for CTA observations of the GC [263]. Similar to the Fermi-LAT analysis, tabulated bin-by-bin likelihoods have been made publicly accessible [294]. These tables enable us the estimation of the anticipated upper limit on the perturbative DM annihilation cross section for any spectrum, analogous to the approach used for dSphs. The binned likelihood presented in the data is given in terms of the $(\text{TS})_i \equiv -2\Delta_i$, which has been constructed only slightly different compared to the Fermi-LAT analysis. It has been tabulated as a function of the energy flux $d\Phi_\gamma/dE_\gamma|_{E_\gamma=\bar{E}_i}$ evaluated at the mean energy \bar{E}_i of the corresponding bin. The potential upper limits on the perturbative cross section are also outlined in Fig. 7.11. As anticipated, the CTA is likely capable to meet or exceed both Fermi-LAT and Planck limits by orders of magnitude within the specified mass range.

Before moving on, we briefly address the influence of the halo profile on the limits and prospects we have derived from observations of the GC. Given that the matter content in the GC is dominated by baryons, the J -factor is not as constrained as for dSphs, resulting in a less robust interpretation of (prospective) observations. Specifically, cuspy profiles tend to predict higher fluxes than cored ones. The Einasto profile, adopted in this study with a parameter choice of $\gamma = 0.17$, falls between a cuspy and a cored profile. However, further investigation is warranted regarding the dependence of the prospects on this choice. To assess the impact of a more clearly cored profile, we adopt the suggestion of the CTA collaboration and examine an artificially cored Einasto profile [263]. In this scenario, the density remains constant in the inner part of the halo below 1 kpc. Since this profile precludes Eddington inversion as the derivatives of ρ_χ would vanish there, we employ an alternative method to estimate the effect on the velocity-dependent cross section. Specifically, we calculate the standard velocity-independent J_0 -factors for s-wave annihilations in both halos and assume that the ratio between the velocity-dependent J -factors remains consistent. Our analysis reveals that the cored J -factor is approximately 50% smaller, resulting in a weaker limit on the cross section by the same ratio. This

relatively small change in the J -factor, contrary to previous studies, has also been noted in Ref. [263]. This phenomenon can be attributed to the larger region of interest considered by the CTA analysis. To validate our approach, we conducted a similar analysis using an NFW profile, which permits the use of the Eddington inversion method. The computation of the ratio of velocity-dependent J -factors using this method revealed that the ratio between the Einasto and the NFW J -factors is largely velocity-independent and agrees to within 10% with the ratio estimated using the velocity-independent J_0 -factors. Therefore, we assert the robustness of our outlined method.⁶⁶

7.4 Complementary searches

In addition to indirect detection constraints, other experimental limitations may exist that could restrict our parameter space. In the following, we will explore those that seem particularly significant from a preliminary perspective and could supplement the constraints imposed by indirect detection. These include potential restrictions arising from direct detection, BBN, *electric dipole moments* (EDMs), and thermalization requirements.

7.4.1 Direct detection and BBN limits

Our model allows for elastic scattering between DM and SM particles due to the mixing of the mediator with the Higgs. Direct detection experiments [218–220] impose stringent constraints on the rates of these processes, which are controlled by the mixing angle δ . The scattering cross section for spin-independent interactions with a nucleon yields [243]

$$\sigma_{\text{SI}} = \frac{4\alpha\mu_{\chi N}^2 m_N^2 f_N^2}{v^2} \sin^2 \delta \cos^2 \delta \left(\frac{1}{m_\phi^2} - \frac{1}{m_h^2} \right)^2. \quad (7.4.1)$$

Here, m_N represents the nucleon mass, $\mu_{\chi N}$ stands for the reduced mass of the DM-nucleon system, and $f_N \approx 0.35$ denotes the effective coupling of the Higgs to the nucleon.⁶⁷ In the limit where direct detection constraints become relevant, i. e. $m_\phi \ll m_h$ and $m_\chi \gg m_N$, we can infer an upper limit on the mixing angle

$$(\sin \delta)_{\text{max}} \simeq \frac{m_\phi^2 v}{2 f_N m_N^2} \sqrt{\frac{\sigma_{\text{SI}}(m_\chi)}{\alpha}}. \quad (7.4.2)$$

At present, the most stringent upper bound on the spin-independent DM-nucleus scattering cross section comes from the LZ experiment [219]. Throughout this work we assume

⁶⁶It is worth noting that, besides the assumed DM density profiles, various other uncertain parameters can affect the statistical limits, including the signal morphology and additional information about correlations in the energy bins. However, addressing these factors would require a specialized statistical analysis, which is beyond the scope of this work.

⁶⁷Pseudo-scalar interactions with SM particles result in a momentum dependent direct detection cross section [295]. These interactions are constrained more loosely, allowing us to disregard processes involving g_5 for the subsequent discussion.

that $\sin \delta$ is sufficiently small to avoid conflict with the direct detection data. Since the exact value is inconsequential for indirect detection, direct detection constraints do not have any impact on the phenomenology discussed above.

Nevertheless, direct detection constraints can be combined with limits from BBN to rule out low-mass mediators [244]. To preserve the abundances of primordial elements, it is essential to guarantee that the mediators decay before the start of BBN (cf. Section 6.5). Therefore, we require that the lifetime of the mediator $\tau_\phi = 1/\Gamma_\phi$ is shorter than the age of the Universe at the onset of BBN, which we consider to be $T_{\text{BBN}} \sim 1 \text{ MeV}$. Employing Eq. 6.5.2, we can see that BBN sets a lower limit on $\sin \delta$, while direct detection establishes an upper limit, such that we can combine both arguments to exclude a range of mediator masses. Numerically, we observe that a kinematically allowed decay into muons is essential for ensuring a sufficiently short mediator lifetime. Consequently, masses of m_ϕ that slightly exceed $2m_\mu$ (and lower) are ruled out.

7.4.2 Electric dipole moments

The pseudo-scalar interaction between the mediator and the DM particle in Eq. 7.1.1 introduces CP violation in the dark sector. Through portal interactions, this CP violation can be transferred to the SM sector, which can induce EDMs [296–298]. In our model, the mixing with the Higgs boson does not generate a pseudo-scalar interaction between the dark scalar ϕ and the SM fermions at the leading order. Instead, only a scalar interaction of the form $\mathcal{L}_{\text{int}} \supset -\sin \delta \bar{f} f \phi$ is found. Consequently, there is no contribution to one-loop topologies. The initial contribution to the EDM of SM fermions can emerge at the two-loop level, where one scalar and one pseudo-scalar vertex, along with a DM fermion loop, are involved.

The electron EDM places the most stringent experimental bound with $|d_e| < 1.1 \times 10^{-29} \text{ cm e}$ [299]. We can estimate our two-loop contribution to it as

$$d_e \approx \frac{e}{(4\pi^2)^2} 4\pi \sqrt{\alpha \alpha_5} y_e^2 \sin^2 \delta \frac{1}{m_e} \times \left(1, \frac{m_e^2}{m_\phi^2}, \frac{m_e^2}{m_\chi^2} \right), \quad (7.4.3)$$

where m_e denotes the electron mass and y_e the electron Yukawa coupling. Possibly relevant combinations from the scales running in the loop, have been included through the very right term with the electron mass indicating the smallest scale. Even by considering the least suppressed contribution possible with the following values for the parameters involved, $m_e \simeq 0.5 \text{ MeV} \simeq 2 \times 10^{10} \text{ cm}^{-1}$, $y_e \simeq 2 \times 10^{-6}$, $\alpha = 0.1$, $\alpha_5/\alpha = 0.1$ and $\sin \delta = 10^{-2}$, we obtain $|d_e| \simeq 10^{-30} \text{ cm e}$, which falls slightly below the experimental limit. However, we want to make two remarks on this conservative estimate, reasoning that the actual electron EDM will be much smaller: 1) The values for the mixing angle employed in this estimation are considerably larger than those considered in our study. A more realistic estimate would suppress d_e by a factor of $\sim 10^{-4}$ or more. 2) The presence of heavy scales in the problem is anticipated to drive the EDM to much smaller values. Therefore, we conclude that the EDM bound from the electron is irrelevant for the parameter space of this model.

In the calculation of the EDM of the muon, a larger Yukawa coupling enters, which enhances the theoretical prediction by a factor of ~ 200 after compensating for the higher muon mass. However, this is not sufficient to counter the $\mathcal{O}(10^{10})$ weaker experimental constraint.

7.4.3 Thermalization of the dark sector

The calculation of the relic density performed in Section 7.2.3 assumes that the SM and the dark sector share a common temperature and that thermal contact is maintained during FO. Although a deviation from this assumption is not inherently problematic, a more sophisticated analysis of the FO process would be in order, and the accuracy of the relic density prediction will depend on the specifics of the thermal decoupling between the sectors. Hence, it is essential to verify the validity of our assumptions. To ensure an efficient thermal contact between the two sectors, we follow standard arguments in the literature, as outlined e. g. in Ref. [300].

Before EWSB, the predominant processes are $2 \rightarrow 2$ scatterings of the form $\phi H \leftrightarrow \phi H$ and $\phi\phi \leftrightarrow HH^\dagger$. Thermal contact is maintained, when these processes are efficient, i. e. the interaction rates surpass the expansion rate of the Universe. As usual, this can be rephrased as $\mathcal{C}_{2 \rightarrow 2} \geq 3Hn_\phi^{\text{eq}}$, where H is the Hubble rate during radiation domination (cf. Eq. 2.3.11), n_ϕ^{eq} denotes the equilibrium number density of the mediator, and $\mathcal{C}_{2 \rightarrow 2}$ represents the rate density (i. e. the integrated collision term without back-reaction as defined in Eq. 4.1.11). For a rough estimate, it suffices to consider the leading T dependence entering the BE. This is captured by $\mathcal{C}_{2 \rightarrow 2}^{\text{high-}T} \propto \lambda_{\phi h}^2 T^4 / (32\pi^2)$ at high temperatures. Further approximating $n_\phi^{\text{eq}} \approx T^3 / \pi^2$, we can estimate

$$\lambda_{\phi h} \gtrsim 12.6 g_{\text{eff}}^{1/4}(T) \sqrt{\frac{T}{M_{\text{Pl}}}}. \quad (7.4.4)$$

For $T \in [150, 1000]$ GeV, we find $\lambda_{\phi h} \gtrsim [10^{-7}, 5 \times 10^{-7}]$. In Fig. 7.12, we present limits on $\lambda_{\phi h}$ obtained from a more sophisticated analysis based on the full thermally averaged cross section of the processes $\phi H \leftrightarrow \phi H$ (left) and $\phi\phi \leftrightarrow HH^\dagger$ (right), which also accounts for the finite mass of the mediator. The values displayed have been calculated for the two most extreme benchmark points $m_\phi = 0.27$ GeV (green) and $m_\phi = 2$ TeV (orange), together with our approximation in Eq. 7.4.4 (blue). We can see that the elastic scattering $\phi H \leftrightarrow \phi H$ is more efficient. Across the range of scalar masses considered throughout our work, $\lambda_{\phi h} \simeq 10^{-6}$ is sufficient to maintain thermal contact.

At temperatures below the EWSB scale, the primary thermal connection between the SM and the dark sector is facilitated by the mixing between the Higgs and the mediator. In this scenario, the most relevant processes for establishing thermal contact involve $f\phi \leftrightarrow fV$ scattering processes, where f denotes an SM fermion and V is a gauge boson (see e. g. App. A.2 of Ref. [301] for a detailed discussion). The size of the mixing angle, needed to ensure thermal contact between the sectors as a function of the FO temperature T_{FO} , can be extracted from Fig. 2 of Ref. [301]. In our region of interest, e. g. $T_{\text{FO}} \gtrsim 25$ GeV, we find that $\sin \delta \gtrsim 10^{-6} - 10^{-7}$ is required to establish thermal

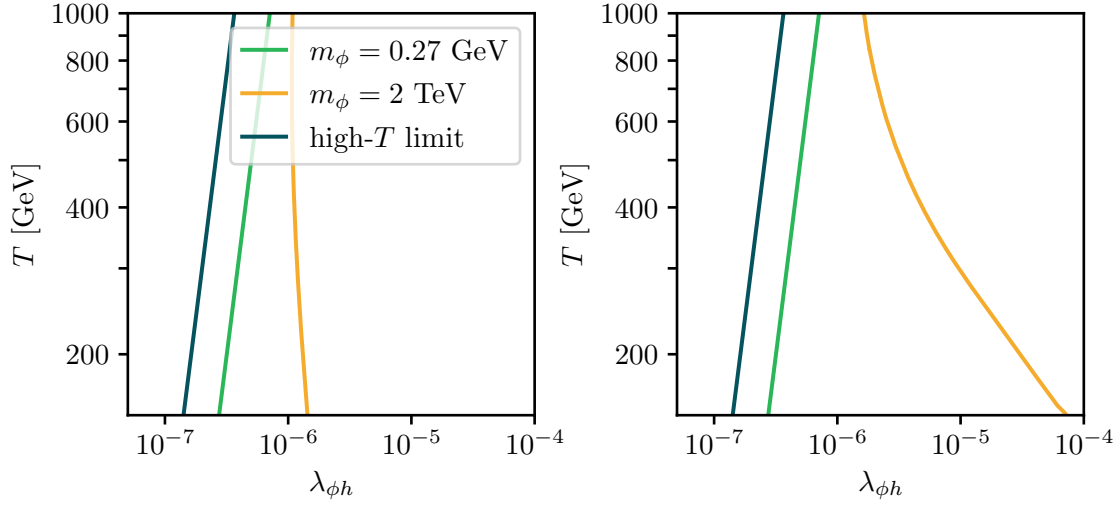


Figure 7.12: Thermalization limits on the quartic $\lambda_{\phi h}$ coupling using the condition $\mathcal{C}_{2 \rightarrow 2} = 3Hn_\phi^{\text{eq}}$ for the $2 \rightarrow 2$ processes $\phi H \leftrightarrow \phi H$ (left) and $\phi\phi \leftrightarrow HH^\dagger$ (right) at temperatures above EWSB. The green and orange curves (in both plots) fulfill this condition for the two most extreme values for the mediator mass m_ϕ employed in this context. The blue lines display the approximate result of Eq. 7.4.4. Adapted from Ref. [6].

contact. For most of the parameter space explored in this study, these values remain well below the experimental limits. Nevertheless, for very light scalars with $m_\phi \lesssim 500$ MeV, the constraints from direct detection become highly restrictive and start to rule out the mixing angles necessary to sustain thermal contact. This specific region, however, largely overlaps with the region excluded by the combined constraints from direct detection and BBN, so we will not display it separately.

7.5 The parameter space of thermal dark matter

One of our main interests in this work is to gain insight about the status of our indirect detection limits and prospects when compared to the theoretical predictions for thermally produced DM. Hence, we direct our focus to the parameter space of our model that enables a full production of the relic density through the FO mechanism. There are five free parameters which characterize our model: the DM and mediator masses (denoted as m_χ and m_ϕ), the scalar and pseudo-scalar interaction strengths in the dark sector (α and α_5), and the mixing angle between the mediator ϕ and the SM Higgs. Provided the mixing angle remains sufficiently small to evade constraints from direct detection and large enough not to trouble BBN, its precise value is irrelevant to phenomenology (cf. Section 7.4.1). This reduces the number of relevant parameters to four. The relic density, which is accurately measured at the percent level [8], enables a further reduction of free parameters by requiring the correct DM abundance in the early Universe after FO. We choose to fix α in this manner, allowing for the variation of the two masses and α_5 . With

only three parameters in play, we can illustrate slices through the parameter space for two of them by keeping the third fixed. Since the phenomenology is primarily influenced by the masses of the involved particles, our analysis considers m_χ and m_ϕ as variables, showcasing fixed ratios of α_5/α to explore this direction.

Figure 7.13 shows representative examples of slices through the cosmologically preferred parameter space. The analysis is confined to the region $0.5 \text{ TeV} \leq m_\chi \leq 10 \text{ TeV}$. We also require $m_\phi \lesssim \alpha m_\chi$ as an upper limit to ensure the applicability of the NREFT used in deriving the cross sections and non-perturbative effects from long-range interactions. Constraints and prospects related to gamma-rays are assessed for $m_\phi \geq 2m_{\pi^0}$ (cf. Section 7.3.3) while CMB limits are not constrained by this condition. However, the joint limit imposed by BBN and direct detection searches excludes mediator masses slightly below this threshold anyways (shaded in red). In regions where relic density computations suggest values of $\alpha \gtrsim 0.25$ (shaded in gray), certain corrections in our derivations, such as α and α_5 corrections to the matching coefficients in Eqs. 5.3.15 to 5.3.18 and corrections to the binding energy of BS, become significant. However, accounting for these corrections is very challenging and clearly beyond the scope of this work. Hence, we will exclude this region from our discussion.

We observe that indirect detection limits can be highly restrictive when α_5 is not significantly smaller than α . This is because larger values of α_5 amplify the s-wave cross section, which is not velocity suppressed at any m_ϕ . Further including SE, this essentially excludes configurations with $m_\phi \lesssim 3 \text{ GeV}$ by Planck measurements for $\alpha_5/\alpha = 0.1$. At higher mediator masses, CMB exclusions rely on resonances in the generalized J -factors due to SE, resulting in excluded parameter space stripes which extend to very high values of m_χ and m_ϕ . These stripes become thinner with a decreasing total cross section for an increasing DM mass, as the resonance condition must be fulfilled with higher precision. Gamma-ray telescopes can provide additional information in this regime. The Fermi-LAT limits are mostly comparable to the CMB ones, however, due to Fermi's higher sensitivity, they result in broader stripes that encompass the CMB ones for low m_χ . At the higher end of the mass range, this effect diminishes due to the sensitivity scaling differently with the DM mass. Therefore, Fermi-LAT does not contribute significantly to CMB bounds on the edge of our parameter space for $m_\chi \approx 10 \text{ TeV}$. Remarkably, CTA presents a significant advancement, offering stronger exclusion prospects without relying on resonance features. This effectively closes gaps in between the stripes and enables a probe of nearly the entire parameter space. Only very high DM masses and large m_ϕ can potentially evade these prospects. It is noteworthy that gamma-ray searches also contribute at low m_ϕ , where the low mediator mass regime ($2m_{\pi^0} \leq m_\phi \leq 1 \text{ GeV}$) is excluded by Fermi-LAT. These limits are intentionally overlaid below the CMB ones to enhance the readability.

For lower α_5/α ratios, the significance of p-wave and BSF contributions increases. For $\alpha_5/\alpha = 10^{-2}$, the overall qualitative picture remains similar, with new features becoming visible for $\alpha_5/\alpha = 10^{-3}$. In this regime, bounds from Planck decrease substantially in the low mediator mass regime, causing configurations with $m_\phi \lesssim 1 \text{ GeV}$ to no longer be entirely constrained by CMB limits alone. However, Fermi-LAT limits remain significant

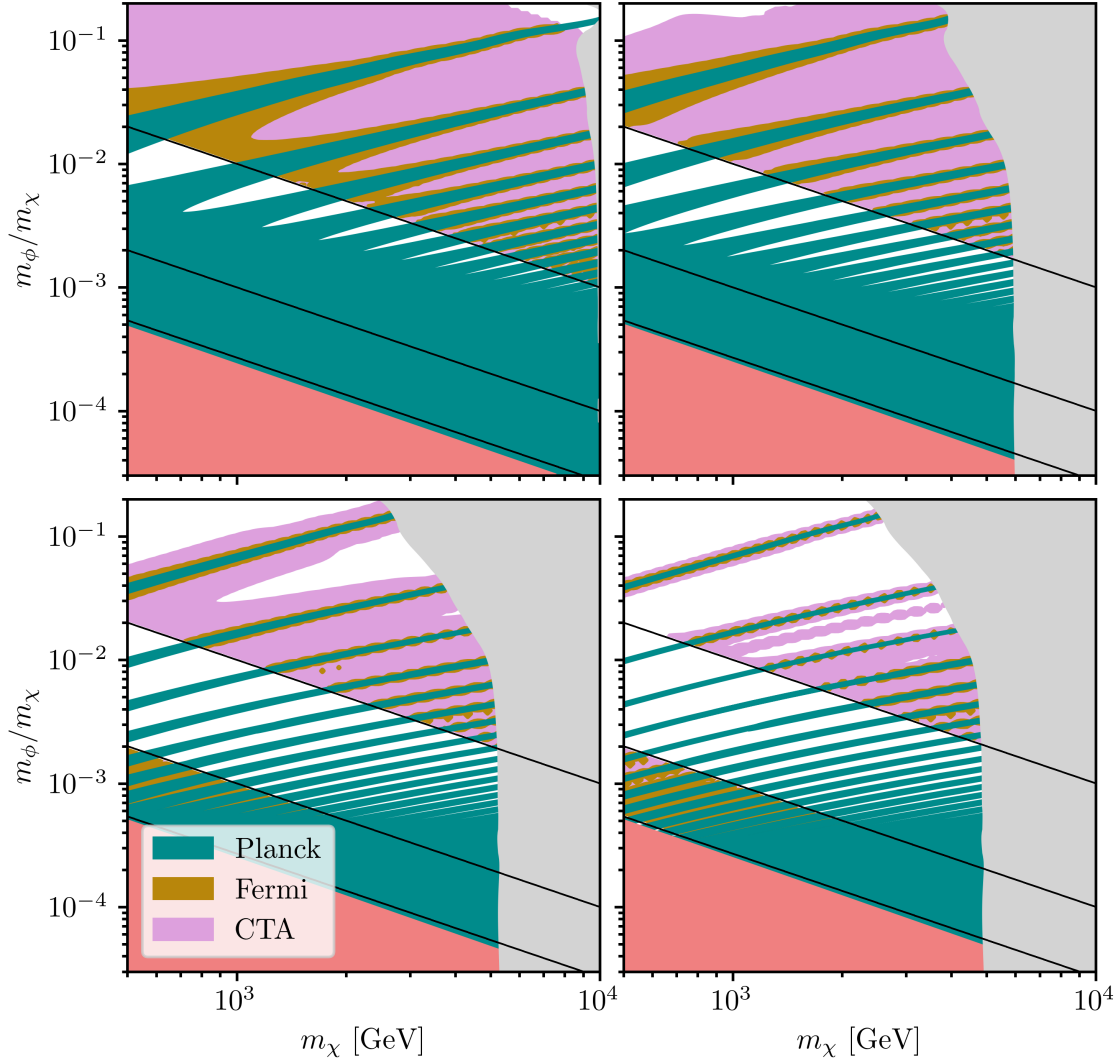


Figure 7.13: Slices through the cosmologically preferred parameter space in the m_χ - m_ϕ/m_χ plane for four benchmark values of $\alpha_5/\alpha \in \{10^{-1}, 10^{-2}, 10^{-3}, 10^{-4}\}$ (left-to-right, top-to-bottom). The value of α has been fixed by the relic density requirement. Exclusion limits from indirect detection have been overlaid in the following order (starting with the top layer): Regions excluded by Planck are shown in turquoise and the Fermi-LAT exclusion limits are presented in gold, whereas prospects for CTA are depicted in pink. Mediator mass regions, which are excluded by the combined BBN and direct detection limits on the mixing angle, are shaded in red. Regions where relic density requires $\alpha > 0.25$ are shown in gray. Black lines indicate characteristic values of $m_\phi = 2m_{\pi^0}$, 1 GeV and 10 GeV that separate the different gamma-ray production regimes defined in Section 7.3.3. Adapted from Ref. [6].

in this region due to the substantial number of energetic photons produced in the pion cascade regime. As a result, a significant portion of this parameter space is still excluded by current experiments. For $m_\phi > 10$ GeV, only narrow stripes with a strong resonant enhancement are excluded by existing experiments. CTA prospects remain excellent, and most gaps between enhanced stripes can be closed if the CTA sensitivity aligns with our expectations. It is important to note that the granularity of the gamma-ray limits, evident compared to the Planck limits in this figure, is a numerical artifact arising from the lower resolution of Fermi-LAT and CTA scans. Determining the generalized J -factors required for gamma-ray limits and prospects is computationally expensive. Therefore, we chose a coarser scanning grid given the available computing power.

At $\alpha_5/\alpha = 10^{-4}$, signals are predominantly influenced by p-wave and BSF. Existing limits are relatively weak, and CTA is crucial in closing gaps in the low mediator mass region. For $m_\phi \geq 10$ GeV, most of the parameter space is presently unconstrained. While the CTA remains influential, for $m_\phi/m_\chi \gtrsim 10^{-2}$, it also depends on resonances in the SE factors. Additional strips are resolved in this figure, driven by resonances of p-wave SE factors, which do not coincide with those of the s-wave (cf. Fig. 7.3). Overall, indirect detection proves highly effective in testing the model where s-wave annihilation is relevant. In the p-wave and BSF-dominated regime, some promising limits and good prospects exist for parts of the parameter space. However, a definitive test of the model for low α_5/α ratios remains challenging even with near-future experiments like the CTA.

8 Conclusion

Over the past two decades, researchers in the DM community have increasingly focused on non-perturbative effects in DM interactions. These effects have gained attention for their importance in accurately predicting DM properties in various models. Particularly, the exploration of BS alongside SE has become an active area of research in recent years. This thesis, centered around two publications [5, 6], has been dedicated to investigating these phenomena and their impact on the production and detection of DM.

In the first study, we focused on DM models with non-thermal production, comprising a DM candidate with feeble couplings to the visible sector and a mediator with SM quantum numbers. Such models present markedly different experimental signatures compared to the prevalent WIMP paradigm, rendering them intriguing subjects for study. Additionally, due to the mediator interactions with the SM, significant portions of the models' parameter space are accessible to collider searches at the LHC. This is particularly interesting, considering the impending HL-LHC upgrade. Given that gauge interactions with the mediator may also lead to substantial non-perturbative corrections for DM production in the early Universe, a comprehensive study of the cosmologically favored parameter space must account for these effects to provide a realistic evaluation of experimental capabilities.

In Section 6, we conducted a comprehensive analysis of non-thermal DM production within a specific class of simplified models. These models feature a fermionic singlet DM candidate and a scalar (color-)charged mediator. We accounted for both FI and sW production of DM and factored in corrections from SE and BS effects. Comparing our findings with perturbative calculations, we observed a significant discrepancy in the case of a color-charged mediator, where neglecting non-perturbative effects led to an overestimation of the sW contribution to the DM abundance by an order of magnitude. This underscores the necessity of accounting for such corrections and reveals a much broader parameter space conducive to non-thermal DM production than previously anticipated. In contrast, for a lepto-philic mediator, the non-perturbative effects were more subdued, with a $\sim 15\%$ correction to the DM yield from sW production. However, this scenario is sensitive to the coupling between the mediator and the Higgs field, where even modest changes can result in considerable alterations to the sW contribution.

By combining constraints from LHC searches, cosmological bounds from BBN, and predictions from DM production in the early Universe, we scrutinized the viable parameter space of both models. We found that while a small mass gap between DM and the mediator is feasible for relatively low mediator masses in the range of a few TeV, larger mediator masses necessitate a substantial mass separation to prevent a DM overabundance. Therefore, overall larger DM masses are preferred. Non-perturbative effects significantly expand this viable parameter space. Altogether, our findings indicate that collider tests of these models pose greater challenges than initially anticipated. The increased luminosity at the HL-LHC may enhance experimental reach, but a collider with higher energy levels would be highly advantageous for probing these type of DM models effectively.

The focus of the second study was to investigate how non-perturbative effects impact the detectability of DM in cosmological searches. For this purpose, we utilized a thermal DM model with annihilations occurring within the dark sector. This setup naturally circumvents direct detection and collider constraints, singling out indirect detection as the preferred avenue for DM searches. This is particularly pertinent given the imminent availability of new, more sensitive instruments like the CTA, which will provide new data in the near future. Thus, it is crucial to understand the sensitivity of the CTA with respect to thermal DM and compare its abilities with existing constraints. Given the wide range of potential observables, we selected robust limits from Planck and Fermi-LAT as our benchmarks.

In Section 7, we therefore concentrated on a model featuring fermionic DM, which possesses (pseudo)-scalar couplings to a massive scalar mediator. The mediator in turn interacts with the SM through mixing with the Higgs. When the mass of the mediator is relatively light compared to the DM mass and the potential created by the mediator is attractive, SE can become sizeable in DM observables and BS can form. As a result of these non-perturbative effects, the cross sections of interest, specifically for DM indirect detection, exhibit a pronounced and intricate dependence on the relative DM velocity. This contradicts a conventional assumption in indirect detection, which suggests that only the leading velocity-independent contribution to s-wave annihilation is detectable in a realistic experiment. We accounted for this in our computation of appropriate velocity-averaged J -factors, which necessitates position-dependent velocity distributions for the targets under consideration. These have been derived using Eddington inversion from density profiles for four dSphs and the GC of the Milky Way. This enabled us to predict the photon flux from DM annihilation based on particle physics parameters and establish upper limits (or identify prospects).

Combining this with our predictions for the relic density allowed us to evaluate the status of thermal DM in this model. If the suppression of the coupling parameter α_5 relative to α is modest, s-wave annihilations play a significant role, leading to stringent constraints on light mediators regardless of the DM mass. At higher mediator masses, the resonant enhancement due to SE factors becomes significant, enabling exclusion of regions near a resonance with Planck and Fermi-LAT observations. Interestingly, remaining gaps in the testable parameter space can be addressed by the CTA in this scenario. Testing the model becomes more challenging for smaller α_5/α , where the sensitivity of Planck and Fermi-LAT to the cosmologically favored parameter space diminishes, making CTA crucial, as it will cover large regions of the parameter space for the first time.

We hope to have convinced the reader that research on non-perturbative effects in DM model building is to equal terms an important and exciting field, with the potential to study the nature of DM to an unprecedented level of precision. The challenges ahead are manifold, such as the consistent and automatised inclusion of higher-order bound states or the consideration of the SM bath as a thermal background, to name only a few. With the rapid improvement of our theoretical toolkit, we are confident that our field will overcome all these challenges, eventually providing the most robust predictions on DM observables for experimental exploration.

Appendices

A Special functions

In this appendix, we list all special functions, along with their properties and identities, that we will use throughout this work. The information provided below is by no means exhaustive, as the properties are well-known. Therefore, we will refrain from citations or proofs.

Gamma function

The *gamma function* is an extension of the factorial to the complex plane and can be defined in the regime $z \in \mathbb{C} \setminus (-\mathbb{N})$. It copies the properties of the factorial function $\Gamma(z+1) = z\Gamma(z)$, and reduces to it $\Gamma(n+1) = n!$ for $n \in \mathbb{N}$. For $\text{Re}\{z\} > 0$, there also exists an integral representation

$$\Gamma(z, x) \equiv \int_x^\infty dt t^{z-1} e^{-t}, \quad \Gamma(z) \equiv \Gamma(z, 0), \quad (\text{A.1})$$

where (for $x \geq 0$) the former quantity is often called *incomplete gamma function*. A property, which will be used often throughout this work is

$$|\Gamma(1+l-i\zeta)|^2 = \frac{2\pi\zeta}{1-e^{-2\pi\zeta}} e^{-\pi\zeta} \prod_{r=1}^l (r^2 + \zeta^2) \quad \text{for } l \in \mathbb{N}, \quad \zeta \in \mathbb{R}. \quad (\text{A.2})$$

Bessel functions

Bessel functions are canonical solutions $y(x)$ to Bessel's differential equation

$$\left[x^2 \frac{d^2}{dx^2} + x \frac{d}{dx} + (x^2 - \alpha^2) \right] y(x) = 0 \quad (\text{A.3})$$

for an arbitrary complex number $\alpha \in \mathbb{C}$. For real x , there are two linearly independent solutions

$$J_\alpha(x) \equiv \sum_{m=0}^{\infty} \frac{(-1)^m}{m! \Gamma(m+\alpha+1)} \left(\frac{x}{2}\right)^{2m+\alpha}, \quad (\text{A.4})$$

$$Y_\alpha(x) \equiv \frac{J_\alpha(x) \cos(\alpha\pi) - J_{-\alpha}(x)}{\sin(\alpha\pi)}, \quad (\text{A.5})$$

denoted as *Bessel functions of first and second kind*, where for $\alpha = n$ an integer, the latter is defined as $Y_n(x) \equiv \lim_{\alpha \rightarrow n} Y_\alpha(x)$. For purely imaginary arguments ix , $x \in \mathbb{R}$, the solutions are called *modified Bessel functions of first and second kind* and are connected to the real solutions via

$$I_\alpha(x) \equiv i^{-\alpha} J_\alpha(ix), \quad (\text{A.6})$$

$$K_\alpha(x) \equiv \frac{\pi}{2} \frac{I_{-\alpha}(x) - I_\alpha(x)}{\sin(\alpha\pi)}. \quad (\text{A.7})$$

Within this work, we are chiefly interested in $K_n(x)$, $n \in \mathbb{N}$, which possess an integral representation

$$K_n(x) \equiv \frac{\sqrt{\pi}}{\Gamma(n + \frac{1}{2})} \left(\frac{x}{2}\right)^n \int_1^\infty dy e^{-xy} (y^2 - 1)^{n-\frac{1}{2}}, \quad (\text{A.8})$$

as well as a series expansion for large arguments

$$K_n(x) = \sqrt{\frac{\pi}{2x}} e^{-x} \sum_{k=0}^{\infty} \frac{1}{k!(8x)^k} \prod_{l=0}^{k-1} (4n^2 - (2l+1)^2). \quad (\text{A.9})$$

The two linearly independent solutions for $\alpha^2 = l(l+1)$, $l \in \mathbb{Z}$, are called *spherical Bessel and Neumann functions* and can be defined via

$$j_l(x) \equiv \sqrt{\frac{\pi}{2x}} J_{n+\frac{1}{2}}(x) = \sum_{s=0}^{\infty} \frac{(-1)^s x^{l+2s}}{2^s s! (2s+2l+1)!!}, \quad (\text{A.10})$$

$$n_l(x) \equiv \sqrt{\frac{\pi}{2x}} Y_{n+\frac{1}{2}}(x) = (-1)^{n+1} \sqrt{\frac{\pi}{2x}} J_{-n-\frac{1}{2}}(x). \quad (\text{A.11})$$

Closely related are the *spherical Hankel functions*, which are just linear combinations of the spherical Bessel and Neumann functions

$$h_l^{(1)}(x) \equiv j_l(x) + in_l(x), \quad h_l^{(2)}(x) \equiv j_l(x) - in_l(x). \quad (\text{A.12})$$

Laguerre polynomials

The *associated Laguerre polynomials* are solutions to Laguerre's differential equation

$$\left[x \frac{d^2}{dx^2} + (\alpha + 1 - x) \frac{d}{dx} + n \right] L_n^{(\alpha)}(x) = 0, \quad (\text{A.13})$$

with $n \in \mathbb{N}$, $\alpha \in \mathbb{R}$ and reduce to the regular *Laguerre polynomials* L_n for $\alpha = 0$. For this work, we only need the case where $\alpha \in \mathbb{N}$. They can be defined through a polynomial series

$$L_n^{(\alpha)}(x) = \sum_{k=1}^n \frac{(-1)^k (n+\alpha)! x^k}{(n-k)! (k+\alpha)! k!}, \quad (\text{A.14})$$

and thus expressed through a confluent hypergeometric function via

$$L_n^{(\alpha)}(x) = \frac{(\alpha+1)_n}{n!} {}_1F_1(-n; \alpha+1; x), \quad (\text{A.15})$$

with $(\alpha+1)_n$ defined in Eq. A.35.

Legendre polynomials

The *associated Legendre polynomials* are solutions to the differential equation

$$\left[\frac{d}{dx} \left((1-x^2) \frac{d}{dx} \right) + \left(l(l+1) - \frac{m^2}{1-x^2} \right) \right] P_l^m(x) = 0, \quad (\text{A.16})$$

with $l, m \in \mathbb{N}$, where the special case $m = 0$ yields the usual *Legendre polynomials* $P_l(x) \equiv P_l^0(x)$. Identifying $x \equiv \cos \theta$, the latter are also eigenfunctions to the Laplace operator in spherical coordinates

$$\Delta_{\mathbf{r}} P_l(\cos \theta) = -\frac{l(l+1)}{r^2} P_l(\cos \theta), \quad (\text{A.17})$$

which can easily be derived from Eq. A.16. The Legendre polynomials form a complete and orthogonal system of polynomials. The standard condition $P_l(1) \equiv 1$ fixes their normalization (with respect to the L^2 norm) on the interval $-1 \leq x \leq 1$. Their orthogonality as well as completeness relations are given by

$$\int_{-1}^1 dx P_l(x) P_{l'}(x) = \frac{2}{2l+1} \delta_{ll'}, \quad (\text{A.18})$$

$$\sum_{l=0}^{\infty} \frac{2l+1}{2} P_l(x) P_l(y) = \delta(x-y). \quad (\text{A.19})$$

We will make extensive use of the special case $x = 1$, $y = \hat{\mathbf{r}} \cdot \hat{\mathbf{r}}'$ of Eq. A.19, yielding

$$\sum_{l=0}^{\infty} \frac{2l+1}{2} P_l(\hat{\mathbf{r}} \cdot \hat{\mathbf{r}}') = \delta(1 - \hat{\mathbf{r}} \cdot \hat{\mathbf{r}}'). \quad (\text{A.20})$$

Due to the properties described above, we can use the Legendre polynomials as a basis for any analytic azimuthally symmetric function

$$f(r, \theta) = \sum_{l=0}^{\infty} f_l(r) P_l(\cos \theta), \quad (\text{A.21})$$

with coefficients $f_l(r)$ solely depending on r . A special analytic function used in the following is the plane wave, given as

$$e^{i\mathbf{k} \cdot \mathbf{r}} = \sum_{l=0}^{\infty} (2l+1) i^l j_l(kr) P_l(\cos \theta), \quad (\text{A.22})$$

with j_l the spherical Bessel functions and $\cos \theta \equiv \hat{\mathbf{k}} \cdot \hat{\mathbf{r}}$. The Legendre polynomials of a scalar product of unit vectors can, in turn, be expanded in terms of spherical harmonics

$$P_l(\hat{\mathbf{r}} \cdot \hat{\mathbf{r}}') = \frac{4\pi}{2l+1} \sum_{m=-l}^l Y_{lm}^*(\Omega_{\mathbf{r}}) Y_{lm}(\Omega_{\mathbf{r}'}), \quad (\text{A.23})$$

from which also the following property can be derived

$$\int d\Omega_{\mathbf{k}} P_l(\hat{\mathbf{k}} \cdot \hat{\mathbf{r}}) P_{l'}(\hat{\mathbf{k}} \cdot \hat{\mathbf{r}}') = \frac{4\pi}{2l+1} \delta_{ll'} P_l(\hat{\mathbf{r}} \cdot \hat{\mathbf{r}}'). \quad (\text{A.24})$$

A useful identity concerning Legendre polynomials, which has been derived e. g. in App. D of Ref. [129] and will be used in App. D is

$$\begin{aligned} \int d\Omega_{\mathbf{p}} P_{l'}(\cos \theta_{\mathbf{p}}) \int \frac{d^3 \mathbf{q}}{(2\pi)^3} \tilde{f}(\mathbf{q}) |\mathbf{q}|^l P_l(\cos \theta_{\mathbf{q}, \mathbf{p}}) \\ = \frac{\delta_{ll'} (2l+1)!!}{i^l (2l+1)!} \left[\frac{d^l}{dr^l} \int d\Omega_{\mathbf{r}} P_l(\cos \theta_{\mathbf{r}}) f(\mathbf{r}) \right]_{r=0}, \end{aligned} \quad (\text{A.25})$$

for an arbitrary analytic function $f(\mathbf{r})$ with Fourier transform $\tilde{f}(\mathbf{q})$.

Spherical harmonics

Spherical harmonics are a complete set of orthonormal functions defined on the surface of a sphere $Y_{lm} : S^2 \rightarrow \mathbb{C}$ and, therefore, form an orthonormal basis of the Hilbert space of square-integrable (complex) functions $L^2_{\mathbb{C}}(S^2)$. They can be defined through the associated Legendre polynomials

$$Y_{lm}(\Omega) \equiv (-1)^m \sqrt{\frac{2l+1}{4\pi} \frac{(l-m)!}{(l+m)!}} P_l^m(\cos \theta) e^{im\phi}, \quad (\text{A.26})$$

with $Y_{lm}^*(\Omega) = (-1)^m Y_{l-m}(\Omega)$, and their orthonormality and completeness conditions are given by

$$\int d\Omega_{\mathbf{r}} Y_{lm}(\Omega) Y_{l'm'}^*(\Omega) = \delta_{ll'} \delta_{mm'}, \quad (\text{A.27})$$

$$\sum_{l=0}^{\infty} \sum_{m=-l}^l Y_{lm}^*(\Omega) Y_{lm}(\Omega') = \delta(\cos \theta - \cos \theta') \delta(\phi - \phi'). \quad (\text{A.28})$$

From Eq. A.23 we can derive Unsöld's theorem

$$\sum_{m=-l}^l Y_{lm}^*(\Omega) Y_{lm}(\Omega) = \frac{2l+1}{4\pi}, \quad (\text{A.29})$$

by setting $\hat{\mathbf{r}} = \hat{\mathbf{r}}'$. Spherical harmonics are also eigenfunctions of the Laplace operator in spherical coordinates, yielding

$$\Delta_{\mathbf{r}} Y_{lm}(\Omega) = -\frac{l(l+1)}{r^2} Y_{lm}(\Omega). \quad (\text{A.30})$$

Wigner-3j symbols

The *Wigner 3j-symbols* can be considered an alternative formulation to *Clebsch-Gordon coefficients* and are linked to them via

$$\begin{pmatrix} l_1 & l_2 & l_3 \\ m_1 & m_2 & m_3 \end{pmatrix} \equiv \frac{(-1)^{l_1-l_2-m_3}}{\sqrt{2l_3+1}} \langle l_1, m_1, l_2, m_2 | l_3, -m_3 \rangle, \quad (\text{A.31})$$

where l_i, m_i are angular momentum quantum numbers with $m_i \in \{-l_i, -l_i + 1, \dots, l_i - 1, l_i\}$. They vanish unless, the following additional conditions are satisfied: 1) $m_1 + m_2 + m_3 = 0$, 2) $|l_1 - l_2| \leq l_3 \leq l_1 + l_2$, and 3) $l_1 + l_2 + l_3 \in \mathbb{N}$ (and also even, if $m_1 = m_2 = m_3 = 0$). We will need in the following the orthogonality condition

$$(2l_3 + 1) \sum_{m_1, m_2} \begin{pmatrix} l_1 & l_2 & l_3 \\ m_1 & m_2 & m_3 \end{pmatrix} \begin{pmatrix} l_1 & l_2 & l'_3 \\ m_1 & m_2 & m'_3 \end{pmatrix} = \delta_{l_3 l'_3} \delta_{m_3 m'_3} \{l_1 \ l_2 \ l_3\}, \quad (\text{A.32})$$

where $\{l_1 \ l_2 \ l_3\}$ is 1 when the triangular condition 2) is fulfilled and 0 otherwise, and the connection of the Wigner 3j-symbols to the spherical harmonics is given by

$$\begin{aligned} & \int d\Omega Y_{l_1 m_1}(\Omega) Y_{l_2 m_2}(\Omega) Y_{l_3 m_3}(\Omega) \\ &= \sqrt{\frac{(2l_1+1)(2l_2+1)(2l_3+1)}{4\pi}} \begin{pmatrix} l_1 & l_2 & l_3 \\ 0 & 0 & 0 \end{pmatrix} \begin{pmatrix} l_1 & l_2 & l_3 \\ m_1 & m_2 & m_3 \end{pmatrix}. \end{aligned} \quad (\text{A.33})$$

Hypergeometric functions

A *generalized hypergeometric function* is a convergent polynomial series, defined via

$${}_pF_q(a_1, \dots, a_p; b_1, \dots, b_q; z) \equiv \sum_{k=0}^{\infty} \frac{(a_1)_k \cdots (a_p)_k}{(b_1)_k \cdots (b_q)_k} \frac{z^k}{k!}, \quad (\text{A.34})$$

with $p, q \in \mathbb{N}$, where we introduced *Pochhammer symbols*

$$(x)_n \equiv \frac{\Gamma(x+n)}{\Gamma(x)} \quad (\text{A.35})$$

for a more compact notation. We employ in the main text two functions of these type. The first one is the *confluent hypergeometric function*

$${}_1F_1(a; b; x) \equiv \sum_{k=0}^{\infty} \frac{(a)_k}{(b)_k} \frac{z^k}{k!}, \quad (\text{A.36})$$

which has an integral representation

$${}_1F_1(a; b; x) = \frac{\Gamma(b)}{\Gamma(b-a)\Gamma(a)} \int_0^1 dt e^{zt} t^{a-1} (1-t)^{b-a-1}, \quad (\text{A.37})$$

for $\text{Re}\{b\} > \text{Re}\{a\} > 0$. The second one is the *hypergeometric function*

$${}_2F_1(a, b; c; x) \equiv \sum_{k=0}^{\infty} \frac{(a)_k (b)_k}{(c)_k} \frac{z^k}{k!}, \quad (\text{A.38})$$

with an integral representation

$${}_2F_1(a, b; c; x) = \frac{\Gamma(c)}{\Gamma(c-b)\Gamma(b)} \int_0^1 dt \frac{t^{b-1}(1-t)^{c-b-1}}{(1-tz)^a}, \quad (\text{A.39})$$

if $\text{Re}\{c\} > \text{Re}\{b\} > 0$. For our calculations in this work, we will make use of the following identities

$$e^x {}_1F_1(a; c; -x) = {}_1F_1(c-a; c; x), \quad (\text{A.40})$$

$$\frac{d^n({}_1F_1(a; b; z))}{dz^n} = \frac{(a)_n}{(b)_n} {}_1F_1(a+n; b+n; z), \quad (\text{A.41})$$

$$\frac{d^n(z^{b-1} {}_1F_1(a; b; z))}{dz^n} = (b-n)_n z^{b-n-1} {}_1F_1(a; b-n; z), \quad (\text{A.42})$$

alongside with (for $\text{Re}\{c\} > 0$)

$$\int_0^{\infty} dt e^{-\rho t} t^{c-1} {}_1F_1(a; c; t) {}_1F_1(b; c; \lambda t) = \frac{\Gamma(c) \rho^{a+b-c}}{(\rho-1)^a (\rho-\lambda)^b} {}_2F_1\left(a, b; c; \frac{\lambda}{(\rho-1)(\rho-\lambda)}\right). \quad (\text{A.43})$$

Other identities

There are three more identities used in this work, which do not fit into the classification above:

1. The three-dimensional delta distribution in spherical coordinates assuming azimuthal symmetry, can be written for non-vanishing $\hat{\mathbf{r}} \cdot \hat{\mathbf{r}}'$ as

$$\delta^{(3)}(\mathbf{r} - \mathbf{r}') = \frac{1}{r^2} \delta(r - r') \frac{1}{2\pi} \delta(1 - \hat{\mathbf{r}} \cdot \hat{\mathbf{r}}'). \quad (\text{A.44})$$

2. The integral representation of the Heavyside step function is given by

$$\Theta(z) = \lim_{\epsilon \rightarrow 0^+} \frac{i}{2\pi} \int_{-\infty}^{\infty} dk \frac{e^{-ikz}}{k + i\epsilon} = \begin{cases} 1 & z \geq 0 \\ 0 & z < 0 \end{cases}. \quad (\text{A.45})$$

3. An identity, which will be used to compute the SE factors for BSF, reads

$$\left| \left(\frac{n + i\zeta_2}{n - i\zeta_2} \right)^{-i\zeta_1} \right|^2 = e^{-4\zeta_1 \text{arccot}(\zeta_2/n)}. \quad (\text{A.46})$$

B Partial wave analysis

We will give here a brief insight into partial wave analysis, a method developed in scattering theory to calculate the wave functions and cross sections of interacting particles in the non-relativistic limit. For this purpose, we closely follow Ref. [302].

We can describe a scattering process by starting with an incoming plane wave in the z -direction $\phi_{\mathbf{k},\text{in}} \propto e^{ikz}$, with $k = \sqrt{2\mu\mathcal{E}_{\mathbf{k}}}$ being the wave-number (see Eq. 5.1.3) and $z = r \cos \theta$. The plane wave eventually meets a potential where it gets scattered, producing an outgoing spherical wave $\phi_{\mathbf{k},\text{out}} \propto e^{ikr}/r$. If we are sufficiently far from the potential (i. e. $r \rightarrow \infty$), the solution to the Schrödinger equation is of the form

$$\phi_{\mathbf{k}}(\mathbf{r}) \approx A \left(e^{ikz} + f(\mathcal{E}_{\mathbf{k}}, \theta_r) \frac{e^{ikr}}{r} \right), \quad (\text{B.1})$$

with $|A|$ being the amplitude of the wave function and $f(\mathcal{E}_{\mathbf{k}}, \theta_r)$ denotes the scattering amplitude, a measure of the probability of scattering in a given direction θ_r (assuming azimuthal symmetry in the following). The scattering amplitude is related to the cross section of the process via

$$\frac{d\sigma}{d\Omega} = |f(\mathcal{E}_{\mathbf{k}}, \theta_r)|^2. \quad (\text{B.2})$$

Due to the azimuthal symmetry of the problem, we can expand $\phi_{\mathbf{k},\text{out}}$ in the basis of Legendre polynomials (Eq. A.21)

$$\phi_{\mathbf{k},\text{out}}(\mathbf{r}) = \frac{1}{\sqrt{4\pi}} \sum_{l=0}^{\infty} \sqrt{2l+1} \frac{u_{\mathbf{k},l}(r)}{r} P_l(\cos \theta_r), \quad (\text{B.3})$$

with the prefactors chosen for later convenience. The Schrödinger equation in terms of $u_{\mathbf{k},l}$ then reads

$$u_{\mathbf{k},l}''(r) - \underbrace{\frac{l(l+1)}{r^2} u_{\mathbf{k},l}(r)}_{\text{“centrifugal term”}} - \underbrace{2\mu V(r) u_{\mathbf{k},l}(r)}_{\text{“potential term”}} = -k^2 u_{\mathbf{k},l}(r). \quad (\text{B.4})$$

For pedagogical reasons, we will now consider three situations and compare them to the outgoing spherical wave in the large r limit: 1) where r is so large that we can neglect the potential as well as the centrifugal term, 2) where r is in the intermediate regime where we can only neglect the potential term and 3) where we are close to the interaction point and have to take into account the whole Schrödinger equation. Scenario 3) will also correspond to the situation where we will have a long-ranged potential as used often throughout this work.

If we can neglect both the centrifugal and potential term in scenario 1), the general solution to Schrödinger equation is given by

$$u_{\mathbf{k},l}(r) = C e^{ikr} + D e^{-ikr}, \quad (\text{B.5})$$

where e^{ikr} represents an outgoing and e^{-ikr} an incoming spherical wave. Comparing this solution to Eq. B.1, it is obvious that $D = 0$.

In scenario 2), where we can only neglect the potential term, the solution yields

$$u_{\mathbf{k},l}(r) = Arj_l(kr) + Brn_l(kr) = \tilde{A}rh_l^{(1)}(kr) + \tilde{B}rh_l^{(2)}(kr), \quad (\text{B.6})$$

with $j_l(x)$, $n_l(x)$, $h_l^{(1)}(x)$, $h_l^{(2)}(x)$ being the spherical Bessel, Neumann and Hankel functions of first and second kind as defined in App. A. Since $h_l^{(1)}(kr) \rightarrow (-i)^{l+1}e^{ikr}/(kr)$ and $h_l^{(2)}(kr) \rightarrow i^{l+1}e^{-ikr}/(kr)$ for large r , we deduce $\tilde{B} = 0$ such that $u_{\mathbf{k},l}(r)/r \propto h_l^{(1)}(kr)$. Inserting this proportionality requirement into Eq. B.3, the expression for the wave function is then given by

$$\begin{aligned} \phi_{\mathbf{k}}(\mathbf{r}) &= A \left(e^{ikz} + \frac{1}{4\pi} \sum_{l=0}^{\infty} \sqrt{2l+1} C_l h_l^{(1)}(kr) P_l(\cos \theta_r) \right) \\ &= A \left(e^{ikz} + k \sum_{l=0}^{\infty} i^{l+1} (2l+1) a_l h_l^{(1)}(kr) P_l(\cos \theta_r) \right), \end{aligned} \quad (\text{B.7})$$

where we substituted $C_l \equiv i^{l+1}k\sqrt{4\pi(2l+1)}a_l$ in the second line. Expanding also the scattering amplitude in partial waves

$$f(\mathcal{E}_{\mathbf{k}}, \theta_r) = \sum_{l=0}^{\infty} (2l+1) a_l P_l(\cos \theta_r) \quad \Rightarrow \quad \sigma = 4\pi \sum_{l=0}^{\infty} (2l+1) |a_l|^2, \quad (\text{B.8})$$

we can easily match the a_l in Eq. B.7 to the expansion coefficients of $f(\mathcal{E}_{\mathbf{k}}, \theta_r)$ if we compare the expression with Eq. B.1 in the large r limit. Using Rayleigh's formula (see e. g. Ref. [303]) for the incident plane wave (cf. Eq. A.22)

$$e^{ikz} = \sum_{l=0}^{\infty} \frac{i^l (2l+1)}{2} \left(h_l^{(1)}(kr) + h_l^{(2)}(kr) \right) P_l(\cos \theta_r), \quad (\text{B.9})$$

with $\cos \theta_r \equiv \hat{\mathbf{k}} \cdot \hat{\mathbf{r}}$ and where we have split $j_l(x)$ into an incoming and outgoing spherical wave part (cf. Eq. A.12), the wave function yields

$$\phi_{\mathbf{k}}(\mathbf{r}) = A \sum_{l=0}^{\infty} \frac{i^l (2l+1)}{2} \left[(1 + 2ika_l) h_l^{(1)}(kr) + h_l^{(2)}(kr) \right] P_l(\cos \theta_r). \quad (\text{B.10})$$

Thus, we have reduced the problem to the task of finding the expansion coefficients of the scattering amplitude a_l for each partial wave.

If we take into account the potential as in scenario 3), outgoing spherical wave functions receive corrections if they are sufficiently close to the interaction point (since they cannot be considered to be free waves anymore). Since the amplitude of the incoming and outgoing spherical waves has to be the same in order to conserve probability, the

change can only be a phase, defined as $e^{2i\delta}$, which depends on the potential under consideration. Due to conservation of angular momentum in a spherically symmetric potential, all partial waves scatter independently from each other, which means that if we perform a partial wave expansion on the whole wave function, each partial wave l will have an independent phase δ_l . Therefore, we can write Eq. B.1 as

$$\phi_{\mathbf{k}}(\mathbf{r}) = \sum_{l=0}^{\infty} \phi_{\mathbf{k}}^{(l)}(\mathbf{r}) \xrightarrow{r \rightarrow \infty} A \sum_{l=0}^{\infty} \frac{i^l(2l+1)}{2ikr} \left[(-i)^l e^{2i\delta_l} e^{ikr} - i^l e^{-ikr} \right] P_l(\cos \theta_r), \quad (\text{B.11})$$

where we started with the expansion of the solution $\phi_{\mathbf{k}}^0(\mathbf{r}) = Ae^{ikz}$ for no potential present (i. e. no scattering), took the asymptotic limit for $r \rightarrow \infty$ and added a phase δ_l to each outgoing spherical partial wave. Comparing this asymptotic result to Eq. B.10, we can identify $a_l = (e^{2i\delta_l} - 1)/(2ik)$ reducing the problem even further from having a complex a_l to a single phase for each partial wave. The wave function can then also be written as

$$\phi_{\mathbf{k}}(\mathbf{r}) \approx \sum_{l=0}^{\infty} i^l e^{i\delta_l} (2l+1) \frac{\tilde{u}_{\mathbf{k},l}(r)}{r} P_l(\cos \theta_r), \quad (\text{B.12})$$

with

$$\tilde{u}_{\mathbf{k},l}(r) \xrightarrow{r \rightarrow \infty} \frac{A}{k} \sin \left(kr - \frac{l\pi}{2} + \delta_l \right). \quad (\text{B.13})$$

The phase has to be computed by solving the full Schrödinger equation for the potential under consideration after choosing appropriate initial conditions. The amplitude can then in principle be calculated from the phase shift (cf. Ref. [304]). However, since we are only interested in the difference of the wave functions with and without a potential present, we can normalize the result with $|\phi_{\mathbf{k}}^0(\mathbf{r})|^2 = |A|^2 \equiv 1$, without loss of generality.

C The non-relativistic potential for different mediator interactions

We will determine in the following the potential strength α alongside with the (potentially long-ranged) non-relativistic potential $V(\mathbf{r})$ arising from the interaction Lagrangian of two scalar particles and a mediator φ . We will do this by employing Eq. 5.2.47

$$V(\mathbf{r}) \equiv -\frac{1}{i4m\mu} \int \frac{d^3p}{(2\pi)^3} \mathcal{W}(|\mathbf{p}|) e^{i\mathbf{p}\cdot\mathbf{r}},$$

where m and μ denote the total and reduced mass of the two-particle system and \mathcal{W} describes the interaction kernel \tilde{W} after having taken the instantaneous approximation as described in Section 5.2.1. We will consider in the following only interaction Lagrangians and particle types relevant for this thesis.

As sketched in Fig. C.1, where we used the same parametrization of total and relative momenta as in Section 5.2, to leading order in the couplings the interaction kernel is given by a one particle exchange process of the mediator φ , which we take to be either a scalar or a vector boson. We further assume an interacting particle antiparticle system of scalars. The interaction kernel of a one boson exchange diagram in the non-relativistic regime is then given by

$$\tilde{W}(p, p'; Q) \simeq -\frac{i\epsilon_{\mu\nu} G^{ab} \Sigma_a^\mu(p, p'; Q) \Sigma_b^\nu(p, p'; Q)}{(p - p')^2 - m_\varphi^2} \xrightarrow[\text{approx.}]{\text{inst.}} \frac{i\Sigma}{(\mathbf{p} - \mathbf{p}')^2 + m_\varphi^2} = \mathcal{W}(|\mathbf{p} - \mathbf{p}'|), \quad (\text{C.1})$$

where $\Sigma_a^\mu(p, p'; Q)$, $\Sigma_b^\nu(p, p'; Q)$ denote the vertex couplings at the corresponding vertices, $\epsilon_{\mu\nu}$ is the polarization sum of the mediator states and G^{ab} describes the color matrix.⁶⁸ The product of $\epsilon_{\mu\nu} G^{ab} \Sigma_a^\mu(p, p'; Q) \Sigma_b^\nu(p, p'; Q) \simeq \Sigma$ can usually be expanded to leading order in the relative momenta such that Σ is independent of p, p' and Q . Inserting $\mathcal{W}(|\mathbf{p}|)$ into Eq. 5.2.47 yields the Yukawa potential

$$\begin{aligned} V(\mathbf{r}) &= -\frac{\Sigma}{4m\mu} \int \frac{d^3p}{(2\pi)^3} \frac{e^{i\mathbf{p}\cdot\mathbf{r}}}{\mathbf{p}^2 + m_\varphi^2} = -\frac{\Sigma}{4m\mu} \int_0^\infty \frac{dp}{(2\pi)^2} \frac{p^2}{p^2 + m_\varphi^2} \int_{-1}^{+1} d\cos\theta e^{ipr\cos\theta} \\ &= -\frac{\Sigma}{2m\mu r} \int_0^\infty \frac{dp}{(2\pi)^2} \frac{p \sin(pr)}{p^2 + m_\varphi^2} = -\frac{\Sigma}{16\pi m\mu r} e^{-m_\varphi r} \equiv -\frac{\alpha}{r} e^{-m_\varphi r}, \end{aligned} \quad (\text{C.2})$$

where we labelled $p \equiv |\mathbf{p}|$ within the calculation and defined the potential strength to be $\alpha \equiv \Sigma/(16\pi m\mu)$. As usual, the Yukawa potential simplifies to the Coulomb potential for massless mediators $m_\varphi \rightarrow 0$. If $\Sigma > 0$ the potential is attractive, in the other case it is considered repulsive. Our goal in the following is to determine α from the interaction kernels of the Lagrangians under consideration and single out the most important potentials for the corresponding model.

$$\tilde{W}(p, p'; Q) = \begin{array}{c} \eta_1 Q + p \\ \text{---} \\ \text{---} \\ \eta_2 Q - p \end{array} \begin{array}{c} \text{---} \\ \text{---} \\ \text{---} \end{array} \begin{array}{c} \eta_1 Q + p' \\ \text{---} \\ \text{---} \\ \eta_2 Q - p' \end{array} \simeq \begin{array}{c} \eta_1 Q + p \\ \text{---} \\ \text{---} \\ \eta_2 Q - p \end{array} \begin{array}{c} \mu, a \\ \text{---} \\ \text{---} \\ \nu, b \end{array} \begin{array}{c} \eta_1 Q + p' \\ \text{---} \\ \text{---} \\ \eta_2 Q - p' \end{array}$$

Figure C.1: Interaction kernel of a $2 \rightarrow 2$ scattering process exchanging an arbitrary number of mediators φ . Its leading order approximation comprises a single boson exchange. The mediator can either be a scalar or a vector boson and the external scalar particles are allowed to carry color charge. Adapted from Ref. [129].

Non-relativistic potentials for a t -channel mediator model

In the first model under consideration employed in Section 6, we look at the three point interactions of an (un-)colored scalar mediator \tilde{t} ($\tilde{\tau}$), neutral under $SU(2)_L$, with the SM gauge fields after EWSB

$$\mathcal{L}_{\text{int}}^{\tilde{t}} \supset -ieQ_{\text{em}}^{\tilde{t}} \tilde{t}^* \partial^\mu \tilde{t} A_\mu + ie \tan \theta_W Q_{\text{em}}^{\tilde{t}} \tilde{t}^* \partial^\mu \tilde{t} Z_\mu - ig_s T_a^{ij} \tilde{t}_i^* \partial^\mu \tilde{t}_j G_\mu^a + \lambda_H v \tilde{t} \tilde{t}^* h + h.c., \quad (\text{C.3})$$

$$\mathcal{L}_{\text{int}}^{\tilde{\tau}} \supset -ieQ_{\text{em}}^{\tilde{\tau}} \tilde{\tau}^* \partial^\mu \tilde{\tau} A_\mu + ie \tan \theta_W Q_{\text{em}}^{\tilde{\tau}} \tilde{\tau}^* \partial^\mu \tilde{\tau} Z_\mu + \lambda_H v \tilde{\tau} \tilde{\tau}^* h + h.c., \quad (\text{C.4})$$

where A_μ, Z_μ, G_μ^a, h denote the photon, Z boson, gluon and Higgs fields, respectively. The electromagnetic and strong coupling constants are given by e and g_s , with $Q_{\text{em}}^{\tilde{t}} = 2/3$ ($Q_{\text{em}}^{\tilde{\tau}} = -1$) the electromagnetic charge of the (un-)colored mediator and T_a^{ij} the $SU(3)$ generators of the strong interaction in the fundamental representation. The variable λ_H parameterizes the scalar Higgs coupling and v, θ_W denote the usual SM Higgs vev and Weinberg angle.

Higgs boson exchange

The coupling strength for the Higgs boson exchange can be determined straight forwardly. In this case the interaction kernel in the instantaneous approximation is simply given by

$$\mathcal{W}_h(p, p'; Q) \simeq -\frac{i\lambda_H^2 v^2}{(p-p')^2 - m_H^2} \xrightarrow[\text{approx.}]{\text{inst.}} \frac{i\lambda_H^2 v^2}{(\mathbf{p}-\mathbf{p}')^2 + m_H^2}, \quad (\text{C.5})$$

such that we identify $m_\varphi = m_H$ and $\Sigma = \lambda_H^2 v^2$, leading to $\alpha_H = \lambda_H^2 v^2 / (16\pi M^2)$ with $M \equiv m_{\tilde{t}}$ ($M \equiv m_{\tilde{\tau}}$) the mass of the (un-)colored mediator.

⁶⁸The polarization sum $\epsilon_{\mu\nu}$ only occurs if φ is a vector boson and the color matrix enters solely for gluon exchange for which $G^{ab} \equiv \delta^{ab}$.

Photon exchange

The interaction kernel for the one-photon exchange is given by (see e. g. Ref. [305])

$$\mathcal{W}_\gamma(p, p'; Q) \simeq \frac{ie^2 Q_{\text{em},1} Q_{\text{em},2}}{(p-p')^2} g_{\mu\nu} (2\eta_a Q + p + p')^\mu (2\eta_b Q - p - p')^\nu. \quad (\text{C.6})$$

In the non-relativistic regime up to leading order in the relative momenta and setting $Q^2 = m^2$, we can approximate this by

$$\mathcal{W}_\gamma(p, p'; Q) \simeq \frac{4ie^2 Q_{\text{em},1} Q_{\text{em},2} m_1 m_2}{(p-p')^2} \xrightarrow[\text{approx.}]{\text{inst.}} -\frac{4ie^2 Q_{\text{em},1} Q_{\text{em},2} m_1 m_2}{(\mathbf{p} - \mathbf{p}')^2}, \quad (\text{C.7})$$

where we identify $m_\varphi = 0$ and $\Sigma = -4e^2 Q_{\text{em},1} Q_{\text{em},2} m_1 m_2$. For $m_1 = m_2 = M$ and $Q_{\text{em},1} = -Q_{\text{em},2} \equiv Q_{\text{em}}$ we obtain $\alpha_\gamma = Q_{\text{em}}^2 e^2 / (4\pi) = Q_{\text{em}}^2 \alpha_{\text{em}}$ with $\alpha_{\text{em}} \equiv e^2 / (4\pi)$ the typical electromagnetic potential strength.

Z boson exchange

The case for the Z boson can be treated very similarly to the photon exchange. We start with

$$\mathcal{W}_Z(p, p'; Q) \simeq \frac{ie^2 \tan^2 \theta_W Q_{\text{em},1} Q_{\text{em},2}}{q^2 - m_Z^2} \left(g_{\mu\nu} - \frac{q_\mu q_\nu}{m_Z^2} \right) (2\eta_a Q + p + p')^\mu (2\eta_b Q - p - p')^\nu, \quad (\text{C.8})$$

where $q = p - p'$. The $q_\mu q_\nu / m_Z^2$ term cancels completely (because we do not couple to the longitudinal Z mode), such that in the non-relativistic limit we obtain

$$\mathcal{W}_Z(p, p'; Q) \simeq \frac{4ie^2 \tan^2 \theta_W Q_{\text{em},1} Q_{\text{em},2} m_1 m_2}{(p-p')^2 - m_Z^2} \xrightarrow[\text{approx.}]{\text{inst.}} -\frac{4ie^2 \tan^2 \theta_W Q_{\text{em},1} Q_{\text{em},2} m_1 m_2}{(\mathbf{p} - \mathbf{p}')^2 + m_Z^2}. \quad (\text{C.9})$$

We identify $m_\varphi = m_Z$ and $\Sigma = -4e^2 \tan^2 \theta_W Q_{\text{em},1} Q_{\text{em},2} m_1 m_2$. Using $m_1 = m_2 = M$ and $Q_{\text{em},1} = -Q_{\text{em},2} \equiv Q_{\text{em}}$ the potential strength for the Z is given by $\alpha_Z = Q_{\text{em}}^2 \tan^2 \theta_W e^2 / (4\pi) = Q_{\text{em}}^2 \tan^2 \theta_W \alpha_{\text{em}}$. Due to the exponential suppression of the Yukawa interaction and the $\tan^2 \theta_W$ term, the Z -potential is typically much weaker than the Coulomb potential for the photon exchange.

Gluon exchange

The potential due to gluon exchange can only be generated for a $\tilde{t} \tilde{t}^*$ pair. The kernel (in Feynman gauge) reads

$$\mathcal{W}_g(p, p'; Q) = \frac{ig_s^2 T_{ii'}^a T_{jj'}^b \delta_{ab}}{(p-p')^2} g_{\mu\nu} (2\eta_a Q + p + p')^\mu (2\eta_b Q - p - p')^\nu. \quad (\text{C.10})$$

In the non-relativistic limit using the instantaneous approximation we arrive at

$$\mathcal{W}_g(p, p'; Q) \simeq \frac{4ig_s^2 T_{ii'}^a T_{jj'}^a m_1 m_2}{(p-p')^2} \xrightarrow[\text{approx.}]{\text{inst.}} -\frac{4ig_s^2 T_{ii'}^a T_{jj'}^a m_1 m_2}{(\mathbf{p} - \mathbf{p}')^2}, \quad (\text{C.11})$$

Table C.1: Potentials and fine structure constants from top-philic (lepto-philic) mediator interactions $\tilde{t} \tilde{t}^*$ ($\tilde{\tau} \tilde{\tau}^*$) with SM particles. The electric charge of the top-philic (lepto-philic) mediator is $Q_{\text{em}}^{\tilde{t}} = 2/3$ ($Q_{\text{em}}^{\tilde{\tau}} = -1$). The gluon potential is only generated by the top-philic mediator, for which we consider $\mathbf{R}_1 = \mathbf{3}$, $\mathbf{R}_2 = \bar{\mathbf{3}}$ and $\hat{\mathbf{R}} \in \{\mathbf{1}, \mathbf{8}\}$.

gauge boson	$V(r)$	α
gluon	$V_g(r) = -\frac{\alpha_g}{r}$	$\alpha_g = \frac{1}{2} \left[C_2(\mathbf{R}_1) + C_2(\mathbf{R}_2) - C_2(\hat{\mathbf{R}}) \right] \alpha_s$
photon	$V_\gamma(r) = -\frac{\alpha_\gamma}{r}$	$\alpha_\gamma = Q_{\text{em}}^2 \alpha_{\text{em}}$
Z boson	$V_Z(r) = -\frac{\alpha_Z}{r} e^{-m_Z r}$	$\alpha_Z = Q_{\text{em}}^2 \tan^2 \theta_W \alpha_{\text{em}}$
Higgs boson	$V_H(r) = -\frac{\alpha_H}{r} e^{-m_H r}$	$\alpha_H = \frac{\lambda_H^2 v^2}{16\pi m_{\tilde{t}}^2}$

where we identify $m_\varphi = 0$ and $\Sigma = -4g_s^2 T_{ii'}^a T_{jj'}^a m_1 m_2$ (summing over a) with i, j ($i' j'$) the initial (final) state color charges of the particles. We again take $m_1 = m_2 = m_{\tilde{t}}$ and set $\alpha_g = -T_{ii'}^a T_{jj'}^a g_s^2 / (4\pi) = -T_{ii'}^a T_{jj'}^a \alpha_s$ with $\alpha_s = g_s^2 / (4\pi)$ the fine structure constant of the strong interaction. It is also advantageous to rewrite $-T_{ii'}^a T_{jj'}^a = [C_2(\mathbf{R}_1) + C_2(\mathbf{R}_2) - C_2(\hat{\mathbf{R}})]/2$, with C_2 denoting the quadratic Casimir operator and $\mathbf{R}_1, \mathbf{R}_2$ ($\hat{\mathbf{R}}$) the initial (final) state representation(s).

Summary

A summary of the potentials and interaction strengths can be found in Table C.1. We can see that for a particle antiparticle pair, the potentials of the γ and Z are attractive. The Higgs potential is always attractive and the gluon potential can be either attractive or repulsive depending on the representation $\hat{\mathbf{R}}$ of the final state. Free colored particles are in the (anti-)fundamental representation $\mathbf{R}_1 = \mathbf{3}$, $\mathbf{R}_2 = \bar{\mathbf{3}}$, such that $\hat{\mathbf{R}}$ can be either the octet or singlet representation, since $\mathbf{3} \otimes \bar{\mathbf{3}} = \mathbf{8} \oplus \mathbf{1}$. With the quadratic Casimir operators $C_2(\mathbf{3}) = C_2(\bar{\mathbf{3}}) = 4/3$, $C_2(\mathbf{8}) = 3$, and $C_2(\mathbf{1}) = 0$, we obtain two possible structure constants $\alpha_{g, [\mathbf{1}]} = 4/3 \alpha_s$ and $\alpha_{g, [\mathbf{8}]} = -1/6 \alpha_s$, depending on the final state representation of the $\tilde{t} \tilde{t}^*$ pair. We can immediately see, that the singlet final state potential is attractive and the octet one repulsive.

Considering a colored mediator, $Q_{\text{em}}^{\tilde{t}} = 2/3$, $\tan^2 \theta_W = 0.287$, $v = 246$ GeV, $\alpha_{\text{em}} \sim 0.0078$, $\alpha_s \sim 0.15$, mediator masses $m_{\tilde{t}} \gtrsim 1$ TeV, and natural choices for $\lambda_H \sim \mathcal{O}(1)$, we can immediately see that the gluon potential always dominates, given that the temperature $T \gg \Lambda_{\text{QCD}} \sim 400$ MeV remains well above the confinement scale of QCD in the regime of interest, which we will assume throughout this work. Thus, we will assume a Coulomb potential for the colored mediator \tilde{t} generated by gluon interactions and neglect all other contributions in the following.

For an uncolored mediator $\tilde{\tau}$ with $Q_{\text{em}}^{\tilde{\tau}} = -1$, the γ , Z and h contributions are sizeable due to the absence of the gluon potential and have to be taken into account for the calculation of the SE factor in annihilations. A remaining open question is, if the potentials created by Higgs and Z boson exchange are strong enough to support BS. The answer follows from the discussion in Section 5.1.3, where we formulated the condition $\xi > \xi_c$ for BS to exist. Only considering the ground state, for the Z -potential this bound can be translated to $m_{\tilde{\tau}} \gtrsim 68$ TeV, which is well above our regime of interest. Employing a Higgs potential, even for sizable $\lambda_H \sim \mathcal{O}(1)$ the bound leads to $m_{\tilde{\tau}} \lesssim 6$ GeV, which has been ruled out by collider experiments (cf. Section 6.5). Therefore, also in case of an uncolored mediator we can restrict ourselves to a Coulomb (γ -)potential when calculating the BSF cross section and decay rate.

Non-relativistic potentials for a (pseudo-)scalar mediator model

The model considered in Section 7 involves the interaction Lagrangian

$$\mathcal{L}_{\text{int}}^{\phi} \supset -\bar{\chi} (g + ig_5 \gamma^5) \chi \phi, \quad (\text{C.12})$$

where $\bar{\chi}\chi$ is a fermion antifermion pair and ϕ denotes a scalar mediator with g (g_5) the interaction strength of the (pseudo-)scalar coupling. For a purely scalar interaction, the interaction kernel is given by

$$\mathcal{W}_{\phi}^{g^2}(p, p'; Q) \simeq -\frac{ig^2 \delta_{rr'} \delta_{ss'}}{(p - p')^2 - m_{\phi}^2} \xrightarrow[\text{approx.}]{\text{inst.}} \frac{ig^2}{(\mathbf{p} - \mathbf{p}')^2 + m_{\phi}^2}, \quad (\text{C.13})$$

where $r^{(i)}$, $s^{(i)}$ denote the spin indices of the incoming (outgoing) particles, which are dropped in the non-relativistic limit. We identify $m_{\varphi} = m_{\phi}$, $\Sigma = g^2$, and thus $\alpha \equiv \alpha_{g^2} = g^2/(4\pi)$ due to the extra factor of $4m\mu$ in the definition of the non-relativistic potential for a fermionic system (cf. end of Section 5.2.1).

For interactions involving pseudo-scalar couplings, the simple modifications performed in Section 5.2.1 to obtain a non-relativistic potential for a fermionic system starting from a scalar one cannot be applied any longer. However, we argue that the strength of such potentials (apart from assuming $g_5 < g$) will be suppressed by factors of $\mathbf{p}^2/(2\mu)$ (cf. Section 5.3.2). Therefore, the scalar potential will always dominate over the pseudo-scalar contributions, such that we will neglect the latter in our derivation of the Schrödinger wave functions.

D Sommerfeld enhancement from the Bethe-Salpeter approach

Here, we want to derive the SE factors for annihilation and BS decay that we used in Sections 5.1.2 and 5.1.3 employing the tools introduced in Section 5.2. The steps taken will be similar to the ones in Section 5.2.2. We start with the corresponding S-matrix elements of a two-particle (bound) state annihilating (decaying) into N final states, which are given by

$$\langle f_1 f_2 \dots f_N | \mathcal{U}_{\mathbf{K}, \mathbf{k}} \rangle_{\text{in}} = \langle f_1 f_2 \dots f_N | \mathbf{S} | \mathcal{U}_{\mathbf{K}, \mathbf{k}} \rangle, \quad (\text{D.1})$$

$$\langle f_1 f_2 \dots f_N | \mathcal{B}_{\mathbf{K}, n} \rangle_{\text{in}} = \langle f_1 f_2 \dots f_N | \mathbf{S} | \mathcal{B}_{\mathbf{K}, n} \rangle, \quad (\text{D.2})$$

and define the Green's function (which is structurally the same for both processes) as well as its Fourier transform

$$G(x_1, x_2; y_1, \dots, y_n) \equiv \langle \Omega | T \varphi(X_\varphi) \chi_1(y_1) \dots \chi_N(y_N) \chi_1^\dagger(x_1) \chi_2^\dagger(x_2) | \Omega \rangle, \quad (\text{D.3})$$

$$\tilde{G}(k_1, k_2; p_1, \dots, p_N) \equiv \prod_{j=1}^N \int d^4 y_j d^4 x_1 d^4 x_2 e^{-i(k_1 x_1 + k_2 x_2 - p_j x_j)} G(x_1, x_2; y_1, \dots, y_n). \quad (\text{D.4})$$

With \mathcal{A} denoting the sum of all connected and amputated diagrams with the respective in- and outgoing momenta k_1, k_2 and p_j , $j = 1, \dots, N$, we can decompose the Green's function into

$$\tilde{G}(\eta_1 K + k, \eta_2 K - k; p_1, \dots, p_N) \equiv \prod_{j=1}^N \tilde{S}_{f_j}(p_j) \int \frac{d^4 k'}{(2\pi)^4} \tilde{G}^{(4)}(k, k'; K) \mathcal{A}(\eta_1 K + k', \eta_2 K - k'; p_1, \dots, p_N), \quad (\text{D.5})$$

as sketched in Fig. D.1 with $\tilde{S}_{f_j}(p_j)$ the propagators of the final state particles. Defining further the perturbative matrix element via

$$\mathcal{A}(\eta_1 K + k, \eta_2 K - k; p_1, \dots, p_N) = i(2\pi)^4 \delta^{(4)} \left(K - \sum_{j=1}^N p_j \right) \mathcal{M}_{\text{ann}}^{\text{pert}}(\eta_1 K + k, \eta_2 K - k; p_1, \dots, p_N), \quad (\text{D.6})$$

we can again use the LSZ reduction formula in a similar fashion as in Section 5.2.2 to derive the two-particle annihilation and bound state decay matrix elements

$$\mathcal{M}_{\text{ann}} = \prod_{j=1}^N \sqrt{Z_{f_j}(\mathbf{p}_j)} \int \frac{d^4 q}{(2\pi)^4} \tilde{\Phi}_{\mathbf{K}, \mathbf{k}}(q) \mathcal{M}_{\text{ann}}^{\text{pert}}(\eta_1 K + q, \eta_2 K - q; p_1, \dots, p_N) \quad (\text{D.7})$$

$$\simeq \sqrt{2\varepsilon_{\mathbf{K}, \mathbf{k}}} \int \frac{d^3 q}{(2\pi)^3} \frac{\tilde{\phi}_{\mathbf{k}}(\mathbf{q})}{\sqrt{2\mathcal{N}_{\mathbf{K}}(\mathbf{q})}} \int \frac{dq^0}{2\pi} \frac{S(q; K)}{\mathcal{S}_0(\mathbf{q}; K)} \mathcal{M}_{\text{ann}}^{\text{pert}}(\eta_1 K + q, \eta_2 K - q; p_1, \dots, p_N), \quad (\text{D.8})$$

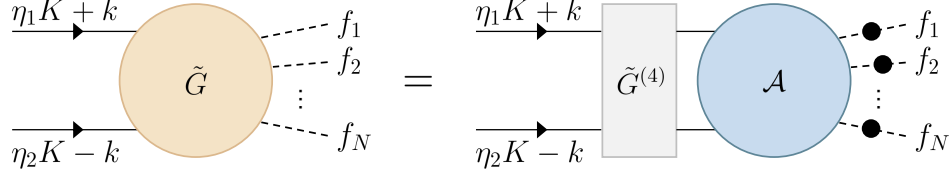


Figure D.1: Decomposition of the two-particle annihilation / BS decay Green's function \tilde{G} of a $\bar{\chi}\chi$ pair into N final states according to Eq. D.5. The black filled dots refer to the full propagators of the final state particles, whereas the gray box on the right denotes the 4-point Green's function $\tilde{G}^{(4)}$. The momenta of the incoming particles are also displayed in terms of total and relative momenta of the system. A definition of \mathcal{A} is given in the text. Adapted from Ref. [129].

$$\begin{aligned} \mathcal{M}_{\text{dec}}^{(n)} &= \prod_{j=1}^N \sqrt{Z_{f_j}(\mathbf{p}_j)} \int \frac{d^4 q}{(2\pi)^4} \tilde{\Psi}_{\mathbf{K},n}(q) \mathcal{M}_{\text{ann}}^{\text{pert}}(\eta_1 K + q, \eta_2 K - q; p_1, \dots, p_N) \quad (\text{D.9}) \\ &\simeq \int \frac{d^3 q}{(2\pi)^3} \frac{\tilde{\psi}_n(\mathbf{q})}{\sqrt{2\mathcal{N}_{\mathbf{K}}(\mathbf{q})}} \int \frac{dq^0}{2\pi} \frac{S(q; K)}{\mathcal{S}_0(\mathbf{q}; K)} \mathcal{M}_{\text{ann}}^{\text{pert}}(\eta_1 K + q, \eta_2 K - q; p_1, \dots, p_N), \quad (\text{D.10}) \end{aligned}$$

where we have taken the instantaneous approximation (cf. Eqs. 5.2.37 and 5.2.38) in the last step and set all renormalization factors $Z_{f_j}(\mathbf{p}_j) \simeq 1$ to leading order in α . For all practical purposes, the diagrams contributing to the perturbative matrix element will be fully connected such that we can replace $\mathcal{M}_{\text{ann}}^{\text{pert}}(\eta_1 K + q, \eta_2 K - q; p_1, \dots, p_N) \simeq \hat{\mathcal{M}}_{\text{ann}}^{\text{pert}}(\eta_1 \mathbf{K} + \mathbf{q}, \eta_2 \mathbf{K} - \mathbf{q}; \mathbf{p}_1, \dots, \mathbf{p}_N)$ with the on-shell annihilation amplitude which is of order \mathbf{q}^2 (cf. *on-shell approximation* in section 3.4 of Ref. [129]). Also approximating $\sqrt{2\mathcal{N}_{\mathbf{K}}(\mathbf{q})} \simeq \sqrt{2\mu}$ and $\varepsilon_{\mathbf{K},\mathbf{k}} \simeq \mu$ to leading order in \mathbf{q}^2 and \mathbf{k}^2 , we arrive at

$$\mathcal{M}_{\text{ann}} \simeq \int \frac{d^3 q}{(2\pi)^3} \tilde{\phi}_{\mathbf{k}}(\mathbf{q}) \hat{\mathcal{M}}_{\text{ann}}^{\text{pert}}(\eta_1 \mathbf{K} + \mathbf{q}, \eta_2 \mathbf{K} - \mathbf{q}; \mathbf{p}_1, \dots, \mathbf{p}_N), \quad (\text{D.11})$$

$$\mathcal{M}_{\text{dec}}^{(n)} \simeq \frac{1}{\sqrt{2\mu}} \int \frac{d^3 q}{(2\pi)^3} \tilde{\psi}_n(\mathbf{q}) \hat{\mathcal{M}}_{\text{ann}}^{\text{pert}}(\eta_1 \mathbf{K} + \mathbf{q}, \eta_2 \mathbf{K} - \mathbf{q}; \mathbf{p}_1, \dots, \mathbf{p}_N), \quad (\text{D.12})$$

for annihilation and decay of a $\bar{\chi}\chi$ pair into N arbitrary final states.

Conforming to Section 5.1, we will now focus on particle antiparticle annihilation and bound state decay into two final state particles. Within the COM frame, the 3-momenta yield $\mathbf{K} = 0$ and $|\mathbf{p}_1| = |\mathbf{p}_2| \equiv |\mathbf{p}|$. The perturbative on-shell matrix element can then be expanded into partial waves like

$$\hat{\mathcal{M}}_{\text{ann}}^{\text{pert}}(\mathbf{q}, -\mathbf{q}; \mathbf{p}, -\mathbf{p}) = \sum_{l=0}^{\infty} \frac{\tilde{a}_l}{(m\mu)^l} |\mathbf{p}|^l |\mathbf{q}|^l P_l(\cos \theta_{\mathbf{q},\mathbf{p}}), \quad (\text{D.13})$$

where we can express the \mathbf{q} -dependence of $\tilde{a}_l(\mathbf{q}) \simeq a_l + \mathcal{F}_l(\mathbf{q}^2, \boldsymbol{\epsilon}_A \cdot \mathbf{q})$ with $\boldsymbol{\epsilon}_A$ denoting the polarization vectors of possible vector boson final states and $\mathcal{F}_l \rightarrow 0$ for $\mathbf{q} \rightarrow 0$. In accordance with the approximations done so far, it will suffice to only consider a_l in the following.⁶⁹ We can also expand the full matrix elements \mathcal{M}_{ann} in terms of partial waves

$$\mathcal{M}_{\text{ann}}(\Omega_{\mathbf{p}}) = \sum_{l=0}^{\infty} \frac{(2l+1)}{4\pi} P_l(\cos \theta_{\mathbf{p}}) \mathcal{M}_{\text{ann},l}, \quad \text{where} \quad (\text{D.14})$$

$$\mathcal{M}_{\text{ann},l} \equiv \int d\Omega_{\mathbf{p}} P_l(\cos \theta_{\mathbf{p}}) \mathcal{M}_{\text{ann}}(\Omega_{\mathbf{p}}) \quad (\text{D.15})$$

are its projected l -wave contributions, and equivalently for $\mathcal{M}_{\text{dec}}^{(n)}$. The partial wave expanded annihilation cross section and decay width are then given by (cf. Eqs. 4.1.14 and 4.3.8)

$$\sigma_{\text{ann}} = \frac{f_s}{64\pi^2 s} \frac{p_c^*}{p_a^*} \int d\Omega_{\mathbf{p}} |\overline{\mathcal{M}_{\text{ann}}(\Omega_{\mathbf{p}})}|^2 = \frac{f_s}{128\pi^2 m \mu v_{\text{rel}}} \sum_{l=0}^{\infty} \frac{2l+1}{4\pi} |\overline{\mathcal{M}_{\text{ann},l}}|^2, \quad (\text{D.16})$$

$$\Gamma_{\text{dec}}^{(n)} = \frac{f_s}{32\pi^2} \frac{p^*}{M_n^2} \int d\Omega_{\mathbf{p}} |\overline{\mathcal{M}_{\text{dec}}(\Omega_{\mathbf{p}})}|^2 = \frac{f_s}{64\pi^2 m} \sum_{l=0}^{\infty} \frac{2l+1}{4\pi} |\overline{\mathcal{M}_{\text{dec},l}^{(n)}}|^2. \quad (\text{D.17})$$

Note that we have in the second step also expanded s and p_a^* to leading order in \mathbf{k} , neglected the final state particle masses for simplicity and set $|\mathbf{p}| \simeq (m + \mathcal{E}_{\mathbf{k}})/2 \simeq m/2$ or $|\mathbf{p}| \simeq M_n/2 = (m + \mathcal{E}_n)/2 \simeq m/2$ to their leading order values in v_{rel} or α , respectively.

Inserting Eq. D.11 (or Eq. D.12, respectively) into Eq. D.15 and using the identity Eq. A.25 we arrive at

$$\mathcal{M}_{\text{ann},l} \simeq \frac{a_l |\mathbf{p}|^l (2l+1)!!}{(m\mu)^l i^l (2l+1)!} \left[\frac{d^l}{dr^l} \int d\Omega_{\mathbf{r}} P_l(\cos \theta_{\mathbf{r}}) \phi_{\mathbf{k}}(\mathbf{r}) \right]_{\mathbf{r}=0}, \quad (\text{D.18})$$

$$\mathcal{M}_{\text{dec},l}^{(n)} \simeq \frac{a_l |\mathbf{p}|^l (2l+1)!!}{\sqrt{2\mu} (m\mu)^l i^l (2l+1)!} \left[\frac{d^l}{dr^l} \int d\Omega_{\mathbf{r}} P_l(\cos \theta_{\mathbf{r}}) \psi_n(\mathbf{r}) \right]_{\mathbf{r}=0}, \quad (\text{D.19})$$

which can in turn be incorporated in Eqs. D.16 and D.17. Defining further

$$\sigma_l \equiv \frac{f_s}{32\pi m \mu} \frac{|a_l|^2}{4^l (2l+1)}, \quad (\text{D.20})$$

$$v_{\text{rel}}^{2l} S_{\text{ann},l} \equiv \frac{[(2l+1)!/(l!)^2]^2}{4^{l+2} \pi^2 \mu^{2l}} \left| \frac{d^l}{dr^l} \int d\Omega_{\mathbf{r}} P_l(\cos \theta_{\mathbf{r}}) \phi_{\mathbf{k}}(\mathbf{r}) \right|_{\mathbf{r}=0}^2, \quad (\text{D.21})$$

$$S_{\text{dec},l}^{(n)} \equiv \frac{[(2l+1)!/(l!)^2]^2}{4^{l+2} \pi^2 \mu^{2l}} \left| \frac{d^l}{dr^l} \int d\Omega_{\mathbf{r}} P_l(\cos \theta_{\mathbf{r}}) \psi_n(\mathbf{r}) \right|_{\mathbf{r}=0}^2, \quad (\text{D.22})$$

⁶⁹Note that a_l and \mathcal{F}_l can still depend on \mathbf{p} through \mathbf{p}^2 and $\mathbf{p} \cdot \boldsymbol{\epsilon}_A$, as well as on $\boldsymbol{\epsilon}_A \cdot \boldsymbol{\epsilon}_B$ contributions.

we can cast $\sigma_{\text{ann}}v_{\text{rel}}$ and $\Gamma_{\text{dec}}^{(n)}$ into the form given in Eqs. 5.1.1 and 5.1.2. Using the partial wave expansion for the Schrödinger wave functions as given in Eqs. 5.1.9 and 5.1.10, we will recover the SE factors for two-particle annihilation and bound state decay as stated in Eqs. 5.1.20 and 5.1.30. To leading order in the momenta, the derivation of the SE factors is not affected by the spin of the interacting particles. Any differences between bosonic and fermionic particles arising in the non-relativistic limit can be absorbed in a redefinition of the a_l .

E Overlap integrals

We want to illustrate the computation of the following overlap integrals

$$\mathcal{I}_{\mathbf{k},n}(\mathbf{b}) \equiv \int \frac{d^3p}{(2\pi)^3} \tilde{\psi}_n^*(\mathbf{p}) \tilde{\phi}_{\mathbf{k}}(\mathbf{p} + \mathbf{b}) = \int d^3r \psi_n^*(\mathbf{r}) \phi_{\mathbf{k}}(\mathbf{r}) e^{-i\mathbf{b}\cdot\mathbf{r}}, \quad (\text{E.1})$$

$$\mathcal{J}_{\mathbf{k},n}(\mathbf{b}) \equiv \int \frac{d^3p}{(2\pi)^3} \mathbf{p} \tilde{\psi}_n^*(\mathbf{p}) \tilde{\phi}_{\mathbf{k}}(\mathbf{p} + \mathbf{b}) = i \int d^3r [\nabla \psi_n^*(\mathbf{r})] \phi_{\mathbf{k}}(\mathbf{r}) e^{-i\mathbf{b}\cdot\mathbf{r}}, \quad (\text{E.2})$$

$$\mathcal{K}_{\mathbf{k},n}(\mathbf{b}) \equiv \int \frac{d^3p}{(2\pi)^3} \mathbf{p}^2 \tilde{\psi}_n^*(\mathbf{p}) \tilde{\phi}_{\mathbf{k}}(\mathbf{p} + \mathbf{b}) = - \int d^3r [\nabla^2 \psi_n^*(\mathbf{r})] \phi_{\mathbf{k}}(\mathbf{r}) e^{-i\mathbf{b}\cdot\mathbf{r}}, \quad (\text{E.3})$$

$$\mathcal{Y}_{\mathbf{k},n} \equiv 8\pi \mu \alpha_{s,[1]}^{\text{NA}} \int \frac{d^3p}{(2\pi)^3} \frac{d^3q}{(2\pi)^3} \frac{\mathbf{q} - \mathbf{p}}{(\mathbf{q} - \mathbf{p})^4} \tilde{\psi}_n^*(\mathbf{p}) \tilde{\phi}_{\mathbf{k}}(\mathbf{q}) = -i \mu \alpha_{s,[1]}^{\text{NA}} \int d^3r \psi_n^*(\mathbf{r}) \phi_{\mathbf{k}}(\mathbf{r}) \hat{\mathbf{r}}, \quad (\text{E.4})$$

for various purposes throughout this work. We note that the squared brackets within the definitions indicate that the derivatives are only taken with respect to $\psi_n^*(\mathbf{r})$. Their derivation has been adapted from the appendices of Refs. [136, 145].

$\mathcal{J}_{\mathbf{k},\{100\}}$ and $\mathcal{Y}_{\mathbf{k},\{100\}}$ in the top-philic mediator model

The following derivation can also be found in App. B of Ref. [136]. We will start here with a more convenient (but equivalent) definition of the Coulomb Schrödinger wave functions (cf. Eqs. 5.1.9, 5.1.10, 5.1.18 and 5.1.19)

$$\phi_{\mathbf{k}}(\mathbf{r}) \equiv \sqrt{S_0(\zeta_S)} {}_1F_1(i\zeta_S; 1; i(kr - \mathbf{k} \cdot \mathbf{r})) e^{i\mathbf{k}\cdot\mathbf{r}}, \quad (\text{E.5})$$

$$\psi_n(\mathbf{r}) \equiv \kappa^{3/2} \sqrt{\frac{4(n-l-1)!}{n^4(n+l)!}} \left(\frac{2\kappa r}{n}\right)^l L_{n-l-1}^{(2l+1)}\left(\frac{2\kappa r}{n}\right) e^{-\kappa r/n} Y_{lm}(\Omega_{\mathbf{r}}), \quad (\text{E.6})$$

where ${}_1F_1(a; c; x)$, $L_n^{(\alpha)}(x)$, and $Y_{lm}(\Omega_{\mathbf{r}})$ are defined in Eqs. A.14, A.26 and A.36, respectively. Using $\hat{\mathbf{r}} e^{-i\mathbf{b}\cdot\mathbf{r}} = i \nabla_{\mathbf{b}} e^{-i\mathbf{b}\cdot\mathbf{r}} / r$ together with the identity [306]

$$\int d^3r \frac{e^{i(\mathbf{k}-\mathbf{b})\cdot\mathbf{r} - \kappa r}}{4\pi r} {}_1F_1(i\zeta_S; 1; i(kr - \mathbf{k} \cdot \mathbf{r})) = \frac{[\mathbf{b}^2 + (\kappa - ik)^2]^{-i\zeta_S}}{[(\mathbf{k} - \mathbf{b})^2 + \kappa^2]^{1-i\zeta_S}} \equiv f_{\mathbf{k},\mathbf{b}}(\kappa), \quad (\text{E.7})$$

we can write the overlap integrals for BSF into the ground state as

$$\mathcal{J}_{\mathbf{k},\{100\}}(\mathbf{b}) = \mu \alpha_{g,[1]}^B \sqrt{16\pi\kappa^3 S_0(\zeta_S)} [\nabla_{\mathbf{b}} f_{\mathbf{k},\mathbf{b}}(\kappa)], \quad (\text{E.8})$$

$$\mathcal{Y}_{\mathbf{k},\{100\}} = \mu \alpha_{s,[1]}^{\text{NA}} \sqrt{16\pi\kappa^3 S_0(\zeta_S)} [\nabla_{\mathbf{b}} f_{\mathbf{k},\mathbf{b}}(\kappa)]_{\mathbf{b}=0}. \quad (\text{E.9})$$

For the BSF cross section in the top-philic mediator model, we only need $\mathcal{J}_{\mathbf{k},\{100\}} \equiv \mathcal{J}_{\mathbf{k},\{100\}}(0)$. In order to calculate the squared matrix element in Eq. 6.3.26 for the ground state, it is therefore sufficient to determine

$$\frac{\mathcal{Y}_{\mathbf{k},\{100\}}}{\mathcal{J}_{\mathbf{k},\{100\}}} = \frac{\alpha_{s,[1]}^{\text{NA}}}{\alpha_{g,[1]}^B} \quad \text{and} \quad |\mathcal{J}_{\mathbf{k},\{100\}}|^2 = \frac{2^6 \pi}{k} S_0(\zeta_S) (1 + \zeta_S^2) \frac{\zeta_B^5 e^{-4\zeta_S \operatorname{arccot} \zeta_B}}{(1 + \zeta_B^2)^4}, \quad (\text{E.10})$$

where for the latter quantity we made use of the identity stated in Eq. A.46.

$\mathcal{I}_{\mathbf{k},\{nlm\}}$ and $\mathcal{K}_{\mathbf{k},\{nlm\}}$ in the (pseudo-)scalar mediator model

The following derivation can also be found in App. B of Ref. [145]. We first split up the Yukawa-type scattering and BS wave functions into radial and angular parts (cf. Eqs. 5.1.9 and 5.1.10), which we insert into the definitions of $\mathcal{I}_{\mathbf{k},\{nlm\}}$ and $\mathcal{K}_{\mathbf{k},\{nlm\}}$. Expanding $e^{-i\mathbf{b}\cdot\mathbf{r}}$ in partial waves (cf. Eq. A.22) and rewriting the Legendre polynomials in terms of spherical harmonics (cf. Eq. A.23), we can apply Eq. A.33 to cast the overlap integrals into the following form

$$\begin{aligned} \mathcal{I}_{\mathbf{k},\{nlm\}}(\mathbf{b}) &= \left(\frac{4\pi}{\kappa}\right)^{3/2} \sum_{s=0}^{\infty} \sum_{l_R=0}^{\infty} \left(\frac{b}{\kappa}\right)^{l_R+2s} \frac{(-1)^{l_R+s} i^{l_R}}{2^s s! (2l_R + 2s + 1)!!} \\ &\quad \sum_{l_I=0}^{\infty} \sum_{m_R=-l_R}^{l_R} \sum_{m_I=-l_I}^{l_I} (-1)^{m_I} Y_{l_I m_I}^*(\Omega_{\mathbf{k}}) Y_{l_R m_R}(\Omega_{\mathbf{b}}) \\ &\quad \sqrt{(2l+1)(2l_R+1)(2l_I+1)} \begin{pmatrix} l & l_R & l_I \\ 0 & 0 & 0 \end{pmatrix} \begin{pmatrix} l & l_R & l_I \\ -m & -m_R & m_I \end{pmatrix} \\ &\quad \int dx x^{l_R+2s} \chi_{nl}^*(x) \chi_{\mathbf{k},l_I}(x), \end{aligned} \quad (\text{E.11})$$

$$\begin{aligned} \mathcal{K}_{\mathbf{k},\{nlm\}}(\mathbf{b}) &= \sqrt{(4\pi)^3 \kappa} \sum_{s=0}^{\infty} \sum_{l_R=0}^{\infty} \left(\frac{b}{\kappa}\right)^{l_R+2s} \frac{(-1)^{l_R+s} i^{l_R}}{2^s s! (2l_R + 2s + 1)!!} \\ &\quad \sum_{l_I=0}^{\infty} \sum_{m_R=-l_R}^{l_R} \sum_{m_I=-l_I}^{l_I} (-1)^{m_I} Y_{l_I m_I}^*(\Omega_{\mathbf{k}}) Y_{l_R m_R}(\Omega_{\mathbf{b}}) \\ &\quad \sqrt{(2l+1)(2l_R+1)(2l_I+1)} \begin{pmatrix} l & l_R & l_I \\ 0 & 0 & 0 \end{pmatrix} \begin{pmatrix} l & l_R & l_I \\ -m & -m_R & m_I \end{pmatrix} \\ &\quad \int dx \left[-\gamma_{nl}^2(\xi) + \frac{2}{x} e^{-x/\xi} \right] x^{l_R+2s} \chi_{nl}^*(x) \chi_{\mathbf{k},l_I}(x), \end{aligned} \quad (\text{E.12})$$

where we used the Schrödinger equation for BS (cf. Eq. 5.1.4) in the last line to replace $\nabla^2 \psi_n^*(\mathbf{r})$. The quantities in the third lines correspond to the Wigner-3j symbols (see App. A). Using their properties, we can write the overlap integrals for the S states (i. e. $l, m = 0$) as an expansion in b/κ

$$\begin{aligned} \mathcal{I}_{\mathbf{k},\{n00\}}(\mathbf{b}) &= -\sqrt{\frac{4\pi}{\kappa^3}} \left\{ \left(\frac{b}{\kappa}\right) i P_1(\hat{\mathbf{k}} \cdot \hat{\mathbf{b}}) \int_0^{\infty} dx x \chi_{n0}^*(x) \chi_{\mathbf{k},1}(x) \right. \\ &\quad + \left(\frac{b}{\kappa}\right)^2 \left[\frac{1}{6} P_0(\hat{\mathbf{k}} \cdot \hat{\mathbf{b}}) \int_0^{\infty} dx x^2 \chi_{n0}^*(x) \chi_{\mathbf{k},0}(x) \right. \\ &\quad \left. \left. + \frac{1}{3} P_2(\hat{\mathbf{k}} \cdot \hat{\mathbf{b}}) \int_0^{\infty} dx x^2 \chi_{n0}^*(x) \chi_{\mathbf{k},2}(x) \right] \right\} + \mathcal{O}((b/\kappa)^3) \end{aligned} \quad (\text{E.13})$$

$$\mathcal{K}_{\mathbf{k},\{n00\}}(\mathbf{b}) = \sqrt{4\pi\kappa} P_0(y) \int_0^{\infty} dx \frac{2}{x} e^{-x/\xi} \chi_{n0}^*(x) \chi_{\mathbf{k},0}(x) + \mathcal{O}((b/\kappa)), \quad (\text{E.14})$$

up to the corresponding order required in our work.⁷⁰ As we can see, the $(b/\kappa)^0$ term in $\mathcal{I}_{\mathbf{k},\{n00\}}$ as well as the γ_{nl}^2 term in $\mathcal{K}_{\mathbf{k},\{n00\}}$ vanish, due to the orthogonality relation

$$\int_0^\infty dx \chi_{nl}^*(x) \chi_{\mathbf{k},l}(x) = 0. \quad (\text{E.15})$$

⁷⁰This expansion is essentially equivalent to an expansion in α and $v_{\text{rel}} \lesssim \alpha$, since in our work $b \propto |\mathbf{P}_\phi|$, which is of $\mathcal{O}(\alpha^2 + v_{\text{rel}}^2)$.

F BSF in thermal freeze-out from the Bethe-Salpeter approach

We will calculate in the following the BSF cross section of thermal DM within the model employed in Section 7 using the methodology outlined in Section 5.2.2. The computation will be similar to the one performed for the non-thermal DM model in Section 6.3.2. The process under consideration is given by $\bar{\chi} + \chi \rightarrow \mathcal{B}(\bar{\chi}\chi) + \phi$ with χ a (Dirac) fermionic DM candidate and ϕ a scalar mediator. We will start again with the transition matrix element (cf. Eq. 5.2.64)

$$\mathcal{M}_{\text{trans}}(\mathbf{p}, \mathbf{q}) \equiv (\mathcal{S}_0^f(\mathbf{p}, P))^{-1} (\mathcal{S}_0^f(\mathbf{q}, K))^{-1} \int \frac{dp^0}{2\pi} \frac{dq^0}{2\pi} \mathcal{C}_{\phi\text{-amp}}^{(5)}(q, p; K, P, P_\phi),$$

where the superscript f highlights the fermionic nature of the corresponding objects. As we will quickly change to a non-relativistic (scalar) interaction picture, following the prescription at the end of Section 5.2.1, we subsequently suppress spin indices as well as spin matching conditions to enhance readability. The two processes contributing to $\mathcal{C}_{\phi\text{-amp}} = \mathcal{C}_1^g + \mathcal{C}_2^g$ at leading order in the couplings are displayed in Fig. F.1. As stated in Section 7.1, all diagrams involving a g_5 vertex can be neglected at this order. The leading order contributions yield

$$\begin{aligned} i\mathcal{C}_1^g &= \tilde{S}_2^f(\eta_2 K - q) \tilde{S}_1^f(\eta_1 K + q) (-ig) \tilde{S}_1^f(\eta_1 P + p) (2\pi)^4 \delta^{(4)}(\eta_1 K + q - \eta_1 P - p - P_\phi) \\ &\simeq (-ig) (2m_1)^2 (2m_2) S(q; K) \tilde{S}_1(\eta_1 P + p) (2\pi)^4 \delta^{(4)}(q - p - \eta_2 P_\phi), \end{aligned} \quad (\text{F.1})$$

$$\begin{aligned} i\mathcal{C}_2^g &= \tilde{S}_1^f(\eta_1 K + q) \tilde{S}_2^f(\eta_2 K - q) (-ig) \tilde{S}_2^f(\eta_2 P - p) (2\pi)^4 \delta^{(4)}(\eta_2 K - q - \eta_2 P + p - P_\phi) \\ &\simeq (-ig) (2m_2)^2 (2m_1) S(q; K) \tilde{S}_2(\eta_2 P - p) (2\pi)^4 \delta^{(4)}(q - p + \eta_1 P_\phi), \end{aligned} \quad (\text{F.2})$$

where we approximated the fermionic propagators $\tilde{S}_i^f \rightarrow 2m_i \tilde{S}_i$ with the scalar ones to leading order in the momenta and used four-momentum conservation $K = P + P_\phi$ within the δ -distributions. Analogously, we transform $(\mathcal{S}_0^f)^{-1} \rightarrow (2m_1)^{-1} (2m_2)^{-1} (\mathcal{S}_0)^{-1}$ and use Eqs. 6.3.21 and 6.3.22 to approximate the integrals, such that the transition matrix element takes the simple form

$$\mathcal{M}_{\text{trans}}(\mathbf{p}, \mathbf{q}) \simeq (-ig) (2\pi)^3 \left[\delta^{(3)}(\mathbf{q} - \mathbf{p} - \eta_2 \mathbf{P}_\phi) + \delta^{(3)}(\mathbf{q} - \mathbf{p} + \eta_1 \mathbf{P}_\phi) \right]. \quad (\text{F.3})$$

The fermionic wave functions can be mapped at leading order to the spin-agnostic Schrödinger wave functions via $(\tilde{\psi}_n^f(\mathbf{p}))^* \tilde{\phi}_\mathbf{k}^f(\mathbf{q}) \rightarrow 4\mu m \tilde{\psi}_n^*(\mathbf{p}) \tilde{\phi}_\mathbf{k}(\mathbf{q})$, such that we obtain the BSF matrix element (cf. Eq. 5.2.66)

$$\mathcal{M}_{\mathbf{k} \rightarrow n} \simeq -4igm_\chi^{3/2} \left[\mathcal{I}_{\mathbf{k},n}(\mathbf{P}_\phi/2) + \mathcal{I}_{\mathbf{k},n}(-\mathbf{P}_\phi/2) - \frac{1}{2m_\chi^2} (\mathcal{K}_{\mathbf{k},n}(\mathbf{P}_\phi/2) + \mathcal{K}_{\mathbf{k},n}(-\mathbf{P}_\phi/2)) \right] \quad (\text{F.4})$$

after identifying $m_1 = m_2 = m_\chi$, $\eta_1 = \eta_2 = 1/2$, and with the definitions of the overlap integrals $\mathcal{I}_{\mathbf{k},n}$ and $\mathcal{K}_{\mathbf{k},n}$ given in Eqs. E.1 and E.3. We will only consider BSF into the ground state in the following, i. e. $n = \{100\}$. After expanding the overlap integrals in

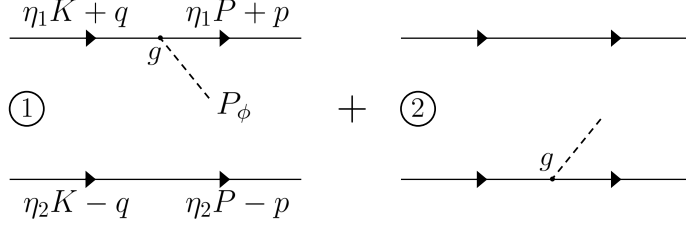


Figure F.1: Leading order diagrams to $\mathcal{C}_{\phi\text{-amp}}^{(5)}$ in the (pseudo-)scalar mediator model. The momenta of the incoming (outgoing) particles are also displayed in terms of the total and relative momenta of the system. The vertices only feature scalar interactions and the spin indices are suppressed.

α , one would usually expect the contributions from $\mathcal{K}_{\mathbf{k},\{100\}}$ to be of higher order, since they are naturally suppressed by a factor α^2 (cf. Eqs. E.13 and E.14). However, due to the vanishing α^0 term and the anti-symmetry of the α^1 term in the expansion of $\mathcal{I}_{\mathbf{k},\{100\}}$, both overlap integrals contribute at the same order in $\mathcal{M}_{\mathbf{k}\rightarrow\{100\}}$, which yields

$$\mathcal{M}_{\mathbf{k}\rightarrow\{100\}} \simeq i \frac{32\sqrt{2}\pi}{\alpha} \left[\frac{|\mathbf{P}_\phi|^2}{2\kappa^2} \left(\frac{1}{6} P_0(\cos\theta) A_0 + \frac{1}{3} P_2(\cos\theta) A_1 \right) - \frac{\kappa^2}{m_\chi^2} P_0(\cos\theta) B(\xi) \right]. \quad (\text{F.5})$$

This expression contains the following *radial overlap integrals*

$$A_j \equiv \int_0^\infty dx x^2 \chi_{10}^*(x) \chi_{\mathbf{k},2j}(x), \quad B(\xi) \equiv - \int_0^\infty dx \frac{2}{x} e^{-x/\xi} \chi_{10}^*(x) \chi_{\mathbf{k},0}(x), \quad (\text{F.6})$$

which have to be determined numerically, and $\cos\theta = \hat{\mathbf{P}}_\phi \cdot \hat{\mathbf{k}}$. The cross section can then be calculated via Eq. 5.2.69, which yields for BSF into the ground state $\sigma_{\text{BSF}v_{\text{rel}}} = \pi\alpha^4/m_\chi^2 S_{\text{BSF}}(\zeta, \xi)$ with

$$S_{\text{BSF}}(\zeta, \xi) \equiv \frac{\sqrt{\mathcal{P}_{10}(\zeta, \xi)}}{720} \left(\frac{1 + \zeta^2 \gamma_{10}^2(\xi)}{\zeta^2} \right) \left[\mathcal{P}_{10}^2(\zeta, \xi) \left(\frac{1 + \zeta^2 \gamma_{10}^2(\xi)}{\zeta^2} \right)^4 (5A_0^2 + 4A_1^2) - 120 \mathcal{P}_{10}(\zeta, \xi) \left(\frac{1 + \zeta^2 \gamma_{10}^2(\xi)}{\zeta^2} \right)^2 \text{Re} \{A_0^* B(\xi)\} + 720 B(\xi)^2 \right]. \quad (\text{F.7})$$

Here, $\mathcal{P}_{10}(\zeta, \xi)$ denotes the phase space suppression factor defined in Eq. 7.2.17. We can see that this expression is equivalent to Eq. 7.2.16 when identifying

$$\langle 1S | \mathbf{r}^2 | \mathbf{k} \rangle = \sqrt{\frac{4\pi}{\kappa^7}} A_0, \quad \langle 1S | \nabla_{\mathbf{r}}^2 | \mathbf{k} \rangle = \sqrt{4\pi\kappa} B(\xi), \quad |\langle \mathbf{k} | r^i r^j | 1S \rangle|^2 = \frac{4\pi}{\kappa^7} \left(\frac{1}{3} A_0^2 + \frac{2}{3} A_1^2 \right). \quad (\text{F.8})$$

G Higher bound states

We eventually want to estimate the effects of the inclusion of higher bound states on the total BSF cross section for the (pseudo-)scalar mediator model in Section 7. For this purpose, we go to the Coulomb regime, which will provide us with an analytic solution and the attained cross section can serve as an upper bound on our Yukawa-type problem. In the Coulomb limit ($\xi \rightarrow \infty$ or $m_\phi \rightarrow 0$), the BSF cross section into an arbitrary (n, l) bound state yields (cf. Eq. 7.2.13)

$$\begin{aligned} \sigma_{\text{BSF}}^{(nl)} v_{\text{rel}}(\zeta) &= \frac{\alpha}{120} \sum_{n,l} (\Delta \mathcal{E}_n^{\mathbf{k}})^5 [|\langle \mathbf{k} | \mathbf{r}^2 | nl \rangle|^2 + 2|\langle \mathbf{k} | r^i r^j | nl \rangle|^2] \\ &\quad + \frac{2\alpha}{m_\chi^2} \sum_{n,l} \Delta \mathcal{E}_n^{\mathbf{k}} |\langle \mathbf{k} | \nabla_{\mathbf{r}}^2 | nl \rangle|^2 - \frac{\alpha}{3m_\chi^2} \sum_{n,l} (\Delta \mathcal{E}_n^{\mathbf{k}})^3 \text{Re} \{ \langle \mathbf{k} | \mathbf{r}^2 | nl \rangle \langle nl | \nabla_{\mathbf{r}}^2 | \mathbf{k} \rangle \}, \end{aligned} \quad (\text{G.1})$$

where the summation over m is implicit, i. e. (cf. Eq. 7.2.14)

$$\langle \mathbf{k} | \mathcal{O} | nl \rangle = \sum_m \langle \mathbf{k} | \mathcal{O} | nlm \rangle = \sum_m \int d^3r \phi_{\mathbf{k}}^*(\mathbf{r}) \mathcal{O} \psi_{nlm}(\mathbf{r}), \quad (\text{G.2})$$

for \mathcal{O} denoting any of the operators above. We recall the decomposition of the scattering and BS wave functions into radial and angular parts (cf. Eqs. 5.1.9 and 5.1.10)

$$\begin{aligned} \phi_{\mathbf{k}}(\mathbf{r}) &= \sum_{l=0}^{\infty} (2l+1) \left[\frac{\chi_{\mathbf{k},l}(\kappa r)}{\kappa r} \right] P_l(\hat{\mathbf{k}} \cdot \hat{\mathbf{r}}), \\ \psi_{nlm}(\mathbf{r}) &= \kappa^{3/2} \left[\frac{\chi_{nl}(\kappa r)}{\kappa r} \right] Y_{lm}(\Omega_{\mathbf{r}}), \end{aligned}$$

where $P_l(\hat{\mathbf{k}} \cdot \hat{\mathbf{r}})$ and $Y_{lm}(\Omega_{\mathbf{r}})$ denote the Legendre polynomials and spherical harmonics, respectively (cf. App. A). For later convenience, we will generalize the definition of the radial overlap integrals in Eq. F.6 to arbitrary angular states and apply them to the Coulomb case. They are given by

$$A_j^{(nl)} \equiv \int_0^\infty dx x^2 \chi_{nl}^*(x) \chi_{\mathbf{k},l+2j}(x), \quad B_C^{(nl)} \equiv - \int_0^\infty dx \frac{2}{x} \chi_{nl}^*(x) \chi_{\mathbf{k},l}(x), \quad (\text{G.3})$$

with $x \equiv \kappa r$, where it is understood that $l+2j \geq 0$ for $j \in \{-1, 0, 1\}$. We will first perform the angular integrations, and calculate in a second step the radial overlap integrals in the Coulomb limit analytically.

The first quadrupole term $|\langle \mathbf{k} | \mathbf{r}^2 | nl \rangle|^2$

Employing the definition of the spherical harmonics given in Eq. A.26, which relates $P_l(\cos \theta) = \sqrt{4\pi/(2l+1)} Y_{l0}(\Omega)$, and using the orthonormality condition of Eq. A.27, we

can immediately write down

$$\langle \mathbf{k} | \mathbf{r}^2 | nlm \rangle = \sqrt{\frac{4\pi}{\kappa^7}} \sqrt{2l+1} \delta_{m0} \int_0^\infty dx x^2 \chi_{\mathbf{k},l}^*(x) \chi_{nl}(x), \quad (\text{G.4})$$

$$|\langle \mathbf{k} | \mathbf{r}^2 | nl \rangle|^2 = \frac{4\pi}{\kappa^7} (2l+1) \left| A_0^{(nl)} \right|^2. \quad (\text{G.5})$$

The derivative term $|\langle \mathbf{k} | \nabla_{\mathbf{r}}^2 | nl \rangle|^2$

Using the BS Schrödinger equation (cf. Eq. 5.1.4), we can rewrite $\nabla^2 \psi_{nlm}(\mathbf{r}) = 2\mu(V(\mathbf{r}) - \mathcal{E}_{nl})\psi_{nlm}(\mathbf{r})$. The term with the potential contribution can be calculated analogously to the first quadrupole term, whereas the BS energy term vanishes due to the orthogonality of the radial waves, given in Eq. E.15. The computation yields

$$\langle \mathbf{k} | \nabla_{\mathbf{r}}^2 | nlm \rangle = \sqrt{4\pi\kappa} \sqrt{2l+1} \delta_{m0} \left(- \int_0^\infty dx \frac{2}{x} \chi_{\mathbf{k},l}^*(x) \chi_{nl}(x) \right), \quad (\text{G.6})$$

$$|\langle \mathbf{k} | \nabla_{\mathbf{r}}^2 | nl \rangle|^2 = 4\pi\kappa (2l+1) \left| B_C^{(nl)} \right|^2. \quad (\text{G.7})$$

The mixed term between the first quadrupole and the derivative term is then given by

$$\text{Re} \left\{ \langle \mathbf{k} | \mathbf{r}^2 | nl \rangle \langle nl | \nabla_{\mathbf{r}}^2 | \mathbf{k} \rangle \right\} = \frac{4\pi}{\kappa^3} (2l+1) \text{Re} \left\{ \left(A_0^{(nl)} \right)^* B_C^{(nl)} \right\}. \quad (\text{G.8})$$

The second quadrupole term $|\langle \mathbf{k} | \mathbf{r}^i \mathbf{r}^j | nl \rangle|^2$

Expressing again $P_l(\cos\theta)$ in terms of $Y_{l0}(\Omega)$, we can write the quadrupole contribution as

$$\langle \mathbf{k} | \mathbf{r}^i \mathbf{r}^j | nlm \rangle = \sqrt{\frac{4\pi}{\kappa^7}} \sum_{l'=0}^{\infty} \sqrt{2l'+1} \int d\Omega_r \frac{r^i r^j}{r^2} Y_{l'0}(\Omega_r) Y_{lm}(\Omega_r) \int_0^\infty dx x^2 \chi_{\mathbf{k},l'}^*(x) \chi_{nl}(x). \quad (\text{G.9})$$

The quantity $r^i r^j / r^2$ is a rank 2 tensor, which can be itself written in terms of spherical harmonics (see e. g. Ref. [307]). The angular part of the squared quadrupole term then yields

$$\begin{aligned} & \left(\int d\Omega_r \frac{r^i r^j}{r^2} Y_{l'0}(\Omega_r) Y_{lm}(\Omega_r) \right)^* \left(\int d\Omega_r \frac{r^i r^j}{r^2} Y_{l''0}(\Omega_r) Y_{lm}(\Omega_r) \right) \\ &= \frac{4\pi}{15} \left[5 \left(\int d\Omega_r Y_{00}(\Omega_r) Y_{l'0}(\Omega_r) Y_{lm}(\Omega_r) \right)^* \left(\int d\Omega_r Y_{00}(\Omega_r) Y_{l''0}(\Omega_r) Y_{lm}(\Omega_r) \right) \right. \\ & \quad \left. + 2 \sum_{m'=-2}^2 \left(\int d\Omega_r Y_{2m'}(\Omega_r) Y_{l'0}(\Omega_r) Y_{lm}(\Omega_r) \right)^* \left(\int d\Omega_r Y_{2m'}(\Omega_r) Y_{l''0}(\Omega_r) Y_{lm}(\Omega_r) \right) \right]. \end{aligned} \quad (\text{G.10})$$

The first line can be evaluated as usual utilizing the orthonormality condition of spherical harmonics (cf. Eq. A.27), whereas the integrals in the second line can be connected to

the Wigner-3j functions via Eq. A.33. Summing over m and employing Eq. A.32, we obtain

$$|\langle \mathbf{k} | r^i r^j | nl \rangle|^2 = \frac{4\pi}{3\kappa^7} (2l+1) |A_0^{(nl)}|^2 + \frac{8\pi}{3\kappa^7} (2l+1) \sum_{j=-1}^1 K_{l+2j} |A_j^{(nl)}|^2, \quad (\text{G.11})$$

where we defined

$$K_{l'} \equiv (2l'+1) \begin{pmatrix} l & 2 & l' \\ 0 & 0 & 0 \end{pmatrix}^2 = \begin{cases} \frac{3}{2} \frac{(l-1)l}{(2l-1)(2l+1)} & \text{for } l' = l-2 \\ \frac{l(l+1)}{(2l-1)(2l+3)} & \text{for } l' = l \\ \frac{3}{2} \frac{(l+1)(l+2)}{(2l+1)(2l+3)} & \text{for } l' = l+2 \end{cases}, \quad (\text{G.12})$$

and all other relations between l' and l vanish due to the Wigner-3j properties.

Having performed all angular integrations, we can write the BSF cross section as $\sigma_{\text{BSF}}^{(nl)} v_{\text{rel}}(\zeta) = \pi\alpha^4/m_\chi^2 S_{\text{BSF}}^{(nl)}(\zeta)$ with

$$S_{\text{BSF}}^{(nl)}(\zeta) \equiv \frac{2l+1}{720} \left(\frac{1+\zeta^2/n^2}{\zeta^2} \right) \left[\left(\frac{1+\zeta^2/n^2}{\zeta^2} \right)^4 \left(5 |A_0^{(nl)}|^2 + 4 \sum_{j=-1}^1 K_{l+2j} |A_j^{(nl)}|^2 \right) - 120 \left(\frac{1+\zeta^2/n^2}{\zeta^2} \right)^2 \text{Re} \left\{ (A_0^{(nl)})^* B_C^{(nl)} \right\} + 720 |B_C^{(nl)}|^2 \right]. \quad (\text{G.13})$$

We can easily check that this is identical to Eq. F.7 for $(nl) = (10)$, $\xi \rightarrow \infty$ and thus $\mathcal{P}_{10}, \gamma_{10} \rightarrow 1$. On the contrary, Eq. G.13 also holds for the Yukawa case with $m_\phi > 0$, when reinstating generalized phase space suppression factors \mathcal{P}_{nl} in the logic of Eq. F.7 and replacing $1/n^2 \rightarrow \gamma_{nl}^2(\xi)$, $B_C^{(nl)} \rightarrow B^{(nl)}(\xi)$, all defined in analogy to $\mathcal{P}_{10}, \gamma_{10}$ and B .

The next step is to calculate the radial overlap integrals for the Coulomb wave functions (cf. Eqs. 5.1.18 and 5.1.19)

$$\chi_{\mathbf{k}, l'}(x) = \sqrt{S_0(\zeta) \prod_{s=1}^{l'} (s^2 + \zeta^2)} \frac{e^{i\delta_{l'}}}{(2l'+1)!} \left(\frac{2ix}{\zeta} \right)^{l'} x e^{-ix/\zeta} {}_1F_1 \left(1+l'+i\zeta; 2l'+2; \frac{2ix}{\zeta} \right), \quad (\text{G.14})$$

$$\chi_{nl}(x) = \frac{1}{n(2l+1)!} \sqrt{\frac{(n+l)!}{(n-l-1)!}} \left(\frac{2x}{n} \right)^{l+1} e^{-x/n} {}_1F_1 \left(-n+l+1; 2l+2; \frac{2x}{n} \right), \quad (\text{G.15})$$

where we employed Eqs. A.2 and A.15 to attain this particular form, with the confluent hypergeometric functions ${}_1F_1(a; c; x)$ defined in App. A. From there on, we can use Eqs. A.40 to A.43 to calculate the squared radial overlap integrals. The $\Delta l = 0$ integrals

yield

$$\begin{aligned} |A_0^{(nl)}|^2 &= \frac{2^{4(l+1)} n^{2l} (n+l)!}{(n-l-1)! ((2l+1)!)^2} \frac{\zeta^{2(l+2)}}{(n^2 + \zeta^2)^{2(l+1)}} \\ &\quad S_0(\zeta) \left(\prod_{s=1}^l (s^2 + \zeta^2) \right) e^{-4\zeta \operatorname{arccot}(\zeta/n)} |{}_2F_1(a, b; c; z)|^2, \end{aligned} \quad (\text{G.16})$$

$$|B_C^{(nl)}|^2 = \frac{1}{16} \left(\frac{1 + \zeta^2/n^2}{\zeta^2} \right)^4 |A_0^{(nl)}|^2, \quad \operatorname{Re} \left\{ (A_0^{(nl)})^* B_C^{(nl)} \right\} = \frac{1}{4} \left(\frac{1 + \zeta^2/n^2}{\zeta^2} \right)^2 |A_0^{(nl)}|^2, \quad (\text{G.17})$$

with $a \equiv 1 + l - n$, $b \equiv 1 + l + i\zeta$, $c \equiv 2l + 2$, $z \equiv 4in\zeta/(n + i\zeta)^2$ and ${}_2F_1(a, b; c; z)$ the hypergeometric function. This enables us to simplify the SE factor for BSF

$$S_{\text{BSF}}^{(nl)}(\zeta) = \frac{2l+1}{180} \left(\frac{1 + \zeta^2/n^2}{\zeta^2} \right)^5 \left(5 |A_0^{(nl)}|^2 + \sum_{j=-1}^1 K_{l+2j} |A_j^{(nl)}|^2 \right). \quad (\text{G.18})$$

The $\Delta l = 2$ integrals are of the form

$$\begin{aligned} |A_{\pm 1}^{(nl)}|^2 &= \frac{2^{4(l+1)} n^{2(l+2)} (n+l)!}{(l+1)^2 (n-l-1)! ((2l+1)!)^2} \frac{\zeta^{2(l+6)}}{(n^2 + \zeta^2)^{2l+9}} \\ &\quad S_0(\zeta) \left(\prod_{s=1}^l (s^2 + \zeta^2) \right) \frac{e^{-4\zeta \operatorname{arccot}(\zeta/n)}}{(l^2 + \zeta^2)} \\ &\quad \left[K_{\pm}^1 |{}_2F_1(a+1, b-1; c+1; z)|^2 + K_{\pm}^2 |{}_2F_1(a+2, b-1; c+1; z)|^2 \right. \\ &\quad \left. + 2K_{\pm}^{\operatorname{Re}} \operatorname{Re} \left\{ {}_2F_1(a+1, b-1; c+1; z)^* {}_2F_1(a+2, b-1; c+1; z) \right\} \right. \\ &\quad \left. - 2K_{\pm}^{\operatorname{Im}} \operatorname{Im} \left\{ {}_2F_1(a+1, b-1; c+1; z)^* {}_2F_1(a+2, b-1; c+1; z) \right\} \right], \end{aligned} \quad (\text{G.19})$$

with K_{\pm} (ratios of) polynomials of n, l and ζ , which are too extended to display here, and where it is understood that $|A_{-1}^{(nl)}|^2 = 0$ for $l < 2$. To obtain a first estimate on the effects of higher BS, we have displayed in Fig. G.1 the relative size of the (SE factor of the) BSF cross section into the n -th BS with respect to the ground state (a sum over l for each n is implicit). We can see that the biggest contribution comes from the $n = 2$ cross section, whereas the impact of higher BS becomes quickly suppressed. As we are chiefly interested in finite mediator masses, the impact of higher BS is expected to be even lower and the finite number of supported BS by a Yukawa potential prevents a logarithmic growth due to an infinite number of BS, as it has been observed in case of a Coulomb potential (see e. g. Ref. [172]). For a realistic estimate, it is thus sufficient to include only the lowest excited BS in the computations of Section 7.2.3. The explicit SE

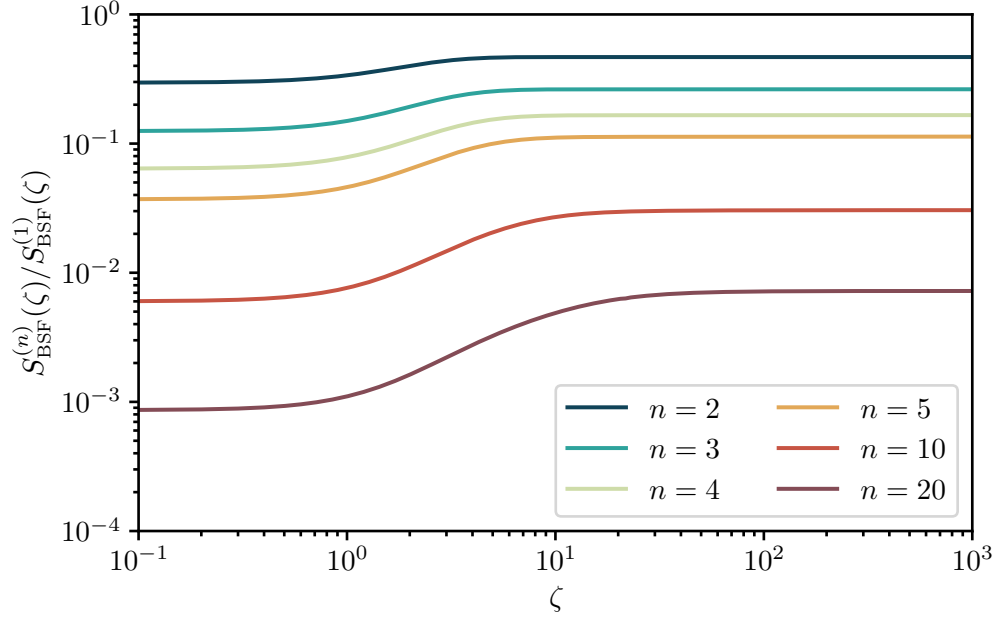


Figure G.1: The SE factor of BSF into the n -th BS compared to the ground state as a function of ζ in the Coulomb limit. The sum over $l = 0, \dots, n - 1$ for each n is left implicit.

factors for BSF up to $n = 2$ in the Coulomb limit from Eq. G.18 are given by

$$S_{\text{BSF}}^{(10)}(\zeta) = S_0(\zeta) \frac{2^6}{15} \frac{\zeta^2(7 + 3\zeta^2)}{(1 + \zeta^2)^2} e^{-4\zeta \operatorname{arccot}(\zeta)}, \quad (\text{G.20})$$

$$S_{\text{BSF}}^{(20)}(\zeta) = S_0(\zeta) \frac{2^5}{15} \frac{\zeta^2(448 + 528\zeta^2 + 100\zeta^4 + 15\zeta^6)}{(4 + \zeta^2)^4} e^{-4\zeta \operatorname{arccot}(\zeta/2)}, \quad (\text{G.21})$$

$$S_{\text{BSF}}^{(21)}(\zeta) = S_0(\zeta) \frac{2^9}{15} \frac{\zeta^4(1 + \zeta^2)(36 + 5\zeta^2)}{(4 + \zeta^2)^4} e^{-4\zeta \operatorname{arccot}(\zeta/2)}, \quad (\text{G.22})$$

with $S_0(\zeta) = 2\pi\zeta/(1 - e^{-2\pi\zeta})$. These results agree well with the literature (see e. g. Ref. [141]).

References

- [1] G. Bertone, D. Hooper, and J. Silk. “Particle dark matter: Evidence, candidates and constraints”. In: *Phys. Rept.* 405 (2005), pp. 279–390. arXiv: [hep-ph/0404175](#).
- [2] J. Silk et al. *Particle Dark Matter: Observations, Models and Searches*. Ed. by G. Bertone. Cambridge: Cambridge Univ. Press, 2010.
- [3] M. Bauer and T. Plehn. *Yet Another Introduction to Dark Matter: The Particle Physics Approach*. Vol. 959. Lecture Notes in Physics. Springer, 2019. arXiv: [1705.01987 \[hep-ph\]](#).
- [4] S. Tulin and H.-B. Yu. “Dark Matter Self-interactions and Small Scale Structure”. In: *Phys. Rept.* 730 (2018), pp. 1–57. arXiv: [1705.02358 \[hep-ph\]](#).
- [5] J. Bollig and S. Vogl. “Impact of bound states on non-thermal dark matter production”. In: *JCAP* 10 (2022), p. 031. arXiv: [2112.01491 \[hep-ph\]](#).
- [6] S. Biondini, J. Bollig, and S. Vogl. “Indirect detection of dark matter with (pseudo)-scalar interactions”. In: *JHEP* 04 (2024), p. 050. arXiv: [2308.14594 \[hep-ph\]](#).
- [7] R. L. Workman et al. “Review of Particle Physics”. In: *PTEP* 2022 (2022), p. 083 C01.
- [8] N. Aghanim et al. “Planck 2018 results. VI. Cosmological parameters”. In: *Astron. Astrophys.* 641 (2020), A6. arXiv: [1807.06209 \[astro-ph.CO\]](#). [Erratum: *Astron. Astrophys.* 652, C4 (2021)].
- [9] D. Baumann. *Cosmology*. Cambridge University Press, 2022.
- [10] S. Dodelson. *Modern Cosmology*. Amsterdam: Academic Press, 2003.
- [11] A. H. Guth. “The Inflationary Universe: A Possible Solution to the Horizon and Flatness Problems”. In: *Phys. Rev. D* 23 (1981). Ed. by L.-Z. Fang and R. Ruffini, pp. 347–356.
- [12] D. Baumann. “Inflation”. In: *Theoretical Advanced Study Institute in Elementary Particle Physics: Physics of the Large and the Small*. 2011, pp. 523–686. arXiv: [0907.5424 \[hep-th\]](#).
- [13] L. Kofman, A. D. Linde, and A. A. Starobinsky. “Reheating after inflation”. In: *Phys. Rev. Lett.* 73 (1994), pp. 3195–3198. arXiv: [hep-th/9405187](#).
- [14] L. Kofman, A. D. Linde, and A. A. Starobinsky. “Towards the theory of reheating after inflation”. In: *Phys. Rev. D* 56 (1997), pp. 3258–3295. arXiv: [hep-ph/9704452](#).
- [15] S. Hannestad. “What is the lowest possible reheating temperature?” In: *Phys. Rev. D* 70 (2004), p. 043506. arXiv: [astro-ph/0403291](#).
- [16] R. E. Lopez, S. Dodelson, A. Heckler, and M. S. Turner. “Precision detection of the cosmic neutrino background”. In: *Phys. Rev. Lett.* 82 (1999), pp. 3952–3955. arXiv: [astro-ph/9803095](#).

- [17] S. Sarkar. “Big bang nucleosynthesis and physics beyond the standard model”. In: *Rept. Prog. Phys.* 59 (1996), pp. 1493–1610. arXiv: [hep-ph/9602260](#).
- [18] B. D. Fields, K. A. Olive, T.-H. Yeh, and C. Young. “Big-Bang Nucleosynthesis after Planck”. In: *JCAP* 03 (2020), p. 010. arXiv: [1912.01132 \[astro-ph.CO\]](#). [Erratum: *JCAP* 11, E02 (2020)].
- [19] Y. B. Zeldovich and R. A. Sunyaev. “The Interaction of Matter and Radiation in a Hot-Model Universe”. In: *Astrophys. Space Sci.* 4 (1969), pp. 301–316.
- [20] P. J. E. Peebles. “Recombination of the Primeval Plasma”. In: *Astrophys. J.* 153 (1968), p. 1.
- [21] A. A. Penzias and R. W. Wilson. “A Measurement of excess antenna temperature at 4080-Mc/s”. In: *Astrophys. J.* 142 (1965), pp. 419–421.
- [22] W. Hu and S. Dodelson. “Cosmic Microwave Background Anisotropies”. In: *Ann. Rev. Astron. Astrophys.* 40 (2002), pp. 171–216. arXiv: [astro-ph/0110414](#).
- [23] A. G. Riess et al. “Observational evidence from supernovae for an accelerating universe and a cosmological constant”. In: *Astron. J.* 116 (1998), pp. 1009–1038. arXiv: [astro-ph/9805201](#).
- [24] S. Perlmutter et al. “Measurements of Ω and Λ from 42 High Redshift Supernovae”. In: *Astrophys. J.* 517 (1999), pp. 565–586. arXiv: [astro-ph/9812133](#).
- [25] E. W. Kolb and M. S. Turner. *The Early Universe*. Vol. 69. 1990.
- [26] M. Laine and M. Meyer. “Standard Model thermodynamics across the electroweak crossover”. In: *JCAP* 07 (2015), p. 035. arXiv: [1503.04935 \[hep-ph\]](#).
- [27] L. Husdal. “On Effective Degrees of Freedom in the Early Universe”. In: *Galaxies* 4.4 (2016), p. 78. arXiv: [1609.04979 \[astro-ph.CO\]](#).
- [28] F. Zwicky. “Die Rotverschiebung von extragalaktischen Nebeln”. In: *Helv. Phys. Acta* 6 (1933), pp. 110–127.
- [29] E. Hubble and M. L. Humason. “The Velocity-Distance Relation among Extra-Galactic Nebulae”. In: *Astrophys. J.* 74 (1931), pp. 43–80.
- [30] V. C. Rubin and W. K. Ford Jr. “Rotation of the Andromeda Nebula from a Spectroscopic Survey of Emission Regions”. In: *Astrophys. J.* 159 (1970), pp. 379–403.
- [31] V. C. Rubin, W. K. Ford Jr., and N. Thonnard. “Extended rotation curves of high-luminosity spiral galaxies. IV. Systematic dynamical properties, Sa through Sc”. In: *Astrophys. J. Lett.* 225 (1978), pp. L107–L111.
- [32] K. C. Freeman. “On the disks of spiral and SO Galaxies”. In: *Astrophys. J.* 160 (1970), p. 811.
- [33] J. Einasto, A. Kaasik, and E. Saar. “Dynamic evidence on massive coronas of galaxies”. In: *Nature* 250.5464 (1974), pp. 309–310.

-
- [34] J. P. Ostriker, P. J. E. Peebles, and A. Yahil. “The Size and Mass of Galaxies, and the Mass of the Universe”. In: *The Astrophysical Journal* 193 (1974), p. L1.
- [35] T. S. van Albada, J. N. Bahcall, K. Begeman, and R. Sancisi. “The Distribution of Dark Matter in the Spiral Galaxy NGC-3198”. In: *Astrophys. J.* 295 (1985), pp. 305–313.
- [36] D. Clowe et al. “A direct empirical proof of the existence of dark matter”. In: *Astrophys. J. Lett.* 648 (2006), pp. L109–L113. arXiv: [astro-ph/0608407](#).
- [37] M. Betoule et al. “Improved cosmological constraints from a joint analysis of the SDSS-II and SNLS supernova samples”. In: *Astron. Astrophys.* 568 (2014), A22. arXiv: [1401.4064 \[astro-ph.CO\]](#).
- [38] L. Anderson et al. “The clustering of galaxies in the SDSS-III Baryon Oscillation Spectroscopic Survey: Baryon Acoustic Oscillations in the Data Release 9 Spectroscopic Galaxy Sample”. In: *Mon. Not. Roy. Astron. Soc.* 427.4 (2013), pp. 3435–3467. arXiv: [1203.6594 \[astro-ph.CO\]](#).
- [39] S. D. McDermott, H.-B. Yu, and K. M. Zurek. “Turning off the Lights: How Dark is Dark Matter?” In: *Phys. Rev. D* 83 (2011), p. 063509. arXiv: [1011.2907 \[hep-ph\]](#).
- [40] P. J. Peebles. *The Large-Scale Structure of the Universe*. Princeton University Press, 1980.
- [41] V. Iršič et al. “New Constraints on the free-streaming of warm dark matter from intermediate and small scale Lyman- α forest data”. In: *Phys. Rev. D* 96.2 (2017), p. 023522. arXiv: [1702.01764 \[astro-ph.CO\]](#).
- [42] M. Milgrom. “A Modification of the Newtonian dynamics as a possible alternative to the hidden mass hypothesis”. In: *Astrophys. J.* 270 (1983), pp. 365–370.
- [43] M. Milgrom. “A Modification of the Newtonian dynamics: Implications for galaxies”. In: *Astrophys. J.* 270 (1983), pp. 371–383.
- [44] M. Milgrom. “A modification of the Newtonian dynamics: implications for galaxy systems”. In: *Astrophys. J.* 270 (1983), pp. 384–389.
- [45] J. D. Bekenstein. “Relativistic gravitation theory for the MOND paradigm”. In: *Phys. Rev. D* 70 (2004), p. 083509. arXiv: [astro-ph/0403694](#). [Erratum: *Phys. Rev. D* 71, 069901 (2005)].
- [46] A. C. Becker et al. “The SuperMACHO Microlensing Survey”. In: *IAU Symp.* 225 (2005), p. 357. arXiv: [astro-ph/0409167](#).
- [47] B. J. Carr and S. W. Hawking. “Black holes in the early Universe”. In: *Mon. Not. Roy. Astron. Soc.* 168 (1974), pp. 399–415.
- [48] B. Carr and F. Kuhnel. “Primordial Black Holes as Dark Matter: Recent Developments”. In: *Ann. Rev. Nucl. Part. Sci.* 70 (2020), pp. 355–394. arXiv: [2006.02838 \[astro-ph.CO\]](#).

- [49] J. L. Feng. “Dark Matter Candidates from Particle Physics and Methods of Detection”. In: *Ann. Rev. Astron. Astrophys.* 48 (2010), pp. 495–545. arXiv: [1003.0904 \[astro-ph.CO\]](#).
- [50] S. Dodelson and L. M. Widrow. “Sterile-neutrinos as dark matter”. In: *Phys. Rev. Lett.* 72 (1994), pp. 17–20. arXiv: [hep-ph/9303287](#).
- [51] A. Boyarsky, M. Drewes, T. Lasserre, S. Mertens, and O. Ruchayskiy. “Sterile neutrino Dark Matter”. In: *Prog. Part. Nucl. Phys.* 104 (2019), pp. 1–45. arXiv: [1807.07938 \[hep-ph\]](#).
- [52] B. Dasgupta and J. Kopp. “Sterile Neutrinos”. In: *Phys. Rept.* 928 (2021), pp. 1–63. arXiv: [2106.05913 \[hep-ph\]](#).
- [53] C.-Y. Seng. “Reexamination of The Standard Model Nucleon Electric Dipole Moment”. In: *Phys. Rev. C* 91.2 (2015), p. 025502. arXiv: [1411.1476 \[hep-ph\]](#).
- [54] R. D. Peccei and H. R. Quinn. “Constraints imposed by CP conservation in the presence of pseudoparticles”. In: *Phys. Rev. D* 16 (1977), pp. 1791–1797.
- [55] R. D. Peccei and H. R. Quinn. “CP Conservation in the Presence of Pseudoparticles”. In: *Phys. Rev. Lett.* 38 (1977), pp. 1440–1443.
- [56] S. Weinberg. “A New Light Boson?” In: *Phys. Rev. Lett.* 40 (1978), pp. 223–226.
- [57] F. Wilczek. “Problem of Strong P and T Invariance in the Presence of Instantons”. In: *Phys. Rev. Lett.* 40 (1978), pp. 279–282.
- [58] J. Jaeckel and A. Ringwald. “The Low-Energy Frontier of Particle Physics”. In: *Ann. Rev. Nucl. Part. Sci.* 60 (2010), pp. 405–437. arXiv: [1002.0329 \[hep-ph\]](#).
- [59] K. Choi, S. H. Im, and C. Sub Shin. “Recent Progress in the Physics of Axions and Axion-Like Particles”. In: *Ann. Rev. Nucl. Part. Sci.* 71 (2021), pp. 225–252. arXiv: [2012.05029 \[hep-ph\]](#).
- [60] G. Steigman and M. S. Turner. “Cosmological Constraints on the Properties of Weakly Interacting Massive Particles”. In: *Nucl. Phys. B* 253 (1985), pp. 375–386.
- [61] G. Arcadi et al. “The waning of the WIMP? A review of models, searches, and constraints”. In: *Eur. Phys. J. C* 78.3 (2018), p. 203. arXiv: [1703.07364 \[hep-ph\]](#).
- [62] G. Jungman, M. Kamionkowski, and K. Griest. “Supersymmetric dark matter”. In: *Phys. Rept.* 267 (1996), pp. 195–373. arXiv: [hep-ph/9506380](#).
- [63] J. Abdallah et al. “Simplified Models for Dark Matter Searches at the LHC”. In: *Phys. Dark Univ.* 9-10 (2015), pp. 8–23. arXiv: [1506.03116 \[hep-ph\]](#).
- [64] A. Albert et al. “Towards the next generation of simplified Dark Matter models”. In: *Phys. Dark Univ.* 16 (2017), pp. 49–70. arXiv: [1607.06680 \[hep-ex\]](#).
- [65] E. Morgante. “Simplified Dark Matter Models”. In: *Adv. High Energy Phys.* 2018 (2018), p. 5012043. arXiv: [1804.01245 \[hep-ph\]](#).
- [66] T. Bringmann, T. E. Gonzalo, F. Kahlhoefer, J. Matuszak, and C. Tasillo. “Hunting WIMPs with LISA: Correlating dark matter and gravitational wave signals”. 2023. arXiv: [2311.06346 \[astro-ph.CO\]](#).

-
- [67] T. Marrodán Undagoitia and L. Rauch. “Dark matter direct-detection experiments”. In: *J. Phys. G* 43.1 (2016), p. 013001. arXiv: [1509.08767 \[physics.ins-det\]](#).
- [68] M. Klasen, M. Pohl, and G. Sigl. “Indirect and direct search for dark matter”. In: *Prog. Part. Nucl. Phys.* 85 (2015), pp. 1–32. arXiv: [1507.03800 \[hep-ph\]](#).
- [69] J. M. Gaskins. “A review of indirect searches for particle dark matter”. In: *Contemp. Phys.* 57.4 (2016), pp. 496–525. arXiv: [1604.00014 \[astro-ph.HE\]](#).
- [70] F. Kahlhoefer. “Review of LHC Dark Matter Searches”. In: *Int. J. Mod. Phys. A* 32.13 (2017), p. 1730006. arXiv: [1702.02430 \[hep-ph\]](#).
- [71] G. Aad et al. “The ATLAS Experiment at the CERN Large Hadron Collider”. In: *JINST* 3 (2008), S08003.
- [72] S. Chatrchyan et al. “The CMS Experiment at the CERN LHC”. In: *JINST* 3 (2008), S08004.
- [73] O. Buchmueller, C. Doglioni, and L. T. Wang. “Search for dark matter at colliders”. In: *Nature Phys.* 13.3 (2017), pp. 217–223. arXiv: [1912.12739 \[hep-ex\]](#).
- [74] A. Boveia and C. Doglioni. “Dark Matter Searches at Colliders”. In: *Ann. Rev. Nucl. Part. Sci.* 68 (2018), pp. 429–459. arXiv: [1810.12238 \[hep-ex\]](#).
- [75] M. Schumann. “Direct Detection of WIMP Dark Matter: Concepts and Status”. In: *J. Phys. G* 46.10 (2019), p. 103003. arXiv: [1903.03026 \[astro-ph.CO\]](#).
- [76] X. Cao et al. “PandaX: A Liquid Xenon Dark Matter Experiment at CJPL”. In: *Sci. China Phys. Mech. Astron.* 57 (2014), pp. 1476–1494. arXiv: [1405.2882 \[physics.ins-det\]](#).
- [77] E. Aprile et al. “The XENONnT Dark Matter Experiment”. 2024. arXiv: [2402.10446 \[physics.ins-det\]](#).
- [78] D. S. Akerib et al. “The LUX-ZEPLIN (LZ) Experiment”. In: *Nucl. Instrum. Meth. A* 953 (2020), p. 163047. arXiv: [1910.09124 \[physics.ins-det\]](#).
- [79] M. Cirelli et al. “PPPC 4 DM ID: A Poor Particle Physicist Cookbook for Dark Matter Indirect Detection”. In: *JCAP* 03 (2011), p. 051. arXiv: [1012.4515 \[hep-ph\]](#). [Erratum: *JCAP* 10, E01 (2012)].
- [80] T. R. Slatyer. “Indirect Detection of Dark Matter”. In: *Theoretical Advanced Study Institute in Elementary Particle Physics: Anticipating the Next Discoveries in Particle Physics*. 2018, pp. 297–353. arXiv: [1710.05137 \[hep-ph\]](#).
- [81] T. R. Slatyer. “Les Houches Lectures on Indirect Detection of Dark Matter”. In: *SciPost Phys. Lect. Notes* 53 (2022), p. 1. arXiv: [2109.02696 \[hep-ph\]](#).
- [82] J. Tauber et al. “The Scientific programme of Planck”. 2006. arXiv: [astro-ph/0604069](#).
- [83] M. Aguilar et al. “Precision Measurement of the Proton Flux in Primary Cosmic Rays from Rigidity 1 GV to 1.8 TV with the Alpha Magnetic Spectrometer on the International Space Station”. In: *Phys. Rev. Lett.* 114 (2015), p. 171103.

- [84] A. Cuoco, M. Krämer, and M. Korsmeier. “Novel Dark Matter Constraints from Antiprotons in Light of AMS-02”. In: *Phys. Rev. Lett.* 118.19 (2017), p. 191102. arXiv: [1610.03071 \[astro-ph.HE\]](#).
- [85] J. Heisig, M. Korsmeier, and M. W. Winkler. “Dark matter or correlated errors: Systematics of the AMS-02 antiproton excess”. In: *Phys. Rev. Res.* 2.4 (2020), p. 043017. arXiv: [2005.04237 \[astro-ph.HE\]](#).
- [86] O. Adriani et al. “An anomalous positron abundance in cosmic rays with energies 1.5-100 GeV”. In: *Nature* 458 (2009), pp. 607–609. arXiv: [0810.4995 \[astro-ph\]](#).
- [87] M. Aguilar et al. “Towards Understanding the Origin of Cosmic-Ray Positrons”. In: *Phys. Rev. Lett.* 122.4 (2019), p. 041102.
- [88] I. John and T. Linden. “Cosmic-Ray Positrons Strongly Constrain Leptophilic Dark Matter”. In: *JCAP* 12 (2021), p. 007. arXiv: [2107.10261 \[astro-ph.HE\]](#).
- [89] M. Ackermann et al. “Searching for Dark Matter Annihilation from Milky Way Dwarf Spheroidal Galaxies with Six Years of Fermi Large Area Telescope Data”. In: *Phys. Rev. Lett.* 115.23 (2015), p. 231301. arXiv: [1503.02641 \[astro-ph.HE\]](#).
- [90] A. Albert et al. “Searching for Dark Matter Annihilation in Recently Discovered Milky Way Satellites with Fermi-LAT”. In: *Astrophys. J.* 834.2 (2017), p. 110. arXiv: [1611.03184 \[astro-ph.HE\]](#).
- [91] M. Ackermann et al. “The Fermi Galactic Center GeV Excess and Implications for Dark Matter”. In: *Astrophys. J.* 840.1 (2017), p. 43. arXiv: [1704.03910 \[astro-ph.HE\]](#).
- [92] H. Abdallah et al. “Search for dark matter annihilations towards the inner Galactic halo from 10 years of observations with H.E.S.S”. In: *Phys. Rev. Lett.* 117.11 (2016), p. 111301. arXiv: [1607.08142 \[astro-ph.HE\]](#).
- [93] S. Archambault et al. “Dark Matter Constraints from a Joint Analysis of Dwarf Spheroidal Galaxy Observations with VERITAS”. In: *Phys. Rev. D* 95.8 (2017), p. 082001. arXiv: [1703.04937 \[astro-ph.HE\]](#).
- [94] S. Hoof, A. Geringer-Sameth, and R. Trotta. “A Global Analysis of Dark Matter Signals from 27 Dwarf Spheroidal Galaxies using 11 Years of Fermi-LAT Observations”. In: *JCAP* 02 (2020), p. 012. arXiv: [1812.06986 \[astro-ph.CO\]](#).
- [95] S. Adrian-Martinez et al. “Search of Dark Matter Annihilation in the Galactic Centre using the ANTARES Neutrino Telescope”. In: *JCAP* 10 (2015), p. 068. arXiv: [1505.04866 \[astro-ph.HE\]](#).
- [96] R. Abbasi et al. “Searches for connections between dark matter and high-energy neutrinos with IceCube”. In: *JCAP* 10 (2023), p. 003. arXiv: [2205.12950 \[hep-ex\]](#).
- [97] R. Abbasi et al. “Search for GeV-scale dark matter annihilation in the Sun with IceCube DeepCore”. In: *Phys. Rev. D* 105.6 (2022), p. 062004. arXiv: [2111.09970 \[astro-ph.HE\]](#).

-
- [98] L. E. Strigari. “Dark matter in dwarf spheroidal galaxies and indirect detection: a review”. In: *Rept. Prog. Phys.* 81.5 (2018), p. 056901. arXiv: [1805.05883 \[astro-ph.CO\]](#).
- [99] W. B. Atwood et al. “The Large Area Telescope on the Fermi Gamma-ray Space Telescope Mission”. In: *Astrophys. J.* 697 (2009), pp. 1071–1102. arXiv: [0902.1089 \[astro-ph.IM\]](#).
- [100] B. S. Acharya et al. *Science with the Cherenkov Telescope Array*. WSP, 2018. arXiv: [1709.07997 \[astro-ph.IM\]](#).
- [101] P. Gondolo and G. Gelmini. “Cosmic abundances of stable particles: Improved analysis”. In: *Nucl. Phys. B* 360 (1991), pp. 145–179.
- [102] J. Bernstein. *Kinetic theory in the expanding Universe*. Cambridge Monographs on Mathematical Physics. Cambridge, U.K.: Cambridge University Press, 1988.
- [103] M. Srednicki, R. Watkins, and K. A. Olive. “Calculations of Relic Densities in the Early Universe”. In: *Nucl. Phys. B* 310 (1988). Ed. by M. A. Srednicki, p. 693.
- [104] P. Gondolo and J. Edsjo. “Neutralino relic density including coannihilations”. In: *Phys. Atom. Nucl.* 61 (1998). Ed. by V. A. Bednyakov, V. B. Brudanin, and S. G. Kovalenko, pp. 1081–1097.
- [105] A. Sommerfeld. “Über die Beugung und Bremsung der Elektronen”. In: *Annalen Phys.* 403.3 (1931), pp. 257–330.
- [106] A. D. Sakharov. “Interaction of an Electron and Positron in Pair Production”. In: *Zh. Eksp. Teor. Fiz.* 18 (1948), pp. 631–635.
- [107] M. J. Strassler and M. E. Peskin. “The Heavy top quark threshold: QCD and the Higgs”. In: *Phys. Rev. D* 43 (1991), pp. 1500–1514.
- [108] V. S. Fadin, V. A. Khoze, and T. Sjostrand. “On the Threshold Behavior of Heavy Top Production”. In: *Z. Phys. C* 48 (1990), pp. 613–622.
- [109] Y. Sumino, K. Fujii, K. Hagiwara, H. Murayama, and C. K. Ng. “Top quark pair production near threshold”. In: *Phys. Rev. D* 47 (1993), pp. 56–81.
- [110] V. S. Fadin, V. A. Khoze, A. D. Martin, and A. Chapovsky. “Coulomb effects in W^+W^- production”. In: *Phys. Rev. D* 52 (1995), pp. 1377–1385. arXiv: [hep-ph/9501214](#).
- [111] M. Jezabek, J. H. Kuhn, M. Peter, Y. Sumino, and T. Teubner. “The Perturbative QCD potential and the $t\bar{t}$ threshold”. In: *Phys. Rev. D* 58 (1998), p. 014006. arXiv: [hep-ph/9802373](#).
- [112] B. Grinstein and M. Trott. “A Higgs-Higgs bound state due to new physics at a TeV”. In: *Phys. Rev. D* 76 (2007), p. 073002. arXiv: [0704.1505 \[hep-ph\]](#).
- [113] A. C. A. Oliveira and R. Rosenfeld. “Hidden sector effects on double higgs production near threshold at the LHC”. In: *Phys. Lett. B* 702 (2011), pp. 201–204. arXiv: [1009.4497 \[hep-ph\]](#).

- [114] S. Mohorovičić. “Möglichkeit neuer Elemente und ihre Bedeutung für die Astrophysik”. In: *Astronomische Nachrichten* 253.4 (1934), p. 93.
- [115] M. Deutsch. “Evidence for the Formation of Positronium in Gases”. In: *Phys. Rev.* 82 (1951), pp. 455–456.
- [116] J. J. Aubert et al. “Experimental Observation of a Heavy Particle J ”. In: *Phys. Rev. Lett.* 33 (1974), pp. 1404–1406.
- [117] J. E. Augustin et al. “Discovery of a Narrow Resonance in e^+e^- Annihilation”. In: *Phys. Rev. Lett.* 33 (1974), pp. 1406–1408.
- [118] S. W. Herb et al. “Observation of a Dimuon Resonance at 9.5 GeV in 400 GeV Proton-Nucleus Collisions”. In: *Phys. Rev. Lett.* 39 (1977), pp. 252–255.
- [119] N. Brambilla et al. “Heavy Quarkonium: Progress, Puzzles, and Opportunities”. In: *Eur. Phys. J. C* 71 (2011), p. 1534. arXiv: [1010.5827 \[hep-ph\]](#).
- [120] J. Hisano, S. Matsumoto, and M. M. Nojiri. “Unitarity and higher order corrections in neutralino dark matter annihilation into two photons”. In: *Phys. Rev. D* 67 (2003), p. 075014. arXiv: [hep-ph/0212022](#).
- [121] J. Hisano, S. Matsumoto, and M. M. Nojiri. “Explosive dark matter annihilation”. In: *Phys. Rev. Lett.* 92 (2004), p. 031303. arXiv: [hep-ph/0307216](#).
- [122] J. Hisano, S. Matsumoto, M. M. Nojiri, and O. Saito. “Non-perturbative effect on dark matter annihilation and gamma ray signature from galactic center”. In: *Phys. Rev. D* 71 (2005), p. 063528. arXiv: [hep-ph/0412403](#).
- [123] N. Arkani-Hamed, D. P. Finkbeiner, T. R. Slatyer, and N. Weiner. “A Theory of Dark Matter”. In: *Phys. Rev. D* 79 (2009), p. 015014. arXiv: [0810.0713 \[hep-ph\]](#).
- [124] R. Iengo. “Sommerfeld enhancement: General results from field theory diagrams”. In: *JHEP* 05 (2009), p. 024. arXiv: [0902.0688 \[hep-ph\]](#).
- [125] S. Cassel. “Sommerfeld factor for arbitrary partial wave processes”. In: *J. Phys. G* 37 (2010), p. 105009. arXiv: [0903.5307 \[hep-ph\]](#).
- [126] S. El Hedri, A. Kaminska, and M. de Vries. “A Sommerfeld Toolbox for Colored Dark Sectors”. In: *Eur. Phys. J. C* 77.9 (2017), p. 622. arXiv: [1612.02825 \[hep-ph\]](#).
- [127] K. Blum, R. Sato, and T. R. Slatyer. “Self-consistent Calculation of the Sommerfeld Enhancement”. In: *JCAP* 06 (2016), p. 021. arXiv: [1603.01383 \[hep-ph\]](#).
- [128] B. von Harling and K. Petraki. “Bound-state formation for thermal relic dark matter and unitarity”. In: *JCAP* 12 (2014), p. 033. arXiv: [1407.7874 \[hep-ph\]](#).
- [129] K. Petraki, M. Postma, and M. Wiechers. “Dark-matter bound states from Feynman diagrams”. In: *JHEP* 06 (2015), p. 128. arXiv: [1505.00109 \[hep-ph\]](#).
- [130] J. Ellis, J. L. Evans, F. Luo, and K. A. Olive. “Scenarios for Gluino Coannihilation”. In: *JHEP* 02 (2016), p. 071. arXiv: [1510.03498 \[hep-ph\]](#).

-
- [131] S. P. Liew and F. Luo. “Effects of QCD bound states on dark matter relic abundance”. In: *JHEP* 02 (2017), p. 091. arXiv: [1611.08133 \[hep-ph\]](#).
- [132] M. Beneke et al. “Relic density of wino-like dark matter in the MSSM”. In: *JHEP* 03 (2016), p. 119. arXiv: [1601.04718 \[hep-ph\]](#).
- [133] M. Cirelli, P. Panci, K. Petraki, F. Sala, and M. Taoso. “Dark Matter’s secret liaisons: phenomenology of a dark $U(1)$ sector with bound states”. In: *JCAP* 05 (2017), p. 036. arXiv: [1612.07295 \[hep-ph\]](#).
- [134] M. Beneke, A. Bharucha, A. Hryczuk, S. Recksiegel, and P. Ruiz-Femenia. “The last refuge of mixed wino-Higgsino dark matter”. In: *JHEP* 01 (2017), p. 002. arXiv: [1611.00804 \[hep-ph\]](#).
- [135] A. Mitridate, M. Redi, J. Smirnov, and A. Strumia. “Cosmological Implications of Dark Matter Bound States”. In: *JCAP* 05 (2017), p. 006. arXiv: [1702.01141 \[hep-ph\]](#).
- [136] J. Harz and K. Petraki. “Radiative bound-state formation in unbroken perturbative non-Abelian theories and implications for dark matter”. In: *JHEP* 07 (2018), p. 096. arXiv: [1805.01200 \[hep-ph\]](#).
- [137] S. Biondini and M. Laine. “Thermal dark matter co-annihilating with a strongly interacting scalar”. In: *JHEP* 04 (2018), p. 072. arXiv: [1801.05821 \[hep-ph\]](#).
- [138] R. Oncala and K. Petraki. “Dark matter bound state formation via emission of a charged scalar”. In: *JHEP* 02 (2020), p. 036. arXiv: [1911.02605 \[hep-ph\]](#).
- [139] T. Binder, K. Mukaida, and K. Petraki. “Rapid bound-state formation of Dark Matter in the Early Universe”. In: *Phys. Rev. Lett.* 124.16 (2020), p. 161102. arXiv: [1910.11288 \[hep-ph\]](#).
- [140] R. Oncala and K. Petraki. “Bound states of WIMP dark matter in Higgs-portal models. Part I. Cross-sections and transition rates”. In: *JHEP* 06 (2021), p. 124. arXiv: [2101.08666 \[hep-ph\]](#).
- [141] S. Biondini and V. Shtabovenko. “Bound-state formation, dissociation and decays of darkonium with potential non-relativistic Yukawa theory for scalar and pseudoscalar mediators”. In: *JHEP* 03 (2022), p. 172. arXiv: [2112.10145 \[hep-ph\]](#).
- [142] M. Garny and J. Heisig. “Bound-state effects on dark matter coannihilation: Pushing the boundaries of conversion-driven freeze-out”. In: *Phys. Rev. D* 105.5 (2022), p. 055004. arXiv: [2112.01499 \[hep-ph\]](#).
- [143] T. Binder, A. Filimonova, K. Petraki, and G. White. “Saha equilibrium for metastable bound states and dark matter freeze-out”. In: *Phys. Lett. B* 833 (2022), p. 137323. arXiv: [2112.00042 \[hep-ph\]](#).
- [144] L. D. Landau and E. M. Lifshits. *Quantum Mechanics: Non-Relativistic Theory*. Vol. 3. Course of Theoretical Physics. Oxford: Butterworth-Heinemann, 1991.
- [145] K. Petraki, M. Postma, and J. de Vries. “Radiative bound-state-formation cross-sections for dark matter interacting via a Yukawa potential”. In: *JHEP* 04 (2017), p. 077. arXiv: [1611.01394 \[hep-ph\]](#).

- [146] K. Griest and M. Kamionkowski. “Unitarity Limits on the Mass and Radius of Dark Matter Particles”. In: *Phys. Rev. Lett.* 64 (1990), p. 615.
- [147] I. Baldes and K. Petraki. “Asymmetric thermal-relic dark matter: Sommerfeld-enhanced freeze-out, annihilation signals and unitarity bounds”. In: *JCAP* 09 (2017), p. 028. arXiv: [1703.00478 \[hep-ph\]](#).
- [148] F. J. Rogers, H. C. Graboske, and D. J. Harwood. “Bound Eigenstates of the Static Screened Coulomb Potential”. In: *Phys. Rev. A* 1 (1970), pp. 1577–1586.
- [149] J. Harz and K. Petraki. “Higgs Enhancement for the Dark Matter Relic Density”. In: *Phys. Rev. D* 97.7 (2018), p. 075041. arXiv: [1711.03552 \[hep-ph\]](#).
- [150] R. Oncala and K. Petraki. “Dark matter bound states via emission of scalar mediators”. In: *JHEP* 01 (2019), p. 070. arXiv: [1808.04854 \[hep-ph\]](#).
- [151] J. Harz and K. Petraki. “Higgs-mediated bound states in dark-matter models”. In: *JHEP* 04 (2019), p. 130. arXiv: [1901.10030 \[hep-ph\]](#).
- [152] R. Oncala and K. Petraki. “Bound states of WIMP dark matter in Higgs-portal models. Part II. Thermal decoupling”. In: *JHEP* 08 (2021), p. 069. arXiv: [2101.08667 \[hep-ph\]](#).
- [153] C. Itzykson and J. B. Zuber. *Quantum Field Theory*. International Series In Pure and Applied Physics. New York: McGraw-Hill, 1980.
- [154] Z. K. Silagadze. “Wick-Cutkosky model: An Introduction”. 1998. arXiv: [hep-ph/9803307](#).
- [155] E. E. Salpeter and H. A. Bethe. “A Relativistic equation for bound state problems”. In: *Phys. Rev.* 84 (1951), pp. 1232–1242.
- [156] J. S. Schwinger. “Quantum electrodynamics. I. A covariant formulation”. In: *Phys. Rev.* 74 (1948). Ed. by K. A. Milton, p. 1439.
- [157] J. S. Schwinger. “On the Green’s functions of quantized fields. 1.” In: *Proc. Nat. Acad. Sci.* 37 (1951), pp. 452–455.
- [158] J. S. Schwinger. “On the Green’s functions of quantized fields. 2.” In: *Proc. Nat. Acad. Sci.* 37 (1951), pp. 455–459.
- [159] W. Lucha and F. F. Schöberl. “Exact Solutions of Bethe-Salpeter Equations with Instantaneous Interactions”. In: *Phys. Rev. D* 87.1 (2013), p. 016009. arXiv: [1211.4716 \[hep-ph\]](#).
- [160] J. Carbonell and V. A. Karmanov. “Solving Bethe-Salpeter equation for two fermions in Minkowski space”. In: *Eur. Phys. J. A* 46 (2010), pp. 387–397. arXiv: [1010.4640 \[hep-ph\]](#).
- [161] M. E. Peskin and D. V. Schroeder. *An Introduction to quantum field theory*. Reading, USA: Addison-Wesley, 1995.
- [162] M. E. Luke and M. J. Savage. “Power counting in dimensionally regularized NRQCD”. In: *Phys. Rev. D* 57 (1998), pp. 413–423. arXiv: [hep-ph/9707313](#).

-
- [163] G. T. Bodwin, E. Braaten, and G. P. Lepage. “Rigorous QCD analysis of inclusive annihilation and production of heavy quarkonium”. In: *Phys. Rev. D* 51 (1995), pp. 1125–1171. arXiv: [hep-ph/9407339](#). [Erratum: *Phys. Rev. D* 55, 5853 (1997)].
- [164] W. E. Caswell and G. P. Lepage. “Effective Lagrangians for Bound State Problems in QED, QCD, and Other Field Theories”. In: *Phys. Lett. B* 167 (1986), pp. 437–442.
- [165] A. Pineda and J. Soto. “Effective field theory for ultrasoft momenta in NRQCD and NRQED”. In: *Nucl. Phys. B Proc. Suppl.* 64 (1998). Ed. by S. Narison, pp. 428–432. arXiv: [hep-ph/9707481](#).
- [166] A. Pineda and J. Soto. “Potential NRQED: The Positronium case”. In: *Phys. Rev. D* 59 (1999), p. 016005. arXiv: [hep-ph/9805424](#).
- [167] N. Brambilla, D. Eiras, A. Pineda, J. Soto, and A. Vairo. “Inclusive decays of heavy quarkonium to light particles”. In: *Phys. Rev. D* 67 (2003), p. 034018. arXiv: [hep-ph/0208019](#).
- [168] N. Brambilla, A. Pineda, J. Soto, and A. Vairo. “Effective Field Theories for Heavy Quarkonium”. In: *Rev. Mod. Phys.* 77 (2005), p. 1423. arXiv: [hep-ph/0410047](#).
- [169] S. Biondini and S. Vogl. “Coloured coannihilations: Dark matter phenomenology meets non-relativistic EFTs”. In: *JHEP* 02 (2019), p. 016. arXiv: [1811.02581 \[hep-ph\]](#).
- [170] S. Biondini and V. Shtabovenko. “Non-relativistic and potential non-relativistic effective field theories for scalar mediators”. In: *JHEP* 08 (2021), p. 114. arXiv: [2106.06472 \[hep-ph\]](#).
- [171] S. Biondini, N. Brambilla, G. Qerimi, and A. Vairo. “Effective field theories for dark matter pairs in the early universe: cross sections and widths”. In: *JHEP* 07 (2023), p. 006. arXiv: [2304.00113 \[hep-ph\]](#).
- [172] T. Binder, M. Garny, J. Heisig, S. Lederer, and K. Urban. “Excited bound states and their role in dark matter production”. In: *Phys. Rev. D* 108.9 (2023), p. 095030. arXiv: [2308.01336 \[hep-ph\]](#).
- [173] M. E. Luke and A. V. Manohar. “Bound states and power counting in effective field theories”. In: *Phys. Rev. D* 55 (1997), pp. 4129–4140. arXiv: [hep-ph/9610534](#).
- [174] T. Kinoshita and M. Nio. “Radiative corrections to the muonium hyperfine structure. 1. The α^2 ($Z\alpha$) correction”. In: *Phys. Rev. D* 53 (1996), pp. 4909–4929. arXiv: [hep-ph/9512327](#).
- [175] A. V. Manohar. “The HQET / NRQCD Lagrangian to order α/m^3 ”. In: *Phys. Rev. D* 56 (1997), pp. 230–237. arXiv: [hep-ph/9701294](#).
- [176] G. Paz. “An Introduction to NRQED”. In: *Mod. Phys. Lett. A* 30.26 (2015), p. 1550128. arXiv: [1503.07216 \[hep-ph\]](#).
- [177] L. Covi, J. E. Kim, and L. Roszkowski. “Axinos as cold dark matter”. In: *Phys. Rev. Lett.* 82 (1999), pp. 4180–4183. arXiv: [hep-ph/9905212](#).

- [178] J. L. Feng, A. Rajaraman, and F. Takayama. “Superweakly interacting massive particles”. In: *Phys. Rev. Lett.* 91 (2003), p. 011302. arXiv: [hep-ph/0302215](#).
- [179] L. J. Hall, K. Jedamzik, J. March-Russell, and S. M. West. “Freeze-In Production of FIMP Dark Matter”. In: *JHEP* 03 (2010), p. 080. arXiv: [0911.1120 \[hep-ph\]](#).
- [180] S. Chang, R. Edezhath, J. Hutchinson, and M. Luty. “Effective WIMPs”. In: *Phys. Rev. D* 89.1 (2014), p. 015011. arXiv: [1307.8120 \[hep-ph\]](#).
- [181] H. An, L.-T. Wang, and H. Zhang. “Dark matter with t -channel mediator: a simple step beyond contact interaction”. In: *Phys. Rev. D* 89.11 (2014), p. 115014. arXiv: [1308.0592 \[hep-ph\]](#).
- [182] A. DiFranzo, K. I. Nagao, A. Rajaraman, and T. M. P. Tait. “Simplified Models for Dark Matter Interacting with Quarks”. In: *JHEP* 11 (2013), p. 014. arXiv: [1308.2679 \[hep-ph\]](#). [Erratum: *JHEP* 01, 162 (2014)].
- [183] M. Papucci, A. Vichi, and K. M. Zurek. “Monojet versus the rest of the world I: t -channel models”. In: *JHEP* 11 (2014), p. 024. arXiv: [1402.2285 \[hep-ph\]](#).
- [184] M. Garny, A. Ibarra, S. Rydbeck, and S. Vogl. “Majorana Dark Matter with a Coloured Mediator: Collider vs. Direct and Indirect Searches”. In: *JHEP* 06 (2014), p. 169. arXiv: [1403.4634 \[hep-ph\]](#).
- [185] A. Ibarra, A. Pierce, N. R. Shah, and S. Vogl. “Anatomy of Coannihilation with a Scalar Top Partner”. In: *Phys. Rev. D* 91.9 (2015). Ed. by M. Tecchio and D. Levin, p. 095018. arXiv: [1501.03164 \[hep-ph\]](#).
- [186] C. Arina et al. “Closing in on t -channel simplified dark matter models”. In: *Phys. Lett. B* 813 (2021), p. 136038. arXiv: [2010.07559 \[hep-ph\]](#).
- [187] G. Arcadi, L. Calibbi, M. Fedele, and F. Mescia. “Systematic approach to B -physics anomalies and t -channel dark matter”. In: *Phys. Rev. D* 104.11 (2021), p. 115012. arXiv: [2103.09835 \[hep-ph\]](#).
- [188] Q. Decant, J. Heisig, D. C. Hooper, and L. Lopez-Honorez. “Lyman- α constraints on freeze-in and superWIMPs”. In: *JCAP* 03 (2022), p. 041. arXiv: [2111.09321 \[astro-ph.CO\]](#).
- [189] M. Garny, J. Heisig, B. Lülz, and S. Vogl. “Coannihilation without chemical equilibrium”. In: *Phys. Rev. D* 96.10 (2017), p. 103521. arXiv: [1705.09292 \[hep-ph\]](#).
- [190] M. Garny and J. Heisig. “Interplay of super-WIMP and freeze-in production of dark matter”. In: *Phys. Rev. D* 98.9 (2018), p. 095031. arXiv: [1809.10135 \[hep-ph\]](#).
- [191] S. Biondini and J. Ghiglieri. “Freeze-in produced dark matter in the ultra-relativistic regime”. In: *JCAP* 03 (2021), p. 075. arXiv: [2012.09083 \[hep-ph\]](#).
- [192] J. L. Feng, A. Rajaraman, and F. Takayama. “SuperWIMP dark matter signals from the early universe”. In: *Phys. Rev. D* 68 (2003), p. 063504. arXiv: [hep-ph/0306024](#).

-
- [193] W. Fischler. “Quark-antiquark potential in QCD”. In: *Nucl. Phys. B* 129 (1977), pp. 157–174.
- [194] A. De Simone, G. F. Giudice, and A. Strumia. “Benchmarks for Dark Matter Searches at the LHC”. In: *JHEP* 06 (2014), p. 081. arXiv: [1402.6287 \[hep-ph\]](#).
- [195] A. Deur, S. J. Brodsky, and G. F. de Teramond. “The QCD Running Coupling”. In: *Nucl. Phys.* 90 (2016), p. 1. arXiv: [1604.08082 \[hep-ph\]](#).
- [196] J. Ellis, F. Luo, and K. A. Olive. “Gluino Coannihilation Revisited”. In: *JHEP* 09 (2015), p. 127. arXiv: [1503.07142 \[hep-ph\]](#).
- [197] P. Peter and J.-P. Uzan. *Primordial Cosmology*. Oxford Graduate Texts. Oxford University Press, 2013.
- [198] M. N. Saha. “On a physical theory of stellar spectra”. In: *Proceedings of the Royal Society of London. Series A, Containing Papers of a Mathematical and Physical Character* 99.697 (1921), pp. 135–153.
- [199] R. T. Co, F. D’Eramo, L. J. Hall, and D. Pappadopulo. “Freeze-In Dark Matter with Displaced Signatures at Colliders”. In: *JCAP* 12 (2015), p. 024. arXiv: [1506.07532 \[hep-ph\]](#).
- [200] L. Calibbi, F. D’Eramo, S. Junius, L. Lopez-Honorez, and A. Mariotti. “Displaced new physics at colliders and the early universe before its first second”. In: *JHEP* 05 (2021), p. 234. arXiv: [2102.06221 \[hep-ph\]](#).
- [201] A. G. Hessler, A. Ibarra, E. Molinaro, and S. Vogl. “Impact of the Higgs boson on the production of exotic particles at the LHC”. In: *Phys. Rev. D* 91.11 (2015), p. 115004. arXiv: [1408.0983 \[hep-ph\]](#).
- [202] G. Belanger, F. Boudjema, A. Pukhov, and A. Semenov. “MicrOMEGAs: A Program for calculating the relic density in the MSSM”. In: *Comput. Phys. Commun.* 149 (2002), pp. 103–120. arXiv: [hep-ph/0112278](#).
- [203] G. Belanger, F. Boudjema, A. Pukhov, and A. Semenov. “micrOMEGAs_3: A program for calculating dark matter observables”. In: *Comput. Phys. Commun.* 185 (2014), pp. 960–985. arXiv: [1305.0237 \[hep-ph\]](#).
- [204] A. Belyaev, N. D. Christensen, and A. Pukhov. “CalcHEP 3.4 for collider physics within and beyond the Standard Model”. In: *Comput. Phys. Commun.* 184 (2013), pp. 1729–1769. arXiv: [1207.6082 \[hep-ph\]](#).
- [205] M. Aaboud et al. “Search for heavy charged long-lived particles in the ATLAS detector in 36.1 fb^{-1} of proton-proton collision data at $\sqrt{s} = 13 \text{ TeV}$ ”. In: *Phys. Rev. D* 99.9 (2019), p. 092007. arXiv: [1902.01636 \[hep-ex\]](#).
- [206] C. Collaboration. *Search for heavy stable charged particles with 12.9 fb^{-1} of 2016 data*. Tech. rep. Geneva: CERN, 2016.
- [207] K. Jedamzik. “Bounds on long-lived charged massive particles from Big Bang nucleosynthesis”. In: *JCAP* 03 (2008), p. 008. arXiv: [0710.5153 \[hep-ph\]](#).

- [208] M. Kawasaki, K. Kohri, T. Moroi, and Y. Takaesu. “Revisiting Big-Bang Nucleosynthesis Constraints on Long-Lived Decaying Particles”. In: *Phys. Rev. D* 97.2 (2018), p. 023502. arXiv: [1709.01211 \[hep-ph\]](#).
- [209] P. Bode, J. P. Ostriker, and N. Turok. “Halo formation in warm dark matter models”. In: *Astrophys. J.* 556 (2001), pp. 93–107. arXiv: [astro-ph/0010389](#).
- [210] R. Barkana, Z. Haiman, and J. P. Ostriker. “Constraints on warm dark matter from cosmological reionization”. In: *Astrophys. J.* 558 (2001), p. 482. arXiv: [astro-ph/0102304](#).
- [211] A. Dekker, S. Ando, C. A. Correa, and K. C. Y. Ng. “Warm dark matter constraints using Milky Way satellite observations and subhalo evolution modeling”. In: *Phys. Rev. D* 106.12 (2022), p. 123026. arXiv: [2111.13137 \[astro-ph.CO\]](#).
- [212] J.-W. Hsueh et al. “SHARP–VII. New constraints on the dark matter free-streaming properties and substructure abundance from gravitationally lensed quasars”. In: *Mon. Not. Roy. Astron. Soc.* 492.2 (2020), pp. 3047–3059. arXiv: [1905.04182 \[astro-ph.CO\]](#).
- [213] D. Gilman et al. “Warm dark matter chills out: constraints on the halo mass function and the free-streaming length of dark matter with eight quadruple-image strong gravitational lenses”. In: *Mon. Not. Roy. Astron. Soc.* 491.4 (2020), pp. 6077–6101. arXiv: [1908.06983 \[astro-ph.CO\]](#).
- [214] J. Heeck and D. Teresi. “Cold keV dark matter from decays and scatterings”. In: *Phys. Rev. D* 96.3 (2017), p. 035018. arXiv: [1706.09909 \[hep-ph\]](#).
- [215] K. Jedamzik, M. Lemoine, and G. Moulta. “Gravitino, Axino, Kaluza-Klein Graviton Warm and Mixed Dark Matter and Reionization”. In: *JCAP* 07 (2006), p. 010. arXiv: [astro-ph/0508141](#).
- [216] M. Pospelov, A. Ritz, and M. B. Voloshin. “Secluded WIMP Dark Matter”. In: *Phys. Lett. B* 662 (2008), pp. 53–61. arXiv: [0711.4866 \[hep-ph\]](#).
- [217] M. Pospelov and A. Ritz. “Astrophysical Signatures of Secluded Dark Matter”. In: *Phys. Lett. B* 671 (2009), pp. 391–397. arXiv: [0810.1502 \[hep-ph\]](#).
- [218] Y. Meng et al. “Dark Matter Search Results from the PandaX-4T Commissioning Run”. In: *Phys. Rev. Lett.* 127.26 (2021), p. 261802. arXiv: [2107.13438 \[hep-ex\]](#).
- [219] J. Aalbers et al. “First Dark Matter Search Results from the LUX-ZEPLIN (LZ) Experiment”. In: *Phys. Rev. Lett.* 131.4 (2023), p. 041002. arXiv: [2207.03764 \[hep-ex\]](#).
- [220] E. Aprile et al. “First dark matter search with nuclear recoils from the XENONnT experiment”. In: *Phys. Rev. Lett.* 131.4 (2023), p. 041003. arXiv: [2303.14729 \[hep-ex\]](#).
- [221] M. Aaboud et al. “Constraints on mediator-based dark matter and scalar dark energy models using $\sqrt{s} = 13$ TeV pp collision data collected by the ATLAS detector”. In: *JHEP* 05 (2019), p. 142. arXiv: [1903.01400 \[hep-ex\]](#).

-
- [222] G. Aad et al. “Search for new phenomena in events with an energetic jet and missing transverse momentum in pp collisions at $\sqrt{s} = 13$ TeV with the ATLAS detector”. In: *Phys. Rev. D* 103.11 (2021), p. 112006. arXiv: [2102.10874 \[hep-ex\]](#).
- [223] A. M. Sirunyan et al. “Search for dark matter produced with an energetic jet or a hadronically decaying W or Z boson at $\sqrt{s} = 13$ TeV”. In: *JHEP* 07 (2017), p. 014. arXiv: [1703.01651 \[hep-ex\]](#).
- [224] A. M. Sirunyan et al. “Search for narrow and broad dijet resonances in proton-proton collisions at $\sqrt{s} = 13$ TeV and constraints on dark matter mediators and other new particles”. In: *JHEP* 08 (2018), p. 130. arXiv: [1806.00843 \[hep-ex\]](#).
- [225] J. L. Feng, M. Kaplinghat, and H.-B. Yu. “Sommerfeld Enhancements for Thermal Relic Dark Matter”. In: *Phys. Rev. D* 82 (2010), p. 083525. arXiv: [1005.4678 \[hep-ph\]](#).
- [226] T. R. Slatyer, N. Toro, and N. Weiner. “Sommerfeld-enhanced annihilation in dark matter substructure: Consequences for constraints on cosmic-ray excesses”. In: *Phys. Rev. D* 86 (2012), p. 083534. arXiv: [1107.3546 \[hep-ph\]](#).
- [227] K. N. Abazajian and J. P. Harding. “Constraints on WIMP and Sommerfeld-Enhanced Dark Matter Annihilation from HESS Observations of the Galactic Center”. In: *JCAP* 01 (2012), p. 041. arXiv: [1110.6151 \[hep-ph\]](#).
- [228] B.-Q. Lu, Y.-L. Wu, W.-H. Zhang, and Y.-F. Zhou. “Constraints on the Sommerfeld-enhanced dark matter annihilation from the gamma rays of subhalos and dwarf galaxies”. In: *JCAP* 04 (2018), p. 035. arXiv: [1711.00749 \[astro-ph.HE\]](#).
- [229] S. Ando and K. Ishiwata. “Sommerfeld-enhanced dark matter searches with dwarf spheroidal galaxies”. In: *Phys. Rev. D* 104.2 (2021), p. 023016. arXiv: [2103.01446 \[astro-ph.CO\]](#).
- [230] J. D. March-Russell and S. M. West. “WIMPonium and Boost Factors for Indirect Dark Matter Detection”. In: *Phys. Lett. B* 676 (2009), pp. 133–139. arXiv: [0812.0559 \[astro-ph\]](#).
- [231] R. Laha. “Directional detection of dark matter in universal bound states”. In: *Phys. Rev. D* 92 (2015), p. 083509. arXiv: [1505.02772 \[hep-ph\]](#).
- [232] P. Asadi, M. Baumgart, P. J. Fitzpatrick, E. Krupczak, and T. R. Slatyer. “Capture and Decay of Electroweak WIMPonium”. In: *JCAP* 02 (2017), p. 005. arXiv: [1610.07617 \[hep-ph\]](#).
- [233] A. Coskuner, D. M. Grabowska, S. Knapen, and K. M. Zurek. “Direct Detection of Bound States of Asymmetric Dark Matter”. In: *Phys. Rev. D* 100.3 (2019), p. 035025. arXiv: [1812.07573 \[hep-ph\]](#).
- [234] X. Chu, C. Garcia-Cely, and H. Murayama. “Finite-size dark matter and its effect on small-scale structure”. In: *Phys. Rev. Lett.* 124.4 (2020), p. 041101. arXiv: [1901.00075 \[hep-ph\]](#).
- [235] S. Bottaro, A. Strumia, and N. Vignaroli. “Minimal Dark Matter bound states at future colliders”. In: *JHEP* 06 (2021), p. 143. arXiv: [2103.12766 \[hep-ph\]](#).

- [236] H. An, M. B. Wise, and Y. Zhang. “Effects of Bound States on Dark Matter Annihilation”. In: *Phys. Rev. D* 93.11 (2016), p. 115020. arXiv: [1604.01776 \[hep-ph\]](#).
- [237] L. Pearce, K. Petraki, and A. Kusenko. “Signals from dark atom formation in halos”. In: *Phys. Rev. D* 91 (2015), p. 083532. arXiv: [1502.01755 \[hep-ph\]](#).
- [238] I. Baldes, F. Calore, K. Petraki, V. Poireau, and N. L. Rodd. “Indirect searches for dark matter bound state formation and level transitions”. In: *SciPost Phys.* 9.5 (2020), p. 068. arXiv: [2007.13787 \[hep-ph\]](#).
- [239] F. Kahlhoefer, K. Schmidt-Hoberg, and S. Wild. “Dark matter self-interactions from a general spin-0 mediator”. In: *JCAP* 08 (2017), p. 003. arXiv: [1704.02149 \[hep-ph\]](#).
- [240] M. Kaplinghat, S. Tulin, and H.-B. Yu. “Direct Detection Portals for Self-interacting Dark Matter”. In: *Phys. Rev. D* 89.3 (2014), p. 035009. arXiv: [1310.7945 \[hep-ph\]](#).
- [241] A. De Simone and T. Jacques. “Simplified models vs. effective field theory approaches in dark matter searches”. In: *Eur. Phys. J. C* 76.7 (2016), p. 367. arXiv: [1603.08002 \[hep-ph\]](#).
- [242] F. Kahlhoefer, K. Schmidt-Hoberg, T. Schwetz, and S. Vogl. “Implications of unitarity and gauge invariance for simplified dark matter models”. In: *JHEP* 02 (2016), p. 016. arXiv: [1510.02110 \[hep-ph\]](#).
- [243] M. Duerr, F. Kahlhoefer, K. Schmidt-Hoberg, T. Schwetz, and S. Vogl. “How to save the WIMP: global analysis of a dark matter model with two s-channel mediators”. In: *JHEP* 09 (2016), p. 042. arXiv: [1606.07609 \[hep-ph\]](#).
- [244] M. B. Wise and Y. Zhang. “Stable Bound States of Asymmetric Dark Matter”. In: *Phys. Rev. D* 90.5 (2014), p. 055030. arXiv: [1407.4121 \[hep-ph\]](#). [Erratum: *Phys. Rev. D* 91, 039907 (2015)].
- [245] K. Kainulainen, K. Tuominen, and V. Vaskonen. “Self-interacting dark matter and cosmology of a light scalar mediator”. In: *Phys. Rev. D* 93.1 (2016), p. 015016. arXiv: [1507.04931 \[hep-ph\]](#). [Erratum: *Phys. Rev. D* 95, 079901 (2017)].
- [246] M. Beneke, T. Binder, L. De Ros, and M. Garny. “Enhancement of p-wave dark matter annihilation by quasi-bound states”. In: (2024). arXiv: [2403.07108 \[hep-ph\]](#).
- [247] S. Biondini and M. Laine. “Re-derived overclosure bound for the inert doublet model”. In: *JHEP* 08 (2017), p. 047. arXiv: [1706.01894 \[hep-ph\]](#).
- [248] M. L. Bellac. *Thermal Field Theory*. Cambridge Monographs on Mathematical Physics. Cambridge University Press, 2011.
- [249] J. I. Kapusta. *Finite Temperature Field Theory*. Cambridge Monographs on Mathematical Physics. Cambridge University Press, 1989.
- [250] N. Brambilla, J. Ghiglieri, A. Vairo, and P. Petreczky. “Static quark-antiquark pairs at finite temperature”. In: *Phys. Rev. D* 78 (2008), p. 014017. arXiv: [0804.0993 \[hep-ph\]](#).

-
- [251] F. Ferrer and D. R. Hunter. “The impact of the phase-space density on the indirect detection of dark matter”. In: *JCAP* 09 (2013), p. 005. arXiv: [1306.6586 \[astro-ph.HE\]](#).
- [252] K. K. Boddy, J. Kumar, L. E. Strigari, and M.-Y. Wang. “Sommerfeld-enhanced J -factors for dwarf spheroidal galaxies”. In: *Phys. Rev. D* 95.12 (2017), p. 123008. arXiv: [1702.00408 \[astro-ph.CO\]](#).
- [253] J. Binney and S. Tremaine. *Galactic dynamics*. Vol. 20. Princeton university press, 2011.
- [254] T. Lacroix, M. Stref, and J. Lavalle. “Anatomy of Eddington-like inversion methods in the context of dark matter searches”. In: *JCAP* 09 (2018), p. 040. arXiv: [1805.02403 \[astro-ph.GA\]](#).
- [255] E. Board et al. “Velocity-dependent J -factors for annihilation radiation from cosmological simulations”. In: *JCAP* 04 (2021), p. 070. arXiv: [2101.06284 \[astro-ph.CO\]](#).
- [256] D. McKeown et al. “Amplified J -factors in the Galactic Centre for velocity-dependent dark matter annihilation in FIRE simulations”. In: *Mon. Not. Roy. Astron. Soc.* 513.1 (2022), pp. 55–70. arXiv: [2111.03076 \[astro-ph.GA\]](#).
- [257] V. F. Cardone, E. Piedipalumbo, and C. Tortora. “Spherical galaxy models with power law logarithmic slope”. In: *Mon. Not. Roy. Astron. Soc.* 358 (2005), pp. 1325–1336. arXiv: [astro-ph/0501151](#).
- [258] J. F. Navarro, C. S. Frenk, and S. D. M. White. “The Structure of cold dark matter halos”. In: *Astrophys. J.* 462 (1996), pp. 563–575. arXiv: [astro-ph/9508025](#).
- [259] J. F. Navarro, C. S. Frenk, and S. D. M. White. “A Universal density profile from hierarchical clustering”. In: *Astrophys. J.* 490 (1997), pp. 493–508. arXiv: [astro-ph/9611107](#).
- [260] B. Moore et al. “Dark matter substructure within galactic halos”. In: *Astrophys. J. Lett.* 524 (1999), pp. L19–L22. arXiv: [astro-ph/9907411](#).
- [261] J. F. Navarro et al. “The Inner structure of Lambda-CDM halos 3: Universality and asymptotic slopes”. In: *Mon. Not. Roy. Astron. Soc.* 349 (2004), p. 1039. arXiv: [astro-ph/0311231](#).
- [262] A. W. Graham, D. Merritt, B. Moore, J. Diemand, and B. Terzic. “Empirical models for Dark Matter Halos. I. Nonparametric Construction of Density Profiles and Comparison with Parametric Models”. In: *Astron. J.* 132 (2006), pp. 2685–2700. arXiv: [astro-ph/0509417](#).
- [263] A. Acharyya et al. “Sensitivity of the Cherenkov Telescope Array to a dark matter signal from the Galactic centre”. In: *JCAP* 01 (2021), p. 057. arXiv: [2007.16129 \[astro-ph.HE\]](#).
- [264] G. Battaglia, A. Helmi, and M. Breddels. “Internal kinematics and dynamical models of dwarf spheroidal galaxies around the Milky Way”. In: *New Astron. Rev.* 57 (2013), pp. 52–79. arXiv: [1305.5965 \[astro-ph.CO\]](#).

- [265] M. Walker. “Dark Matter in the Galactic Dwarf Spheroidal Satellites”. In: *Planets, Stars and Stellar Systems: Volume 5: Galactic Structure and Stellar Populations*. Ed. by T. D. Oswalt and G. Gilmore. Dordrecht: Springer Netherlands, 2013, pp. 1039–1089.
- [266] A. Djouadi. “The Anatomy of electro-weak symmetry breaking. I: The Higgs boson in the standard model”. In: *Phys. Rept.* 457 (2008), pp. 1–216. arXiv: [hep-ph/0503172](#).
- [267] K. G. Chetyrkin, J. H. Kuhn, and M. Steinhauser. “RunDec: A Mathematica package for running and decoupling of the strong coupling and quark masses”. In: *Comput. Phys. Commun.* 133 (2000), pp. 43–65. arXiv: [hep-ph/0004189](#).
- [268] J. F. Gunion, H. E. Haber, G. L. Kane, and S. Dawson. *The Higgs Hunter’s Guide*. Vol. 80. 2000.
- [269] M. Spira, A. Djouadi, D. Graudenz, and P. M. Zerwas. “Higgs boson production at the LHC”. In: *Nucl. Phys. B* 453 (1995), pp. 17–82. arXiv: [hep-ph/9504378](#).
- [270] A. Denner, S. Heinemeyer, I. Puljak, D. Rebuszi, and M. Spira. “Standard Model Higgs-Boson Branching Ratios with Uncertainties”. In: *Eur. Phys. J. C* 71 (2011), p. 1753. arXiv: [1107.5909 \[hep-ph\]](#).
- [271] S. Dittmaier et al. “Handbook of LHC Higgs Cross Sections: 2. Differential Distributions”. In: (2012). arXiv: [1201.3084 \[hep-ph\]](#).
- [272] M. W. Winkler. “Decay and detection of a light scalar boson mixing with the Higgs boson”. In: *Phys. Rev. D* 99.1 (2019), p. 015018. arXiv: [1809.01876 \[hep-ph\]](#).
- [273] C. Bierlich et al. “A comprehensive guide to the physics and usage of PYTHIA 8.3”. In: *SciPost Phys. Codeb.* 2022 (2022), p. 8. arXiv: [2203.11601 \[hep-ph\]](#).
- [274] J. Bellm et al. “Herwig 7.0/Herwig++ 3.0 release note”. In: *Eur. Phys. J. C* 76.4 (2016), p. 196. arXiv: [1512.01178 \[hep-ph\]](#).
- [275] T. Bringmann, J. Edsjö, P. Gondolo, P. Ullio, and L. Bergström. “DarkSUSY 6 : An Advanced Tool to Compute Dark Matter Properties Numerically”. In: *JCAP* 07 (2018), p. 033. arXiv: [1802.03399 \[hep-ph\]](#).
- [276] J. Mardon, Y. Nomura, D. Stolarski, and J. Thaler. “Dark Matter Signals from Cascade Annihilations”. In: *JCAP* 05 (2009), p. 016. arXiv: [0901.2926 \[hep-ph\]](#).
- [277] T. Plehn, P. Reimitz, and P. Richardson. “Hadronic Footprint of GeV-Mass Dark Matter”. In: *SciPost Phys.* 8 (2020), p. 092. arXiv: [1911.11147 \[hep-ph\]](#).
- [278] A. Coogan, L. Morrison, T. Plehn, S. Profumo, and P. Reimitz. “Hazma meets HERWIG4DM: precision gamma-ray, neutrino, and positron spectra for light dark matter”. In: *JCAP* 11 (2022), p. 033. arXiv: [2207.07634 \[hep-ph\]](#).
- [279] G. Elor, N. L. Rodd, T. R. Slatyer, and W. Xue. “Model-Independent Indirect Detection Constraints on Hidden Sector Dark Matter”. In: *JCAP* 06 (2016), p. 024. arXiv: [1511.08787 \[hep-ph\]](#).

-
- [280] G. Elor, N. L. Rodd, and T. R. Slatyer. “Multistep cascade annihilations of dark matter and the Galactic Center excess”. In: *Phys. Rev. D* 91 (2015), p. 103531. arXiv: [1503.01773 \[hep-ph\]](#).
- [281] T. Bringmann, F. Calore, G. Vertongen, and C. Weniger. “On the Relevance of Sharp Gamma-Ray Features for Indirect Dark Matter Searches”. In: *Phys. Rev. D* 84 (2011), p. 103525. arXiv: [1106.1874 \[hep-ph\]](#).
- [282] T. Bringmann, X. Huang, A. Ibarra, S. Vogl, and C. Weniger. “Fermi LAT Search for Internal Bremsstrahlung Signatures from Dark Matter Annihilation”. In: *JCAP* 07 (2012), p. 054. arXiv: [1203.1312 \[hep-ph\]](#).
- [283] M. Ackermann et al. “Dark Matter Constraints from Observations of 25 Milky Way Satellite Galaxies with the Fermi Large Area Telescope”. In: *Phys. Rev. D* 89 (2014), p. 042001. arXiv: [1310.0828 \[astro-ph.HE\]](#).
- [284] Fermi-LAT Collaboration. *Supplementary material for Fermi-LAT dwarf spheroidal paper*. http://www-glast.stanford.edu/pub_data/1048/. 2015.
- [285] M. S. Bartlett. “Approximate Confidence Intervals. II. More than one Unknown Parameter”. In: *Biometrika* 40.3/4 (1953), pp. 306–317.
- [286] W. A. Rolke, A. M. Lopez, and J. Conrad. “Limits and confidence intervals in the presence of nuisance parameters”. In: *Nucl. Instrum. Meth. A* 551 (2005). Ed. by L. Lyons and M. Karagoz, pp. 493–503. arXiv: [physics/0403059](#).
- [287] G. Cowan. “Statistics for Searches at the LHC”. In: *69th Scottish Universities Summer School in Physics: LHC Physics*. 2013, pp. 321–355. arXiv: [1307.2487 \[hep-ex\]](#).
- [288] X.-L. Chen and M. Kamionkowski. “Particle decays during the cosmic dark ages”. In: *Phys. Rev. D* 70 (2004), p. 043502. arXiv: [astro-ph/0310473](#).
- [289] N. Padmanabhan and D. P. Finkbeiner. “Detecting dark matter annihilation with CMB polarization: Signatures and experimental prospects”. In: *Phys. Rev. D* 72 (2005), p. 023508. arXiv: [astro-ph/0503486](#).
- [290] S. Galli, F. Iocco, G. Bertone, and A. Melchiorri. “Updated CMB constraints on Dark Matter annihilation cross-sections”. In: *Phys. Rev. D* 84 (2011), p. 027302. arXiv: [1106.1528 \[astro-ph.CO\]](#).
- [291] D. P. Finkbeiner, S. Galli, T. Lin, and T. R. Slatyer. “Searching for Dark Matter in the CMB: A Compact Parameterization of Energy Injection from New Physics”. In: *Phys. Rev. D* 85 (2012), p. 043522. arXiv: [1109.6322 \[astro-ph.CO\]](#).
- [292] T. R. Slatyer. “Indirect dark matter signatures in the cosmic dark ages. I. Generalizing the bound on s-wave dark matter annihilation from Planck results”. In: *Phys. Rev. D* 93.2 (2016), p. 023527. arXiv: [1506.03811 \[hep-ph\]](#).
- [293] T. R. Slatyer. “Indirect Dark Matter Signatures in the Cosmic Dark Ages II. Ionization, Heating and Photon Production from Arbitrary Energy Injections”. In: *Phys. Rev. D* 93.2 (2016), p. 023521. arXiv: [1506.03812 \[astro-ph.CO\]](#).

- [294] Cherenkov Telescope Array Consortium. *Likelihoods for the CTA sensitivity to a dark matter signal from the Galactic centre*. <https://doi.org/10.5281/zenodo.4057987>. 2020.
- [295] N. Anand, A. L. Fitzpatrick, and W. C. Haxton. “Weakly interacting massive particle-nucleus elastic scattering response”. In: *Phys. Rev. C* 89.6 (2014), p. 065501. arXiv: [1308.6288](https://arxiv.org/abs/1308.6288) [[hep-ph](#)].
- [296] W. Bernreuther and M. Suzuki. “The electric dipole moment of the electron”. In: *Rev. Mod. Phys.* 63 (1991), pp. 313–340. [Erratum: *Rev. Mod. Phys.* 64, 633 (1992)].
- [297] T. Chupp, P. Fierlinger, M. Ramsey-Musolf, and J. Singh. “Electric dipole moments of atoms, molecules, nuclei, and particles”. In: *Rev. Mod. Phys.* 91.1 (2019), p. 015001. arXiv: [1710.02504](https://arxiv.org/abs/1710.02504) [[physics.atom-ph](#)].
- [298] R. Alarcon et al. “Electric dipole moments and the search for new physics”. In: *Snowmass 2021*. 2022. arXiv: [2203.08103](https://arxiv.org/abs/2203.08103) [[hep-ph](#)].
- [299] V. Andreev et al. “Improved limit on the electric dipole moment of the electron”. In: *Nature* 562.7727 (2018), pp. 355–360.
- [300] O. Lebedev. “The Higgs portal to cosmology”. In: *Prog. Part. Nucl. Phys.* 120 (2021), p. 103881. arXiv: [2104.03342](https://arxiv.org/abs/2104.03342) [[hep-ph](#)].
- [301] J. A. Evans, S. Gori, and J. Shelton. “Looking for the WIMP Next Door”. In: *JHEP* 02 (2018), p. 100. arXiv: [1712.03974](https://arxiv.org/abs/1712.03974) [[hep-ph](#)].
- [302] D. J. Griffiths and D. F. Schroeter. *Introduction to quantum mechanics*. Third edition. Cambridge ; New York, NY: Cambridge University Press, 2018.
- [303] G. Arfken, G. Arfken, H. Weber, and F. Harris. *Mathematical Methods for Physicists: A Comprehensive Guide*. Elsevier Science, 2013.
- [304] F. Calogero. *Variable Phase Approach to Potential Scattering by F Calogero*. Elsevier Science, 1967.
- [305] M. Böhm, A. Denner, and H. Joos. *Gauge theories of the strong and electroweak interaction*. Vieweg+Teubner Verlag, 2001.
- [306] A. Akhiezer and N. Merenkov. “The theory of lepton bound-state production”. In: *Journal of Physics B: Atomic, Molecular and Optical Physics* 29.10 (1996), p. 2135.
- [307] E. Merzbacher. *Quantum mechanics*. John Wiley & Sons, 1998.